Persistent holographic storage in Photorefractive crystals

Thesis by

Ali Adibi

In Partial Fulfillment of the Requirements

for the Degree of

Doctor of Philosophy

California Institute of Technology

Pasadena, California

2000

(Submitted May 30, 2000)

In the name of God

To my mother, my wife, and in the loving memory of my father

Acknowledgements

First and foremost, I am indebted to my thesis advisor, Dr. Demetri Psaltis, without whom this work would not have been possible. I would like to thank Dr. Psaltis for his unerring support and advice, and for many contributions to this work and to my own intellectual development. Dr. Psaltis, with his broad expertise and superb intuition, has been the brightest highlight of my educational career, and I will greatly miss his inspiration and enthusiasm when I leave Caltech. He has been both an outstanding advisor and a very good friend for me. I think it is impossible to thank all his help, support, and friendship with only a few words. I just say that I am proud of being one of Dr. Psaltis's students.

A very interesting part of my Ph.D. work was collaborating with outstanding Caltech people, especially the members of Dr. Psaltis's group. My most pleasant and rewarding experience is meeting and collaborating with Dr. Karsten Buse. Dr. Buse's amazing knowledge and dedication to science along with his nice and humble personality makes him an excellent collaborator. His role in this work and in my educational career is very important. Karsten's great intuition and outstanding experience helped me a lot and saved me from taking wrong turns. I would like to thank him from my heart for all his help. I would like to thank Dr. Kelvin Wagner, Dr. Chuan Xie, Dr. Xuefeng Yue, Gregory Steckman, Yunping Yang, Jose Mumbru, George Panotopoulos, and Chris Moser for their help, collaboration, and comments. I would like to thank other members of Dr. Psaltis's group, especially Wenhai Liu, Zhiewen Liu, Greg Billock, Dr. Allen Pu, Dr. Xin An, Dr. Ernest Chuang, Dr. George Barbastathis, Dr. Michael Levene, Dr. Geoffrey Burr, Dr. Jean–Jacques Drolet, Benjamin Schupp, and Irena Maravic for their friendship and help. I would like to thank Caltech professors for their comments and help, especially Dr. Amnon Yariv, Dr. Kerry Vahala, Dr. Axel Scherer, Dr. Yaser Abu–Mostafa, Dr. Robert McEliece, and Dr. Joel Franklin. I am also very grateful of Mrs. Ya–Yun Liu for

helping me with the lab equipment, Dimitris Sakellariou for solving the problems with the computer cluster, and Mrs. Helen Carrier and Mrs. Lyn Hein for administrative tasks and equipment ordering. My special thanks goes to Mrs. Lucinda Acosta for her help in preparing the numerous documents related to my work. I will never forget her dedication, friendship, and patience in helping me with what I needed even after working hours.

I feel that I am indebted to my teachers from the elementary school to the graduate school. All of them have had their important roles in my education. Unfortunately, it is not possible to list all of them, but I would like to mention Dr. Mohammad H. Rahnavard and Dr. Habibollah Abiri, the professors of the Electrical Engineering Department of Shiraz University (Shiraz, Iran), for their important role in my undergraduate studies, and Dr. Thomas Gaylord, Dr. Elias Glytsis, Dr. Glenn Smith, Dr. Kevin Brennan, and Dr. Dale Ray (all from Georgia Institute of Technology) for their important role in my graduate career.

I would like to thank all my friends for their friendship and advice. Among them, I would like to mention Mr. Mohammad Karimi and his family for their friendship.

My greatest appreciation goes to my family. Most of all, I would like to thank my mother Mrs. S. Sharif and the memory of my father Mr. Abdolhossein Adibi for their encouraging and supporting my interests in science and their helps and sacrifices in my life. I would like to thank my wife Mrs. S. Salimijahromi for her support and patience during the time of hard work. I would like also to thank my sisters Mrs. Z. Adibi and Miss. M. Adibi for their friendly advice in my life.

Finally, I would like to thank God for his blessings during my entire life. I believe in my heart that I could not do any thing without his support. Thank God for giving me such generous and sacrificing mother, father, and sisters. Thank God for giving me such a nice and sacrificing wife. Thank God for giving me such nice friends, and thank God for putting me in such a nice environment as Caltech.

Abstract

The work presented in this thesis has been focused on solving the most important and long-lasting problem of destructive read–out in holographic recording in photorefractive crystals. Several interesting methods for solving this problem were proposed and demonstrated by researchers for more than two decades. However, none of them were practical for read / write applications. The most promising all-optical method, which is still being pursued by some researchers, was two-step recording. However, the method suffers from low sensitivity and dynamic range, even in the optimized conditions. Furthermore, several experimental results were not explained due to the lack of a complete understanding of the dominant phenomena that were involved.

Our strategy in solving the problem of destructive read-out of holograms was to first provide a complete understanding of the physics of the two-step recording method by appropriate modeling, and to explain the experimental results that had not been explained before. Such an understanding gave us a good idea about the major problem of the method, and we were able to find a solution to that problem by adding one dopand to the recording crystal. The method we developed both theoretically and experimentally in this thesis is called two-center holographic recording. The initial results of the method (without any optimization) offer more than one order of magnitude (and for some parameters, two orders of magnitude) improvement over the optimized two-step recording method.

In this thesis, we provide a complete modeling for two-center recording that agrees very well with the experimental results, provides us with the understanding of the main physical phenomena that are involved, and helps us in optimizing the method. The next step is to relate the material and system parameters for the system design. We present in this thesis a standard framework for such a relation, and outline the main general steps in the system design using two-center recording. The idea developed in this thesis opens us several avenues for further thinking and research, and

some of them are already being investigated by different research groups.

Contents

List of Figures

List of Tables

Chapter 1 Introduction

1.1 Holography: basic idea and applications

Holography was developed in the late 1940s by Dennis Gabor [2]. However, first substantial advances in this field were achieved in the early 1960s stimulated by the invention of laser systems. A further important step forward was the work of Leith and Upatnieks who introduced holographic recording schemes with off–axis reference beams. A large number of investigations in the field of holography took place in the 1960s and early 1970s [3, 4]. Nowadays, holography has found many applications in industry as well as in science, and is still a rapidly developing field of research.

The basic principle of holography is rather simple: Two coherent waves, an information–bearing signal beam and a reference beam of known shape, are superimposed. The created interference pattern is stored as an amplitude pattern (amplitude hologram, absorption hologram) or as a phase pattern (phase hologram, refractive–index hologram, relief hologram). The stored interference pattern itself is called a "hologram." Subsequent illumination of the hologram with the reference wave causes diffraction of the reference light from the absorption or phase hologram and by these means the original signal wave is reconstructed. Unlike photography, not only the amplitude of the signal wave but also the complete phase information is correctly retrieved.

Holography covers many different areas of applications. To name a few examples: (1) Security issues. To copy holograms requires sophisticated optical setups or, in the case of printed holograms, master stamps. Thus copying of holograms is rather difficult. Therefore, holograms are used, e.g., on credit–cards. (2) Holography became a direction of art. New effects can be realized. Furthermore, expensive objects in exhibitions can be replaced by holograms once again for security reasons. (3) Holograms attract attention which is used more and more in advertising of products. (4)

Holography became a very important measurement technique. Especially holographic interferometry is a powerful tool for non–destructive testing of object deformations and also for vibration analysis (a nice summary is given in, e.g., [5]). (5) Holographical optical elements can be used in telecommunication for, e.g., optical interconnects or wavelength division multiplexers [6, 7].

An application of special importance is volume holographic data storage [8]. This technique promises large storage capacities, short access times, large data transfer rates and the capability of optical processing. Such storage systems have been investigated since the 1970s. The basic components needed are a laser light source, a spatial light modulator which imposes the information on the object beam, the storage medium and a camera system to retrieve the data. Nowadays small, powerful and reliable diode or diode–pumped solid–state lasers are available. Liquid crystal light modulators became a product for the mass market, and CCD cameras ('charge–coupled devices') are also rapidly developing if we think, e.g., about digital photography. These advances and an increasing demand for storage capacity renewed the interest in holographic storage systems and especially within the last years remarkable advantages were achieved and impressive demonstrations were performed. Examples are storage systems presented by Rockwell Intl. [9] and IBM [10].

The holographic storage systems are often called 'volume' storage devices because successful reconstruction of stored information requires fulfillment of the Bragg condition which is also called the momentum condition. The wavevectors of incoming and diffracted waves must match a grating vector of the hologram (conservation of momentum). Bragg mismatch can be achieved by rotation of the sample or of the reference beam (angular multiplexing), by changing the wavelength of the read–out light (wavelength multiplexing) or by several other techniques. This allows the superposition of many holograms in the same volume and yields a volume storage method instead of conventional surface storage which is utilized, e.g., in compact–disc (CD) or hard–disk drives. Multiplexing many holograms requires small Bragg tolerance which can be achieved by using thick materials. The term "thick" refers to the thickness of the recording medium compared to the period of the light wavelength. Thus samples

where the light interacts over 100 μm or more with the material are thick in the sense of the Bragg criterion.

1.2 Holographic recording materials: organic and inorganic

The critical problem of holography in general and of holographic storage in particular is the availability of a suitable recording medium with the desired properties such as high resolution (more than 10,000 Lines/mm), large dynamic range (high refractive index or absorption changes), large sensitivity (high diffraction efficiencies of the produced hologram upon small recording exposures), long lifetime, low light scattering, reversibility / fixing on demand, and low price. Besides standard materials (silver halide photographic materials, dichromated gelatin, inorganic photochromic materials, thermoplastics, photoresists; for a review see, e.g., [11]) several other inorganic and organic materials are known which can be useful for holographic applications.

Photorefractive crystals are very attractive candidates for holographic recording [12]. Nonuniform illumination with visible light excites charge carriers from impurities either into the conduction or into the valence band. These charge carriers migrate and generate a spatially modulated electric current density due to diffusion, drift, and the bulk photovoltaic effect [13]. Finally, the electrons are trapped by empty impurities. A space–charge field arises which modulates the refractive index via the electrooptic effect and a volume phase hologram is formed.

The photorefractive effect in electrooptic crystals was discovered in lithium–niobate ($LiNbO_3$) [14]. Iron is known to be a photorefractive dopand of this material [15]. For visible light the charge transport in $LiNbO_3$:Fe is through the conduction band, and Fe^{2+} and Fe^{3+} are sources and traps of the charge carriers. However, besides $LiNbO_3$ several further inorganic photorefractive materials exist and are studied intensively such as the perovskite crystals barium titanate ($BaTiO_3$) and potassium niobate ($KNbO_3$), the tungsten–bonze–type crystal strontium–barium niobate

($Sr_{0.61}Ba_{0.39}Nb_2O_6$, SBN), the sillenite–type crystals bismuth–silicon oxide ($Bi_{12}SiO_{20}$, BSO), bismuth–titanium oxide ($Bi_{12}TiO_{20}$, BTO) and bismuth–germanium oxide ($Bi_{12}GeO_{20}$, BGO), and the semiconductor crystals gallium arsenide (GaAs) and cadmium telluride (CdTe), to name just some examples.

The crystals have several properties which are highly desired for holographic applications: (1) High spatial resolution, (2) excellent optical quality and therefore very weak light scattering, (3) good long–term stability even in unpleasant chemical or electrical environments, (4) commercial availability of samples of reproducible properties, and (5) large thickness (up to some cm).

The major drawback of inorganic photorefractive crystals is a relatively low sensitivity. For this reason several different types of organic materials are also intensively studied. Here we mention only four different systems: (1) Several photosensitive organic recording media are based on photo–assisted polymerization of, e.g., methyl–methacrylate (MMA) to poly–methyl–methacrylate (PMMA). This process gains sensitivity from irreversible chemical reactions [16]. Photopolymers of this type continue to be developed and tested [17, 18]. Light–induced shrinkage, light scattering, and the limitation to relatively thin samples are the major drawbacks of this class of materials. (2) Photoadressable polymers contain azo–benzene chromophors which occur in the cis and trans states. Polarized light yields an alignment of side–chains containing azo–benzene chromophors which causes strong optical dichroism and via the Kramers–Kronig principle also large refractive–index changes [19]. The process is fully reversible, i.e., intense unpolarized light yields a random orientation of the molecules and erases the stored refractive index patterns. However, the sensitivity is much less compared to that of the photopolymers. (3) Organic crystals are also grown, e.g., the system called 'DAST' (4–N, N–dimethylamino–4'–N'–methyl–stilbazolium toluene–p–sulfonate) received some attention [20]. These crystals exhibit large electro–optic coefficients and they are shown to be photorefractive, but currently the overall performance of this material (magnitude of the refractive–index changes, response time) is disappointing. (4) Photorefractive polymers appear to be much more promising. Although previous work existed, a breakthrough in this area was achieved in 1994

[21]. Diffraction efficiencies up to almost 100% were achieved with 100 μm thick samples. The process is the same as in photorefractive crystals: Inhomogeneous illumination builds space–charge fields up which modulate the refractive index via the linear electro–optic effect. The major problem of this material is that external electrical fields of the order of 100 kV/mm are required. The external fields are the main charge driving force and they are also necessary to align nonlinear molecules in order to create a linear electro–optic effect.

Which class of materials is preferable, inorganic crystals or organic compounds, may depend on the actual application. Reversibility together with the ability of all–optical fixing is required for several applications, and in particular for holographic storage. No such fixing method exists so far for organic materials, but, as we will see below, inorganic electro–optic crystals allow all–optical fixing of data without loosing the ability of desired optical erasure. In this thesis, we only consider holographic recording in photorefractive crystals, particularly $LiNbO_3$.

The photorefractive effect in electro–optic crystals is completely reversible, i.e., homogeneous illumination redistributes the charge carriers back and new holograms can be recorded. However, this implies also that the holograms are erased during reading due to the homogeneous read–out illumination. This has been known as the major problem in holographic recording in photorefractives for many years. Thus, methods are needed which allow to fix the stored information and to reconstruct all data without erasing the holograms. These methods can be considered as different schemes for persistent (non–destructive read–out) holographic recording.

1.3 Persistent holographic recording methods: copying and all–optical schemes

Several solutions to the fundamental problem of destructive read–out in photorefractives have been proposed and experimentally demonstrated. The techniques might be grouped into two categories: (1) *Copying of the electronic space–charge pattern to*

other properties of the material. Thermal fixing [22] and electrical fixing [23] belong to this group. (2) *All–optical fixing.* Two–step excitations [24, 25], read–out with wavevector spectra [26, 27], frequency–difference holograms [28], and the interaction of deep and shallow traps [29] are examples for this type of fixing.

Upon thermal fixing the electron pattern is transposed to a modulated concentration of ions (protons for example) [22]. This is achieved by heating the crystal during or after recording. At higher temperatures (typically 180 °C) ions are mobile and drift in the space–charge fields. After cooling to room temperature the ions are immobile and the ionic pattern is fixed. Homogeneous illumination creates spatially modulated currents because of strongly modulated concentrations of electron sources and traps (Fe^{2+} and Fe^{3+} in $LiNbO_3$:Fe) [30]. Thus homogeneous light develops the hologram instead of erasing it. Although thermal fixing provides excellent lifetimes of the stored information [31], inhomogeneous thermal expansion of the crystals, and the inconvenience of heating and cooling are serious problems of this method. Furthermore, adding or deleting of one fixed hologram in a previously fixed holographic system can not be performed without heating the crystal again and, therefore, affecting the pre–existing holograms. Therefore, thermal fixing is not appropriate for read / write storage applications.

Electrical fixing is another copying approach [23]. The space–charge field together with an externally applied electric field may exceed locally the coercitive field and causes switching of domains. The created domain pattern is a replica of the space–charge pattern, and the polarization changes are compensated by a modulated concentration of electron sources and traps [32, 33]. Once again, homogeneous light develops the space–charge pattern because of spatially modulated currents arising from the modulated concentrations of photorefractive centers. Although 1000 holograms were multiplexed in a single crystal by this technique [34], the storage capacity is limited because ferroelectric domains tend to have minimum dimensions which are significantly larger than the light wavelength.

Two–step excitatons via an imaginary or a real intermediate state [24, 25] are examples of all–optical solutions. The combined energy of two photons is necessary

to generate a free electron. In the case of two photons of equal energy, reduction of the read–out light intensity yields a quadratic drop of the erasure speed [24]. This technique is not persistent, but a large asymmetry between recording and erasure speed can be achieved. Usage of different wavelengths for sensitizing (short wavelength, 'gating light') and recording (long wavelengths) yields a better persistence of the stored information [25]. Anyhow, both techniques employ pulse lasers of high intensity.

Other all–optical techniques use wave–vector spectra to achieve Bragg matching [26, 27], but losses of storage capacity occur because the cross–talk increases strongly. Frequency–difference holograms use lower harmonics which come into the picture because of the product between conductivity and space–charge field in the charge–transport equations [28, 35, 36]. Recording a new hologram (conductivity pattern) over an already existing one (space–charge field pattern) creates sub–harmonics which allow non–destructive retrieval of the information, because the photon energy of the subharmonic wavelength is not sufficient to excite charge carriers. The major problem of this technique is a substantial loss of dynamic range.

Another solution to the problem of destructive read–out (sometimes called volatility) is the usage of a combination of a deep and a shallow center [29]. Visible light excites charge carriers from the deep center either to the conduction or the valence band. Some of the free carriers are trapped by shallow levels from which they can be re–excited by long–wavelength light. After recording, the holograms can be read with the long–wavelength light without erasure because the shallow levels are empty if no sensitizing light is present. However, thermal excitations also depopulate the shallow levels and large light intensities are required to use this process [29].

1.4 Outline of the thesis

The work presented in this thesis has been focused on solving the most important and long–lasting problem of destructive read–out in holographic recording in photorefractive crystals. To obtain persistence (non–destructive read–out) for read /

write holographic storage systems, we need to use an all optical method as explained previously.

To solve the problems of the existing methods and propose new methods in each research area, it is essential to carefully understand the basic mechanisms of the method along with the main sources of the problem. In Chapter 2, we explain the basic physical mechanisms in two–step holographic recording in $LiNbO_3$: Fe crystals. We develop an approximate analytic solution set to the governing equations of the two–step recording. This analytic solution helps us a lot in the understanding the dominant mechanisms in two–step recording. With the help of this analytic solution, we explain all of the observed experimental results including ones that were not successfully explained previously. We then explain the major drawback of two–step recording as the short lifetime of the electrons in the shallow polaron levels. Knowing the source of the drawback, we propose the usage of doubly–doped $LiNbO_3$ crystals in which both traps are due to dopands and have very long electron lifetime. This method, which we call two–center holographic recording, is described in detail in Chapter 3. We show that using doubly–doped $LiNbO_3$ crystals results in obtaining very good persistence while improving the other performance characteristics compared to two–step recording in singly–doped $LiNbO_3$ crystals. We also develop a theoretical model that explains all the experimental observations in two–center recording very well. Using this model, we propose and demonstrate a strategy for optimizing the performance of two–center recording by choosing the design parameters appropriately.

Some important system issues in two–center recording are discussed in Chapter 4. We propose and demonstrate a solution for the problem of low sensitivity observed in the first demonstrations of two–center recording. We also develop a recording schedule for recording multiple holograms in the same volume using two–center recording.

A conclusive comparison of two–step and two–center recording is presented in Chapter 5. It is shown that the performance characteristics obtained with low intensities in the early stages of two–center recording are at least one order of magnitude better than that obtained with much higher intensities in the highly optimized stages of two–step recording. The major conclusion made in Chapter 5 is that two–center

recording is the best existing method for persistent holographic recording in $LiNbO_3$ crystals.

In Chapter 6, we discuss the range of performance characteristics that can be obtained by using a doubly–doped $LiNbO_3$ crystal even if persistence is not required. It is shown in Chapter 6 that the performance range obtained by using doubly–doped crystals is much larger than that obtained by using a singly–doped crystal. Furthermore, we show that the main challenge in holographic recording is how to use the trade off among dynamic range, sensitivity, and persistence to obtain the desired performance.

Most of the focus in Chapters 2–6 is on the material properties. In Chapter 7, we derive the relationship among the material parameters (dynamic range and sensitivity) and system parameters (recording and read–out rates, access time, and storage capacity). We show that the system parameters of two–center recording with the existing materials are very promising for the realization of practical read / write holographic memory systems. We also present an outline for the design of a practical memory module. We also propose some guidelines for future research for improving material properties for two–center recording. Finally the main conclusions of the thesis along with guidelines for future research in the different aspects of two–center recording are summarized in Chapter 8.

The main goal in the work presented in this thesis has been the understanding of the basic physical principles in each recording scheme, and using such understanding to find the main sources for each problem that needs to be solved. Knowing the source of a problem is always helpful in finding possible solutions faster. To reach the main goal, we tried to develop an appropriate model for each recording method and use the model to explain the experimental observations. On the other hand, we performed different experiments to test the theoretical predictions of each model. Such a combination of theory and experiment is very helpful in developing a good understanding of the basic physical mechanisms involved in each case, and the research is much more successful if we carefully understand what is going on!

Chapter 2 Two–step holographic recording

2.1 Introduction

Volume holographic memories are promising for high density digital or analog data storage [8]. Excellent light sources, spatial light modulators and camera systems are available nowadays due to boosting applications of optics in communications and entertainment industries. The critical issue for holographic storage is still the recording material. Volume holographic storage systems are tried and tested with photorefractive crystals as the recording medium [37, 9, 10]. Inhomogeneous illumination with an interference pattern of reference and signal beams excites charge carriers from impurity levels into the conduction or valence bands, the charge carriers migrate and they are trapped by empty impurities elsewhere. A space–charge field builds up and modulates the refractive index via the electro–optic effect. Different photorefractive centers can interact and the performance depends strongly on the host material, intrinsic and extrinsic defects, and experimental conditions [38, 39].

The photorefractive effect is reversible, i.e., homogeneous illumination redistributes the electrons back and new recording is possible. Thus, read/write memories can be implemented. However, the major obstacle is that readout also requires homogeneous illumination, which erases the stored information. Thermal fixing [22], electrical fixing [23], two–photon recording [24], frequency–difference holograms [40] and readout with wavevector spectra [26] are known techniques to overcome the problem of destructive read–out. From all these techniques, two–step (or as sometimes called, two–photon) processes appear to be the most promising. They require no heating, no external electric fields and they may enable recording with a high dynamic range, i.e., multiplexing of many holograms with high efficiency.

Two–step recording can be realized in materials where two photons are required for generation of one free electron or hole. The first photon excites the charge carrier into an intermediate level and the second either into the conduction or valence band. Typically different wavelengths are chosen for the first and the second excitation. Low energy photons contain the holographic information and homogeneous illumination with high energy photons sensitizes the material for recording. During readout only light of the recording wavelength is present and persistent (or as sometimes called, non–volatile) read–out is achieved.

Multiphoton photorefractive storage has been discovered in lithium niobate ($LiNbO_3$) crystals [24], and the first persistent storage experiments utilizing two–photon excitations were performed with $LiTaO_3$ [25], which is isomorphic to $LiNbO_3$. Picosecond light pulses (wavelengths 1064 and 532 nm) were used in these early investigations. More recently, larger refractive index changes and better sensitivities were achieved using $LiNbO_3$ and nanosecond light pulses of the same wavelengths [41, 42, 43]. The crystals were doped with iron or with copper as the photorefractive centers. Iron and copper occur in $LiNbO_3$ and $LiTaO_3$ in the valence states $Fe^{2+/3+}$ and $Cu^{+/2+}$ [15]. Charge transport via the conduction band dominates, i.e., Fe^{2+} and Cu^{+} are the filled impurities.

Two–step recording requires the presence of intermediate energy levels. Excitations via virtual levels are possible for recording with femtosecond light pulses [44], but they can not play a role in experiments with nanosecond pulses. Crystal–field splitting yields an excited state of Fe^{2+}, which matches well with the 1064 nm radiation [15], but the filled copper level, Cu^{+}, does not have such an excited electron state and very similar two–photon effects were observed in $LiNbO_3$:Fe and in $LiNbO_3$:Cu, ruling out that the excited state of the Fe^{2+} ions plays a significant role [42].

Congruent lithium niobate has a substantial lack of lithium ions. The lithium concentration is only 48.3 mol % [45]. At least 1% of the intrinsic defect niobium on lithium site (Nb_{Li}) is present [46, 47]. The valence state of this center is 5+, but one electron can be trapped, reducing the valence state to 4+ and creating a small polaron. All photorefractive properties of $LiNbO_3$:Fe for illumination with continuous wave

visible light and with high intensity green light pulses are quantitatively explained by a two–center charge transport model considering the photorefractive sites $Fe^{2+/3+}$ and $Nb_{Li}^{4+/5+}$. Two–step transitions of electrons from Fe^{2+} via the small polaron into the conduction band are possible, because the concentration of small polarons is large and each Fe^{2+} ions has some empty Nb_{Li} close to its location. Effects like light–induced absorption changes, intensity dependent saturation values of the refractive index changes and photoconductivities, which are superlinear in the light intensity, can be explained within this model [48]. It is straightforward to employ this charge transport model also for the explanation of the two–photon recording processes used for persistent storage. The large lifetime of the excited charge carriers in the polarons [49] makes it more appropriate to use the term 'two–step excitation' rather than 'two–photon excitation'.

A theoretical analysis of the two–step persistent storage in $LiNbO_3$:Fe is still missing. The question is whether the iron/polaron model can describe quantitatively the obtained experimental results using all charge transport parameters known for $LiNbO_3$ from literature. The aim is to achieve a model and a parameter set which explains *all* photorefractive features of congruent $LiNbO_3$, at low and high light intensities, for one–step and for two–step recording. A full theoretical description and understanding of the processes is highly desired, because then the optimum performance of the material and the conditions to achieve this performance can be predicted. Furthermore, there are several experimental observations that have not been explained yet. Having a reliable model is very helpful in understanding the physical mechanisms responsible for two–step recording and the explanation of the experimental observations. First general attempts of a formal analysis of the processes involved in different two–step recording schemes are performed only for materials with negligible bulk photovoltaic effect [50].

We present in this chapter a full theoretical analysis of the two–step recording processes in congruent iron–doped lithium niobate. The two–center charge transport model for $LiNbO_3$ is explained in Section 2.3. We first present a complete numerical solution to the governing equations of the model and show its validity by comparing

the theoretical expectations with several experimental results. Then, we use several approximations to derive an analytic solution to the equations of the model. Such an analytic solution is very important in understanding the dominant physical mechanisms in two–step recording. Using the analytic solution, we explain all experimental observations, especially those that were not explained before. Although we mainly concentrate on two–step recording with high intensity pulses, we can also use the model to analyze two–step recording with cw light. Based on the model, we explain the main deficit in two–step recording in singly–doped $LiNbO_3$ crystals. We also propose a way to overcome this deficit by using doubly–doped $LiNbO_3$ crystals. The details of the proposed method (two–center recording) will be discussed in Chapters 3 and 4.

2.2 Experiments

Melt–doped single domain $LiNbO_3$:Fe samples grown by the Czochralski technique are investigated. The total Fe concentration c_{Fe} of the samples is determined by X–ray fluorescence and atomic absorption spectroscopy. The samples contain typically between 370 and 1070 mol ppm Fe. The uncertainties of the determined c_{Fe} values are about $\pm$ 15%.

The valence states of the Fe ions are varied by suitable annealing treatments [15]. Heating in pure oxygen atmosphere, e.g., to a temperature of 1000 °C, tends to oxidize the ions to Fe^{3+}, whereas heating in argon atmosphere or vacuum (low oxygen partial pressure) yields a reduction of the ions to Fe^{2+}.

Determination of the concentrations $c_{Fe^{2+}}$ and $c_{Fe^{3+}}$ is based on Mössbauer experiments [15]. From the comparison of the Mössbauer results with optical absorption measurements, the oscillator strength of the bands are calculated [51]. The absorption coefficient at 477 nm for ordinarily polarized light, determined by a Cary 17D spectrometer, yields $c_{Fe^{2+}}$. Then, $c_{Fe^{3+}}$ can be determined because the entire Fe concentration of the crystal is known, and the Mössbauer results clearly demonstrate that only Fe^{2+} and Fe^{3+} states of Fe ions are present in $LiNbO_3$:Fe crystals. Typically

ratios of $c_{Fe^{2+}}/c_{Fe^{3+}}$ in the range from 0.01 to 1 can be adjusted easily.

Figure 2.1 shows a schematic illustration of the holographic setup [1]. A Q–switched Nd:YAG laser with a frequency doubler produces simultaneously infrared ($\lambda = 1064$ nm, pulse duration 25 ns) and green ($\lambda = 532$ nm, pulse duration 15 ns) ordinarily polarized TEM_{00} light pulses. The repetition rate of the system used is only about 0.1 Hz. A dielectric beam splitter separates the infrared and green light. An additional beam splitter divides the infrared light into two coherent waves of equal intensity. These beams enter the crystal symmetrically in a plane containing the crystal's $\vec{c}$–axis. The green pulse enters the sample simultaneously or with a delay of up to 100 ns achieved by an optical path difference.

Holographic read–out is performed by low intensity ordinarily polarized continuous–wave HeNe laser light ($\lambda = 633$ nm) entering the crystal under the Bragg angle. Photodiodes behind the sample detect transmitted and diffracted light intensities. The diffraction efficiency is defined as the ratio of the intensities of the diffracted and total transmitted light. From Kogelnik's formula [52] we then calculate the refractive index changes. The intersection angle of the infrared pulses and the light wavelength determine the fringe spacing Λ. This Λ value is in the employed transmission geometry typically about 1 to 2 μm. Neutral density filters provide variations of infrared and green light intensities.

Figure 2.2 illustrates a typical hologram writing and erasing cycle. The time scale corresponds to the exposure time of the green ($\lambda = 532$ nm) light. The circles represent experimental data and the solid lines are exponential fits taking into account absorption effects [1]. Typical total infrared and green light intensities are $I_{1064} = 250$ GWm^{-2} and $I_{532} = 110$ GWm^{-2}.

2.3 Two–center model

The two–center charge transport model for $LiNbO_3$:Fe was introduced in 1993 by Jermann and Otten [48] and Figure 2.3 illustrates the model in a band diagram.

[1] Experiments were performed by K. Buse.

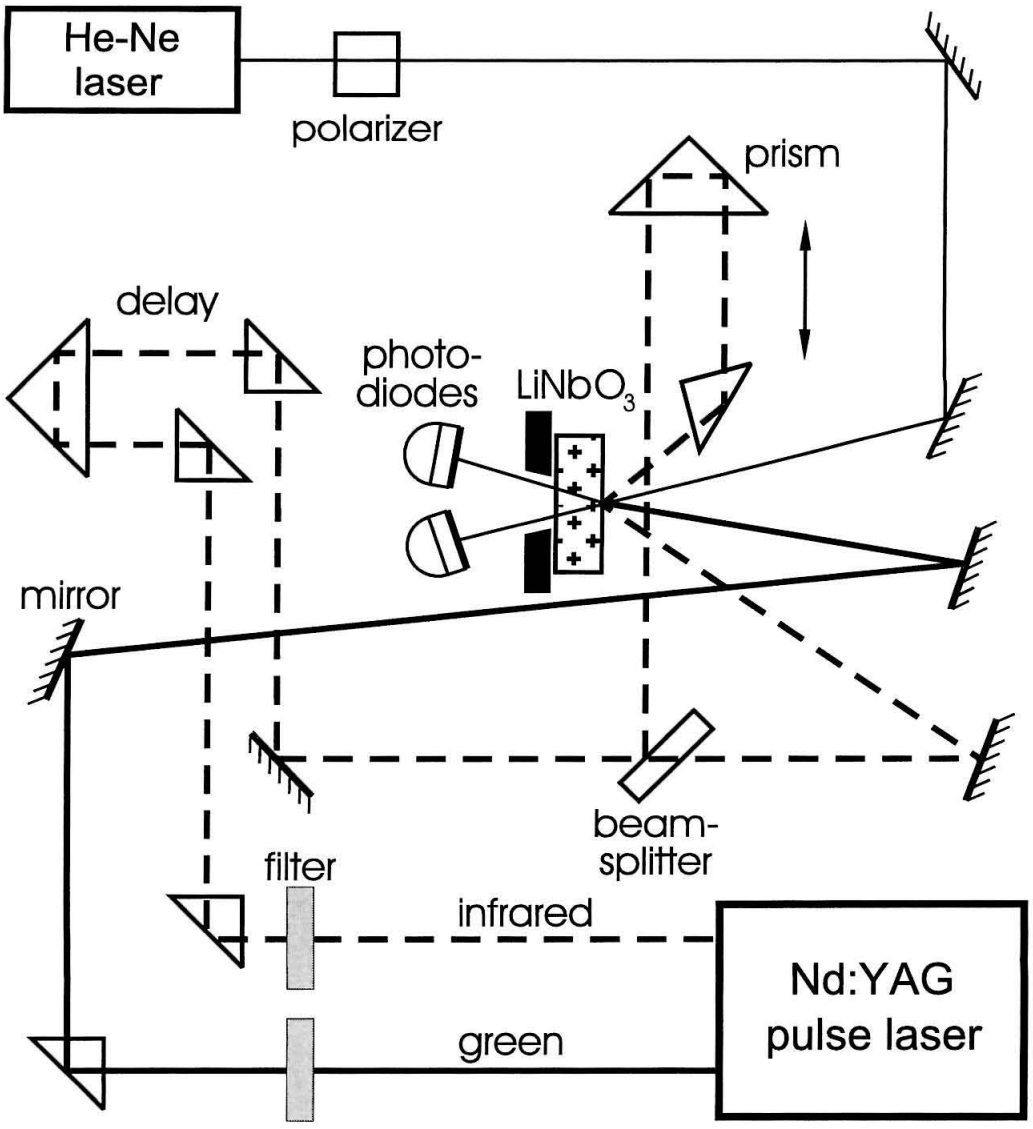

Figure 2.1: Schematic drawing of the experimental setup for two–step holographic recording.

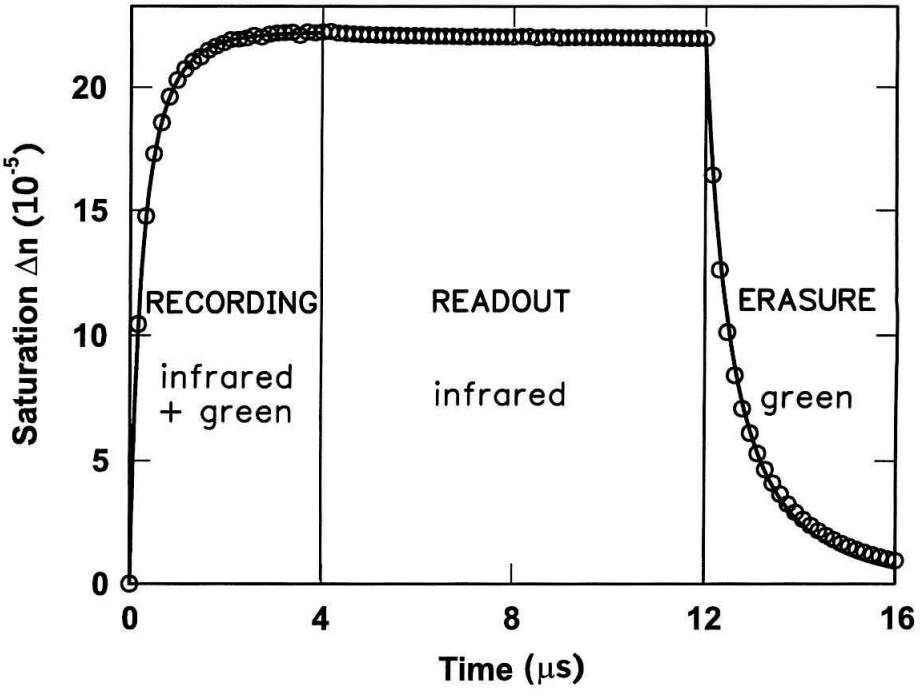

Figure 2.2: Refractive–index amplitude Δn of a holographic grating during a typical writing and erasing cycle. The circles illustrate the experimental data and the solid lines are monoexponential fits taking into account absorption effects [1]. The time scale corresponds to the exposure time of the green ($\lambda = 532$ nm) light. During the first 4 μs infrared and green light (wavelengths: $\lambda = 1064$ nm, $\lambda = 532$ nm; intensities: $I_{1064} = 250$ GWm^{-2}, $I_{532} = 110$ GWm^{-2}) are simultaneously present. The next 8 μs read–out of the hologram with one of the infrared writing beams (I_{1064} =125 GWm^{-2}, $I_{532} = 0$) is performed. After this second step, the hologram is erased by green light ($I_{1064} = 0$, $I_{532} = 110$ GWm^{-2}).

Electrons can be excited from Fe^{2+} by light either into the conduction band or into Nb_{Li}^{5+} forming Nb_{Li}^{4+}. Direct excitation into Nb_{Li} requires that there are always some Nb_{Li} centers close to each Fe^{2+}. This is the case, because Nb_{Li} is an intrinsic defect which occurs in a very high concentration [46, 47]. The electrons in the shallower Nb_{Li}^{4+} traps can be excited to the conduction band by light or thermally. Otherwise, they recombine directly with the iron ions where they come from. The conduction band electrons can recombine either with Fe^{3+} or with Nb_{Li}^{5+}. The iron level is 'deep' and the polaron level is often called 'shallow' although these words have a different meaning in semiconductor physics, where shallow levels are characterized by a strong thermal generation rate.

Green light (wavelength 532 nm) has sufficient photon energy to excite electrons from Fe^{2+} either into the conduction band or into the secondary centers, or from Nb_{Li}^{4+} into the conduction band. Infrared light (wavelength 1064 nm), however, has a smaller photon energy that is sufficient to excite electrons from Nb_{Li}^{4+} into the conduction band, only.

Excitation and recombination of the electrons can be described by the rate equations [48]

$$\begin{aligned}
\frac{\partial N_{\mathrm{Fe}}^{-}}{\partial t} &= -[q_{\mathrm{Fe}} s_{\mathrm{Fe}} + q_{\mathrm{FeX}} s_{\mathrm{FeX}} (N_{\mathrm{X}} - N_{\mathrm{X}}^{-})] I_{\mathrm{G}} N_{\mathrm{Fe}}^{-} \\
&\quad + (\gamma_{\mathrm{Fe}} n + \gamma_{\mathrm{FeX}} N_{\mathrm{X}}^{-})(N_{\mathrm{Fe}} - N_{\mathrm{Fe}}^{-}) \,, \qquad (2.1) \\
\frac{\partial N_{\mathrm{X}}^{-}}{\partial t} &= -[\beta_{\mathrm{X}} + q_{\mathrm{X,G}} s_{\mathrm{X,G}} I_{\mathrm{G}} + q_{\mathrm{X,IR}} s_{\mathrm{X,IR}} I_{\mathrm{IR}} + \gamma_{\mathrm{XFe}} (N_{\mathrm{Fe}} - N_{\mathrm{Fe}}^{-})] N_{\mathrm{X}}^{-} \\
&\quad + (\gamma_{\mathrm{X}} n + q_{\mathrm{FeX}} s_{\mathrm{FeX}} I_{\mathrm{G}} N_{\mathrm{Fe}}^{-})(N_{\mathrm{X}} - N_{\mathrm{X}}^{-}) \,. \qquad (2.2)
\end{aligned}$$

All symbols are introduced in Table 2.1. Excitation of electrons from Nb_{Li}^{4+} is possible by green light (wavelength 532 nm) and by infrared light (wavelength 1064 nm). Thus, we added in the Equation (2.2) a generation term to account for the presence of the infrared light. Some parameters have a subscript 'G' or 'IR' to indicate whether they correspond to green or infrared light.

We treat the situation where the light intensity and therefore all other spatially dependent quantities vary only along one direction. The coordinate along this direction

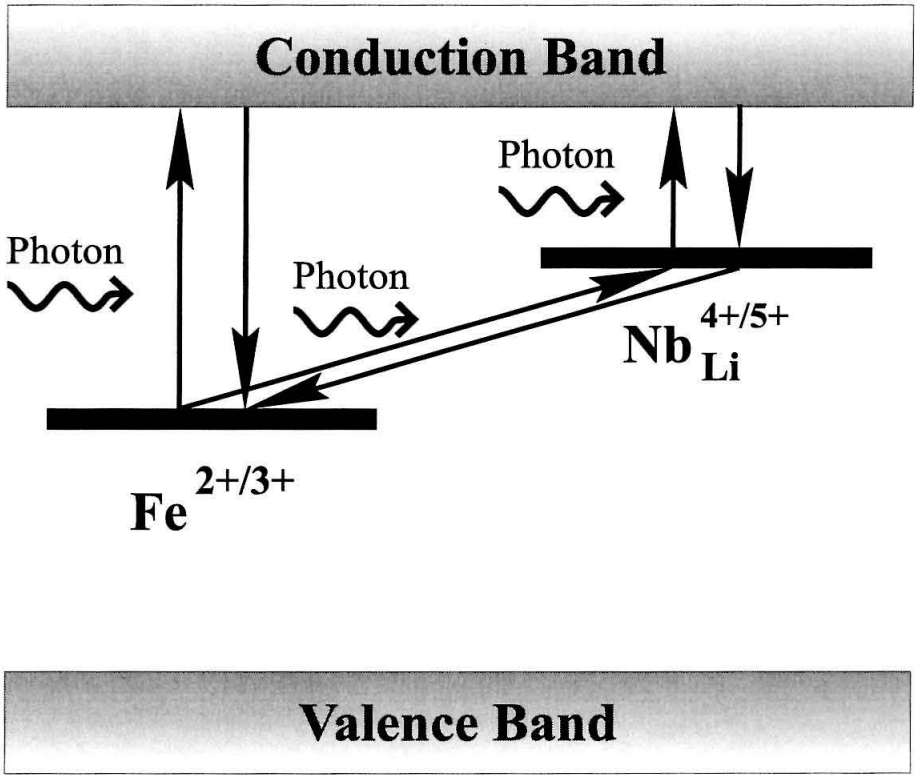

Figure 2.3: Band diagram of the charge transport situation in congruent iron–doped lithium niobate ($LiNbO_3$). The arrows indicate excitation and recombination of electrons. A detailed description is given in the text.

Quantity (unit)	Meaning	Value	Reference
	Parameters of Fe		
N_{Fe} (m^{-3})	total concentration of Fe	(1.2×10^{25})	
N_{Fe}^{-} (m^{-3})	concentration of Fe^{2+}	(5.7×10^{24})	
$q_{\mathrm{Fe}} s_{\mathrm{Fe}}$ (m^2/J)	absorption cross section of Fe^{2+} for absorption of a photon *and* excitation of an electron from Fe^{2+} into the conduction band (light wavelength 532 nm)	1.0×10^{-5}	[48]
γ_{Fe} (m^3/s)	coefficient for recombination of conduction band electrons with Fe^{3+}	1.65×10^{-14}	[48]
$-\kappa_{\mathrm{Fe}}$ (m^3/V)	bulk photovoltaic coefficient for excitation of electrons from Fe^{2+} into the conduction band (light wavelength 532 nm)	3.5×10^{-33}	[48]
	Parameters of Nb_{Li}		
N_{X} (m^{-3})	total concentration of Nb_{Li}	10^{26}	[46, 47, 48]
N_{X}^{-} (m^{-3})	concentration of Nb_{Li}^{4+}	variable	
β_{X} (s^{-1})	rate of thermal excitation of electrons from Nb_{Li}^{4+} into the conduction band	0	[48]
$q_{\mathrm{X,G}} s_{\mathrm{X,G}}$ (m^2/J)	absorption cross section of Nb_{Li}^{4+} for absorption of a photon *and* excitation of an electron into the conduction band (light wavelength 532 nm)	5.0×10^{-5}	[48]
$q_{\mathrm{X,IR}} s_{\mathrm{X,IR}}$ (m^2/J)	absorption cross section of Nb_{Li}^{4+} for absorption of a photon *and* excitation of an electron into the conduction band (light wavelength 1064 nm)	5.4×10^{-5}	[this work]
γ_{X} (m^3/s)	coefficient for recombination of conduction band electrons with Nb_{Li}^{5+}	0	[48]
$-\kappa_{\mathrm{X,G}}$ (m^3/V)	bulk photovoltaic coefficient for excitation of electrons from Nb_{Li}^{4+} into the conduction band (light wavelength 532 nm)	21.2×10^{-33}	[48]
$-\kappa_{\mathrm{X,IR}}$ (m^3/V)	bulk photovoltaic coefficient for excitation of electrons from Nb_{Li}^{4+} into the conduction band (light wavelength 1064 nm)	32×10^{-33}	[this work]
	Parameters related to Fe and Nb_{Li}		
$q_{\mathrm{FeX}} s_{\mathrm{FeX}}$ (m^5/J)	absorption cross section of Fe^{2+} for absorption of a photon *and* excitation of an electron into Nb_{Li}^{4+} (light wavelength 532 nm)	3.22×10^{-30}	[48]
γ_{XFe} (m^3/s)	coefficient for recombination of electrons from Nb_{Li}^{4+} with Fe^{3+}	1.14×10^{-21}	[48]

Quantity (unit)	Meaning	Value	Reference
	Parameters of $LiNbO_3$		
ϵ	dielectric coefficient	28	[53, 54]
r_{13} (m/V)	electro–optic coefficient (light wavelength 632.8 nm)	10.9×10^{-12}	[55]
n_o	refractive index for ordinarily polarized light (wavelength 632.8 nm)	2.286	[56]
	Charge transport parameters		
j (A/m^2)	current density	variable	
μ (m^2/Vs)	electron mobility in the conduction band	7.4×10^{-5}	[57]
n (m^{-3})	density of free electrons in the conduction band	variable	
ρ (As/m^3)	total charge density	variable	
N_A (m^{-3})	concentration of nonmobile positive compensation charge, which maintains overall charge neutrality	(5.7×10^{24})	
E (V/m)	space–charge field	variable	
	Fundamental constants		
k_B (J/K)	Boltzmann constant	1.38×10^{-23}	
ϵ_0 (As/Vm)	primitivity of free space	8.85×10^{-12}	
	Parameters related to the experimental conditions		
T (K)	crystal temperature	293	
K (m^{-1})	spatial frequency of the interference pattern	2.9×10^6	
Λ (m)	period length of the interference pattern	2.2×10^{-6}	
I_G (W/m^2)	intensity of the spatially homogeneous green light (wavelength 532 nm)	variable	
I_{IR} (W/m^2)	intensity of the infrared light (wavelength 1064 nm)	variable	
m	modulation degree of the interference pattern of the infrared light	variable	
t_p (s)	duration of each green and infrared light pulse	15×10^{-9}	

Table 2.1: Units, meaning and values of all quantities used involved in the analysis of two–step holographic recording in $LiNbO_3$:Fe. Subscripts '0' and '1' are added in the text to the spatially dependent quantities to indicate zeroth and first Fourier components. Values in parentheses show standard values, which are valid if nothing else is mentioned.

is x. Then, the current, continuity, charge and Poisson equations are

$$
\begin{aligned}
j &= e\mu n E + \kappa_{\mathrm{Fe}} N_{\mathrm{Fe}}^{-} I_{\mathrm{G}} + \kappa_{\mathrm{X,G}} N_{\mathrm{X}}^{-} I_{\mathrm{G}} + \kappa_{\mathrm{X,IR}} N_{\mathrm{X}}^{-} I_{\mathrm{IR}} + \mu k_{\mathrm{B}} T \frac{\partial n}{\partial x} , && (2.3)\\
\frac{\partial j}{\partial x} &= -e \left(\frac{\partial N_{\mathrm{Fe}}^{-}}{\partial t} + \frac{\partial N_{\mathrm{X}}^{-}}{\partial t} + \frac{\partial n}{\partial t} \right) , && (2.4)\\
\rho &= -e(N_{\mathrm{Fe}}^{-} + N_{\mathrm{X}}^{-} + n - N_{\mathrm{A}}) , && (2.5)\\
\frac{\partial E}{\partial x} &= \frac{\rho}{\epsilon \epsilon_0} . && (2.6)
\end{aligned}
$$

Drift, bulk photovoltaic and diffusion currents are considered. All symbols are introduced in Table 2.1.

Jermann and Otten determined a set of parameters, which describes excellently all photorefractive features of $LiNbO_3$:Fe observed in experiments with green light at continuous–wave and at pulsed laser intensities [48]. Their parameter set will be also employed in this work. Thus, our model is immediately consistent with all usual photorefractive properties of $LiNbO_3$:Fe for recording with light of one wavelength. Only two of the many parameters occurring in the Equations (2.1)-(2.6) are new and unknown: $q_{\mathrm{X,IR}} s_{\mathrm{X,IR}}$ and $\kappa_{\mathrm{X,IR}}$, the photon absorption cross section and the bulk photovoltaic coefficient of $\mathrm{Nb}_{\mathrm{Li}}^{4+/5+}$ for excitations with infrared light.

To study this model we will investigate the situation of simultaneous illumination with spatially homogeneous green light and with a sinusoidally modulated infrared interference pattern

$$
I_{\mathrm{IR}} = I_{\mathrm{IR},0}[1 + m \sin(Kx)] . \qquad (2.7)
$$

The symbols are explained in Table 2.1. We assume that the light intensity does not change with time during illumination. All calculations are performed with $m = 0.1$ and the obtained space–charge fields are normalized to m, i.e., they are divided by m.

2.4 Numerical solution

2.4.1 Algorithm

One may argue that typical approximations like the adiabatic approximation [58] or Fourier development with the neglection of higher Fourier orders [59] can not be applied to our situation. Therefore, Equations (2.1)-(2.7) are solved numerically in space without any approximation. The calculations are performed for one period length of the grating, and cyclic boundary conditions are used.

The starting condition is the steady–state situation in the dark with a homogeneous concentration of Fe^{2+}, which is equal to the concentration of compensators (or acceptors) N_A, because the Nb_{Li} centers are initially not populated, i.e., $N_X^- = 0$. Calculations are done in time steps dt: First, the concentration patterns $N_{Fe}^-(x, t+dt)$ and $N_X^-(x, t+dt)$ are calculated using the Equations (2.1) and (2.2), and the values $N_{Fe}^-(x, t)$ and $N_X^-(x, t)$. The current density $j(x, t)$ is calculated from Equation (2.3) and the concentration pattern $n(x, t+dt)$ is finally obtained from $n(x, t)$ and from the Equations (2.1), (2.2) and (2.4). Then Equation (2.5) and integration of Equation (2.6) finally yield the space–charge field $E(x, t+dt)$. This cycle is periodically repeated until the end of one light pulse is reached. The typical repetition frequency of pulsed lasers is low, i.e., around 10 Hz. The time between the pulses is sufficient that all electrons that were excited to Nb_{Li}^{4+} recombine locally with Fe^{3+}. Thus, the program adds to N_{Fe}^- the actual N_X^- values at the end of each pulse and sets N_X^- to zero afterwards. The created refractive index changes for ordinarily polarized red light (wavelength 632.8 nm) are calculated with $\Delta n(x) = -(1/2) n_o^3 r_{13} E(x)$, using the parameters introduced in Table 2.1.

The time steps are always chosen so small that further reduction has no influence on the calculated results. A typical time step for the calculations is 1 ps, and 100 points in space are used to represent one period length of the interference pattern.

Numerical solution of the high intensity properties, as it is done here, benefits from one fact: the concentration of the electrons in the conduction band n is only two or three orders of magnitude smaller than the defect concentrations. The difference is

much larger for low light intensities, and n can not be obtained in the way described above because of limited calculation accuracy, i.e., n is the tiny difference of two large and almost completely compensating rates. Anyhow, the algorithm is fine for pulsed *illumination* and no approximations have to be introduced.

2.4.2 Shape and evolution of the space–charge field

Figure 2.4 shows the space–charge field pattern for different times. The space–charge field is a replica of the light pattern and has an almost perfect sinusoidal shape. Thus, the amplitude of the space–charge field modulation can be easily determined from a sinusoidal fit to the computed data. This result is a first indication that Fourier development will be a useful approach for obtaining an analytical solution to the problem.

The evolution of the space–charge field amplitude during recording and erasure is presented in Figure 2.5. No electrons are in the $Nb_{Li}^{4+/5+}$ centers at the beginning of each light pulse. Thus, the green light starts to erase the previously written hologram due to direct excitation of electrons into the conduction band and the created conductivity. However, the $Nb_{Li}^{4+/5+}$ is populated more and more during the pulse. The infrared light excites electrons from this level into the conduction band, a modulated bulk photovoltaic current arises and the space–charge field grows. These processes are the origin of what we observe in the saturation regime, i.e., after long recording times, during each pulse at first a decrease and then an increase of the space–charge field amplitude. Saturation means that erasure and recording effects compensate each other completely. From Figure 2.5 it becomes also clear that the evolution of the space–charge field during the pulse illumination can be very well approximated by a parabolic function. Furthermore, it can be seen that considering the fields at the end of each pulse, growth and erasure of the grating are described by monoexponential functions.

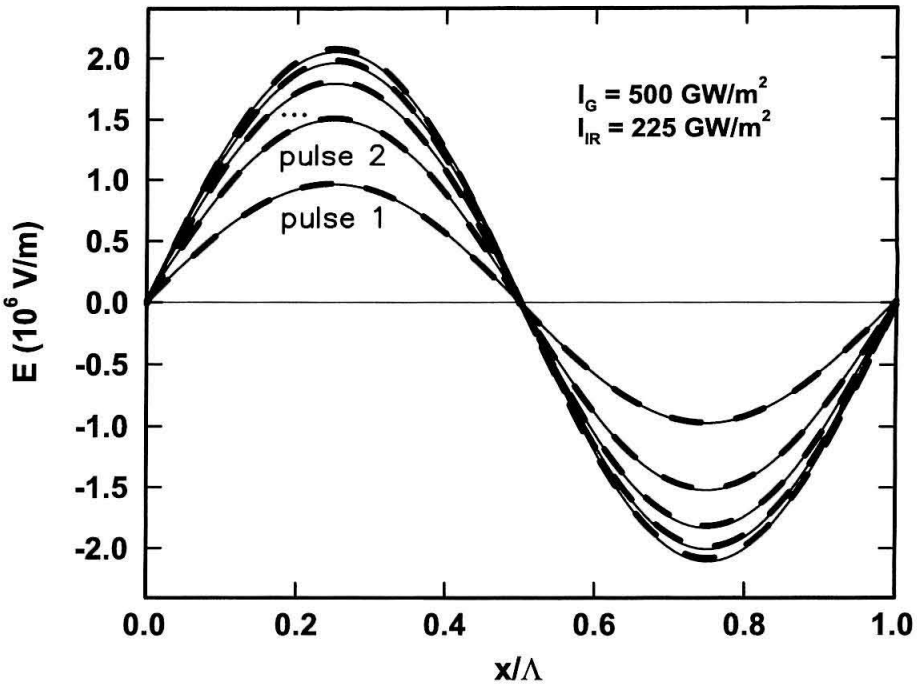

Figure 2.4: Space charge field E versus spatial coordinate x normalized to the grating period length Λ. The solid line shows the computed space–charge field after illumination with one, two, three, four and five light pulses of high intensity ($I_{\mathrm{G}} = 500$ GW/m^2, $I_{\mathrm{IR}} = 225$ GW/m^2). The dashed lines are sinusoidal fits to the calculated curves.

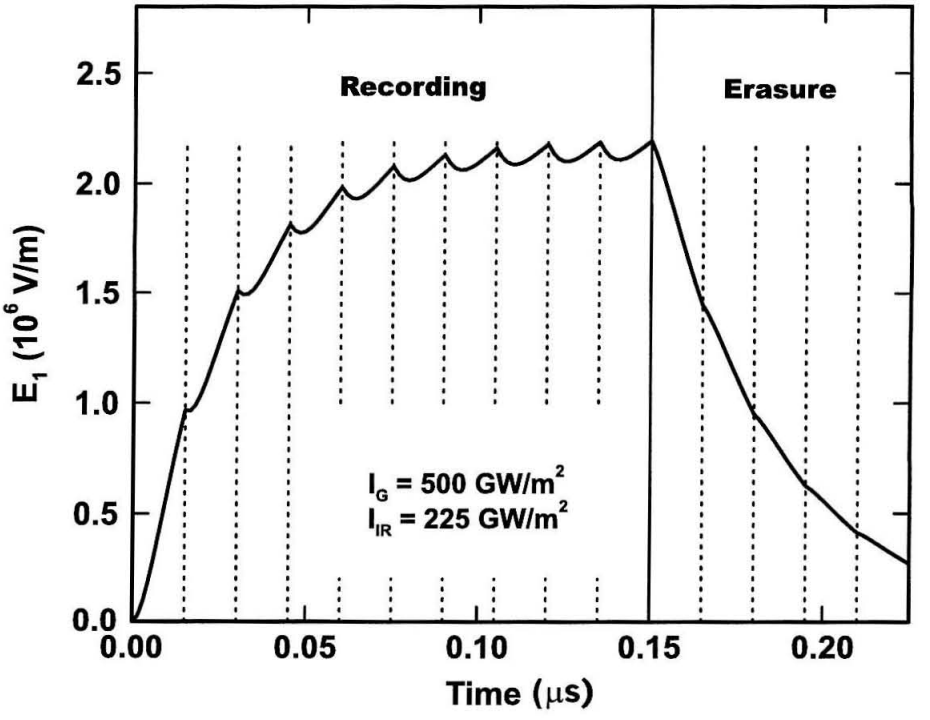

Figure 2.5: Amplitude E_1 of the space–charge field versus exposure time for recording and erasure. The light intensities are $I_G = 500$ GW/m^2 and $I_{IR,0} = 225$ GW/m^2. The averaged light intensities are equal for recording and erasure. The thin vertical lines indicate the end of each 15 ns long pulse.

2.4.3 Intensity and concentration dependences

The dependence of the saturation value of the created refractive index modulations and of the recording time constant on the intensities of green and infrared light were experimentally investigated [41, 43]. Furthermore, the influence of the initial homogeneous Fe^{2+} concentration on the sensitivity, i.e., on the change of the refractive index amplitude per unit time at the beginning of the recording, and of the initial homogeneous concentration of Fe^{3+} on the saturation values of the refractive index changes were also carefully determined in several experiments [41, 43].

Only two parameters remain free and can be varied in order to explain all these dependences, the photon absorption cross section $q_{X,IR}s_{X,IR}$ and the bulk photovoltaic coefficient $\kappa_{X,IR}$ of the $Nb_{Li}^{4+/5+}$ center for infrared light. Figures 2.6 – 2.9 show impressively that all experimental results mentioned above can be excellently described by proper selection of just these two parameters. The results obtained for $q_{X,IR}s_{X,IR}$ and $\kappa_{X,IR}$ are shown in Table 2.1. This success is a clear indication that the model is appropriate and that the determined parameters are very reliable.

2.5 Analytic solution

In this section, we develop an approximate analytic solution for Equations (2.1)–(2.6). To do this, we need some assumptions to simplify the equations. We can test the validity of each assumption by comparing results of the complete numerical solutions with and without that assumption.

2.5.1 Assumptions

Assumption #1: We neglect the trapping of conduction band electrons by the shallow traps during one pulse width. Therefore, we assume that the shallow traps are mainly populated by direct electron transfer from the deep traps, and the conduction band electrons are mainly trapped by the deep traps.

Assumption #2: We neglect thermal depopulation of the shallow traps within one

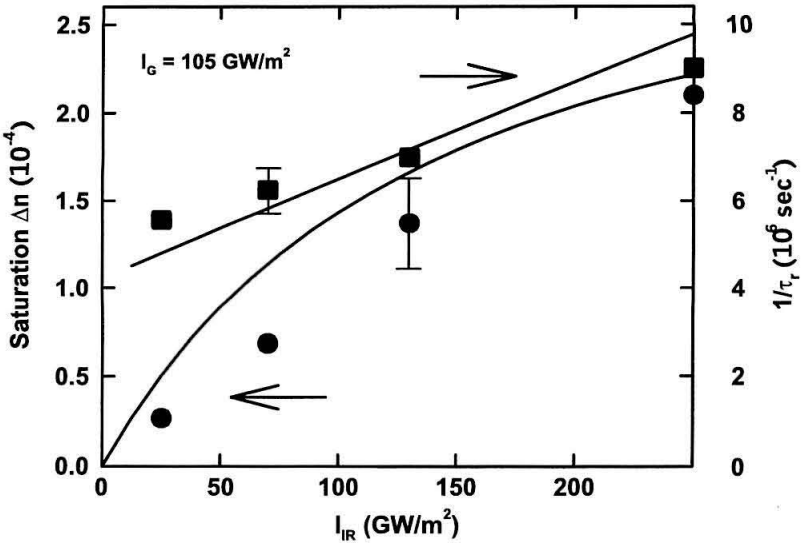

Figure 2.6: Variation of the saturation value of the amplitude of the refractive index grating (Δn) and recording speed τ_r^{-1} (inverse of recording time constant) with average infrared light intensity I_{IR} (with constant $I_G = 105$ GW/m^2). The curves are calculated in terms of the two–center model and the symbols are experimental data.

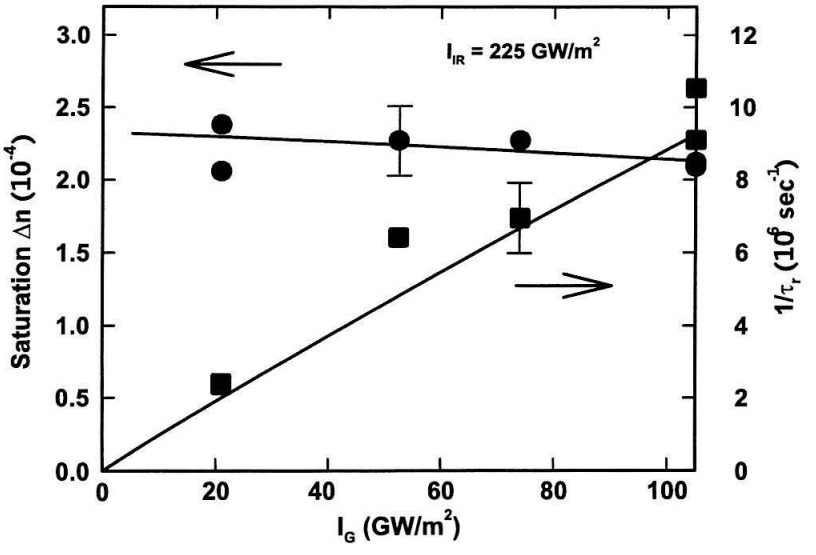

Figure 2.7: Variation of the saturation value of the amplitude of the refractive index grating (Δn) and recording speed τ_r^{-1} (inverse of recording time constants) with green light intensity I_G (with constant $I_{IR} = 225$ GW/m^2). The curves are calculated in terms of the two–center model and the symbols are experimental data.

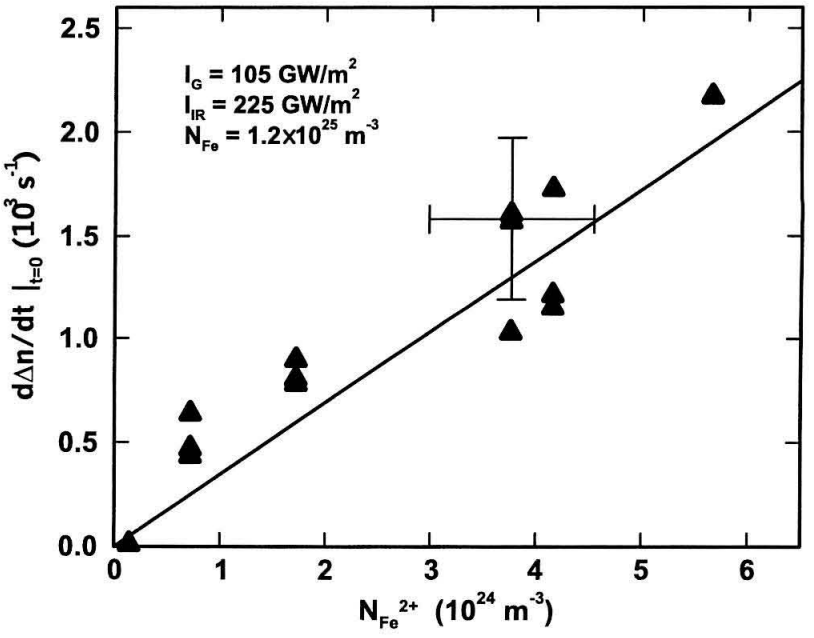

Figure 2.8: Variation of sensitivity (changes of the amplitude of the refractive index changes per time at the beginning of recording, $d\Delta n/dt|_{t=0}$) with the averaged concentration of Fe^{2+}, $N_{Fe^{2+}}$ (that is equal to N_A). The light intensities are $I_G = 105$ GW/m^2 and $I_{IR} = 225$ GW/m^2. The curve is calculated in terms of the two–center model and the symbols are experimental data.

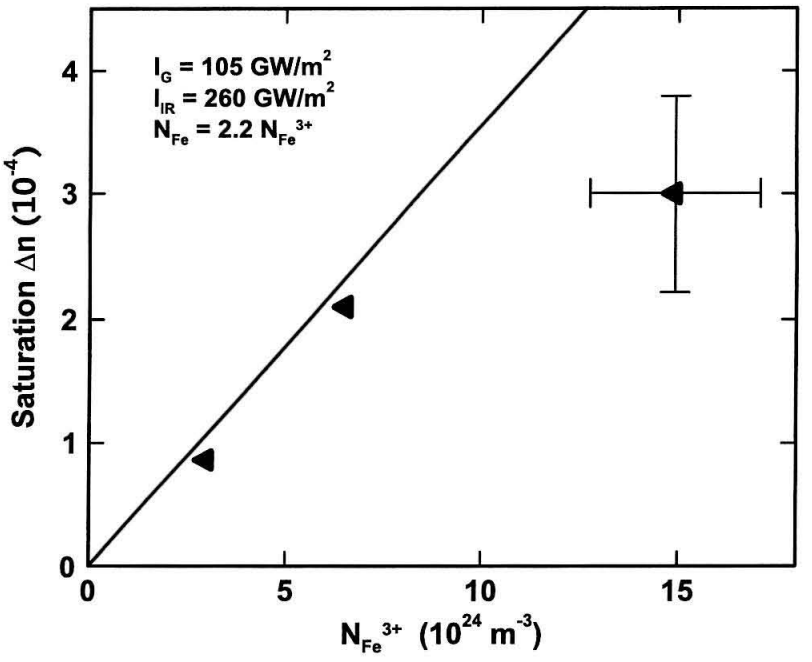

Figure 2.9: Variation of the saturation value of the amplitude of the refractive index grating (Δn) with concentration of Fe^{3+}, $N_{Fe^{3+}}$ (that is equal to $N_{Fe} - N_A$). It is assumed that the iron concentration increases according to $N_{Fe} = 2.2 \times N_{Fe^{3+}}$. The light intensities are $I_G = 105$ GW/m^2 and $I_{IR} = 260$ GW/m^2. The curve is calculated in terms of the two–center model and the symbols are experimental data.

pulse at room temperature. This is a valid assumption as the lifetime of the electrons in shallow traps is normally a few milliseconds while the pulse width is typically a few nanoseconds.

Assumption #3: We neglect direct electron transfer (recombination) from shallow traps to deep traps within one pulse width. This is a valid assumption due to the same reason as in assumption 2. Combining assumptions 2 and 3 is equivalent to assuming that the depopulation of the shallow traps within one pulse width (a few nanoseconds) is negligible.

Assumption #4: We assume that any change in the concentration of electrons in the conduction band occurs much faster than that in the concentration of electrons in either trap. Therefore, in the time scale of variation of electrons in the traps, we can assume $\partial n/\partial t = 0$. This is called the adiabatic approximation [58]. Numerical solutions of the system of differential equations with and without this assumption are practically the same as also reported by other authors (Ref. [48]).

Assumption #5: We assume that the electron concentration in the conduction band (n) is much smaller than that in the deep and shallow traps (N_{Fe}^{-} and N_{X}^{-}, respectively) as well as ($N_{\mathrm{Fe}}^{-} + N_{\mathrm{X}}^{-} - N_{\mathrm{A}}$). So, we neglect n in Equation (2.5).

Assumption #6: We neglect the diffusion term in Equation (2.3). This is a valid assumption in $LiNbO_3$ since the major source of the current is bulk photovoltaic current.

Numerical solutions of the governing differential equations are practically the same with and without these assumptions. In the next section, we add more approximations to get an analytic solution set for Equations (2.1)–(2.6).

Assumption #7: We assume that the sample is short–circuited, i.e., the electric field (E) does not have any DC component.

2.5.2 Fourier development

We assume that with sinusoidal intensity variation (Equation (2.7)), each variable in Equations (2.1)–(2.6) can be represented by the first two terms in its Fourier series

expansion. For example, the concentration of electrons in the deep traps ($N^-_{\rm Fe}$) can be represented as

$$N^-_{\rm Fe} = N^-_{\rm Fe0} + N^-_{\rm Fe1} \exp(jKx) \ . \tag{2.8}$$

Using this assumption, we can replace $\partial/\partial x$ by zero for the zeroth order variables (e.g.,$N^-_{\rm Fe0}$) and by iK for the first order ones (e.g.,$N^-_{\rm Fe0}$). Replacing every variable in Equations (2.1)–(2.6) with its first two Fourier expansion term and separating the equations for the zeroth and first order variables, we obtain the following two sets of equations:

$$\begin{aligned}
\frac{dN^-_{\rm Fe0}}{dt} &= -[q_{\rm Fe}s_{\rm Fe} + q_{\rm FeX}s_{\rm FeX}(N_{\rm X} - N^-_{\rm X0})]I_{\rm G}N^-_{\rm Fe0} \\
&\quad +\gamma_{\rm Fe}n_0(N_{\rm Fe} - N^-_{\rm Fe0}) \ , && (2.9) \\
\frac{dN^-_{\rm X0}}{dt} &= -(q_{\rm X,G}s_{\rm X,G}I_{\rm G} + q_{\rm X,IR}s_{\rm X,IR}I_{\rm IR0})N^-_{\rm X0} \\
&\quad +q_{\rm FeX}s_{\rm FeX}I_{\rm G}N^-_{\rm Fe0}(N_{\rm X} - N^-_{\rm X0}) \ , && (2.10) \\
\frac{dN^-_{\rm Fe0}}{dt} + \frac{dN^-_{\rm X0}}{dt} &= 0 \ , && (2.11) \\
N^-_{\rm Fe0} + N^-_{\rm X0} &= N_{\rm A} \ , && (2.12)
\end{aligned}$$

for the zeroth order variables, and

$$\begin{aligned}
\frac{dN^-_{\mathrm{Fe1}}}{dt} &= -\left([q_{\mathrm{Fe}}s_{\mathrm{Fe}} + q_{\mathrm{FeX}}s_{\mathrm{FeX}}(N_{\mathrm{X}} - N^-_{\mathrm{X0}})]I_{\mathrm{G}} + \gamma_{\mathrm{Fe}}n_0\right) N^-_{\mathrm{Fe1}} \\
&\quad +\gamma_{\mathrm{Fe}}n_1(N_{\mathrm{Fe}} - N^-_{\mathrm{Fe0}}) + q_{\mathrm{FeX}}s_{\mathrm{FeX}}N^-_{\mathrm{Fe0}}I_{\mathrm{G}}N^-_{\mathrm{X1}} \ , \qquad (2.13) \\
\frac{dN^-_{\mathrm{X1}}}{dt} &= -(q_{\mathrm{X,G}}s_{\mathrm{X,G}}I_{\mathrm{G}} + q_{\mathrm{X,IR}}s_{\mathrm{X,IR}}I_{\mathrm{IR0}} + q_{\mathrm{FeX}}s_{\mathrm{FeX}}I_{\mathrm{G}}N^-_{\mathrm{Fe0}})N^-_{\mathrm{X1}} \\
&\quad +q_{\mathrm{FeX}}s_{\mathrm{FeX}}I_{\mathrm{G}}(N_{\mathrm{X}} - N^-_{\mathrm{X0}})N^-_{\mathrm{Fe1}} - q_{\mathrm{X,IR}}s_{\mathrm{X,IR}}N^-_{\mathrm{X0}}I_{\mathrm{IR1}} \ , \qquad (2.14) \\
j_1 &= \frac{ie}{K}\left(\frac{dN^-_{\mathrm{Fe1}}}{dt} + \frac{dN^-_{\mathrm{X1}}}{dt}\right) \ , \qquad (2.15) \\
j_1 &= e\mu n_0 E_1 + \kappa_{\mathrm{Fe}}I_{\mathrm{G}}N^-_{\mathrm{Fe1}} + (\kappa_{\mathrm{X,G}}I_{\mathrm{G}} + \kappa_{\mathrm{X,IR}}I_{\mathrm{IR0}})N^-_{\mathrm{X1}} \\
&= +\kappa_{\mathrm{X,IR}}N^-_{\mathrm{X0}}I_{\mathrm{IR1}} \ , \qquad (2.16) \\
E_1 &= \frac{-ie}{K\epsilon\epsilon_0}(N^-_{\mathrm{Fe1}} + N^-_{\mathrm{X1}}) \ , \qquad (2.17)
\end{aligned}$$

for the first order variables. The goal is to find the first Fourier term of the space–charge field (E_1) that can be used to find the change in the index of refraction through electro–optic effect. To find E_1, we first need to solve the equations for the zeroth order variables (Equations (2.9)–(2.12)). We can then put the zeroth order variables into the first order equations and find E_1. To check the validity of the above assumptions, we solved the given zeroth and first order equations (with all assumptions applied) numerically. Figure 2.10 shows the variation of space–charge field E_1 with time during recording a hologram. The same variation calculated by the exact numerical solution is also shown in Figure 2.10 confirming the validity of all assumptions and approximations.

2.5.3 Solution of the zeroth order equations

To solve the zeroth order equations, we first put Equations (2.9) and (2.10) into Equation (2.11) and use $N^-_{\mathrm{Fe0}} = N_{\mathrm{A}} - N^-_{\mathrm{X0}}$ from Equation (2.12) to find n_0 in terms of N^-_{X0}

$$n_0 = \frac{q_{\mathrm{Fe}}s_{\mathrm{Fe}}I_{\mathrm{G}}N_{\mathrm{A}} + (q_{\mathrm{X,G}}s_{\mathrm{X,G}}I_{\mathrm{G}} + q_{\mathrm{X,IR}}s_{\mathrm{X,IR}}I_{\mathrm{IR0}} - q_{\mathrm{Fe}}s_{\mathrm{Fe}}I_{\mathrm{G}})N^-_{\mathrm{X0}}}{\gamma_{\mathrm{Fe}}(N_{\mathrm{Fe}} - N_{\mathrm{A}} + N^-_{\mathrm{X0}})} \ . \qquad (2.18)$$

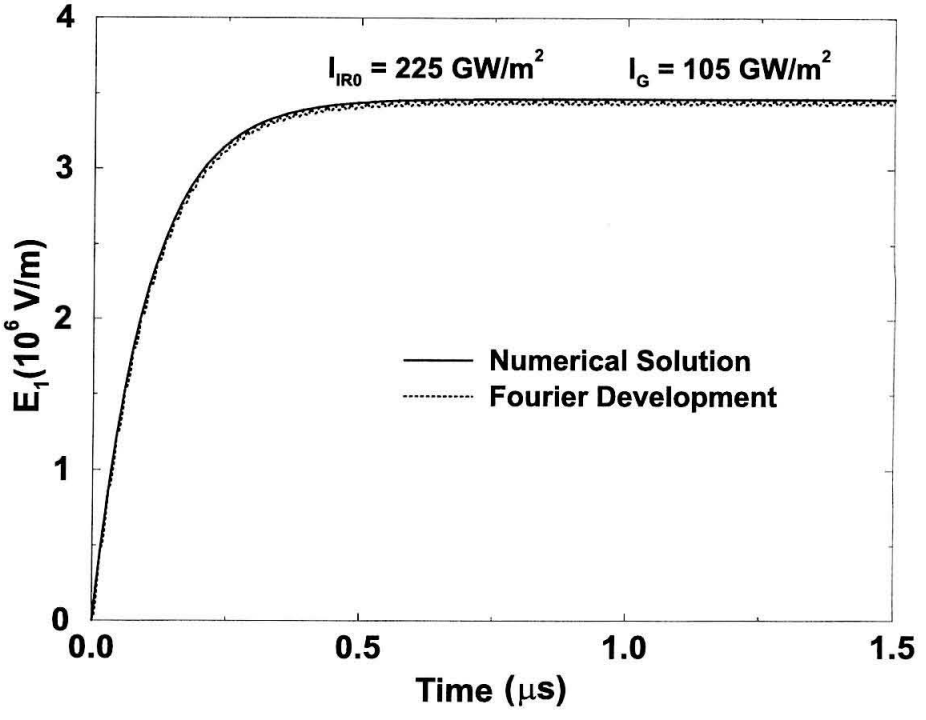

Figure 2.10: Theoretical calculation of the space–charge field versus time during recording of a hologram using two–step recording. The two curves are calculated using the complete numerical solution and the approximate solution based on Fourier development with several assumptions given in the text. The agreement between the curves is excellent. The light intensities used in these calculations are $I_{\mathrm{G}} = 105$ GW/m^2 and $I_{\mathrm{IR0}} = I_{\mathrm{IR1}} = 225$ GW/m^2.

Therefore, we only need to solve for N_{X0}^-. This can be done by putting $N_{Fe0}^- = N_A - N_{X0}^-$ into Equation (2.10) to obtain

$$\begin{aligned}\frac{dN_{X0}^-}{dt} &= q_{FeX}s_{FeX}I_G(N_{X0}^-)^2 - [(q_{X,G}s_{X,G} + q_{FeX}s_{FeX}(N_X + N_A))I_G + q_{X,IR}s_{X,IR}I_{IR0}]N_{X0}^- \\ &\quad + q_{FeX}s_{FeX}I_G N_X N_A \end{aligned} \tag{2.19}$$

with the initial condition being $N_{X0}^-(t = 0) = 0$.

Assumption #8: We assume that

$$q_{FeX}s_{FeX}I_G(N_{X0}^-)^2 \ll q_{FeX}s_{FeX}(N_X + N_A)N_{X0}^- , \tag{2.20}$$

or

$$N_{X0}^- \ll N_X + N_A . \tag{2.21}$$

Since we usually have $N_A \ll N_X$, the assumption of Equation (2.21) is equivalent to assuming that only a very small portion of the shallow traps is populated during one pulse width by electron transfer from the deep traps. Using this assumption, we can neglect $q_{FeX}s_{FeX}I_G(N_{X0}^-)^2$ in Equation (2.19) and solve for N_{X0}^- to obtain

$$N_{X0}^- = \frac{q_{FeX}s_{FeX}I_G N_X N_A[1 - \exp(-t/\tau_x)]}{q_{X,G}s_{X,G}I_G + q_{X,IR}s_{X,IR}I_{IR0} + q_{FeX}s_{FeX}(N_X + N_A)I_G} \tag{2.22}$$

where

$$\tau_x = \frac{1}{q_{X,G}s_{X,G}I_G + q_{X,IR}s_{X,IR}I_{IR0} + q_{FeX}s_{FeX}(N_X + N_A)I_G} . \tag{2.23}$$

Using the parameter values from Table 2.1 and assuming that sensitizing and recording intensities (I_G and I_{IR0}) of about 10^{12} W/m^2, we obtain $\tau_x \simeq 100$ nsec. For

a pulse width of $t_{\rm p} \simeq 15$ nsec, we can calculate $1 - \exp(-t_{\rm p}/\tau_{\rm x}) \simeq 0.14$. For $I_{\rm G} \simeq I_{\rm IR0} \simeq 10^{11}$ W/m^2, and the same pulse width, we obtain $1-\exp(-t_{\rm p}/\tau_{\rm x}) \simeq 0.015$. Therefore, we can use the following approximation for the time within one pulse width ($t \leq t_{\rm p}$)

$$1 - \exp(-t/\tau_{\rm x}) \simeq -\frac{t}{\tau_{\rm x}} . \tag{2.24}$$

With this approximation, we can summarize the zeroth order variables as

$$N^-_{\rm X0} = q_{\rm FeX} s_{\rm FeX} I_{\rm G} N_{\rm X} N_{\rm A} t , \tag{2.25}$$

$$N^-_{\rm Fe0} = N_{\rm A} - q_{\rm FeX} s_{\rm FeX} I_{\rm G} N_{\rm X} N_{\rm A} t \tag{2.26}$$

$$\begin{aligned} n_0 &= \frac{q_{\rm Fe} s_{\rm Fe} I_{\rm G} N_{\rm A} + (q_{\rm X,G} s_{\rm X,G} I_{\rm G} + q_{\rm X,IR} s_{\rm X,IR} I_{\rm IR0} - q_{\rm Fe} s_{\rm Fe} I_{\rm G}) N^-_{\rm X0}}{\gamma_{\rm Fe}(N_{\rm Fe} - N_{\rm A} + N^-_{\rm X0})} \\ &= \frac{q_{\rm Fe} s_{\rm Fe} I_{\rm G} N_{\rm A}}{\gamma_{\rm Fe}(N_{\rm Fe} - N_{\rm A})} + \\ &\quad \frac{q_{\rm X,G} s_{\rm X,G} I_{\rm G} + q_{\rm X,IR} s_{\rm X,IR} I_{\rm IR0} - \dfrac{N_{\rm Fe}}{N_{\rm Fe} - N_{\rm A}} q_{\rm Fe} s_{\rm Fe} I_{\rm G}}{\gamma_{\rm Fe}(N_{\rm Fe} - N_{\rm A})} q_{\rm FeX} s_{\rm FeX} I_{\rm G} N_{\rm X} N_{\rm A} t \\ &= n_{00} + n_{01} t , \end{aligned} \tag{2.27}$$

where we used binomial expansion of the denominator on the right–hand side of Equation (2.27) to obtain a solution in the form of $n_0 = n_{00} + n_{01}t$.

Note that we could have obtained the same result by assuming that the variables do not change much during one pulse width and approximating each variable by the first two terms in its Taylor series expansion around $t = 0$. In other words, we could have approximated each variable during one pulse width by a simple linear function of time (i.e., $C_1 + C_2 t$). The solution of the zeroth order equations would then consist of finding the unknown constants (i.e., C_1 and C_2).

2.5.4 Solution of the first order equations

We can put the solutions of the zeroth order equations into first order equations (Equations (2.13)–(2.17)) and solve them. To solve the first order equations, we first

combine Equations (2.16) and (2.17) to obtain

$$\begin{aligned} j_1 &= -\frac{ie^2\mu n_0}{K\epsilon\epsilon_0}(N^-_{\mathrm{Fe1}}+N^-_{\mathrm{X1}})+\kappa_{\mathrm{Fe}}I_{\mathrm{G}}N^-_{\mathrm{Fe1}}+(\kappa_{\mathrm{X,G}}I_{\mathrm{G}}+\kappa_{\mathrm{X,IR}}I_{\mathrm{IR0}})N^-_{\mathrm{X1}} \\ &\quad +\kappa_{\mathrm{X,IR}}N^-_{\mathrm{X0}}I_{\mathrm{IR1}}\ . \end{aligned} \tag{2.28}$$

Then, we put Equations (2.13), (2.14), and (2.28) into Equation (2.15), and solve for n_1 as a function of N^-_{Fe1} and N^-_{X1}. The result is

$$\begin{aligned} n_1 &= -\frac{\dfrac{e\mu n_0}{\epsilon\epsilon_0}+q_{\mathrm{X,G}}s_{\mathrm{X,G}}I_{\mathrm{G}}+q_{\mathrm{X,IR}}s_{\mathrm{X,IR}}I_{\mathrm{IR0}}-\left(\dfrac{iK}{e}\right)(\kappa_{\mathrm{X,G}}I_{\mathrm{G}}+\kappa_{\mathrm{X,IR}}I_{\mathrm{IR0}})}{\gamma_{\mathrm{Fe}}(N_{\mathrm{Fe}}-N_{\mathrm{A}}+N^-_{\mathrm{X0}})}N^-_{\mathrm{X1}} \\ &\quad +\frac{-\dfrac{e\mu n_0}{\epsilon\epsilon_0}+q_{\mathrm{Fe}}s_{\mathrm{Fe}}I_{\mathrm{G}}+\gamma_{\mathrm{Fe}}n_0-\dfrac{iK}{e}\kappa_{\mathrm{Fe}}I_{\mathrm{G}}}{\gamma_{\mathrm{Fe}}(N_{\mathrm{Fe}}-N_{\mathrm{A}}+N^-_{\mathrm{X0}})}N^-_{\mathrm{Fe1}} \\ &\quad +\frac{\left(q_{\mathrm{X,IR}}s_{\mathrm{X,IR}}-\dfrac{iK}{e}\kappa_{\mathrm{X,IR}}\right)N^-_{\mathrm{X0}}I_{\mathrm{IR1}}}{\gamma_{\mathrm{Fe}}(N_{\mathrm{Fe}}-N_{\mathrm{A}}+N^-_{\mathrm{X0}})}\ . \end{aligned} \tag{2.29}$$

The next step is to substitute n_1 from Equation (2.29) into Equations (2.13) and (2.14), and combine these two equations to obtain a set of two ordinary differential equations for two unknowns N^-_{X1} and $N^-_{\mathrm{Fe1}}+N^-_{\mathrm{X1}}$ as

$$\begin{aligned} \frac{d(N^-_{\mathrm{Fe1}}+N^-_{\mathrm{X1}})}{dt} &= -\left[\frac{e\mu(n_{00}+n_{01}t)}{\epsilon\epsilon_0}+\frac{iK}{e}\kappa_{\mathrm{Fe}}I_{\mathrm{G}}\right](N^-_{\mathrm{Fe1}}+N^-_{\mathrm{X1}}) \\ &\quad -\frac{iK}{e}(\kappa_{\mathrm{X,G}}I_{\mathrm{G}}+\kappa_{\mathrm{X,IR}}I_{\mathrm{IR0}}-\kappa_{\mathrm{Fe}}I_{\mathrm{G}})N^-_{\mathrm{X1}} \\ &\quad -\frac{iK}{e}\kappa_{\mathrm{X,IR}}I_{\mathrm{IR1}}(q_{\mathrm{FeX}}s_{\mathrm{FeX}}I_{\mathrm{G}}N_{\mathrm{X}}N_{\mathrm{A}})t\ , \end{aligned} \tag{2.30}$$

$$\begin{aligned} \frac{dN^-_{\mathrm{X1}}}{dt} &= q_{\mathrm{FeX}}s_{\mathrm{FeX}}I_{\mathrm{G}}[N_{\mathrm{X}}-(q_{\mathrm{FeX}}s_{\mathrm{FeX}}I_{\mathrm{G}}N_{\mathrm{X}}N_{\mathrm{A}})t](N^-_{\mathrm{Fe1}}+N^-_{\mathrm{X1}}) \\ &\quad -(q_{\mathrm{X,G}}s_{\mathrm{X,G}}I_{\mathrm{G}}+q_{\mathrm{X,IR}}s_{\mathrm{X,IR}}I_{\mathrm{IR0}})N^-_{\mathrm{X1}} \\ &\quad +q_{\mathrm{FeX}}s_{\mathrm{FeX}}I_{\mathrm{G}}[N_{\mathrm{X}}+N_{\mathrm{A}}-2(q_{\mathrm{FeX}}s_{\mathrm{FeX}}I_{\mathrm{G}}N_{\mathrm{X}}N_{\mathrm{A}})t]N^-_{\mathrm{X1}} \\ &\quad -q_{\mathrm{X,IR}}s_{\mathrm{X,IR}}I_{\mathrm{IR1}}(q_{\mathrm{FeX}}s_{\mathrm{FeX}}I_{\mathrm{G}}N_{\mathrm{X}}N_{\mathrm{A}})t\ , \end{aligned} \tag{2.31}$$

where we replaced the zeroth order variables (N^-_{X0}, N^-_{Fe0}, and n_0) by their equivalents from Equations (2.25)–(2.27). Note that we deliberately chose $N^-_{\mathrm{Fe1}}+N^-_{\mathrm{X1}}$ as one

variable since it is related to space–charge field as

$$E_1 = -\frac{ie}{K\epsilon\epsilon_0}(N^-_{\mathrm{Fe1}} + N^-_{\mathrm{X1}}) \; . \tag{2.32}$$

The initial conditions for Equations (2.30) and (2.31) are

$$N^-_{\mathrm{Fe1}}(t=0) = A \; , \tag{2.33}$$

$$N^-_{\mathrm{X1}}(t=0) = 0 \; , \tag{2.34}$$

where we assumed that all electrons in the shallow traps are transferred to the deep traps in the time interval between adjacent pulses resulting in fully empty shallow traps at the beginning of every pulse ($t = 0$). The value of N^-_{Fe1} at the beginning of each pulse (A) depends on time (or the total number of previous pulses) as space–charge is built up in Fe traps with time.

Assumption #9: We assume that the variations in first order variables (i.e., N^-_{Fe1} and N^-_{X1}) within one pulse width are small. Therefore, we can approximate every first order variable with the first few terms in its Taylor series expansion about $t = 0$. Since the right–hand sides of Equations (2.30) and (2.31) contain terms like $C_1 + C_2 t$, we approximate both $N^-_{\mathrm{Fe1}} + N^-_{\mathrm{X1}}$ and N^-_{X1} by the first three terms in their Taylor series expansions. Using the initial conditions given by Equations (2.33) and (2.34) and assuming that the pulse starts at time $t = 0$, we can write

$$N^-_{\mathrm{Fe1}} + N^-_{\mathrm{X1}} = A + Bt + Ct^2 \; , \tag{2.35}$$

$$N^-_{\mathrm{X1}} = Dt + Et^2 \; . \tag{2.36}$$

Putting Equations(2.35)–(2.36) into Equations (2.30)–(2.31), we obtain

$$\begin{aligned} B+2Ct &= -(\frac{e\mu(n_{00}+n_{01}t)}{\epsilon\epsilon_0}+\frac{iK}{e}\kappa_{\mathrm{Fe}}I_{\mathrm{G}})(A+Bt+Ct^2) \\ &\quad -\frac{iK}{e}(\kappa_{\mathrm{X,G}}I_{\mathrm{G}}+\kappa_{\mathrm{X,IR}}I_{\mathrm{IR0}}-\kappa_{\mathrm{Fe}}I_{\mathrm{G}})(Dt+Et^2) \\ &\quad -\frac{iK}{e}\kappa_{\mathrm{X,IR}}I_{\mathrm{IR1}}(q_{\mathrm{FeX}}s_{\mathrm{FeX}}I_{\mathrm{G}}N_{\mathrm{X}}N_{\mathrm{A}})t\ , \qquad (2.37) \\ D+2Et &= q_{\mathrm{FeX}}s_{\mathrm{FeX}}I_{\mathrm{G}}[N_{\mathrm{X}}-(q_{\mathrm{FeX}}s_{\mathrm{FeX}}I_{\mathrm{G}}N_{\mathrm{X}}N_{\mathrm{A}})t](A+Bt+Ct^2) \\ &\quad -(q_{\mathrm{X,G}}s_{\mathrm{X,G}}I_{\mathrm{G}}+q_{\mathrm{X,IR}}s_{\mathrm{X,IR}}I_{\mathrm{IR0}})(Dt+Et^2) \\ &\quad +q_{\mathrm{FeX}}s_{\mathrm{FeX}}I_{\mathrm{G}}[N_{\mathrm{X}}+N_{\mathrm{A}}-2(q_{\mathrm{FeX}}s_{\mathrm{FeX}}I_{\mathrm{G}}N_{\mathrm{X}}N_{\mathrm{A}})t](Dt+Et^2) \\ &\quad -q_{\mathrm{X,IR}}s_{\mathrm{X,IR}}I_{\mathrm{IR1}}(q_{\mathrm{FeX}}s_{\mathrm{FeX}}I_{\mathrm{G}}N_{\mathrm{X}}N_{\mathrm{A}})t\ . \qquad (2.38) \end{aligned}$$

$$(2.39)$$

Equating the coefficients of the first two powers of t (DC and linear terms) on the two sides of Equations (2.37) and (2.38), we can find a set of four equations for four unknowns, B, C, D, and E. Solving such a set of equations results in

$$\begin{aligned} B &= -(\frac{e\mu n_{00}}{\epsilon\epsilon_0}+\frac{iK}{e}\kappa_{\mathrm{Fe}}I_{\mathrm{G}})A\ , \qquad (2.40) \\ C &= \frac{1}{2}\left[(\frac{e\mu n_{00}}{\epsilon\epsilon_0}+\frac{iK}{e}\kappa_{\mathrm{Fe}}I_{\mathrm{G}})^2-\frac{e\mu n_{01}}{\epsilon\epsilon_0}\right]A \\ &\quad -\frac{1}{2}\left[q_{\mathrm{FeX}}s_{\mathrm{FeX}}I_{\mathrm{G}}N_{\mathrm{X}}\left(\frac{iK}{e}\right)(\kappa_{\mathrm{X,G}}I_{\mathrm{G}}+\kappa_{\mathrm{X,IR}}I_{\mathrm{IR0}}-\kappa_{\mathrm{Fe}}I_{\mathrm{G}})\right]A \\ &\quad -\frac{iK}{2e}\kappa_{\mathrm{X,IR}}q_{\mathrm{FeX}}s_{\mathrm{FeX}}I_{\mathrm{G}}N_{\mathrm{X}}N_{\mathrm{A}}I_{\mathrm{IR1}}\ , \qquad (2.41) \\ D &= (q_{\mathrm{FeX}}s_{\mathrm{FeX}}I_{\mathrm{G}}N_{\mathrm{X}})A\ , \qquad (2.42) \\ E &= -\frac{1}{2}q_{\mathrm{FeX}}s_{\mathrm{FeX}}I_{\mathrm{G}}N_{\mathrm{X}}(q_{\mathrm{X,G}}s_{\mathrm{X,G}}I_{\mathrm{G}}+q_{\mathrm{X,IR}}s_{\mathrm{X,IR}}I_{\mathrm{IR0}})A \\ &\quad -\frac{1}{2}q_{\mathrm{FeX}}s_{\mathrm{FeX}}I_{\mathrm{G}}N_{\mathrm{X}}\left[q_{\mathrm{FeX}}s_{\mathrm{FeX}}I_{\mathrm{G}}(N_{\mathrm{X}}+2N_{\mathrm{A}})+\frac{e\mu n_{00}}{\epsilon\epsilon_0}+\frac{iK}{e}\kappa_{\mathrm{Fe}}I_{\mathrm{G}}\right]A \\ &\quad -\frac{1}{2}q_{\mathrm{X,IR}}s_{\mathrm{X,IR}}q_{\mathrm{FeX}}s_{\mathrm{FeX}}I_{\mathrm{G}}N_{\mathrm{X}}N_{\mathrm{A}}I_{\mathrm{IR1}}\ . \qquad (2.43) \end{aligned}$$

2.5.5 Saturation space–charge field

The space–charge field E_1 within one pulse can be represented as

$$E_1 = \frac{-ie}{K\epsilon\epsilon_0}(A + Bt + Ct^2) , \tag{2.44}$$

with A, B, C defined above. The saturation space–charge field can be easily obtained from Equation (2.44) by noting that the space–charge field at the beginning and at the end of each pulse would be the same at saturation. This can be written mathematically as

$$E_1(t = t_\mathrm{p}) = E_1(t = 0) = \frac{-ie}{K\epsilon\epsilon_0}A , \tag{2.45}$$

or

$$B + Ct_\mathrm{p} = 0 , \tag{2.46}$$

where t_p is the pulse width. Putting B and C from Equations (2.40) and (2.41) into Equation (2.46), we can solve for the saturation space–charge field ($-ieA/(K\epsilon\epsilon_0)$) as

$$E_1|_\mathrm{saturation} = \frac{\beta_1 I_\mathrm{IR1}}{\beta_2 + \beta_3 I_\mathrm{IR0} + \beta_4 I_\mathrm{G}} , \tag{2.47}$$

where

$$\beta_1 = -\frac{t_\mathrm{p}}{2\epsilon\epsilon_0} q_\mathrm{FeX} s_\mathrm{FeX} N_\mathrm{A} \kappa_\mathrm{X,IR} , \tag{2.48}$$

$$\beta_2 = \frac{e\mu N_\mathrm{A}}{\epsilon\epsilon_0 \gamma_\mathrm{Fe}(N_\mathrm{Fe} - N_\mathrm{A})} q_\mathrm{Fe} s_\mathrm{Fe} + \frac{iK}{e}\kappa_\mathrm{Fe} , \tag{2.49}$$

$$\beta_3 = \frac{t_\mathrm{p}}{2} q_\mathrm{FeX} s_\mathrm{FeX} N_\mathrm{X} \left[\frac{e\mu N_\mathrm{A}}{\epsilon\epsilon_0 \gamma_\mathrm{Fe}(N_\mathrm{Fe} - N_\mathrm{A})} q_\mathrm{X,IR} s_\mathrm{X,IR} + \frac{iK}{e}\kappa_\mathrm{X,IR} \right] , \tag{2.50}$$

$$\beta_4 = \frac{t_\mathrm{p}}{2} q_\mathrm{FeX} s_\mathrm{FeX} N_\mathrm{X} \left[\frac{e\mu N_\mathrm{A}}{\epsilon\epsilon_0 \gamma_\mathrm{Fe}(N_\mathrm{Fe} - N_\mathrm{A})} (q_\mathrm{X,G} s_\mathrm{X,G} - \frac{N_\mathrm{Fe}}{N_\mathrm{Fe} - N_\mathrm{A}} q_\mathrm{Fe} s_\mathrm{Fe}) + \frac{iK}{e}(\kappa_\mathrm{X,G} - \kappa_\mathrm{Fe}) \right]$$
$$- \frac{t_\mathrm{p}}{2} \left(\frac{e\mu N_\mathrm{A}}{\epsilon\epsilon_0 \gamma_\mathrm{Fe}(N_\mathrm{Fe} - N_\mathrm{A})} q_\mathrm{Fe} s_\mathrm{Fe} + \frac{iK}{e}\kappa_\mathrm{Fe} \right)^2 . \tag{2.51}$$

Equation (2.47) clearly shows the dependence of the saturation space–charge field (and therefore, saturation hologram strength) on the sensitizing and recording intensities. Later, we will use Equation (2.47) to explain the experimental results on the intensity dependence of saturation hologram strength.

2.5.6 Time-dependence of space–charge field

In the previous calculations, we solved for the space–charge field within one pulse. Due to short lifetime of electrons in the shallow traps compared to the time between adjacent pulses, we can assume that all electrons in shallow traps at the end of each pulse are transferred locally to the deep traps before the beginning of the next pulse. The local transfer of electrons between traps is based on the fact that almost all electrons are transferred directly from the shallow traps to the deep traps without passing through the conduction band.

To find the dynamics of space–charge formation, we need to calculate the space–charge field in the time scale much longer than one pulse. To avoid confusion, we represent the space–charge field in this time scale by $\overline{E_1}$. The change in the space–charge field within one pulse is

$$\begin{aligned} \Delta\overline{E_1} &= E_1(t=t_p) - E_1(t=0) \\ &= -\frac{ie}{K\epsilon\epsilon_0}(Bt_p + Ct_p^2) \,, \end{aligned} \tag{2.52}$$

with t_p being the pulse width. Therefore, we can write an approximate equation for $\overline{E_1}$ as

$$\frac{d\overline{E_1}}{dt} \simeq \frac{\Delta\overline{E_1}}{t_p} = -\frac{ie}{K\epsilon\epsilon_0}(B + Ct_p) \,. \tag{2.53}$$

Note that B and C in Equation (2.53) are now time dependent as they are different within different pulses. Replacing B and C from Equations (2.40) and (2.41) into

Equation (2.53), we obtain

$$\begin{aligned}\frac{d\overline{E_1}}{dt} &= \left(-(\frac{e\mu n_{00}}{\epsilon\epsilon_0}+\frac{iK}{e}\kappa_{\mathrm{Fe}}I_{\mathrm{G}})+\frac{t_{\mathrm{p}}}{2}[(\frac{e\mu n_{00}}{\epsilon\epsilon_0}+\frac{iK}{e}\kappa_{\mathrm{Fe}}I_{\mathrm{G}})^2-\frac{e\mu n_{01}}{\epsilon\epsilon_0}]\right)(-\frac{ie}{K\epsilon\epsilon_0}A)\\ &-\frac{t_{\mathrm{p}}}{2}q_{\mathrm{FeX}}s_{\mathrm{FeX}}I_{\mathrm{G}}N_{\mathrm{X}}(\frac{iK}{e})(\kappa_{\mathrm{X,G}}I_{\mathrm{G}}+\kappa_{\mathrm{X,IR}}I_{\mathrm{IR0}}-\kappa_{\mathrm{Fe}}I_{\mathrm{G}})(-\frac{ie}{K\epsilon\epsilon_0}A)\\ &-(\frac{t_{\mathrm{p}}}{2\epsilon\epsilon_0}\kappa_{\mathrm{X,IR}}q_{\mathrm{FeX}}s_{\mathrm{FeX}}I_{\mathrm{G}}N_{\mathrm{X}}N_{\mathrm{A}})I_{\mathrm{IR1}}\ . \qquad (2.54)\end{aligned}$$

Note that $-ie/(K\epsilon\epsilon_0)A$ is the space-charge field at the beginning of each pulse, and therefore we can write

$$\overline{E_1}(t) \simeq -\frac{ie}{K\epsilon\epsilon_0}A(t)\ . \qquad (2.55)$$

Combining Equations (2.54) and (2.55), we obtain

$$\frac{d\overline{E_1}}{dt} = -\frac{\overline{E_1}}{\tau_{\mathrm{r}}}+\frac{E_1|_{\mathrm{saturation}}}{\tau_{\mathrm{r}}}\ , \qquad (2.56)$$

where the saturation space–charge field $E_1|_{\mathrm{saturation}}$ is the same as that obtained by a simple observation previously (Equation (2.47)), and recording speed (inverse of recording time constant τ_{r}) is given by

$$\begin{aligned}\frac{1}{\tau_{\mathrm{r}}} &= (\frac{e\mu n_{00}}{\epsilon\epsilon_0}+\frac{iK}{e}\kappa_{\mathrm{Fe}}I_{\mathrm{G}})-\frac{t_{\mathrm{p}}}{2}(\frac{e\mu n_{00}}{\epsilon\epsilon_0}+\frac{iK}{e}\kappa_{\mathrm{Fe}}I_{\mathrm{G}})^2\\ &+\frac{t_{\mathrm{p}}}{2}[\frac{e\mu n_{01}}{\epsilon\epsilon_0}+q_{\mathrm{FeX}}s_{\mathrm{FeX}}I_{\mathrm{G}}N_{\mathrm{X}}(\frac{iK}{e})(\kappa_{\mathrm{X,G}}I_{\mathrm{G}}+\kappa_{\mathrm{X,IR}}I_{\mathrm{IR0}}-\kappa_{\mathrm{Fe}}I_{\mathrm{G}})]\\ &= \left(\frac{e\mu}{\epsilon\epsilon_0}\frac{q_{\mathrm{Fe}}s_{\mathrm{Fe}}N_{\mathrm{A}}}{\gamma_{\mathrm{Fe}}(N_{\mathrm{Fe}}-N_{\mathrm{A}})}+\frac{iK}{e}\kappa_{\mathrm{Fe}}\right)I_{\mathrm{G}}-\frac{t_{\mathrm{p}}}{2}\left(\frac{e\mu}{\epsilon\epsilon_0}\frac{q_{\mathrm{Fe}}s_{\mathrm{Fe}}N_{\mathrm{A}}}{\gamma_{\mathrm{Fe}}(N_{\mathrm{Fe}}-N_{\mathrm{A}})}+\frac{iK}{e}\kappa_{\mathrm{Fe}}\right)^2 I_{\mathrm{G}}^2\\ &+\frac{t_{\mathrm{p}}}{2}q_{\mathrm{FeX}}s_{\mathrm{FeX}}N_{\mathrm{X}}\left(\frac{e\mu}{\epsilon\epsilon_0}\frac{N_{\mathrm{A}}}{\gamma_{\mathrm{Fe}}(N_{\mathrm{Fe}}-N_{\mathrm{A}})}\right)\left(q_{\mathrm{X,G}}s_{\mathrm{X,G}}-\frac{N_{\mathrm{Fe}}}{N_{\mathrm{Fe}}-N_{\mathrm{A}}}q_{\mathrm{Fe}}s_{\mathrm{Fe}}\right)I_{\mathrm{G}}^2\\ &+\frac{t_{\mathrm{p}}}{2}q_{\mathrm{FeX}}s_{\mathrm{FeX}}N_{\mathrm{X}}\left(\frac{iK}{e}\right)(\kappa_{\mathrm{X,G}}-\kappa_{\mathrm{Fe}})I_{\mathrm{G}}^2\\ &+\frac{t_{\mathrm{p}}}{2}q_{\mathrm{FeX}}s_{\mathrm{FeX}}N_{\mathrm{X}}(\frac{e\mu}{\epsilon\epsilon_0}\frac{N_{\mathrm{A}}}{\gamma_{\mathrm{Fe}}(N_{\mathrm{Fe}}-N_{\mathrm{A}})}(q_{\mathrm{X,IR}}s_{\mathrm{X,IR}}+\frac{iK}{e}\kappa_{\mathrm{X,IR}})I_{\mathrm{G}}I_{\mathrm{IR0}}\ . \qquad (2.57)\end{aligned}$$

The solution of Equation (2.56) for $\overline{E_1}$ with initial condition $\overline{E_1}(t=0)=0$ is a

monoexponential function like

$$\overline{E_1} = E_1|_{\text{saturation}} \left[1 - \exp(-\frac{t}{\tau_r})\right] . \quad (2.58)$$

This formula does not show the variation of the space–charge field within the individual pulses. This is acceptable since in the experiments we measure the diffraction efficiency of the holograms after pulses and not within them. Note that the time variable t in Equation (2.58) is the time where the pulse is on (exposure time). The space–charge field remains constant between adjacent pulses. Therefore, we delete the times when the pulse is off from the time variable t. Note that Equation (2.56) can also be used with a different initial condition to obtain the space–charge field during erasure. Therefore, the recording and erasure time constants are equal. In Section 2.6 we will use Equations (2.47) and (2.57) to explain the experimental dependence of the saturation space–charge field and recording time constant on the intensities of the sensitizing and recording beams.

We can improve the accuracy of the analytical formula derived above by using more terms in the Taylor series expansion of different variables. The next approximation step is to consider the first three Taylor series terms for the zeroth order variables and the first four ones for the first order variables.

2.5.7 Simplified formulas

Although we derived analytic formulas for the saturation space–charge field and recording time constant (Equations (2.47) and (2.57), respectively), the formulas are so complicated that we can not easily use them to explain the different experimental observations based on the simple physical mechanisms. In this section, we use the parameter values from Table 2.1 to calculate the order of magnitude of different terms in Equations (2.47) and (2.57). We then neglect the terms that are at least one order of magnitude less than the others to obtain simplified formulas. In these calculations, we assume $I_G \sim I_{IR0} \sim 10^7$–$10^8$ W/cm^2 for the sensitizing and recording intensities, $t_p \simeq 5$ nsec for the pulse width, and $\Lambda \simeq 2$ μm for the grating period at recording

wavelength of $\lambda = 1064$ μm. We also assume that the oxidation / reduction state of the crystal is such that $N_{\rm A}/N_{\rm Fe} \sim 0.1$, i.e., about 10% of the Fe traps are initially occupied by electrons. These are typical values used in the experiments.

Simplified formula for saturation space–charge field

Using material parameter values from Table 2.1 and experimental values given above, we can simplify Equation (2.47) by using the following approximations:

$$\frac{K}{e}\kappa_{\rm Fe} \ll \frac{e\mu N_{\rm A}}{\epsilon\epsilon_0\gamma_{\rm Fe}(N_{\rm Fe}-N_{\rm A})}q_{\rm Fe}s_{\rm Fe}\ , \tag{2.59}$$

$$\frac{K}{e}\kappa_{\rm X,IR} \ll \frac{e\mu N_{\rm A}}{\epsilon\epsilon_0\gamma_{\rm Fe}(N_{\rm Fe}-N_{\rm A})}q_{\rm X,IR}s_{\rm X,IR}\ , \tag{2.60}$$

$$\frac{K}{e}|\kappa_{\rm X,G}-\kappa_{\rm Fe}| \ll \frac{e\mu N_{\rm A}}{\epsilon\epsilon_0\gamma_{\rm Fe}(N_{\rm Fe}-N_{\rm A})}\times |q_{\rm X,G}s_{\rm X,G}-\frac{N_{\rm Fe}}{(N_{\rm Fe}-N_{\rm A})}q_{\rm Fe}s_{\rm Fe}|\ , \tag{2.61}$$

$$\frac{e\mu N_{\rm A}}{\epsilon\epsilon_0\gamma_{\rm Fe}(N_{\rm Fe}-N_{\rm A})}(q_{\rm Fe}s_{\rm Fe})^2 \ll q_{\rm FeX}s_{\rm FeX}N_{\rm X}|q_{\rm X,G}s_{\rm X,G}-\frac{N_{\rm Fe}}{N_{\rm Fe}-N_{\rm A}}q_{\rm Fe}s_{\rm Fe}|\ , \tag{2.62}$$

where Equation (2.59) is used for simplification of β_2 in Equation (2.49); Equation (2.60) is used for simplification of β_3 in Equation (2.49); and Equations (2.61) and (2.62) are used for simplification of β_4. Using these approximations, the simplified formula for the saturation space–charge field $E_1|_{\rm saturation}$ becomes

$$E_1|_{\rm saturation} = \frac{-\frac{t_{\rm p}}{2}q_{\rm FeX}s_{\rm FeX}N_{\rm A}N_{\rm X}\kappa_{\rm X,IR}I_{\rm IR1}}{\frac{e\mu N_{\rm A}}{\gamma_{\rm Fe}(N_{\rm Fe}-N_{\rm A})}TERM}, \tag{2.63}$$

where

$$TERM = \frac{t_{\rm p}}{2}q_{\rm FeX}s_{\rm FeX}N_{\rm X}[q_{\rm X,IR}s_{\rm X,IR}I_{\rm IR0}+(q_{\rm X,G}s_{\rm X,G}-\frac{N_{\rm Fe}}{(N_{\rm Fe}-N_{\rm A})}q_{\rm Fe}s_{\rm Fe})I_{\rm G}] + q_{\rm Fe}s_{\rm Fe}\ . \tag{2.64}$$

Equation (2.63) can be rewritten in a form that is very useful for understanding the main physical mechanisms responsible for recording by multiplying the numerator

and the denominator of $E_1|_{\text{saturation}}$ by I_{G}, and comparing them with the values of n_0 and N^-_{X0} averaged over one pulse width ($0 \leq t \leq t_{\text{p}}$) given below by $n_{0,\text{ave}}$ and $N^-_{\text{x0,ave}}$

$$\begin{aligned} n_{0,\text{ave}} &= n_{00} + n_{01}\frac{t_{\text{p}}}{2} \\ &= \frac{N_{\text{A}}}{\gamma_{\text{Fe}}(N_{\text{Fe}} - N_{\text{A}})}\frac{t_{\text{p}}}{2} q_{\text{FeX}} s_{\text{FeX}} N_{\text{X}} (q_{\text{X,G}} s_{\text{X,G}} - \frac{N_{\text{Fe}}}{(N_{\text{Fe}} - N_{\text{A}})} q_{\text{Fe}} s_{\text{Fe}}) I_{\text{G}}^2 \\ &\quad + \frac{N_{\text{A}}}{\gamma_{\text{Fe}}(N_{\text{Fe}} - N_{\text{A}})} (q_{\text{Fe}} s_{\text{Fe}} + \frac{t_{\text{p}}}{2} q_{\text{FeX}} s_{\text{FeX}} N_{\text{X}} q_{\text{X,IR}} s_{\text{X,IR}} I_{\text{IR0}}) I_{\text{G}} \ , \end{aligned} \tag{2.65}$$

$$N^-_{\text{x0,ave}} = \frac{t_{\text{p}}}{2} q_{\text{FeX}} s_{\text{FeX}} N_{\text{X}} N_{\text{A}} I_{\text{G}} \ . \tag{2.66}$$

The resulting simplified formula for the saturation space–charge field is

$$E_1|_{\text{saturation}} = -\frac{\kappa_{\text{X,IR}} N^-_{\text{X0,ave}} I_{\text{IR1}}}{e\mu n_{0,\text{ave}}} \ . \tag{2.67}$$

In the next section, we will use this formula to explain different experimental observations based on very basic physical mechanisms.

Simplified formula for recording time constant

Using the approximations given by Equations (2.59)–(2.62), we can simplify Equation (2.57) for the recording speed as

$$\begin{aligned} \frac{1}{\tau_{\text{r}}} &= \frac{1}{t_{\text{p}}} \Bigg[\frac{e\mu}{2\epsilon\epsilon_0} \frac{N_{\text{A}}}{\gamma_{\text{Fe}}(N_{\text{Fe}} - N_{\text{A}})} q_{\text{FeX}} s_{\text{FeX}} N_{\text{X}} \left(q_{\text{X,G}} s_{\text{X,G}} - \frac{N_{\text{Fe}}}{N_{\text{Fe}} - N_{\text{A}}} q_{\text{Fe}} s_{\text{Fe}} \right) (I_{\text{G}} t_{\text{p}})^2 + \\ &\quad \frac{e\mu}{\epsilon\epsilon_0} \frac{N_{\text{A}}}{\gamma_{\text{Fe}}(N_{\text{Fe}} - N_{\text{A}})} \left(q_{\text{Fe}} s_{\text{Fe}} + \frac{1}{2} q_{\text{FeX}} s_{\text{FeX}} N_{\text{X}} q_{\text{X,IR}} s_{\text{X,IR}} (I_{\text{IR0}} t_{\text{p}}) \right) (I_{\text{G}} t_{\text{p}}) \Bigg] \ . \end{aligned} \tag{2.68}$$

Comparing Equations (2.68) and (2.65), we obtain the following simple formula that can be used to explain the experimental observations based on simple physical mechanisms

$$\frac{1}{\tau_{\text{r}}} = \frac{e\mu n_{0,\text{ave}}}{\epsilon\epsilon_0} \ . \tag{2.69}$$

2.5.8 Comparison with numerical solution

Figures 2.11 (a) and (b) show the variations of saturation change in the index of refraction $\Delta n = -(n^3/2)r_{13}E_1|_{\text{saturation}}$ (n: index of refraction at recording frequency) with recording and sensitizing intensities (I_{IR0} and I_{G}), respectively. In these figures, we have shown both analytical and numerical solutions as well as the experimental results. As Figure 2.11 shows, the agreement between analytical formula for $E_1|_{\text{saturation}}$ (Equation (2.63)) and numerical solution is very good with all levels of assumptions and approximations involved.

Figures 2.12 (a) and (b) show the variations of recording speed ($1/\tau_{\text{r}}$) with recording and sensitizing intensities, respectively. As in Figure 2.11, we have shown analytical and numerical solutions as well as the experimental results. Although the analytic solution from Equation (2.68) shows the appropriate qualitative variation of recording speed with intensities, its deviation from the numerical solution is more than 10% for larger intensities, as shown in Figure 2.12. One of the major sources of error in the analytic solution is the approximation $n_0 \simeq n_{00} + n_{01}t$ given by Equation (2.27). To obtain a more accurate formula for the recording speed, we use the simplified formula given by Equation (2.69), but we calculate $n_{0,\text{ave}}$ by time–averaging n_0 without making a linear approximation. To do this, we first replace the more accurate formula for N_{X0}^{-} from Equation (2.22) into the formula for n_0 given by Equation (2.27) and rearrange the terms to obtain

$$n_0 = \frac{\zeta_1 - \zeta_2 \exp(-t/\tau_{\text{x}})}{\zeta_3 - \zeta_4 \exp(-t/\tau_{\text{x}})}, \tag{2.70}$$

where τ_x is given by Equation (2.23), and ζ_1–ζ_4 are defined by

$$\begin{aligned}
\zeta_1 &= q_{Fe} s_{Fe} I_G N_A (q_{X,G} s_{X,G} I_G + q_{X,IR} s_{X,IR} I_{IR0} + q_{FeX} s_{FeX} I_G N_A) \\
&\quad + q_{FeX} s_{FeX} I_G N_X N_A (q_{X,G} s_{X,G} I_G + q_{X,IR} s_{X,IR} I_{IR0}) \qquad (2.71) \\
\zeta_2 &= q_{FeX} s_{FeX} I_G N_X N_A (q_{X,G} s_{X,G} I_G + q_{X,IR} s_{X,IR} I_{IR0} - q_{Fe} s_{Fe} I_G) , \qquad (2.72) \\
\zeta_3 &= \gamma_{Fe} [(N_{Fe} - N_A)(q_{X,G} s_{X,G} I_G + q_{X,IR} s_{X,IR} I_{IR0} + q_{FeX} s_{FeX} I_G [N_X + N_A])] \\
&\quad + \gamma_{Fe} q_{FeX} s_{FeX} I_G N_X N_A , \qquad (2.73) \\
\zeta_4 &= \gamma_{Fe} q_{FeX} s_{FeX} I_G N_X N_A . \qquad (2.74)
\end{aligned}$$

In the next step, we calculate $n_{0,ave}$ by time–averaging n_0 from Equation (2.70) over one pulse width ($0 \le t \le t_p$),

$$\begin{aligned}
n_{0,ave} &= \frac{1}{t_p} \int_0^{t_p} n_0 dt = \frac{1}{t_p} \int_0^{t_p} \frac{\zeta_1 - \zeta_2 \exp(-t/\tau_x)}{\zeta_3 - \zeta_4 \exp(-t\tau_x)} dt \\
&= \frac{\zeta_1}{\zeta_3} + \frac{\tau_x}{t_p} \left(\frac{\zeta_2}{\zeta_4} - \frac{\zeta_1}{\zeta_3} \right) \ln \left[\frac{\zeta_3 - \zeta_4}{\zeta_3 - \zeta_4 \exp(-t_p/\tau_x)} \right] . \qquad (2.75)
\end{aligned}$$

Putting $n_{0,ave}$ into Equation (2.69), we obtain a more accurate analytic formula for the recording time constant. The variation of recording speed with sensitizing and recording intensities using this more accurate formula is also depicted in Figure 2.12 showing much better agreement with the numerical solution than the approximate formula given by Equation (2.68). Therefore, we have analytic formulas for both saturation space–charge field and recording time constant that agree very well with both the numerical solution and experimental results.

It is important to note that the analytic formulas become less accurate as we increase either the intensities or the pulse width. This is due to the fact that increasing the energy of each pulse (by increasing either its intensity or its width) results in stronger variation of the variables within one pulse and makes the approximation of the variables by a few Taylor series terms less accurate. However, the analytic formulas derived in this section are good enough for most practical applications with current high energy pulsed lasers. The more significant usage of these formulas is the

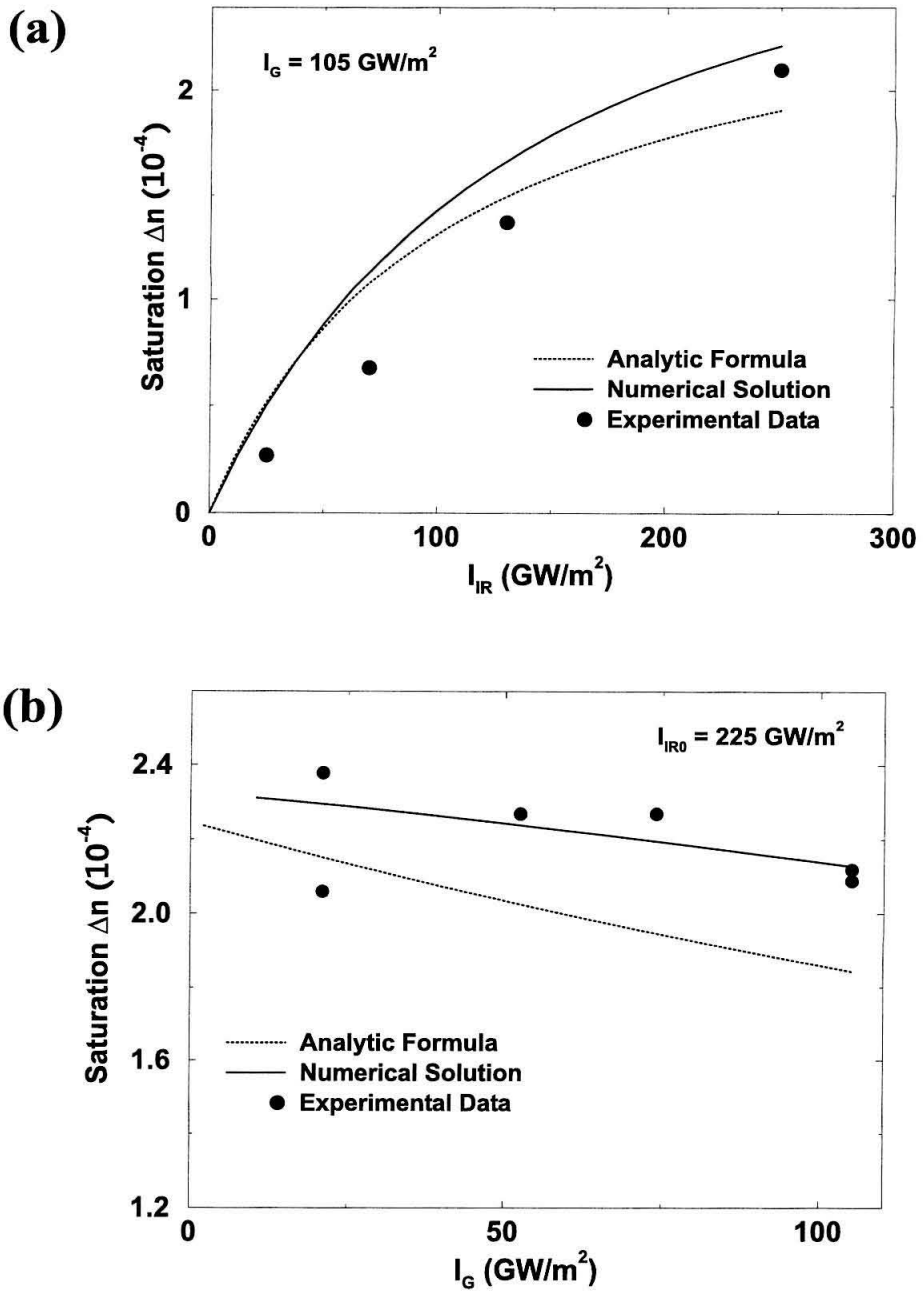

Figure 2.11: Variation of the saturation value of the amplitudes of the refractive index grating (Δn) with (a) average infrared light intensity I_{IR0} while green light intensity is fixed ($I_{\mathrm{G}} = 105$ GW/m^2), and (b) green light intensity I_{G} while infrared light intensity is fixed ($I_{\mathrm{IR0}} = 225$ GW/m^2). The modulation depth of the infrared intensity was 1 ($I_{\mathrm{IR0}} = I_{\mathrm{IR1}}$) in both cases.

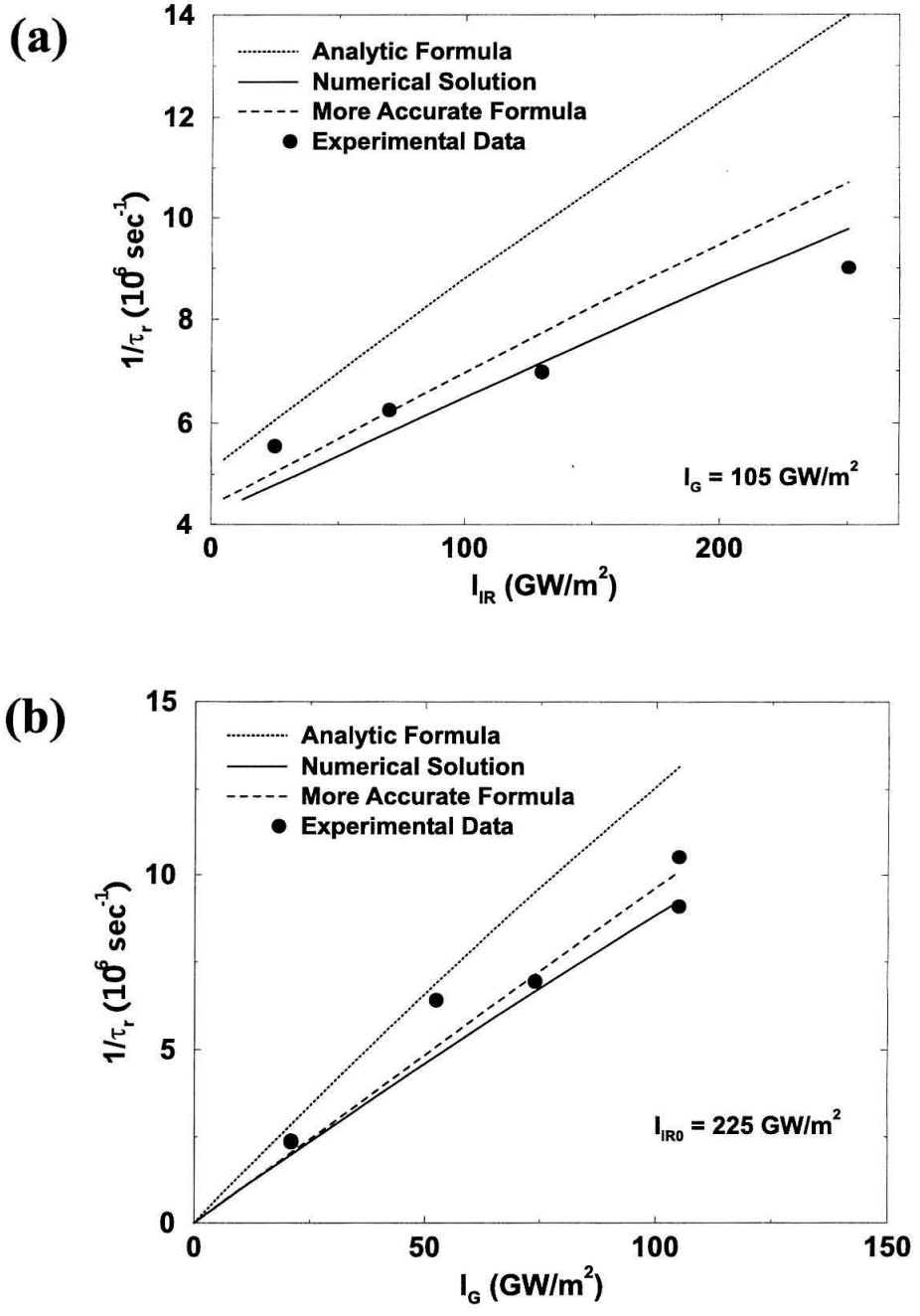

Figure 2.12: Variation of recording speed (τ_r^{-1}) with (a) average infrared light intensity I_{IR0} while green light intensity is fixed (I_G = 105 GW/m^2), and (b) green light intensity I_G while infrared light intensity is fixed (I_{IR0} = 225 GW/m^2). The modulation depth of the infrared intensity was 1 ($I_{IR0} = I_{IR1}$) in both cases.

understanding of main physical mechanisms responsible for holographic recording and using them for the explanation of the experimental observations. This is done in the next section.

2.6 Explanation of the experimental observations

Although the dependence of the saturation hologram strength and recording and erasure time constants on sensitizing and recording intensities and doping level of the crystal in two–step holographic recording was experimentally observed and reported previously [41, 43], some of these results were not understood and explained based on physical mechanisms. In this section, we use the two simplified formulas we derived in the last section to draw a simple physical picture for pulse recording mechanisms and use it to explain the experimental observations discussed in Section 2.4. In this section, we assume the modulation depth of recording intensity to be 1. In other words, we assume that $I_{\mathrm{IR0}} = I_{\mathrm{IR1}}$ in agreement with experimental conditions. Therefore, we use I_{IR0} when the variation with recording intensity is involved. Due to the importance of the simplified formulas (2.67) and (2.69), we repeat them here:

$$\begin{aligned} E_1|_{\mathrm{saturation}} &= -\frac{\kappa_{\mathrm{X,IR}} N^{-}_{\mathrm{X0,ave}} I_{\mathrm{IR1}}}{e\mu n_{0,\mathrm{ave}}}\,, \\ \frac{1}{\tau_{\mathrm{r}}} &= \frac{e\mu n_{0,\mathrm{ave}}}{\epsilon\epsilon_0}\,. \end{aligned}$$

The formula for recording speed is similar to that in normal holographic recording with cw light in $LiNbO_3$:Fe crystals. The only difference is that in the latter we have the DC electron concentration in the conduction band (n_0) in place of $n_{0,\mathrm{ave}}$, the time–averaged DC electron concentration in the conduction band over one pulse width. The formula for saturation space–charge field is also similar to what we have in normal cw recording. This similarity is better understood by recalling that total current density j is zero at saturation (steady–state). Neglecting diffusion, we can

write the above statement mathematically as

$$j_1|_{\text{saturation}} = j_{\text{ph1}} + e\mu n_0 E_1|_{\text{saturation}} = 0 \ , \tag{2.76}$$

or

$$E_1|_{\text{saturation}} = -\frac{j_{\text{ph1}}}{e\mu n_0} \ . \tag{2.77}$$

If we assume that the dominant term in the bulk photovoltaic current is that from the shallow traps due to the recording light, we can rewrite Equation (2.77) as

$$E_1|_{\text{saturation}} = -\frac{\kappa_{\text{X,IR}} N_{\text{X0}}^{-} I_{\text{IR0}}}{e\mu n_0} \ , \tag{2.78}$$

where we assumed $I_{\text{IR1}} = I_{\text{IR0}}$. Equation (2.78) becomes the same simplified formula we derived for $E_1|_{\text{saturation}}$ if we replace N_{X0}^{-} and n_0 by their time–averaged values over one pulse width, $N_{\text{X0,ave}}^{-}$ and $n_{0,\text{ave}}$, respectively.

Although the physical mechanisms in two–step holographic recording with high intensity pulses are similar to those of the normal recording, the intensity dependence of the saturation space–charge filed and recording speed in the two cases are different. This is due to the fact that the trap responsible for electron concentration in the conduction band and the one responsible for photovoltaic current are the same in normal recording while they are different in two–step recording. This can be easily understood from Figure 2.13 that shows the energy band diagrams of the two cases. In normal recording, electron concentration in the conduction band is due to excitation from Fe traps by recording light. The same traps are also responsible for bulk photovoltaic effect caused by recording light. Therefore, both j_{ph1} and n_0 in Equation (2.77) depend linearly on recording intensity. As a result, saturation space–charge field in normal recording is independent of recording intensity. On the other hand, recording speed $(1/\tau_{\text{r}})$ in normal recording increases linearly with recording intensity since n_0 has this intensity dependence.

In two–step recording, the electron concentration in the conduction band is caused

by three different paths: directly from the deep traps by sensitizing light (path 1 in Figure 2.13 (b)), in two steps via the shallow traps by sensitizing light only (path 2 in Figure 2.13 (b)), and from the deep traps to the shallow traps by sensitizing light; then from shallow traps to the conduction band by recording light (path 3 in Figure 2.13 (b)). The strengths of these three mechanisms depend on I_{G}, I_{G}^2, and $I_{\mathrm{G}} I_{\mathrm{IR0}}$, respectively. The time–averaging of n_0 over one pulse does not change the intensity dependence. This explains the experimentally observed dependence of the recording speed on I_{G} and I_{IR0} shown in Figure 2.12. At lower intensities, electron excitation via path 1 in Figure 2.13 (b) becomes dominant and the recording speed varies linearly with I_{G} while it is almost independent of I_{IR0}. As we increase intensities, the two–step excitation mechanisms (paths 2 and 3 in Figure 2.13 (b)) become stronger. Therefore, we might observe a quadratic dependence $(a_1 I_{\mathrm{G}} + a_2 I_{\mathrm{G}}^2)$ of the recording speed with I_{G} at very high intensities. We also observe a small linear increase of recording speed with increasing I_{IR0} while I_{G} is fixed. During erasure with sensitizing light only, we also observe a quadratic dependence of the erasure speed (inverse of erasure time constant) with I_{G} as we have similar dependence of erasure time constant on $n_{0,\mathrm{ave}}$.

As Figure 2.11 shows, saturation hologram strength increases linearly with I_{IR0} and decreases very slowly with I_{G}. The intensity dependence of the saturation hologram strength in two–step recording (space–charge field or Δn) has been puzzling as it is very different from that in normal recording. As a result, there has been no plausible physical explanation of this dependence yet. However, we can easily understand and explain these puzzling observations using our simple model. One important term in the saturation space–charge field is the time–averaged electron concentration in the shallow traps $N_{\mathrm{X0,ave}}^{-}$ that depends on both populating and depopulating mechanisms. The main populating mechanism is direct electron transfer from the deep traps by sensitizing light as the trapping of conduction band electrons by shallow traps can be neglected. The strength of this populating mechanism depends on I_{G}. On the other hand, depopulation of the shallow traps within one pulse is due to excitation of the electrons to the conduction band by both sensitizing and recording light. Note

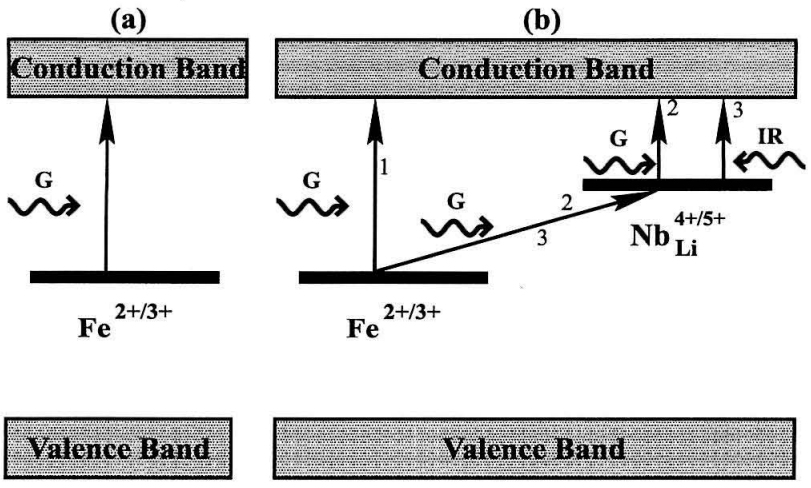

Figure 2.13: Mechanisms for excitation of electrons from deep traps to the conduction band in a $LiNbO_3$:Fe crystal for (a) normal recording with low intensities, and (b) two–step recording with high intensities. There are three different paths for electron generation in two–step recording indicated by 1, 2, and 3. In part (b), electron transfer mechanisms caused by sensitizing (green) light are indicated by G, and those caused by recording (infrared) light are indicated by IR.

that direct electron transfer from shallow traps to deep traps is another depopulating mechanism. However, we neglect this mechanism during one pulse width (a few nanoseconds) due to much longer lifetime of electrons in the shallow traps (a few milliseconds) as explained before. To summarize, we expect $N^-_{X0,ave}$ to increase with I_G in a complicated way and decrease with increasing I_{IR0}. With the assumptions and approximations described before, $N^-_{X0,ave}$ increases linearly with I_G, while it is independent of I_{IR0} (due to minor role of I_{IR0} in depopulation of the shallow traps within one pulse width).

We are now ready to explain the intensity dependence of $E_1|_{saturation}$ as we understand the intensity dependence of all terms involved in Equation (2.67). We expect $E_1|_{saturation}$ to increase linearly with I_{IR0} at lower intensities as both $N^-_{X0,ave}$ and $n_{0,ave}$ are almost independent of I_{IR0} at lower intensities. This dependence on I_{IR0} becomes sublinear and finally turns into independence from I_{IR0} when we increase I_{IR0} without limit while I_G is fixed. The latter behavior is due to the linear dependence of $n_{0,ave}$ on I_{IR0} at higher values of I_{IR0}. The saturation space–charge field is almost independent

of I_G at lower intensities due to approximately linear dependence of both $N^-_{X0,ave}$ and $n_{0,ave}$ on I_G at lower intensities. The exact dependence on I_G is more complicated and depends also on the oxidation / reduction state of the crystal due to more complicated dependence of $N^-_{X0,ave}$ and $n_{0,ave}$ on I_G that becomes more evident at higher intensities. Equation (2.47) describes a more complete dependence of $E_1|_{saturation}$ on sensitizing and recording intensities. It can be seen from this formula that when the oxidation / reduction state of the crystal is such that the coefficient of I_G in the denominator of $E_1|_{saturation}$ (β_4) in Equation (2.47) is positive, the saturation space–charge field decreases with increasing I_G. When the oxidation / reduction state is such that this coefficient is negative, the saturation space–charge field increases with increasing I_G at normal intensities. If we increase I_G without limit, the saturation space–charge field will finally decrease with increasing I_G regardless of the oxidation state of the crystal as suggested by Equation (2.47). Note that Equation (2.47) was derived by assuming that $N^-_{X0,ave} \sim I_G$ as shown in Equation (2.22). Therefore, the exact dependence of $E_1|_{saturation}$ on I_G is more complicated than it was thought previously.

Although we focused above on the dependence of saturation hologram strength and recording speed on sensitizing and recording intensities, our model can explain the dependence of these two variables on other parameters. For example, we expect the recording speed to depend on $N_{Fe^{2+}}/N_{Fe^{3+}}$ (or $N_A/(N_{Fe} - N_A)$) since the main source for electron generation in the conduction band is electron concentration in Fe traps ($N_{Fe^{2+}}$), and the main source for electron trapping from the conduction band is the concentration of empty Fe traps ($N_{Fe^{3+}}$). Therefore,

$$\frac{1}{\tau_r} \propto n_{0,ave} \propto \frac{N_{Fe^{2+}}}{N_{Fe^{3+}}} .$$

We also expect that $N^-_{X0,ave} \sim N_{Fe^{2+}}$ as the shallow traps are populated by direct electron transfer from the deep traps. Putting the dependence of $N^-_{X0,ave}$ and $n_{0,ave}$

into the formula for $E_1|_{\text{saturation}}$, we obtain

$$\Delta n|_{\text{saturation}} \propto E_1|_{\text{saturation}} \quad \propto \quad \frac{N^-_{\text{X0,ave}}}{n_{0,\text{ave}}} \propto N_{\text{Fe}^{3+}} \ , \tag{2.79}$$

which is in agreement to the experimental results depicted in Figure 2.9.

To summarize, the simple model based on Equations (2.68) and (2.67) gives us a complete understanding of the physical mechanisms involved in two–step holographic recording with high intensity pulses and helps us understand and explain the experimental observations that were not all explained before. Furthermore, it helps us understand the main drawbacks of the method and suggests ways for improving it. This is explained in Section 2.8.

2.7 Application of the model to two–step recording with cw light

Although we developed our numerical and analytic solution for the case of recording with pulses, the parameters of the model we found previously can be used for modeling recording with cw light. Although the analytic formulas we derived can not be used for recording with cw light, we can modify our numerical solution to study cw recording. The best way to solve the problem of recording with cw light is to start with the system of Equations (2.9)–(2.17) and apply Fourier development to obtain two sets of equations for the zeroth order and first order variables, and solve those equations numerically.

2.8 Discussion

Although two–step holographic recording using $LiNbO_3$:Fe crystal has excellent persistence, the need of high intensities for recording is the main drawback of the method. The main reason for this drawback is the short lifetime of electrons in the shallow polaron centers due to the strong depopulation mechanisms of these shallow traps.

Another reason for this large intensity requirement is the weak population mechanism of the shallow traps by direct electron transfer from deep traps. The existence of this direct electron transfer mechanism was first proposed by Chen et al. [60]. This mechanism is essential for explaining the experimental observations discussed previously. Without this mechanism, electron transfer from the deep traps to the shallow traps would be performed via the conduction band, and the dark depopulation of the shallow traps would occur due to thermal excitation resulting in an entirely different intensity–dependence of the saturation hologram strength and recording speed from what we observed and explained.

Without direct electron transfer from the shallower traps to the deeper traps (direct depopulation), there would be a partial erasure of the hologram during read–out. This is due to the fact that electrons are transferred from the shallow traps to the deep traps via the conduction band in this case. The electrons can move while they are in the conduction band, and this movement is in the direction of erasing the hologram as in the case of normal holographic recording in $LiNbO_3$:Fe crystals. Such a read–out response is not observed experimentally, confirming the necessity of considering the direct electron transfer between deep and shallow traps in theoretical modeling.

To see the effect of direct depopulation of the shallow traps on the hologram strength, we calculated the recording curve for a non–physical case by neglecting the direct electron transfer from the shallow traps to the deep traps (direct depopulation of shallow traps) while direct electron transfer from the deep traps to the shallow traps is not neglected. In this calculation, we assumed that both recording and sensitization is performed by cw light. The result of this calculation is shown in Figure 2.14, which shows that we could record much stronger holograms (by three orders of magnitude) in the absence of direct depopulation of the shallow traps. This assumption (neglecting direct depopulation of the shallow traps) is of course non–physical as it considers only electron transfer from the deep traps to the shallow traps and not the reverse transfer. However, Figure 2.14 gives us an insight for improving the performance of two–step holographic recording through an increase of the lifetime of electrons in the

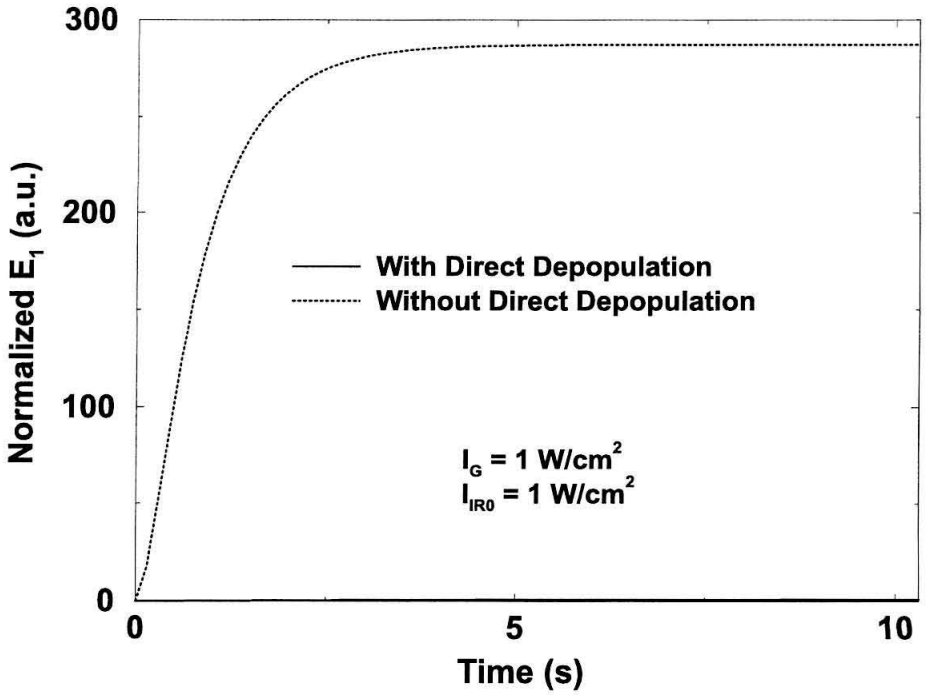

Figure 2.14: Theoretical calculation of recording curves for space–charge field of a hologram using two–step holographic recording in a $LiNbO_3$:Fe crystal with and without neglecting direct depopulation of the shallow traps (direct electron transfer from shallow traps to deep traps). The curves are normalized so that the saturation space–charge field for the case without neglecting direct depopulation is 1. It is assumed in this calculation that recording is performed by cw light with $I_G = I_{IR0} = I_{IR1} = 1$ W/cm^2.

shallow traps.

One way to improve the lifetime of electrons in shallow traps is to replace the shallow traps with some long lifetime traps due to doping. In other words, we can use a doubly–doped crystal instead of a singly–doped one. Both deep and shallow traps in a doubly–doped crystal are due to dopands and can be chosen deep enough in the band gap of $LiNbO_3$ so that thermal depopulation of either trap is negligible. However, the direct electron transfer between traps is also negligible in this case due to low practical concentrations of both dopands. Therefore, sensitization of the shallow traps is performed via the conduction band. The depopulation of the shallow traps in this case is performed by read–out light during read–out via the conduction band.

The electrons can move while they are in the conduction band, and this movement is in the direction of erasing the hologram as in the case of normal holographic recording in $LiNbO_3$:Fe crystals. Therefore, there is a partial erasure of the hologram during read–out in this case. In the next chapter, we will see that two–step holographic recording in doubly–doped materials results in much better performance than two–step holographic recording in a singly–doped material. Another way to improve the performance of two–step recording is to increase the lifetime of shallow traps by lowering the concentration of empty deep traps as well as the concentration of the shallow traps. This has been done by using nominally pure reduced near–stoichiometric $LiNbO_3$ crystals [61, 62] as well as near–stoichiometric $LiNbO_3$:Pr crystals [63, 64]. The usage of near–stoichiometric crystals is important in reducing the concentration of the shallow polaron levels that are due to the presence of Nb ions on Li sites. The concentration of Nb ions on Li sites in a near–stoichiometric crystal is much smaller than that in a congruent crystal resulting in much smaller polaron concentration in a near–stoichiometric crystal. The crystal is also reduced to lower the concentration of the deep empty traps. Another idea is to use bipolarons instead of remnant Fe centers as deep traps [62]. In all these cases, it is possible to record holograms using cw light with much smaller intensities compared to pulsed experiments. In Chapter 5 we will compare the performance of different two–step recording methods.

Finally, a very interesting point is that both saturation space–charge field and recording time constant depend on energy density per pulse (photon flux) of the recording and sensitizing beams ($I_G t_p$ and $I_{IR0} t_p$) instead of the intensities alone (as proposed in the literature). This can be easily understood by looking at Equations (2.63) and (2.68). In these equations, both intensities (I_G and I_{IR0}) always appear in combination with pulse width (t_p). This observation suggests that we can not obtain higher saturation space–charge fields by increasing I_G and I_{IR0} and decreasing the pulse width t_p to have constant photon fluxes $I_G t_p$ and $I_{IR0} t_p$, no matter how many pulses we use.

2.9 Conclusions

We developed a full numerical solution as well as an approximate analytic solution for two–step holographic recording in $LiNbO_3$:Fe crystals. We found the unknown material parameters by fitting the numerical solution to the experimental results. The two important parameters which were unknown so far and found in this work are the bulk photovoltaic coefficient and absorption cross section for the excitation of the electrons from small polarons in $LiNbO_3$ with infrared light (see Table 2.1). The simplified analytic solution we developed agrees very well with the numerical solution for most practical applications. Furthermore, the analytic solution gives us a very good understanding of the physical processes involved. Such a simple model also helps us explain the experimental observations that were not understood before. The numerical solution can also be modified for solving the problem of holographic recording with cw light in $LiNbO_3$:Fe crystals.

Although our method for obtaining an approximate analytic solution was applied to the problem of two–step holographic recording with pulses, the developed strategy can be used in solving a wide variety of problems involving pulses of actions where each pulse is followed by a much longer relaxation time.

Although two–step recording with high intensity pulses has excellent persistence, the need of high intensities for recording strong holograms is a major drawback of the method. This is due to the short lifetime of the shallow polaron centers. Therefore, any effort for improving the performance of two–step holographic recording should focus on increasing this lifetime.

Chapter 3 Two–center holographic recording

3.1 Introduction

In Chapter 2, we discussed two–step holographic recording in $LiNbO_3$:Fe crystals in detail. We showed that the main problem of this method is the strong dark depopulation of the shallower polaron traps resulting in a short effective lifetime for the electrons in these traps. Therefore, the method requires high light intensities to overcome this problem. One way to solve this problem is to replace the polaron traps with other traps that are farther from the conduction band. This can be done by doping the recording material with appropriate dopands. Since the deeper traps are also due to dopands, we need doubly–doped crystals to implement this new idea. We refer to this new method as two–center holographic recording.

In this chapter, we present the details of the two–center holographic recording method. The basic idea of two-center holographic recording is introduced in Section 3.2, and an experimental demonstration of the method is presented in Section 3.3. A theoretical model for the two–center method is introduced in Section 3.4. The model is used for the explanation of the experimental results. Based on the model developed in Section 3.4, the effect of the different design parameters on the holographic recording characteristics are investigated and an optimization scheme is developed in Section 3.5. Different characteristics of the method along with some suggestions for the improvement of the performance are discussed in Section 3.6. Final conclusions are made in Section 3.7.

3.2 Two-center holographic recording

Build-up of space–charge fields in photorefractive materials requires redistribution of charge. Transition metal ions can occur in inorganic crystals in different valence states, e.g., iron is present in $LiNbO_3$ as Fe^{2+} and Fe^{3+} [15]. Figure 3.1 (a) shows the energy band diagram for a $LiNbO_3$:Fe crystal. Inhomogeneous illumination excites electrons from Fe^{2+} to the conduction band, and they move due to the photovoltaic effect, diffusion and drift. The electrons are trapped by Fe^{3+} elsewhere and a space–charge field builds up, which modulates the refractive index via the electro–optic effect. Data can be erased by homogeneous illumination. However, read–out also requires homogeneous exposure, which causes undesirable erasure of the stored information. This is a general problem of all reversible storage media.

Two–center holographic recording is based on the usage of doubly–doped photochromic crystals [65, 66, 67], for example $LiNbO_3$ doped with manganese (Mn) and iron (Fe). It is known that $LiNbO_3$:Fe:Mn is photochromic and that ultraviolet pre–illumination enhances the sensitivity for a few recording and erasure cycles with visible light [68]. The energy band diagram of such a crystal is shown in Figure 3.1 (b). Fe and Mn ions occur in the valence states $Mn^{2+/3+}$ and $Fe^{2+/3+}$ [69], and thermal depletion plays no role. Electrons can be excited by ultraviolet light either from Mn^{2+} or from Fe^{2+} into the conduction band while red light excites electrons only from the shallower Fe^{2+}, because the red light has a smaller photon energy. The conduction band electrons can recombine with both centers, and thus ultraviolet illumination populates the $Fe^{2+/3+}$ level partially while the red light empties the Fe sites. The filled Fe levels cause a broadband absorption in the visible with a maximum at 477 nm light wavelength [15]. Thus ultraviolet light sensitizes the material while red light bleaches it. The basic idea of two–center holographic recording is to bring with the ultraviolet light electrons from Mn to Fe via the conduction band, use these electrons to record the hologram with red light, and eventually transfer the electrons from iron back to the manganese centers by red light. This results in a hologram stored in Mn centers that persists against further red illumination. One of the key

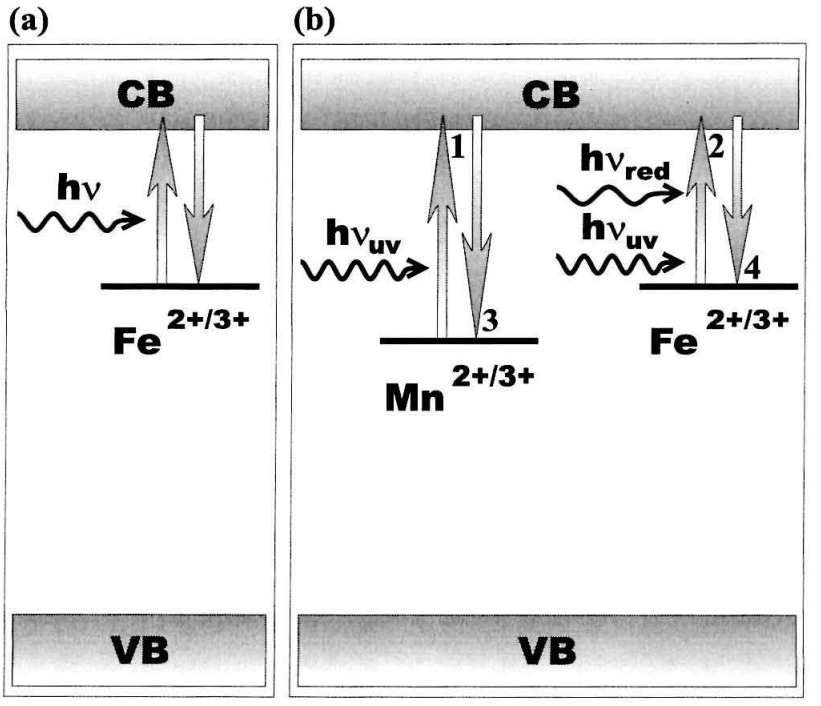

Figure 3.1: Energy band diagram for a typical $LiNbO_3$ crystal doped with **(a)** Fe, and **(b)** Fe and Mn. CB and VB stand for conduction band and valance band, respectively.

material parameters in two–center holographic recording is the initial electron concentration in Mn and Fe traps. These concentrations can be varied by annealing (or so–called oxidation / reduction treatment) [70]. For persistent holographic recording, it is necessary that the final hologram be stored in Mn centers to persist against further read–out by red light. Mn traps are deeper in the band gap than Fe traps. Therefore, electrons would fill the Mn traps before Fe traps. As a result, it is essential for persistent recording that all Fe traps be empty, and only a portion of the Mn traps be filled. This guarantees that the final hologram can be recorded in Mn traps after sufficient read–out.

3.3 Experiments

We performed experiments with a series of congruently melting x–cut $LiNbO_3$:Fe:Mn crystals with different doping levels and different annealing (or oxidation / reduction) states. All characterization experiments were performed with a $LiNbO_3$ crystal doped with 0.075 wt. % Fe_2O_3 and 0.01 wt. % MnO. The crystal was annealed appropriately to have all Fe traps as well as a portion of the Mn traps empty.

3.3.1 Experimental setup

The basic idea of the experimental setup needed for our experiments is shown in Figure 3.2 (a). We need a homogeneous incoherent UV beam for sensitization and two coherent red beams interfering at the crystal for holographic recording. The detailed experimental setup is shown in Figure 3.2 (b). We used a 100 W mercury lamp as the UV light source. The output light of the lamp is filtered (wavelength 365 nm or 404 nm depending on the experiment) and focused by a lens to increase the UV intensity at the crystal. We used a 35 mW HeNe laser for generation of the coherent red light (wavelength 633 nm). By timing the opening and closing of the shutters S1, S2, and S3 in Figure 3.2 (b), we can perform different experiments to help us understand the physical mechanisms responsible for holographic recording and optimizing the performance of the system.

3.3.2 Sensitization and bleaching experiments

A proper ratio between the intensities of the red recording and the ultraviolet sensitizing light, I_{red}/I_{uv}, is essential to get good holographic recording performance. Too much ultraviolet light causes erasure while too much red light causes bleaching and low sensitivity. A convenient way to adjust the intensity ratio is to use sensitization and bleaching experiments. UV light sensitizes the crystal for holographic recording with red light by transferring electrons from Mn to Fe centers via the conduction band. This increases the absorption of the red light. On the other hand, red

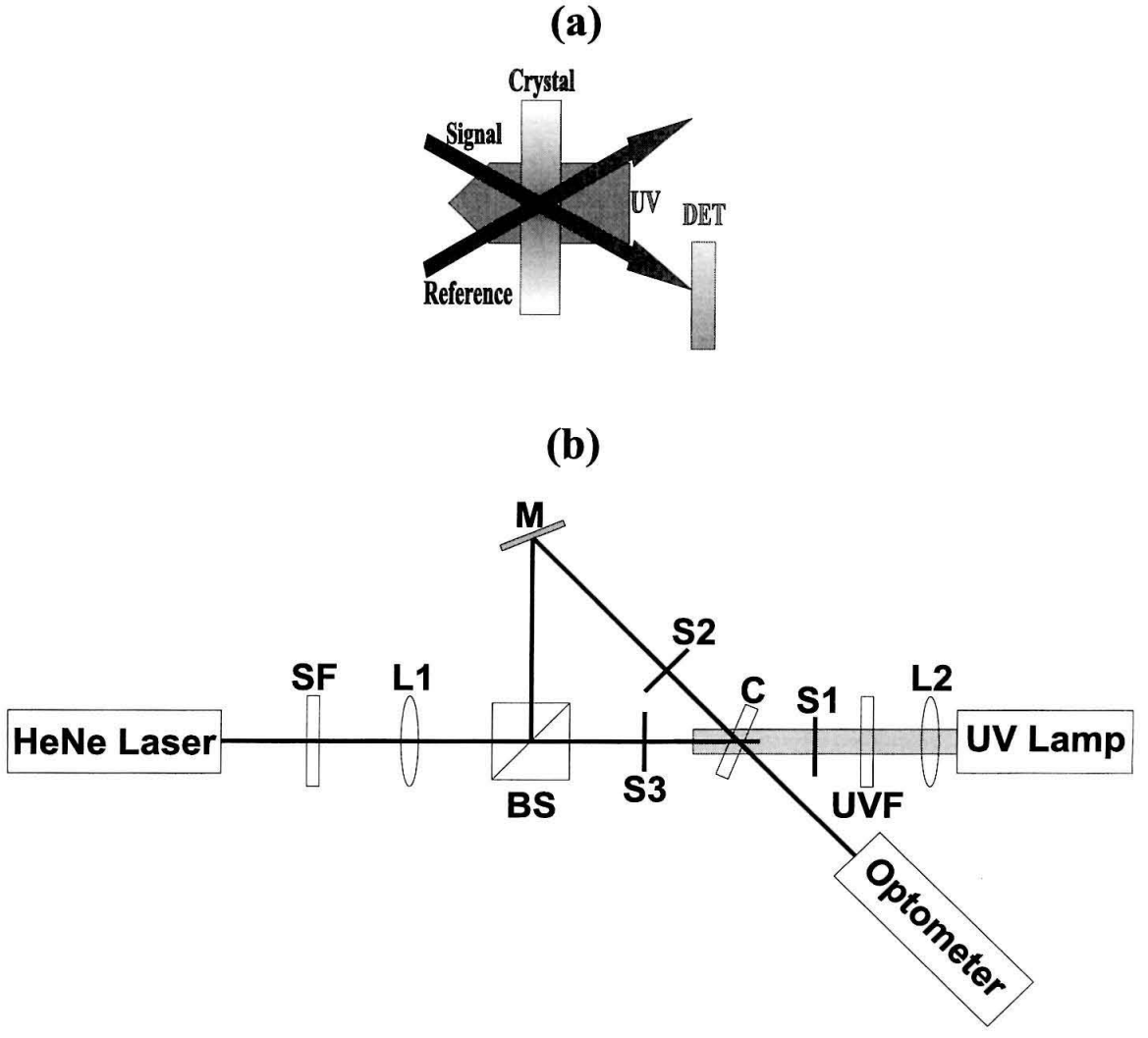

Figure 3.2: Experimental setup for holographic recording experiments: (a) basic idea, (b) actual setup. In the actual setup, L1 and L2 are lenses; M is a mirror; C is the crystal; SF is a spatial filter; UVF is a UV filter; BS is a beam splitter; and S1, S2, and S3 are shutters.

light bleaches the crystal by transferring electrons from Fe to Mn centers resulting in smaller absorption for red light.

To investigate sensitization dynamics, we monitor the absorption of the red light by the crystal. This is performed by illuminating the crystal with a very weak red beam and monitoring the transmitted red power with time. The intensity of the illuminating red light should be low enough to have negligible effect on the electron transfer between the traps. The sensitization experiment is performed using the experimental setup in Figure 3.2 (b) by opening the shutters S1 and S2, and closing shutter S3. On the other hand, red light causes electron transfer from Fe to Mn centers resulting in smaller absorption for red light. We monitor the bleaching dynamics by illuminating the sensitized crystal with only a strong uniform red beam and measuring the transmitted power. This can be performed using the experimental setup in Figure 3.2 (b) by opening the shutter S2, and closing shutters S1 and S3. Figure 3.3 shows typical results of the sensitization and bleaching experiments. The details of the experiments are summarized in the caption.

Figure 3.4 shows the picture of the $LiNbO_3$:Fe:Mn crystal after sensitization and bleaching experiments. The crystal was first sensitized for 3 hours using UV light (wavelength 365 nm, intensity 20 mW/cm^2). Then, the center of the sensitized crystal was bleached using a strong uniform red beam (wavelength 633 nm, intensity 300 mW/cm^2, ordinary polarization) for one hour. The crystal was initially (before any sensitization) transparent due to the lack of electrons in the Fe centers. Sensitization with UV populates some of the Fe traps resulting in the dark appearance of the crystal as shown in Figure 3.4. Bleaching with red light depopulates the Fe traps resulting in the transparent appearance of the bleached portion of the crystal as shown in Figure 3.4.

The time constants of sensitization and bleaching are measures of the rates of population and depopulation of the iron sites. They scale linearly with the light intensities, which allows tuning. The time constants should be of the same order of magnitude to achieve a strongly modulated Fe^{2+} concentration during hologram recording. Too strong UV light (relative to red light) results in too rapid sensitization

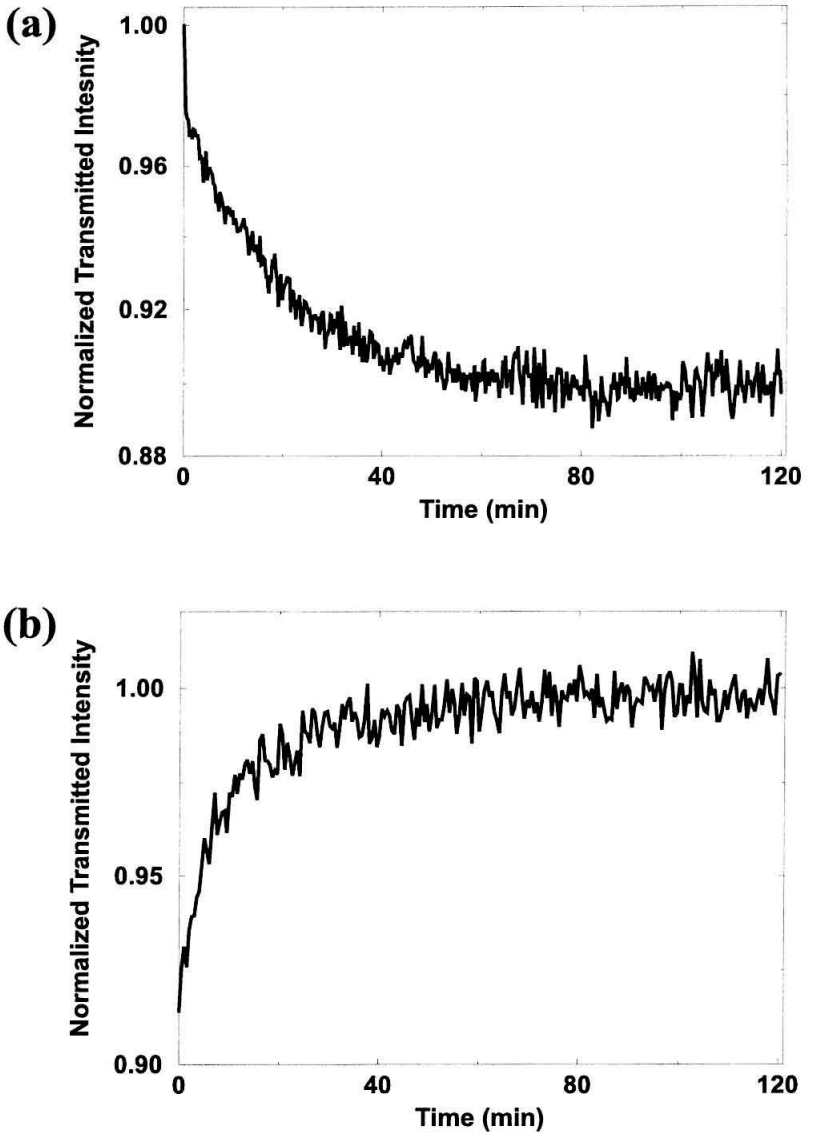

Figure 3.3: Normalized transmitted red intensity in a 0.85 mm $LiNbO_3$:Fe:Mn crystal. (a) Sensitization experiment: The crystal is sensitized with a homogeneous UV beam (wavelength 365 nm, intensity 20 mW/cm^2) while monitored by a weak red beam (wavelength 633 nm, intensity 0.6 mW/cm^2, ordinary polarization), (b) Bleaching experiment: The sensitized crystal is bleached with a strong red beam (wavelength 633 nm, intensity 300 mW/cm^2, ordinary polarization).

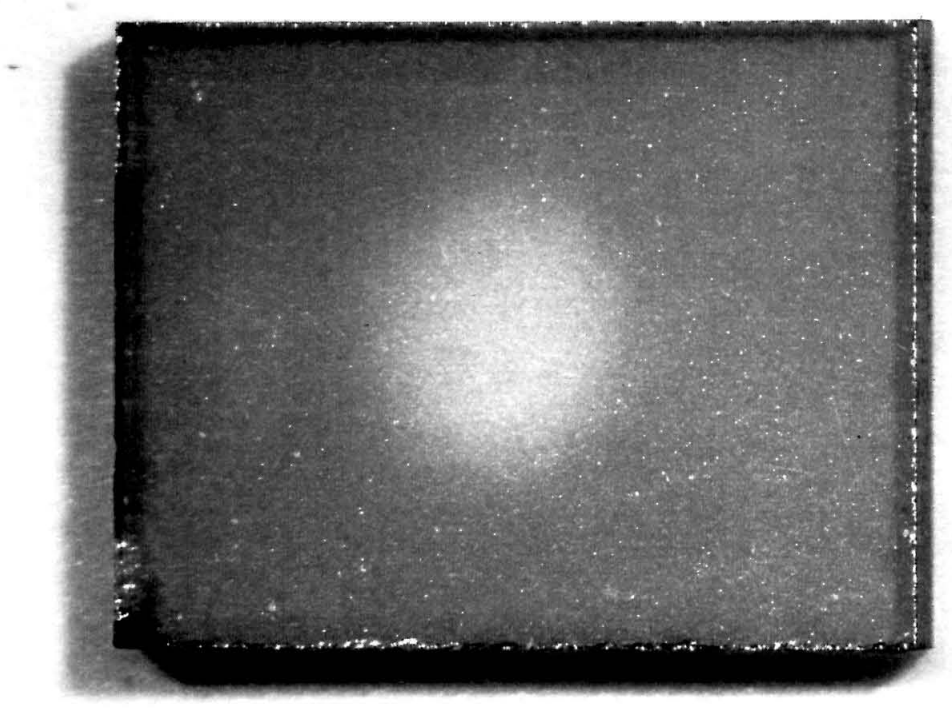

Figure 3.4: Effect of sensitization and bleaching on the appearance of a $LiNbO_3$:Fe:Mn crystal. The crystal is first sensitized with a homogeneous UV beam (wavelength 365 nm, intensity 20 mW/cm^2) for 3 hours. Then the center of the sensitized crystal is bleached with a strong red beam (wavelength 633 nm, intensity 300 mW/cm^2, ordinary polarization). The sensitized portion of the crystal looks dark, while the bleached part as well as the initial crystal (before any sensitization) look transparent.

and also too rapid erasure of the hologram. Therefore, strong holograms can not be recorded. On the other hand, too strong red light (compared to UV light) results in too rapid bleaching of the Fe traps, and lack of enough electrons in Fe traps for efficient holographic recording. Therefore, it is important to optimize the ratio between UV and red intensities. We find from the sensitization / bleaching experiments an optimum intensity ratio of $I_{\mathrm{red}}/I_{\mathrm{uv}} \approx 30$ in order to record the strongest hologram.

3.3.3 Holographic recording experiments

To get information about the holographic performance, plane–wave gratings are recorded and reconstructed using the same $LiNbO_3$:Fe:Mn crystal that we used in the previous experiments. The unpolarized ultraviolet light illuminates the sample homogeneously; the HeNe laser light is split into two plane waves which interfere at the crystal ($1/e^2$ beam diameter 2.0 mm, transmission geometry, period length of the grating 0.9 μm, intensity of each beam 0.3 W/cm^2). The grating vector is aligned parallel to the c–axis of the sample. The crystal is pre–exposed to UV light for at least 3 hours before recording. During recording, one of the HeNe beams is blocked (by closing S2 in Figure 3.2 (b)) from time to time and the second beam is diffracted from the written grating to obtain the diffraction efficiency η as the ratio between diffracted and total incident light powers. Figure 3.5 shows the results. The diffraction efficiency rises quickly and drops afterwards almost to zero with no ultraviolet light present (S1 closed in Figure 3.2 (b)) during the hologram formation. After some reading, the grating finally disappears completely. With assistance of ultraviolet light during recording (S1 open in Figure 3.2 (b)), much higher efficiencies are obtained. Subsequent reading erases first the grating partially, but the remaining grating persists despite further red illumination. It is clear that the presence of ultraviolet light during hologram formation is crucial for obtaining large diffraction efficiencies and persistent read–out. Finally, the hologram can be erased by either the UV light only (S1 open, S2 and S3 closed in Figure 3.2 (b)) or the UV light and one of the red beams simultaneously (S1 and S3 open, S2 closed in Figure 3.2 (b)). Figure 3.6 shows the

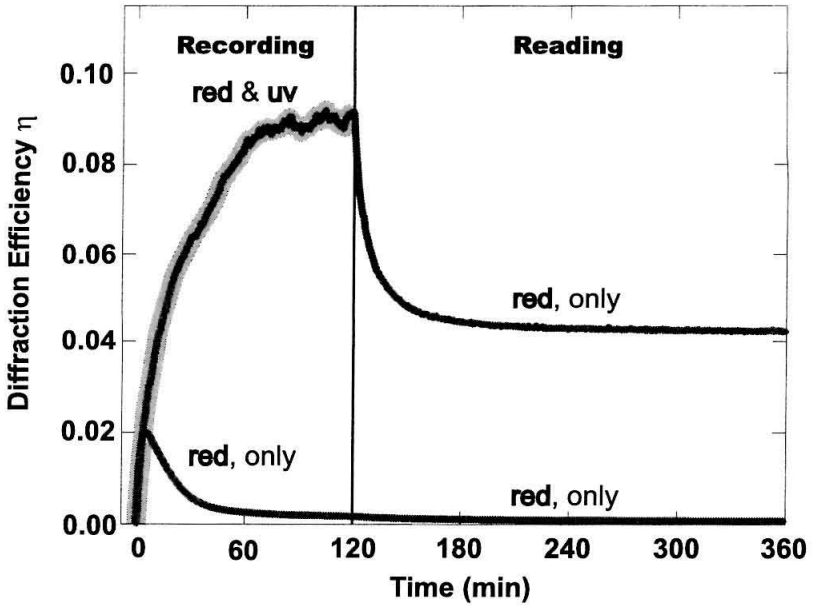

Figure 3.5: Diffraction efficiency η versus time for recording without and with simultaneous presence of ultraviolet light, and for subsequent reading in a $LiNbO_3$:Fe:Mn crystal.

diffraction efficiency vs. time for a plane–wave hologram erased by UV and red beams simultaneously. Recording was performed by two red beams with simultaneous illumination with a UV beam, while erasure was performed by the UV beam and one of the red recording beams. The specifications of the beams are the same as those of the recording experiment.

3.4 Theory

In this section, we discuss a theoretical model that can explain the experimental results. The model is similar to the two–center charge transport model for $LiNbO_3$:Fe introduced in 1993 by Jermann and Otten [48]. The goal of the model is to find the time evolution of the space–charge field recorded by two interfering recording beams in the presence of a homogeneous sensitizing beam.

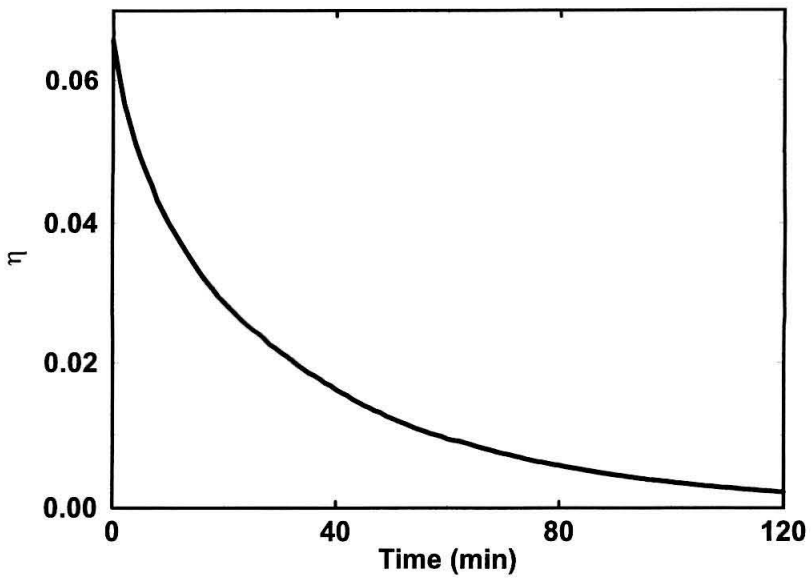

Figure 3.6: Diffraction efficiency η versus time for erasure with simultaneous presence of UV and one of the red recording beams. The hologram was recorded by simultaneous presence of UV and two red recording beams to an arbitrary diffraction efficiency of close to 7%.

3.4.1 Two–center model

In the theoretical modeling of holographic recording in a doubly–doped $LiNbO_3$:Mn:Fe crystal, we employ a set of five equations to solve for five unknowns. These unknowns are electron concentration in the conduction band (n), electron concentration in the deeper and shallower traps (N_{Mn}^{-} and N_{Fe}^{-}, respectively), current density (j), and space–charge (electric) field (E). The system of five equations that needs to be solved for these unknowns is:

$$\frac{\partial N_{\mathrm{Mn}}^{-}}{\partial t} = -[q_{\mathrm{Mn,R}} s_{\mathrm{Mn,R}} I_{\mathrm{R}} + q_{\mathrm{Mn,UV}} s_{\mathrm{Mn,UV}} I_{\mathrm{UV}}] N_{\mathrm{Mn}}^{-} + \gamma_{\mathrm{Mn}} n (N_{\mathrm{Mn}} - N_{\mathrm{Mn}}^{-}) \ , \quad (3.1)$$

$$\frac{\partial N_{\mathrm{Fe}}^{-}}{\partial t} = -[q_{\mathrm{Fe,R}} s_{\mathrm{Fe,R}} I_{\mathrm{R}} + q_{\mathrm{Fe,UV}} s_{\mathrm{Fe,UV}} I_{\mathrm{UV}}] N_{\mathrm{Fe}}^{-} + \gamma_{\mathrm{Fe}} n (N_{\mathrm{Fe}} - N_{\mathrm{Fe}}^{-}) \ , \quad (3.2)$$

$$\frac{\partial j}{\partial x} = -e \left(\frac{\partial N_{\mathrm{Fe}}^{-}}{\partial t} + \frac{\partial N_{\mathrm{Mn}}^{-}}{\partial t} + \frac{\partial n}{\partial t} \right) \ , \quad (3.3)$$

$$j = e\mu n E + k_{\mathrm{B}} T \mu \frac{\partial n}{\partial x} + (\kappa_{\mathrm{Fe,R}} I_{\mathrm{R}} + \kappa_{\mathrm{Fe,UV}} I_{\mathrm{UV}}) N_{\mathrm{Fe}}^{-} + (\kappa_{\mathrm{Mn,R}} I_{\mathrm{R}} + \kappa_{\mathrm{Mn,UV}} I_{\mathrm{UV}}) N_{\mathrm{Mn}}^{-} \ , \quad (3.4)$$

$$\frac{\partial E}{\partial x} = \frac{\rho}{\epsilon \epsilon_0} = -\frac{e}{\epsilon \epsilon_0} (N_{\mathrm{Fe}}^{-} + N_{\mathrm{Mn}}^{-} + n - N_{\mathrm{A}}) \ . \quad (3.5)$$

All symbols are introduced in Tab. 3.1. Some parameters have a subscript 'R' or 'UV' to indicate whether they are for red (in general, recording) or UV (in general, sensitizing) light. In writing Equations (3.1)-(3.5) we implicitly assumed that all variables have one dimensional (x) spatial variations.

The first two equations are rate equations for the deeper (Mn) and shallower (Fe) traps, respectively. These equations simply require that the rate of increase in electron concentration in each trap is equal to the incoming rate of electrons minus the outgoing rate of electrons. The incoming rate of electrons in each trap depends on the recombination coefficient of that trap as the only way of populating a trap is trapping electrons from the conduction band as shown in Figure 3.1 (b). The outgoing rate of electrons from each trap depends on the light intensities involved and the absorption cross section of that trap at the incident light wavelength. Thermal depopulation of the traps is neglected as both Fe and Mn traps are deep enough in the band gap. The third equation is the current continuity equation. The fourth equation is the current equation describing the current density as the sum of drift, diffusion, and four photovoltaic currents. Finally, the fifth equation is Poisson's equation.

Equations (3.1)–(3.5) compose a system of partial differential equations in time and space that is difficult to solve in general. To simplify the solution, we assume that the sensitizing intensity is homogeneous, and the recording intensity (I_{R}) has

Quantity (unit)	Meaning	Value	Reference
	Parameters of Fe		
N_{Fe} (m^{-3})	total concentration of Fe	(2.5×10^{25})	
N_{Fe}^{-} (m^{-3})	concentration of Fe^{2+}	(0)	
$s_{Fe,R}$ (m^2/J)	photon absorption cross section of Fe^{2+} (light wavelength 633 nm)	3.7×10^{-4}	[15, 71]
$q_{Fe,R}s_{Fe,R}$ (m^2/J)	absorption cross section of Fe^{2+} for absorption of a photon *and* excitation of an electron from Fe^{2+} into the conduction band (light wavelength 633 nm)	3.3×10^{-6}	[72]
$q_{Fe,UV}s_{Fe,UV}$ (m^2/J)	absorption cross section of Fe^{2+} for absorption of a photon *and* excitation of an electron from Fe^{2+} into the conduction band (light wavelength 365 nm)	3.8×10^{-5}	[72]
γ_{Fe} (m^3/s)	coefficient for recombination of conduction band electrons with Fe^{3+}	1.65×10^{-14}	[48]
$-\kappa_{Fe,R}$ (m^3/V)	bulk photovoltaic coefficient for excitation of electrons from Fe^{2+} into the conduction band (light wavelength 633 nm)	7×10^{-34}	[71, 72]
$-\kappa_{Fe,UV}$ (m^3/V)	bulk photovoltaic coefficient for excitation of electrons from Fe^{2+} into the conduction band (light wavelength 365 nm)	1.4×10^{-32}	[71, 72]
	Parameters of Mn		
N_{Mn} (m^{-3})	total concentration of Mn	(3.8×10^{24})	
N_{Mn}^{-} (m^{-3})	concentration of Mn^{2+}	(3.4×10^{24})	
$q_{Mn,R}s_{Mn,R}$ (m^2/J)	absorption cross section of Mn^{2+} for absorption of a photon *and* excitation of an electron into the conduction band (light wavelength 633 nm)	(0)	
$q_{Mn,UV}s_{Mn,UV}$ (m^2/J)	absorption cross section of Mn^{2+} for absorption of a photon *and* excitation of an electron into the conduction band (light wavelength 365 nm)	3.6×10^{-5}	this work
γ_{Mn} (m^3/s)	coefficient for recombination of conduction band electrons with Mn^{3+}	2.4×10^{-13}	this work
$-\kappa_{Mn,R}$ (m^3/V)	bulk photovoltaic coefficient for excitation of electrons from Mn^{2+} into the conduction band (light wavelength 633 nm)	0	
$-\kappa_{Mn,UV}$ (m^3/V)	bulk photovoltaic coefficient for excitation of electrons from Mn^{2+} into the conduction band (light wavelength 365 nm)	1.1×10^{-32}	this work

Quantity (unit)	Meaning	Value	Reference
	Parameters of $LiNbO_3$		
ϵ	dielectric coefficient	28	[53, 54]
r_{13} (m/V)	electro–optic coefficient (light wavelength 632.8 nm)	10.9×10^{-12}	[55]
n_o	refractive index for ordinarily polarized light (wavelength 632.8 nm)	2.286	[56]
	Charge transport parameters		
j (A/m^2)	current density	variable	
μ (m^2/Vs)	electron mobility in the conduction band	7.4×10^{-5}	[57]
n (m^{-3})	density of free electrons in the conduction band	variable	
ρ (As/m^3)	total charge density	variable	
N_A (m^{-3})	concentration of nonmobile positive compensation charge, which maintains overall charge neutrality	(3.4×10^{24})	
E (V/m)	space–charge field	variable	
	Fundamental constants		
k_B (J/K)	Boltzmann constant	1.38×10^{-23}	
ϵ_0 (As/Vm)	primitivity of free space	8.85×10^{-12}	
	Parameters related to the experimental conditions		
T (K)	crystal temperature	293	
K (m^{-1})	spatial frequency of the interference pattern	6.9×10^6	
Λ (m)	period length of the interference pattern	0.9×10^{-6}	
I_{UV} (W/m^2)	intensity of the spatially homogeneous UV light (wavelength 365 nm)	variable	
I_R (W/m^2)	intensity of the red light (wavelength 633 nm)	variable	
m	modulation degree of the interference pattern of the infrared light	variable	

Table 3.1: Units, meaning and values of all quantities involved in the analysis of two–center holographic recording in a $LiNbO_3$:Fe:Mn crystal. Subscripts '0' and '1' are added in the text to the spatially dependent quantities to indicate zeroth and first Fourier components. Values in parentheses show standard values, which are valid if nothing else is mentioned. Most of the values are determined by using the experimental data curves in the referenced literature.

one-dimensional sinusoidal variation with space as

$$I_{\mathrm{R}} = I_{\mathrm{R},0}[1 + m\cos(Kx)] \tag{3.6}$$

where K and m are the magnitude of the grating vector and modulation depth of the recording intensity pattern, respectively. The above system of equations is one-to-one, i.e., it gives only one set of outputs for one set of inputs. For such a system, a periodic set of inputs result in a periodic set of outputs with (at least) the same period. Therefore, with periodic I_{R} as in Equation (3.6), every output variable is periodic with the same period as the input and can be represented by a Fourier series in x. Since we are mainly interested in the zeroth (DC) and first order terms of the Fourier series of each variable, we represent each variable by the first two terms of its Fourier series. For example, the concentration of electrons in Mn traps can be represented as

$$N^-_{\mathrm{Mn}} = N^-_{\mathrm{Mn0}} + N^-_{\mathrm{Mn1}}\exp(iKx)\ . \tag{3.7}$$

By replacing each variable in Equations (3.1)–(3.5) with the first two terms in its Fourier series and separating zeroth and first order equations, we obtain two sets of equations as

$$\begin{aligned}
\frac{dN^-_{\mathrm{Mn0}}}{dt} &= -[q_{\mathrm{Mn,R}}s_{\mathrm{Mn,R}}I_{\mathrm{R0}} + q_{\mathrm{Mn,UV}}s_{\mathrm{Mn,UV}}I_{\mathrm{UV}}]N^-_{\mathrm{Mn0}} \\
&\quad +\gamma_{\mathrm{Mn}}n_0(N_{\mathrm{Mn}} - N^-_{\mathrm{Mn0}})\ , && (3.8)\\
\frac{dN^-_{\mathrm{Fe0}}}{dt} &= -[q_{\mathrm{Fe,R}}s_{\mathrm{Fe,R}}I_{\mathrm{R0}} + q_{\mathrm{Fe,UV}}s_{\mathrm{Fe,UV}}I_{\mathrm{UV}}]N^-_{\mathrm{Fe0}} + \gamma_{\mathrm{Fe}}n_0(N_{\mathrm{Fe}} - N^-_{\mathrm{Fe0}})\ , && (3.9)\\
0 &= \frac{dN^-_{\mathrm{Fe0}}}{dt} + \frac{dN^-_{\mathrm{Mn0}}}{dt} + \frac{dn_0}{dt}\ , && (3.10)\\
0 &= N^-_{\mathrm{Fe}} + N^-_{\mathrm{Mn}} + n - N_{\mathrm{A}} && (3.11)
\end{aligned}$$

and

$$\frac{dN^-_{\mathrm{Mn1}}}{dt} = -[q_{\mathrm{Mn,R}}s_{\mathrm{Mn,R}}I_{\mathrm{R0}} + q_{\mathrm{Mn,UV}}s_{\mathrm{Mn,UV}}I_{\mathrm{UV}}]N^-_{\mathrm{Mn1}} - q_{\mathrm{Mn,R}}s_{\mathrm{Mn,R}}mI_{\mathrm{R0}}N^-_{\mathrm{Mn0}}$$
$$+\gamma_{\mathrm{Mn}}n_1(N_{\mathrm{Mn}} - N^-_{\mathrm{Mn0}}) - \gamma_{\mathrm{Mn}}n_0N^-_{\mathrm{Mn1}} \ , \tag{3.12}$$

$$\frac{dN^-_{\mathrm{Fe1}}}{dt} = -[q_{\mathrm{Fe,R}}s_{\mathrm{Fe,R}}I_{\mathrm{R0}} + q_{\mathrm{Fe,UV}}s_{\mathrm{Fe,UV}}I_{\mathrm{UV}}]N^-_{\mathrm{Fe1}} - q_{\mathrm{Fe,R}}s_{\mathrm{Fe,R}}mI_{\mathrm{R0}}N^-_{\mathrm{Fe0}}$$
$$+\gamma_{\mathrm{Fe}}n_1(N_{\mathrm{Fe}} - N^-_{\mathrm{Fe0}}) - \gamma_{\mathrm{Fe}}n_0N^-_{\mathrm{Fe1}} \ , \tag{3.13}$$

$$\frac{-iK}{e}j_1 = \left(\frac{dN^-_{\mathrm{Fe1}}}{dt} + \frac{dN^-_{\mathrm{Mn1}}}{dt} + \frac{dn_1}{dt}\right) \ , \tag{3.14}$$

$$j_1 = e\mu n_0E_1 + e\mu n_1E_0 - ik_{\mathrm{B}}T\mu Kn_1 + (\kappa_{\mathrm{Fe,R}}I_{\mathrm{R0}} + \kappa_{\mathrm{Fe,UV}}I_{\mathrm{UV}})N^-_{\mathrm{Fe1}}$$
$$+\kappa_{\mathrm{Fe,R}}mI_{\mathrm{R0}}N^-_{\mathrm{Fe0}} + (\kappa_{\mathrm{Mn,R}}I_{\mathrm{R0}} + \kappa_{\mathrm{Mn,UV}}I_{\mathrm{UV}})N^-_{\mathrm{Mn1}}$$
$$+\kappa_{\mathrm{Mn,R}}mI_{\mathrm{R0}}N^-_{\mathrm{Mn0}} \ , \tag{3.15}$$

$$\frac{iK}{e}E_1 = \frac{N^-_{\mathrm{Fe1}} + N^-_{\mathrm{Mn1}} + n_1}{\epsilon\epsilon_0} \ . \tag{3.16}$$

We need to first solve the system of equations for the zeroth order variables as they appear on the right–hand side of the equations for the first order variables. Note that by assuming sinusoidal variations for the recording intensity, we need to solve two systems of ordinary differential equations (for a total of 10 variables) instead of one smaller system of partial differential equations (for a total of 5 variables). We use a few approximations that simplify the solutions. First of all, we assume that the variations of the electron concentration in the conduction band (n) are instantaneous compared to the variations of the other variables. This is called adiabatic approximation and results in replacing $\frac{\partial n}{\partial t} = \frac{dn_0}{dt} = \frac{dn_1}{dt} = 0$ in the above equations. Performing simulations with and without this approximation results in essentially the same answer. Next, we assume that $n \ll N^-_{\mathrm{Mn}}, N^-_{\mathrm{Fe}}, N_{\mathrm{A}}$. This assumption results in omitting n, n_0, and n_1 from Equations (3.5), (3.11), and (3.16), respectively.

We start with the zeroth order equations. By putting Equations (3.8) and (3.9) into Equation (3.10) and using adiabatic approximation, we can find n_0 as a function

of N^-_{Mn0} and N^-_{Fe0}

$$\begin{aligned} n_0 &= \frac{q_{\mathrm{Fe,R}} s_{\mathrm{Fe,R}} I_{\mathrm{R0}} + q_{\mathrm{Fe,UV}} s_{\mathrm{Fe,UV}} I_{\mathrm{UV}}}{\gamma_{\mathrm{Fe}}(N_{\mathrm{Fe}} - N^-_{\mathrm{Fe0}}) + \gamma_{\mathrm{Mn}}(N_{\mathrm{Mn}} - N^-_{\mathrm{Mn0}})} N^-_{\mathrm{Fe0}} \\ &\quad + \frac{q_{\mathrm{Mn,R}} s_{\mathrm{Mn,R}} I_{\mathrm{R0}} + q_{\mathrm{Mn,UV}} s_{\mathrm{Mn,UV}} I_{\mathrm{UV}}}{\gamma_{\mathrm{Fe}}(N_{\mathrm{Fe}} - N^-_{\mathrm{Fe0}}) + \gamma_{\mathrm{Mn}}(N_{\mathrm{Mn}} - N^-_{\mathrm{Mn0}})} N^-_{\mathrm{Mn0}} \,. \end{aligned} \tag{3.17}$$

Furthermore, by neglecting n_0 in Equation (3.11) we obtain

$$N^-_{\mathrm{Mn0}} = N_{\mathrm{A}} - N^-_{\mathrm{Fe0}} \,. \tag{3.18}$$

Using Equations (3.17) and (3.18) in Equation (3.9), we obtain a first order differential equation for N^-_{Fe0} as

$$\begin{aligned} \frac{dN^-_{\mathrm{Fe0}}}{dt} &= \frac{\gamma_{\mathrm{Fe}}[q_{\mathrm{Mn,R}} s_{\mathrm{Mn,R}} I_{\mathrm{R0}} + q_{\mathrm{Mn,UV}} s_{\mathrm{Mn,UV}} I_{\mathrm{UV}}](N_{\mathrm{A}} - N^-_{\mathrm{Fe0}})(N_{\mathrm{Fe}} - N^-_{\mathrm{Fe0}})}{\gamma_{\mathrm{Fe}}(N_{\mathrm{Fe}} - N^-_{\mathrm{Fe0}}) + \gamma_{\mathrm{Mn}}(N_{\mathrm{Mn}} - N_{\mathrm{A}} + N^-_{\mathrm{Fe0}})} \\ &\quad - \frac{\gamma_{\mathrm{Mn}}[q_{\mathrm{Fe,R}} s_{\mathrm{Fe,R}} I_{\mathrm{R0}} + q_{\mathrm{Fe,UV}} s_{\mathrm{Fe,UV}} I_{\mathrm{UV}}] N^-_{\mathrm{Fe0}}(N_{\mathrm{Mn}} - N_{\mathrm{A}} + N^-_{\mathrm{Fe0}})}{\gamma_{\mathrm{Fe}}(N_{\mathrm{Fe}} - N^-_{\mathrm{Fe0}}) + \gamma_{\mathrm{Mn}}(N_{\mathrm{Mn}} - N_{\mathrm{A}} + N^-_{\mathrm{Fe0}})} \,. \end{aligned} \tag{3.19}$$

The initial condition for Equation (3.19) depends on the crystal and the experimental condition. For example, for a crystal that has all Fe traps empty before sensitization, it would be $N^-_{\mathrm{Fe0}}(0) = 0$. Solving Equation (3.19) with the appropriate initial condition results in the solution for all zeroth order variables that can be used to solve the first order equations [Equations (3.12)–(3.16)].

The next step is to solve the first order equations to obtain the space charge field that results into the calculation of the change in the index of refraction and diffraction efficiency. To solve the first order equations, we first neglect $\frac{dn_1}{dt}$ in Equation (3.14) and n_1 in Equation (3.16), and then combine Equations (3.14), (3.15), (3.16) to obtain

$$\begin{aligned} \frac{d(N^-_{\mathrm{Mn1}} + N^-_{\mathrm{Fe1}})}{dt} &= -\frac{e\mu n_0}{\epsilon\epsilon_0}(N^-_{\mathrm{Mn1}} + N^-_{\mathrm{Fe1}}) - \frac{iK}{e}(\kappa_{\mathrm{Fe,R}} I_{\mathrm{R0}} + \kappa_{\mathrm{Fe,UV}} I_{\mathrm{UV}}) N^-_{\mathrm{Fe1}} \\ &\quad - \frac{iK}{e}(\kappa_{\mathrm{Mn,R}} I_{\mathrm{R0}} + \kappa_{\mathrm{Mn,UV}} I_{\mathrm{UV}}) N^-_{\mathrm{Mn1}} - \frac{k_{\mathrm{B}} T}{e} \mu K^2 n_1 \\ &\quad - iK\mu n_1 E_0 - \frac{iK}{e}(\kappa_{\mathrm{Mn,R}} N^-_{\mathrm{Mn0}} + \kappa_{\mathrm{Fe,R}} N^-_{\mathrm{Fe0}}) m I_{\mathrm{R0}} \,. \end{aligned} \tag{3.20}$$

By combining Equation (3.12), (3.13), and (3.20) we can solve for n_1 as a function of N^-_{Mn1} and N^-_{Fe1}

$$n_1 = \frac{G_{\mathrm{Fe}}N^-_{\mathrm{Fe1}} + G_{\mathrm{Mn}}N^-_{\mathrm{Mn1}} + G_{\mathrm{R}}mI_{\mathrm{R0}}}{\gamma_{\mathrm{Fe}}(N_{\mathrm{Fe}} - N^-_{\mathrm{Fe0}}) + \gamma_{\mathrm{Mn}}(N_{\mathrm{Mn}} - N^-_{\mathrm{Mn0}}) + \frac{k_{\mathrm{B}}T}{e}\mu K^2 + iK\mu E_0}\ , \quad (3.21)$$

where the parameters G_{Fe}, G_{Mn}, and G_{R} are defined as

$$\begin{aligned} G_{\mathrm{Fe}} &= q_{\mathrm{Fe,R}}s_{\mathrm{Fe,R}}I_{\mathrm{R0}} + q_{\mathrm{Fe,UV}}s_{\mathrm{Fe,UV}}I_{\mathrm{UV}} + \gamma_{\mathrm{Fe}}n_0 - \frac{e\mu n_0}{\epsilon\epsilon_0} \\ &\quad -\frac{iK}{e}(\kappa_{\mathrm{Fe,R}}I_{\mathrm{R0}} + \kappa_{\mathrm{Fe,UV}}I_{\mathrm{UV}})\ , \quad (3.22) \\ G_{\mathrm{Mn}} &= q_{\mathrm{Mn,R}}s_{\mathrm{Mn,R}}I_{\mathrm{R0}} + q_{\mathrm{Mn,UV}}s_{\mathrm{Mn,UV}}I_{\mathrm{UV}} + \gamma_{\mathrm{Mn}}n_0 - \frac{e\mu n_0}{\epsilon\epsilon_0} \\ &\quad -\frac{iK}{e}(\kappa_{\mathrm{Mn,R}}I_{\mathrm{R0}} + \kappa_{\mathrm{Mn,UV}}I_{\mathrm{UV}})\ , \quad (3.23) \\ G_{\mathrm{R}} &= (q_{\mathrm{Fe,R}}s_{\mathrm{Fe,R}} - \frac{iK}{e}\kappa_{\mathrm{Fe,R}})N^-_{\mathrm{Fe0}} + (q_{\mathrm{Mn,R}}s_{\mathrm{Mn,R}} - \frac{iK}{e}\kappa_{\mathrm{Mn,R}})N^-_{\mathrm{Mn0}}\ . \quad (3.24) \end{aligned}$$

We make two approximations to simplify the equations. First, we assume that there is no DC electric field, i.e., $E_0 = 0$. This is true when we do not apply any external field to the crystal. The screening field is also negligible due to the presence of the UV beam and a considerable surface conductivity as discussed later. Second, we assume that the diffusion field (E_{D}) is negligible compared to the strong photovoltaic field, i.e., $(k_{\mathrm{B}}T/e)\mu K^2 = \mu K E_{\mathrm{D}}$ in Equation (3.20) and Equation (3.21) is negligible. Putting n_1 from Equation (3.21) into Equation (3.12) and Equation (3.20) results in

a system of two equations for two unknowns N^-_{Mn1} and $(N^-_{\mathrm{Mn1}} + N^-_{\mathrm{Fe1}})$ as

$$\begin{aligned}
\frac{d(N^-_{\mathrm{Mn1}} + N^-_{\mathrm{Fe1}})}{dt} &= -\left[\frac{e\mu n_0}{\epsilon\epsilon_0} + \frac{iK}{e}(\kappa_{\mathrm{Fe,R}} I_{\mathrm{R0}} + \kappa_{\mathrm{Fe,UV}} I_{\mathrm{UV}})\right](N^-_{\mathrm{Mn1}} + N^-_{\mathrm{Fe1}}) \\
&\quad -\frac{iK}{e}[(\kappa_{\mathrm{Mn,R}} - \kappa_{\mathrm{Fe,R}})I_{\mathrm{R0}} + (\kappa_{\mathrm{Mn,UV}} - \kappa_{\mathrm{Fe,UV}})I_{\mathrm{UV}}]N^-_{\mathrm{Mn1}} \\
&\quad -\frac{iK}{e}(\kappa_{\mathrm{Mn,R}} N^-_{\mathrm{Mn0}} + \kappa_{\mathrm{Fe,R}} N^-_{\mathrm{Fe0}})mI_{\mathrm{R0}} \ , \qquad (3.25) \\
\frac{dN^-_{\mathrm{Mn1}}}{dt} &= G_1(q_{\mathrm{Fe,R}} s_{\mathrm{Fe,R}} I_{\mathrm{R0}} + q_{\mathrm{Fe,UV}} s_{\mathrm{Fe,UV}} I_{\mathrm{UV}} + \gamma_{\mathrm{Fe}} n_0)(N^-_{\mathrm{Mn1}} + N^-_{\mathrm{Fe1}}) \\
&\quad -G_1\left[\frac{e\mu n_0}{\epsilon\epsilon_0} + \frac{iK}{e}(\kappa_{\mathrm{Fe,R}} I_{\mathrm{R0}} + \kappa_{\mathrm{Fe,UV}} I_{\mathrm{UV}})\right](N^-_{\mathrm{Mn1}} + N^-_{\mathrm{Fe1}}) \\
&\quad -(q_{\mathrm{Mn,R}} s_{\mathrm{Mn,R}} I_{\mathrm{R0}} + q_{\mathrm{Mn,UV}} s_{\mathrm{Mn,UV}} I_{\mathrm{UV}} + \gamma_{\mathrm{Mn}} n_0 - G_1\, G_2)N^-_{\mathrm{Mn1}} \\
&\quad -\left[q_{\mathrm{Mn,R}} s_{\mathrm{Mn,R}} N^-_{\mathrm{Mn0}} - G_1\left(q_{\mathrm{Mn,R}} s_{\mathrm{Mn,R}} - \frac{iK}{e}\kappa_{\mathrm{Mn,R}}\right)N^-_{\mathrm{Mn0}}\right] mI_{\mathrm{R0}} \\
&\quad -G_1\left(q_{\mathrm{Fe,R}} s_{\mathrm{Fe,R}} - \frac{iK}{e}\kappa_{\mathrm{Fe,R}}\right)N^-_{\mathrm{Fe0}} mI_{\mathrm{R0}} \ , \qquad (3.26)
\end{aligned}$$

where G_1 and G_2 are defined by

$$\begin{aligned}
G_1 &= \frac{\gamma_{\mathrm{Mn}}(N_{\mathrm{Mn}} - N^-_{\mathrm{Mn0}})}{\gamma_{\mathrm{Fe}}(N_{\mathrm{Fe}} - N^-_{\mathrm{Fe0}}) + \gamma_{\mathrm{Mn}}(N_{\mathrm{Mn}} - N^-_{\mathrm{Mn0}})} \ , \qquad (3.27) \\
G_2 &= q_{\mathrm{Mn,R}} s_{\mathrm{Mn,R}} I_{\mathrm{R0}} + q_{\mathrm{Mn,UV}} s_{\mathrm{Mn,UV}} I_{\mathrm{UV}} + \gamma_{\mathrm{Mn}} n_0 - q_{\mathrm{Fe,R}} s_{\mathrm{Fe,R}} I_{\mathrm{R0}} - q_{\mathrm{Fe,UV}} s_{\mathrm{Fe,UV}} I_{\mathrm{UV}} \\
&\quad -\gamma_{\mathrm{Fe}} n_0 - \frac{iK}{e}[(\kappa_{\mathrm{Mn,R}} - \kappa_{\mathrm{Fe,R}})I_{\mathrm{R0}} + (\kappa_{\mathrm{Mn,UV}} - \kappa_{\mathrm{Fe,UV}})I_{\mathrm{UV}}] \ . \qquad (3.28)
\end{aligned}$$

Here we deliberately chose the first unknown as $(N^-_{\mathrm{Mn1}} + N^-_{\mathrm{Fe1}})$ instead of N^-_{Fe1} since we are mainly interested in calculating the space charge field (E_1) that is linearly proportional to $(N^-_{\mathrm{Mn1}} + N^-_{\mathrm{Fe1}})$ [Equation (3.16)]. The initial conditions for this system of equations is $N^-_{\mathrm{Mn1}}(t=0) = N^-_{\mathrm{Fe1}}(t=0) = 0$.

After finding E_1, it is easy to calculate the change in the index of refraction through the electro–optic effect as

$$\Delta n = -\frac{{n_{\mathrm{eff}}}^3}{2} r_{\mathrm{eff}} E_1 \ . \qquad (3.29)$$

Here r_{eff} is the effective electro–optic coefficient that depends on the direction of the space charge field with respect to the c–axis of the crystal and the polarization of the

read–out beam, and n_{eff} is the effective index of refraction for the read–out beam that depends on the polarization of that beam. Finally, we can calculate the diffraction efficiency from Δn by using Kogelnik's formula [52].

3.4.2 Parameters of the model

In order to have a reliable model, we need accurate estimates for the parameters of the model, i.e., absorption cross sections and recombination coefficients for the traps, etc. Although most of the parameters for Fe traps can be extracted from the literature, important parameters for the Mn traps need to be determined.

Absorption cross sections at different wavelengths can be obtained from the absorption spectrum of the crystal with known doping levels and known electron concentration in the traps. Photovoltaic constants for each trap at a specific wavelength can be obtained from the measurement of the short–circuit photovoltaic current of a crystal doped with that trap. The factors qs for each trap (for example, $q_{\text{Fe,UV}}s_{\text{Fe,UV}}$) can be typically found from photoconductivity measurements. The values of the important parameters are listed in Table 3.1. The references used in calculation of parameters of the Fe traps are also listed in Table 3.1. The main challenge is to find the parameters of the Mn traps, and also the initial electron concentration in the Mn traps. One way to find the latter is to use electron paramagnetic resonance (EPR) studies, but it needs careful calibration of the reference electron concentration in Mn traps. Knowing all Fe parameters, we performed experiments to find three additional parameters. These parameters are $q_{\text{Mn,UV}}s_{\text{Mn,UV}}$, γ_{Mn}, and initial electron concentration in the Mn traps $[N^{-}_{\text{Mn0}}(t=0) = N_{\text{A}}]$. We can assume that $q_{\text{Mn,R}}s_{\text{Mn,R}}$ and $\kappa_{\text{Mn,R}}$ are zero due to the deep position of the Mn traps in the band gap of $LiNbO_3$. To find the three parameters mentioned above, we need to obtain three equations. We use bleaching and sensitization experiments to find these equations. After finding these three parameters, we use curve fitting to find the last unknown parameter $\kappa_{\text{Mn,UV}}$. Finally, we optimize our calculation of the parameters by fine tuning these parameters to get the best fit to the sensitization, bleaching, and holographic recording curves.

Bleaching

As mentioned before, the bleaching experiment is performed to find the dynamics of electron transfer from Fe to Mn traps by a homogeneous red beam. When a sensitized crystal is illuminated with a strong red light, electrons are excited only from Fe traps to the conduction band. Some of these electrons are trapped by Fe centers, others are trapped by Mn centers. Those electrons that are trapped in Mn centers can not be re–excited to the conduction band. Therefore, the electron concentration in Fe traps decreases with time. The decrease in electron concentration in the Fe traps results in a decrease in the absorption of red light. The governing equations for the analysis of bleaching dynamics are

$$\frac{\partial N_{\mathrm{Mn}}^{-}}{\partial t} = \gamma_{\mathrm{Mn}} n (N_{\mathrm{Mn}} - N_{\mathrm{Mn}}^{-}) \,, \tag{3.30}$$

$$\frac{\partial N_{\mathrm{Fe}}^{-}}{\partial t} = -q_{\mathrm{Fe,R}} s_{\mathrm{Fe,R}} I_{\mathrm{R}} N_{\mathrm{Fe}}^{-} + \gamma_{\mathrm{Fe}} n (N_{\mathrm{Fe}} - N_{\mathrm{Fe}}^{-}) \,, \tag{3.31}$$

$$\frac{\partial N_{\mathrm{Fe}}^{-}}{\partial t} + \frac{\partial N_{\mathrm{Mn}}^{-}}{\partial t} = -\frac{1}{e}\frac{\partial j}{\partial x} = 0 \,, \tag{3.32}$$

where we assume adiabatic approximation ($\frac{\partial n}{\partial t} = 0$) in Equation (3.32). The initial conditions for N_{Fe}^{-} and N_{Mn}^{-} depend on the sensitization process, but the condition $N_{\mathrm{Fe}}^{-} + N_{\mathrm{Mn}}^{-} = N_{\mathrm{A}}$ must be always satisfied. We can find n as a function of N_{Mn}^{-} and N_{Fe}^{-} by putting $\partial N_{\mathrm{Mn}}^{-}/\partial t$ and $\partial N_{\mathrm{Fe}}^{-}/\partial t$ from Equations (3.30) and (3.31), respectively, into Equation (3.32). Putting $N_{\mathrm{Mn}}^{-} = N_{\mathrm{A}} - N_{\mathrm{Fe}}^{-}$ and the formula found for n in Equation (3.31), we can obtain a differential equation for N_{Fe}^{-} as

$$\frac{\partial N_{\mathrm{Fe}}^{-}}{\partial t} = -\frac{q_{\mathrm{Fe,R}} s_{\mathrm{Fe,R}} I_{\mathrm{R}} \gamma_{\mathrm{Mn}} (N_{\mathrm{Mn}} - N_{\mathrm{Mn}}^{-})}{\gamma_{\mathrm{Mn}} (N_{\mathrm{Mn}} - N_{\mathrm{Mn}}^{-}) + \gamma_{\mathrm{Fe}} (N_{\mathrm{Fe}} - N_{\mathrm{Fe}}^{-})} N_{\mathrm{Fe}}^{-} \simeq -\frac{\partial N_{\mathrm{Fe}}^{-}}{\tau_{\mathrm{b}}} \,. \tag{3.33}$$

To simplify the calculations, we assume that the absorption of the red light in the crystal is not large. Therefore, we can consider the red light intensity (I_{R}) in Equation (3.33) as a constant. We further assume that $N_{\mathrm{Fe}}^{-} \ll N_{\mathrm{Fe}}$ and $N_{\mathrm{Mn}}^{-} \simeq N_{\mathrm{A}}$. This is a good approximation when we neglect the beginning of the bleaching curve [Figure 3.3 (b)], and consider the dynamics of the latter part of the curve.

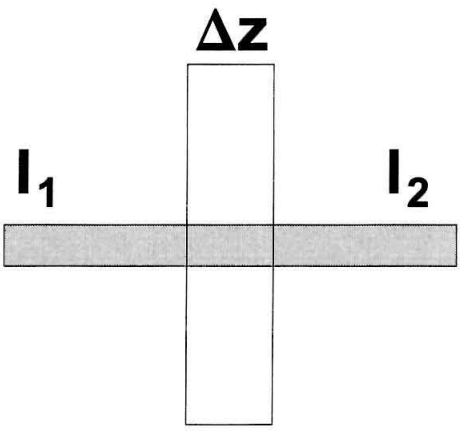

Figure 3.7: Transmission of an optical beam through a very thin portion of the crystal with thickness Δz. I_1 and I_2 are incident and transmitted light intensities.

With all these approximations, the bleaching time constant τ_b in Equation (3.33) becomes a constant independent of the position inside the crystal. The bleaching speed normalized to bleaching light intensity (I_R) can be represented as

$$\frac{1}{\tau_b I_R} = (q_{Fe,R} s_{Fe,R}) \left(1 + \frac{\gamma_{Fe} N_{Fe}}{\gamma_{Mn}(N_{Mn} - N_A)}\right)^{-1} . \quad (3.34)$$

The right–hand side of Equation (3.34) can be found experimentally by fitting the latter part of the bleaching curves at different intensities with monoexponential formulas. The important fact is that in the bleaching experiment, we measure the transmitted light intensity. Therefore, we need to find the relation between light transmission and electron concentration in Fe traps (N_{Fe}^-). For this purpose, consider a very thin portion (Δz) of the crystal as shown in Figure 3.7. The transmitted intensity from this portion, I_2, is related to the incident intensity, I_1, as

$$I_2 - I_1 = -(s_{Fe,R} N_{Fe}^- h\nu)\Delta z I_1 , \quad (3.35)$$

or

$$dI/I = -(s_{Fe,R} h\nu) N_{Fe}^- dz . \quad (3.36)$$

Integrating Equation (3.36) from $z = 0$ to $z = L$, with L being the thickness of the crystal, results in

$$I_t = I_i \exp\left(-s_{Fe,R} h\nu \int_0^L N_{Fe}^-(z)dz\right) , \tag{3.37}$$

where I_i and I_t are incident $[I(z = 0)]$ and transmitted $[I(z = L)]$ intensities, respectively. The experimental bleaching curve (as shown in Figure 3.3 (b)) can be approximately represented by

$$I_t = I_i - \Delta I \simeq I_i - \Delta I_0 \exp(-\frac{t}{\tau_{b2}}) , \tag{3.38}$$

where ΔI is the absorption change due to electron transfer from Mn to Fe centers, and can be represented from Equation (3.37) by

$$\Delta I = I_i \left[1 - \exp\left(-s_{Fe,R} h\nu \int_0^L N_{Fe}^-(z)dz\right)\right] . \tag{3.39}$$

The time constant τ_{b2} for the variation of ΔI can be calculated by taking the derivative of both sides of Equation (3.39)

$$\begin{aligned} \frac{d\Delta I}{dt} &= I_i s_{Fe,R} h\nu \exp\left(-s_{Fe,R} h\nu \int_0^L N_{Fe}^-(z)dz\right) \int_0^L \frac{dN_{Fe}^-(z)}{dt} dz \\ &= \frac{-s_{Fe,R} h\nu \int_0^L \frac{dN_{Fe}^-(z)}{dt} dz}{1 - \exp\left(s_{Fe,R} h\nu \int_0^L N_{Fe}^-(z)dz\right)} \Delta I \\ &= -\frac{\Delta I}{\tau_{b2}} . \end{aligned} \tag{3.40}$$

Assuming the optical density of the crystal for red light to be small ($s_{Fe,R} h\nu \int_0^L N_{Fe}^-(z)dz \ll 1$), we can simplify the denominator of the right–hand side of Equation (3.40). Furthermore, we can use $dN_{Fe}^-/dt \simeq -N_{Fe}^-/\tau_b$ from Equation (3.33) to rewrite Equa-

tion (3.40) as

$$\begin{aligned}\frac{d\Delta I}{dt} &= \frac{\int_0^L \frac{dN_{\mathrm{Fe}}^-(z)}{dt}dz}{\int_0^L N_{\mathrm{Fe}}^-(z)dz}\Delta I \\ &\simeq \frac{\int_0^L \frac{-1}{\tau_{\mathrm{b}}}N_{\mathrm{Fe}}^-(z)dz}{\int_0^L N_{\mathrm{Fe}}^-(z)dz)}\Delta I \\ &\simeq \frac{-\Delta I}{\tau_{\mathrm{b}}}\,. \end{aligned} \tag{3.41}$$

Comparing Equations (3.40) and (3.41) results in $\tau_{\mathrm{b}} = \tau_{\mathrm{b2}}$. Therefore, we can calculate $\frac{1}{\tau_{\mathrm{b2}}}/I_{\mathrm{R}}$ from bleaching experiments and put it in Equation (3.34) to obtain one equation for the unknown parameters. Figure 3.8 shows the variation of the bleaching speed ($1/\tau_{\mathrm{b2}}$) with red light intensity (I_{R}). The solid line in Figure 3.8 shows the linear fit to the experimental data. Using the slope of this line, we can obtain one equation for the unknown parameters as

$$\frac{\gamma_{\mathrm{Fe}}N_{\mathrm{Fe}}}{\gamma_{\mathrm{Mn}}(N_{\mathrm{Mn}} - N_{\mathrm{A}})} = 3.44\,. \tag{3.42}$$

Sensitization

As mentioned before, the sensitization experiment is performed to find the dynamics of electron transfer from Mn to Fe traps by a homogeneous UV beam. The increase in electron concentration in the Fe traps results in an increase in the absorption of red light. The governing equations for the analysis of sensitization dynamics are

$$\frac{\partial N_{\mathrm{Mn}}^-}{\partial t} = -q_{\mathrm{Mn,UV}}s_{\mathrm{Mn,UV}}I_{\mathrm{UV}}N_{\mathrm{Mn}}^- + \gamma_{\mathrm{Mn}}n(N_{\mathrm{Mn}} - N_{\mathrm{Mn}}^-)\,, \tag{3.43}$$

$$\frac{\partial N_{\mathrm{Fe}}^-}{\partial t} = -q_{\mathrm{Fe,UV}}s_{\mathrm{Fe,UV}}I_{\mathrm{UV}}N_{\mathrm{Fe}}^- + \gamma_{\mathrm{Fe}}n(N_{\mathrm{Fe}} - N_{\mathrm{Fe}}^-)\,, \tag{3.44}$$

$$\frac{\partial N_{\mathrm{Fe}}^-}{\partial t} + \frac{\partial N_{\mathrm{Mn}}^-}{\partial t} = -\frac{1}{e}\frac{\partial j}{\partial x} = 0\,, \tag{3.45}$$

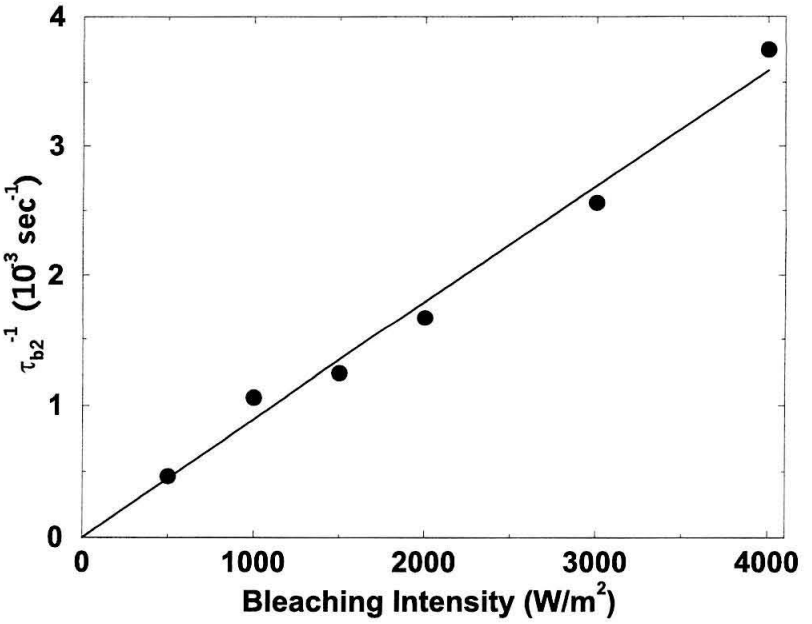

Figure 3.8: Variation of the bleaching speed ($1/\tau_{\mathrm{b2}}$) with bleaching intensity (I_{R}). The solid line shows a linear fit to the experimental data.

where we assume adiabatic approximation ($\frac{\partial n}{\partial t} = 0$) in Equation (3.45). The initial conditions are $N_{\mathrm{Fe}}^{-}(t=0) = 0$ and $N_{\mathrm{Mn}}^{-}(t=0) = N_{\mathrm{A}}$. Using $N_{\mathrm{Mn}}^{-} = N_{\mathrm{A}} - N_{\mathrm{Fe}}^{-}$ from Equation (3.45), we can find the differential equation for the electron concentration in the Fe traps as

$$\frac{\partial N_{\mathrm{Fe}}^{-}}{\partial t} = \frac{-q_{\mathrm{Fe,UV}} s_{\mathrm{Fe,UV}} \gamma_{\mathrm{Mn}} (N_{\mathrm{Mn}} - N_{\mathrm{Mn}}^{-}) N_{\mathrm{Fe}}^{-} + \gamma_{\mathrm{Fe}} q_{\mathrm{Mn,UV}} s_{\mathrm{Mn,UV}} (N_{\mathrm{Fe}} - N_{\mathrm{Fe}}^{-}) N_{\mathrm{Mn}}^{-}}{\gamma_{\mathrm{Fe}} (N_{\mathrm{Fe}} - N_{\mathrm{Fe}}^{-}) + \gamma_{\mathrm{Mn}} (N_{\mathrm{Mn}} - N_{\mathrm{Mn}}^{-})} \times I_{\mathrm{UV}} \, . \tag{3.46}$$

The major complication in finding an analytic solution for Equation (3.46) is the high absorption of the UV light. The measured absorption coefficient of the crystal at 365 nm is $\alpha = 9$ mm^{-1}. Equation (3.46) is a point form formula, i.e., it is valid at any point inside the crystal. To use the experimental results of the sensitization experiment for the calculation of the material parameters, we need to find from Equation (3.46) the total transmission of a weak red beam. For this purpose, consider the very thin portion (Δz) of the crystal as shown in Figure 3.7. Using

Equation (3.39), we can calculate the initial slope of the transmitted intensity ratio vs. time as

$$\frac{d(I_t/I_i)}{dt}|_{t=0} = -s_{Fe,R}h\nu \int_0^L \frac{dN_{Fe}^-(z)}{dt}|_{t=0}dz \ . \tag{3.47}$$

Substituting $\frac{dN_{Fe}^-(z)}{dt}|_{t=0}$ from Equation (3.46) into Equation (3.47), and replacing $I_{UV}(z)$ by $I_{UV0}\exp(-\alpha_{UV}z)$, we obtain

$$\frac{d(I_t/I_i)}{dt}|_{t=0} = \frac{(s_{Fe,R}h\nu)q_{Mn,UV}s_{Mn,UV}N_A}{1+\frac{\gamma_{Mn}(N_{Mn}-N_A)}{\gamma_{Fe}N_{Fe}}}\frac{I_{UV0}}{\alpha_{UV}} \ . \tag{3.48}$$

The left–hand side of Equation (3.48) can be calculated from the experimental results. Figure 3.9 (a) shows the variation of the initial sensitization slope ($\frac{d(I_t/I_i)}{dt}|_{t=0}$) with I_{UV0}. Figure 3.9 (a) shows that initial sensitization slope varies linearly with the UV intensity I_{UV0} as Equation (3.48) suggests. Replacing the slope of the line fitted to the experimental data ($[\frac{d(I_t/I_i)}{dt}|_{t=0}]/I_{UV0}$) in Equation (3.48) results in one equation for the unknowns as

$$\frac{(s_{Fe,R}h\nu)q_{Mn,UV}s_{Mn,UV}N_A}{1+\frac{\gamma_{Mn}(N_{Mn}-N_A)}{\gamma_{Fe}N_{Fe}}}\frac{1}{\alpha_{UV}} = 1.06\times10^{-6} \ . \tag{3.49}$$

Another equation can be obtained using the saturation value of the transmitted red light in the sensitization experiment. Figure 3.9 (b) shows the variation of the ratio of the transmitted to incident red intensity after 3 hours of sensitization vs. UV intensity I_{UV0}. This value is related to the electron concentration in Fe traps after 3 hours of sensitization. The complication in the theoretical calculation is due to the variation of N_{Fe}^- within the thickness of the crystal (as a result of the large UV absorption). We first replace N_{Mn}^- by $N_A - N_{Fe}^-$ in Equation (3.46), and rewrite the

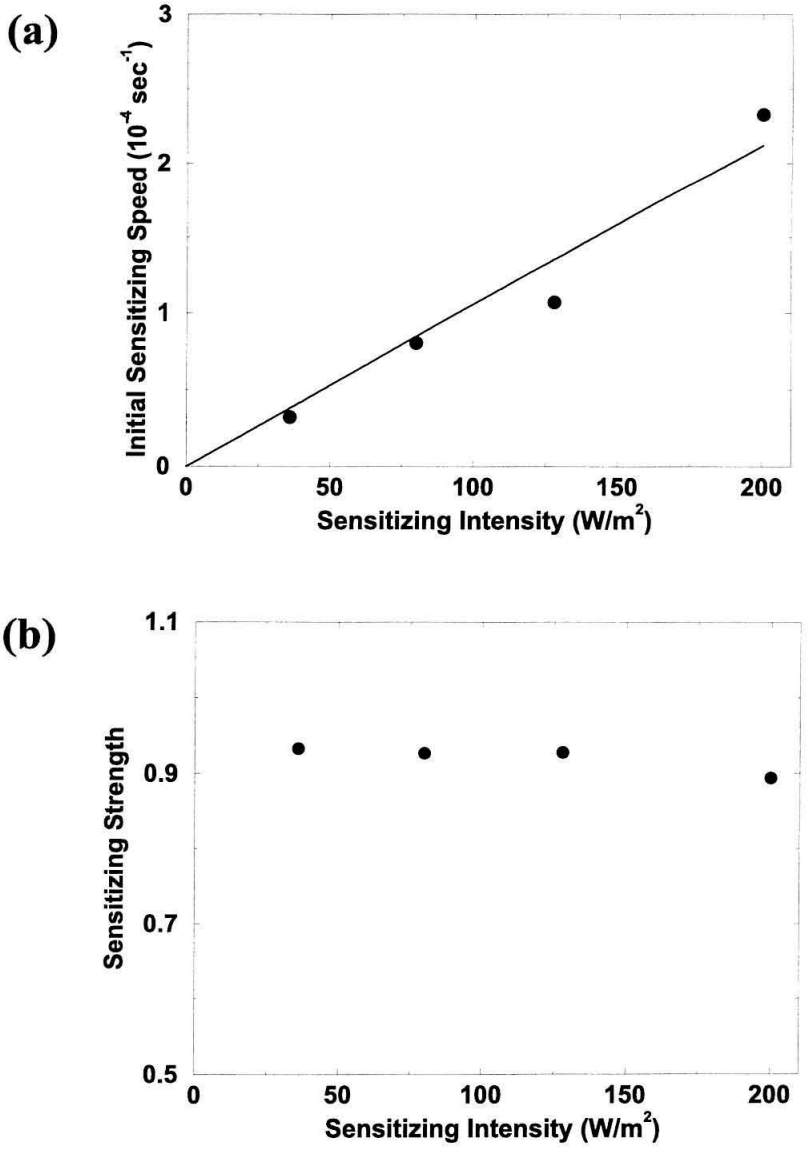

Figure 3.9: Variation of (a) initial sensitization speed ($[\frac{d(I_t/I_i)}{dt}|_{t=0}]/I_{UV0}$), and (b) sensitization strength (ratio of the final transmitted red power to the initial transmitted power) with sensitizing intensity (I_{UV0}). Solid line shows a linear fit to the experimental data.

equation as

$$\begin{aligned}\frac{\partial N_{\mathrm{Fe}}^{-}}{\partial t} &= -\frac{N_{\mathrm{Fe}}^{-}}{\tau(z)} + \frac{\gamma_{\mathrm{Fe}} q_{\mathrm{Mn,UV}} s_{\mathrm{Mn,UV}} N_{\mathrm{Fe}} N_{\mathrm{A}} I_{\mathrm{UV0}} \exp(-\alpha_{\mathrm{UV}} z)}{\gamma_{\mathrm{Fe}} N_{\mathrm{Fe}} + \gamma_{\mathrm{Mn}}(N_{\mathrm{Mn}} - N_{\mathrm{A}}) + (\gamma_{\mathrm{Mn}} - \gamma_{\mathrm{Fe}}) N_{\mathrm{Fe}}^{-}} + O([N_{\mathrm{Fe}}^{-}]^2) \\ &= \frac{N_{\mathrm{Fe,final}}^{-} - N_{\mathrm{Fe}}^{-}}{\tau(z)} , \end{aligned} \tag{3.50}$$

where $\tau(z)$ is the space–dependent sensitization time constant defined by

$$\begin{aligned}\frac{1}{\tau(z)} &= \left[\frac{-q_{\mathrm{Fe,UV}} s_{\mathrm{Fe,UV}} \gamma_{\mathrm{Mn}}(N_{\mathrm{Mn}} - N_{\mathrm{A}}) + \gamma_{\mathrm{Fe}} q_{\mathrm{Mn,UV}} s_{\mathrm{Mn,UV}}(N_{\mathrm{Fe}} + N_{\mathrm{A}})}{\gamma_{\mathrm{Fe}} N_{\mathrm{Fe}} + \gamma_{\mathrm{Mn}}(N_{\mathrm{Mn}} - N_{\mathrm{A}}) + (\gamma_{\mathrm{Mn}} - \gamma_{\mathrm{Fe}}) N_{\mathrm{Fe}}^{-}}\right] \\ &\quad \times I_{\mathrm{UV0}} \exp(-\alpha_{\mathrm{UV}} z) . \end{aligned} \tag{3.51}$$

Therefore, we can approximately express $N_{\mathrm{Fe}}^{-}(z)$ as

$$N_{\mathrm{Fe}}^{-}(z,t) = N_{\mathrm{Fe,final}}^{-} \left[1 - \exp\left(-At \exp(-\alpha_{\mathrm{UV}} z)\right)\right] , \tag{3.52}$$

where

$$A = \frac{q_{\mathrm{Fe,UV}} s_{\mathrm{Fe,UV}} \left[1 + \dfrac{q_{\mathrm{Mn,UV}} s_{\mathrm{Mn,UV}}}{q_{\mathrm{Fe,UV}} s_{\mathrm{Fe,UV}}} \dfrac{\gamma_{\mathrm{Fe}} N_{\mathrm{Fe}}(1 + N_{\mathrm{A}}/N_{\mathrm{Fe}})}{\gamma_{\mathrm{Mn}}(N_{\mathrm{Mn}} - N_{\mathrm{A}})}\right] I_{\mathrm{UV0}}}{1 + \dfrac{\gamma_{\mathrm{Fe}}(N_{\mathrm{Fe}} - N_{\mathrm{Fe}}^{-})}{\gamma_{\mathrm{Mn}}(N_{\mathrm{Mn}} - N_{\mathrm{A}})} + \dfrac{N_{\mathrm{Fe}}^{-}}{(N_{\mathrm{Mn}} - N_{\mathrm{A}})}} . \tag{3.53}$$

Using Equation (3.42) and assuming $N_{\mathrm{A}} \simeq 0.9 N_{\mathrm{Mn}}$ (we check this assumption later), we can calculate $A \simeq 0.01 s^{-1}$. To calculate the total transmitted red light through the crystal, we again divide the crystal into very thin portions as we did before (Figure 3.7). Considering

$$I_{\mathrm{t}} = I_{\mathrm{i}} \exp\left(\int_0^L -\alpha(z,t) dz\right) , \tag{3.54}$$

with

$$\alpha(z,t) = s_{\mathrm{Fe,R}} h\nu N_{\mathrm{Fe}}^{-}(z,t) , \tag{3.55}$$

and using Equation (3.52) yield

$$-\frac{1}{s_{\mathrm{Fe,R}}h\nu}\ln(I_{\mathrm{t}}/I_{\mathrm{i}}) \;=\; N^{-}_{\mathrm{Fe,final}}\int_0^L \left[1-\exp\left(-At\exp(-\alpha_{\mathrm{UV}}z)\right)\right]dz\,. \quad (3.56)$$

The calculation of the integral in Equation (3.56) can be simplified by defining a new variable $u = At\exp(-\alpha_{\mathrm{UV}}z)$. Applying this change of variable results in

$$\int_0^L \left[1-\exp\left(-At\exp(-\alpha_{\mathrm{UV}}z)\right)\right]dz = L\left(1-\frac{1}{\alpha_{\mathrm{UV}}L}\int_{At\exp(-\alpha_{\mathrm{UV}}L)}^{At}\frac{\exp(-u)}{u}du\right) \quad (3.57)$$

For sensitization of about 3 hours, we can calculate $At \simeq 108$. For our $L = 0.85$ mm thick crystal with $\alpha_{\mathrm{UV}} = 9\ \mathrm{mm}^{-1}$ at 365 nm, we have $At\exp(-\alpha_{\mathrm{UV}}L) \simeq 0.05$. The integral in Equation (3.57) can be calculated using the tabulated Exponential Integral Function. The upper bound of this integral can be replaced with ∞. The interesting property of the integral is that it is not a sharp function of the lower bound in the range of values that are relevant to our experiment. For example, for lower bounds ($At\exp(-\alpha_{\mathrm{UV}}L)$) of 0.04, 0.05, and 0.07, the integral is equal to $0.65L$, $0.68L$, and $0.72L$, respectively. This justifies most of the approximations we made in this calculation. Using $0.7L$ as the value of the integral in Equation (3.56), and using $I_{\mathrm{t}}/I_{\mathrm{i}} = 0.9$ from Figure 3.9 (b), we obtain $N^{-}_{\mathrm{Fe,final}} \simeq 1.16\times10^{24}\ \mathrm{m}^{-3}$. To obtain the third equation for calculating the model parameters, we apply the saturation (or steady–state) condition to Equation (3.46). At steady–state, the time derivatives are replaced with zero, and all variables are replaced with their final values. Therefore, we put $\partial N^{-}_{\mathrm{Fe}}/\partial t = 0$, $N^{-}_{\mathrm{Fe}} = N^{-}_{\mathrm{Fe,final}} \simeq 1.16\times10^{24}\ \mathrm{m}^{-3}$, and $N^{-}_{\mathrm{Mn}} = N_{\mathrm{A}} - N^{-}_{\mathrm{Fe,final}}$ into Equation (3.46), and rearrange different terms to obtain

$$\begin{aligned} q_{\mathrm{Fe,UV}}s_{\mathrm{Fe,UV}}\gamma_{\mathrm{Mn}}(N_{\mathrm{Mn}}-N_{\mathrm{A}}+N^{-}_{\mathrm{Fe,final}})N^{-}_{\mathrm{Fe,final}} \;&=\; \gamma_{\mathrm{Fe}}q_{\mathrm{Mn,UV}}s_{\mathrm{Mn,UV}}(N_{\mathrm{Fe}}-N^{-}_{\mathrm{Fe,final}}) \\ &\quad\times(N_{\mathrm{A}}-N^{-}_{\mathrm{Fe,final}})\,. \end{aligned} \quad (3.58)$$

We now need to solve a system of three equations [Equation (3.42), Equation (3.49), and Equation (3.58)] for three unknowns ($q_{\mathrm{Mn,UV}}s_{\mathrm{Mn,UV}}$, γ_{Mn}, and N_{A}). To do this, we use Equations (3.42) and (3.49) to replace the first two variables in terms of N_{A}

in Equation (3.58). This results in a second–order equation for N_A as

$$(N_A/10^{24}\mathrm{m}^{-3})^2 + 4.94(N_A/10^{24}\mathrm{m}^{-3}) + 4.93 = 0\ . \tag{3.59}$$

Equation (3.59) results in two solutions for N_A and, therefore, two sets of solutions for our three unknowns are obtained. It turns out that only one of these sets results in acceptable recording and read–out response as evidenced by experimental results. The values for the three unknowns found by solving Equations (3.42), (3.49), and (3.58) are

$$N_A = 3.1 \times 10^{24} m^{-3} \tag{3.60}$$

$$q_{\mathrm{Mn,UV}} s_{\mathrm{Mn,UV}} = 3.55 \times 10^{-5} m^2/J \tag{3.61}$$

$$\gamma_{\mathrm{Mn}} = 8.5\gamma_{\mathrm{Fe}} = 1.32 \times 10^{-13} m^{-3} s^{-1}\ . \tag{3.62}$$

The value of N_A agrees with our assumption ($N_A \simeq 0.9 N_{\mathrm{Mn}}$). We use N_A, $q_{\mathrm{Mn,UV}} s_{\mathrm{Mn,UV}}$, and γ_{Mn} from Equations (3.60)-(3.62) as the initial values in the simulation of sensitization, bleaching, and holographic recording and read–out curves, and then fine tune these values by trying to get the best fits to the experimental results. The final values of N_A, $q_{\mathrm{Mn,UV}} s_{\mathrm{Mn,UV}}$, and γ_{Mn} are shown in Table 3.1.

3.4.3 Comparison with the experimental results

We calculated three of the unknown parameters for the model in the last section. The only remaining unknown parameter is the photovoltaic constant of the Mn traps at 365 nm ($\kappa_{\mathrm{Mn,UV}}$). We used curve fitting with trial and error to find $\kappa_{\mathrm{Mn,UV}}$, and also to fine tune the values of the three parameters we found in the last section. We try to get the best overall fit to the experimental sensitization, bleaching, and holographic recording and read–out results. The simulation of the sensitization and bleaching curves is based on the numerical solution of Equations (3.50) and (3.33), respectively. To consider the absorption of the UV light within the crystal, the crystal was divided into 50 thin portions with equal thickness. The intensity of UV light was assumed

to be constant in each portion. The corresponding equations were solved within each portion, and the overall optical density of the crystal for red light was calculated by adding up the optical densities of the individual portions. A similar procedure was used to consider the effect of UV absorption in the calculation of recording and read–out response. Since recording is performed after a few hours of sensitization, the initial conditions for the equations in each portion of the crystal were obtained by solving the governing sensitization equations for the specified time. Then the recording and read–out curve was simulated by solving Equations (3.19), (3.25), and (3.26) in each portion. Since the diffracted fields from the different portions of the crystal are in–phase (Bragg condition is satisfied during read–out), we only need to add the diffracted fields (not the diffraction efficiencies) from the different portions. This can be easily performed by replacing ΔnL in Kogelnik's formula [52] by $\sum_i \Delta n_i L_i$, where Δn_i and L_i are the index change and thickness of the i-th portion.

Figure 3.10 shows the comparison of the theoretical and experimental results for the best overall fit. The agreement between theory and experiment shown in Figure 3.10 is quite good. The final values of all parameters resulting in the theoretical curves in Figure 3.10 are summarized in Table 3.1.

3.4.4 Effect of sensitizing and recording intensities

Figure 3.11 (a) shows the variation of theoretical saturation diffraction efficiency with the recording intensity (I_{R0}) when the ratio of the recording intensity to sensitizing intensity is fixed ($I_{R0}/I_{UV0} = 25$). The two curves in Figure 3.11 (a) are calculated with and without neglecting the absorption of the sensitizing beam within the crystal. The neglection of this absorption is an acceptable assumption only for very thin crystals or for cases where we are interested in local hologram strength. However, it does not apply to thick crystals since UV absorption can not be neglected in such crystals. Typical absorption coefficients of the crystals we used are close to 9 mm^{-1} at 365 nm. As Figure 3.11 (a) shows, the final diffraction efficiency is not a function of the absolute intensities while the intensity ratio is constant. Figure 3.11 (b)

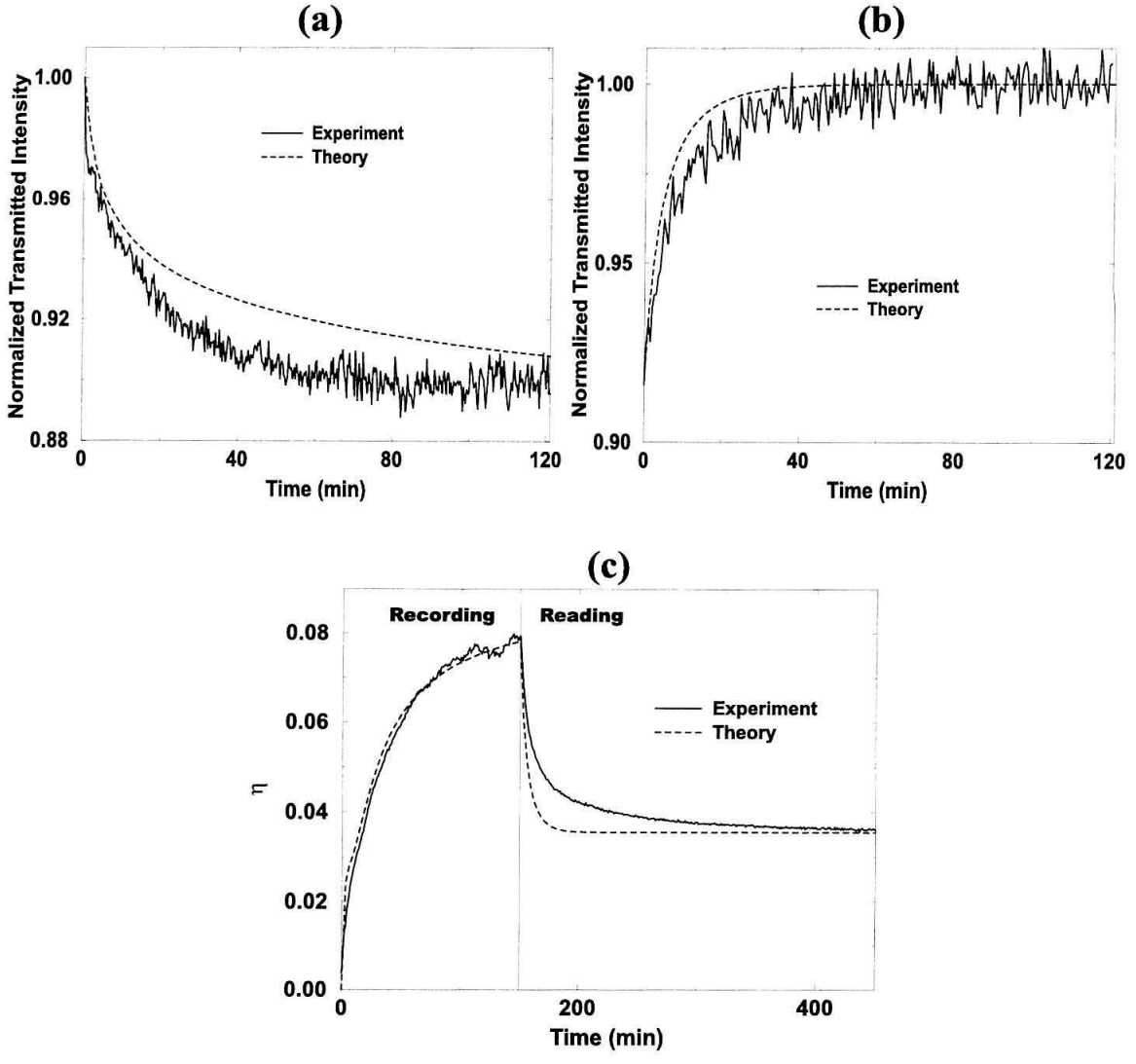

Figure 3.10: Comparison of theory and experiment: (a) sensitization by a 20 mW/cm^2 homogeneous UV beam at 365 nm monitored by a weak red beam (wavelength 633 nm), (b) bleaching of a sensitized crystal by a 300 mW/cm^2 red beam, and (c) holographic recording by simultaneous presence of a UV beam (wavelength 365 nm, intensity 20 mW/cm^2), and two red beams (wavelength 633 nm, intensity of each beam 250 mW/cm^2) with subsequent read–out performed by one of the red recording beams only.

shows the variation of the saturation diffraction efficiency with recording intensity (I_{R0}) with constant sensitizing intensity (I_{UV0}). Figures 3.11 (a) and (b) suggest that the final diffraction efficiency in two–center holographic recording is a function of the intensity ratio (I_{R0}/I_{UV0}) only and not a function of the absolute intensities. This can be intuitively understood from Figure 3.1 (b). While sensitizing light both populates Fe traps and partially erases the hologram, recording light records the hologram by redistributing electrons among traps via the conduction band. Effectively, sensitizing light populates and recording light depopulates the Fe traps. The strengths of the processes caused by sensitizing and recording lights depend on sensitizing and recording intensities, respectively. Therefore, if we change sensitizing and recording intensities while keeping their ratio constant, we will not change the relative strength of the processes involved in recording the hologram, and we will obtain the same saturation diffraction efficiency. Note that holographic recording speed still depends on the absolute intensities as stronger beams result in faster processes.

The dependence of the final diffraction efficiency on the intensity ratio does not depend on the absorption of the sensitizing beam as evidenced by Figure 3.11 (a). However, higher UV absorption results in a smaller maximum obtainable diffraction efficiency by reducing the effective thickness of the crystal. Figure 3.11 (b) shows that the peak in the theoretical variation of the final persistent diffraction efficiency with recording intensity is also broader for higher UV absorption. This is due to the fact that the ratio of the recording and UV intensities (I_{R0}/I_{UV0}) varies through the thickness of the crystal as the absorption of the recording light is much weaker than that of the UV light. Therefore, the best UV intensity corresponding to the approximately fixed recording intensity can not be provided for all points within the thickness of the crystal. If the UV intensity is high enough, there is a relatively narrow region within the crystal with optimum intensity ratio. By increasing the UV intensity, this narrow region moves away from the UV entrance edge. If we increase the UV intensity beyond some maximum value, there is no region within the crystal with optimum intensity ratio as the UV intensity remains too high at all points within the crystal thickness. For UV intensities above that maximum value, the final diffraction

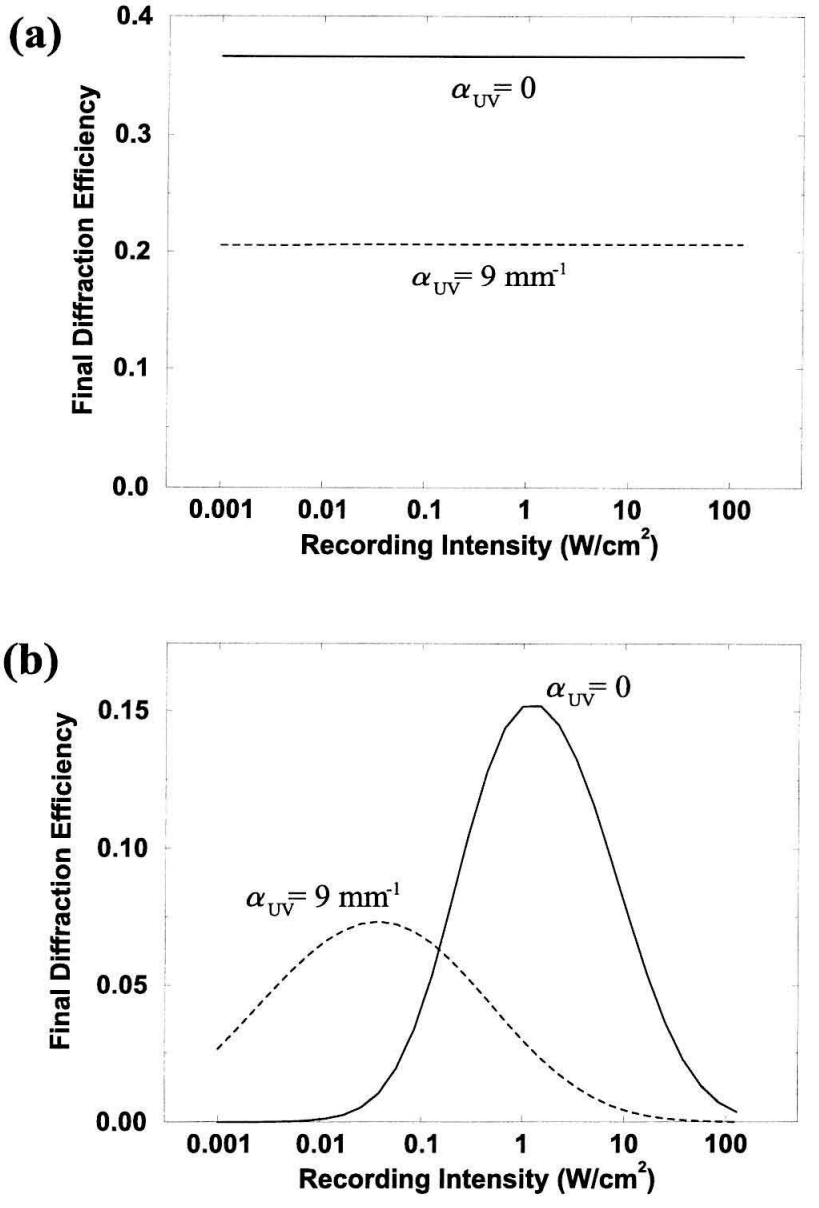

Figure 3.11: Variation of the final persistent diffraction efficiency with recording intensity while (a) the ratio of the recording to sensitizing intensity is fixed (I_{R0}/I_{UV0} = 25), and (b) the sensitizing intensity is fixed (I_{UV0} = 20 mW/cm^2). The wavelength of the sensitizing beam in the calculations is 365 nm. The two curves in each part show the variation with and without neglecting the absorption of the UV light within the crystal.

efficiency decreases with increasing UV intensity. Therefore, we get a broad peak in the variation of the final diffraction efficiency with the UV intensity while recording intensity is fixed. Similar argument holds for the variation of the final diffraction efficiency with recording intensity while the UV intensity is fixed. The width of the peak in the variation of the final diffraction efficiency with recording intensity depends on the UV absorption coefficient: The larger the UV absorption coefficient, the broader the peak.

Finally, it is important to note that there is no intensity threshold for two–center holographic recording as shown in Figure 3.11. We can record holograms with very low recording and UV intensities and obtain large diffraction efficiencies if the intensity ratio is picked properly. This is a big advantage of two–center recording over two–step persistent holographic recording using small polarons in $LiNbO_3$:Fe crystals.

3.4.5 Importance of sensitizing light

As shown in Figure 3.5, the presence of ultraviolet light during hologram formation is crucial for obtaining large diffraction efficiencies. The diffraction efficiency raises quickly and drops afterwards almost to zero with no ultraviolet light present during the hologram formation. After some reading, the grating finally disappears completely. With assistance of ultraviolet light during recording, much higher efficiencies are obtained. Subsequent reading erases first the grating partially, but the remaining grating persists despite further red illumination. This is due to the fact that the grating can not be recorded in the Mn traps in the absence of UV during recording. In this section, we discuss an intuitive reason for this behavior based on the physical mechanisms that are responsible for holographic recording. We also use the theoretical model to verify the intuitive reason.

The electron recombination rates of Mn and Fe centers have the same order of magnitude. Therefore, the probabilities of trapping a conduction band electron at Mn and Fe sites are comparable. As a result, when an electron is excited from Fe centers to the conduction band, it will end up in Mn centers after a few Fe retrapping cycles

(for example, if the trapping probability at each center is 1/2, the average number of retrapping at Fe centers before being trapped at Mn centers is 2). An electron moves only a few nanometers in the conduction band before getting retrapped at either centers due to small mobility of conduction band electrons in $LiNbO_3$. Therefore, if there is no UV illumination during recording, an electron moves only a few nanometers on the average which is much smaller than the grating period (usually around 1 μm). This is due to the fact that red light is not able to excite electrons from Mn centers. Once an electron is trapped in Mn centers, it can not be used for holographic recording any more. Having simultaneous UV illumination during recording makes the Mn electrons available for recording and increases the average distance an electron can move through multiple cycles of excitation. This results in a successful recording of gratings in Mn with large saturation diffraction efficiencies.

In recording a hologram in the $LiNbO_3$:Fe:Mn crystal, the main source for moving electrons in the conduction band is the bulk photovoltaic effect ($j_{\rm ph} = \kappa_{\rm Fe,R} N_{\rm Fe}^- I_{\rm R}$). At the beginning of recording, the electron concentration in the Fe traps ($N_{\rm Fe}^-$) is uniform due to pre–sensitization with a homogeneous UV beam. Therefore, the bulk photovoltaic effect is maximum at the peaks of the red light intensity ($I_{\rm R}$). Without UV during recording, the recording light bleaches the Fe centers. This bleaching is faster in high light intensity regions resulting in 180° phase difference between $N_{\rm Fe}^-$ and $I_{\rm R}$. Assuming sinusoidal variation with space, we can represent the first Fourier component of the bulk photovoltaic current as

$$j_{\rm ph1} = \kappa_{\rm Fe,R}(N_{\rm Fe0}^- I_{\rm R1} - N_{\rm Fe1}^- I_{\rm R0}) , \tag{3.63}$$

where we assumed

$$I_{\rm R} = I_{\rm R0} + I_{\rm R1}\exp(iKx) , \tag{3.64}$$

$$N_{\rm Fe}^- = N_{\rm Fe0}^- - N_{\rm Fe1}^-\exp(iKx) , \tag{3.65}$$

with all parameters defined as before. Therefore, at some point in time, the bulk

photovoltaic current at the peaks of the interference pattern becomes weaker than the bulk photovoltaic current at positions away from the peaks. This reverses the prevailing charge transfer direction and causes erasure. The peak in the recording curve of Figure 3.5 (without UV) corresponds to this reversal of direction. The main term in the grating formation is the first spatial Fourier component of this current that becomes zero at the peak, and changes its phase by 180° afterwards resulting in the erasure of the grating.

The argument presented above is useful for an intuitive understanding of the processes. We can also use our theoretical model to explain the experimental measurements in Figure 3.5. Figure 3.12 shows the concentration of filled Fe centers (N_{Fe}^{-}) and photovoltaic current at different times during hologram formation as a function of position x. In calculating the results shown in Figures 3.12 (a) and (b), we assumed that recording is performed by red only (without UV) and by the simultaneous presence of UV and red, respectively. In both cases, we assumed that recording is performed after pre–sensitization of the crystal with UV light.

Figure 3.12 (a) shows clearly that the reversal in the direction of charge transfer is responsible for the fall of the diffraction efficiency when the UV light is not present during hologram formation. Furthermore, Figure 3.12 (b) shows that the presence of UV during recording results in a nonzero steady–state electron concentration in the Fe traps. This is due to continuous sensitization (electron transfer from Mn traps to Fe traps) by UV light. As a result, the reversal in the charge transfer direction in the conduction band does not occur, and a strong hologram can be recorded.

It is important to note that the space charge pattern resides in both centers since the recombination rate of the electrons from the conduction band for the Fe and Mn centers are close to each other. Therefore, modulated Fe^{2+} and Mn^{2+} gratings are formed during recording. The phase difference between the two gratings is close to 180°. This is due to the fact that in bright red regions, electrons are transferred from Fe to Mn centers (via the conduction band) at maximum rate. The electron transfer in low red light intensity regions is much weaker due to the smaller number of red photons available in those regions. Therefore, the modulated Mn^{2+} grating is

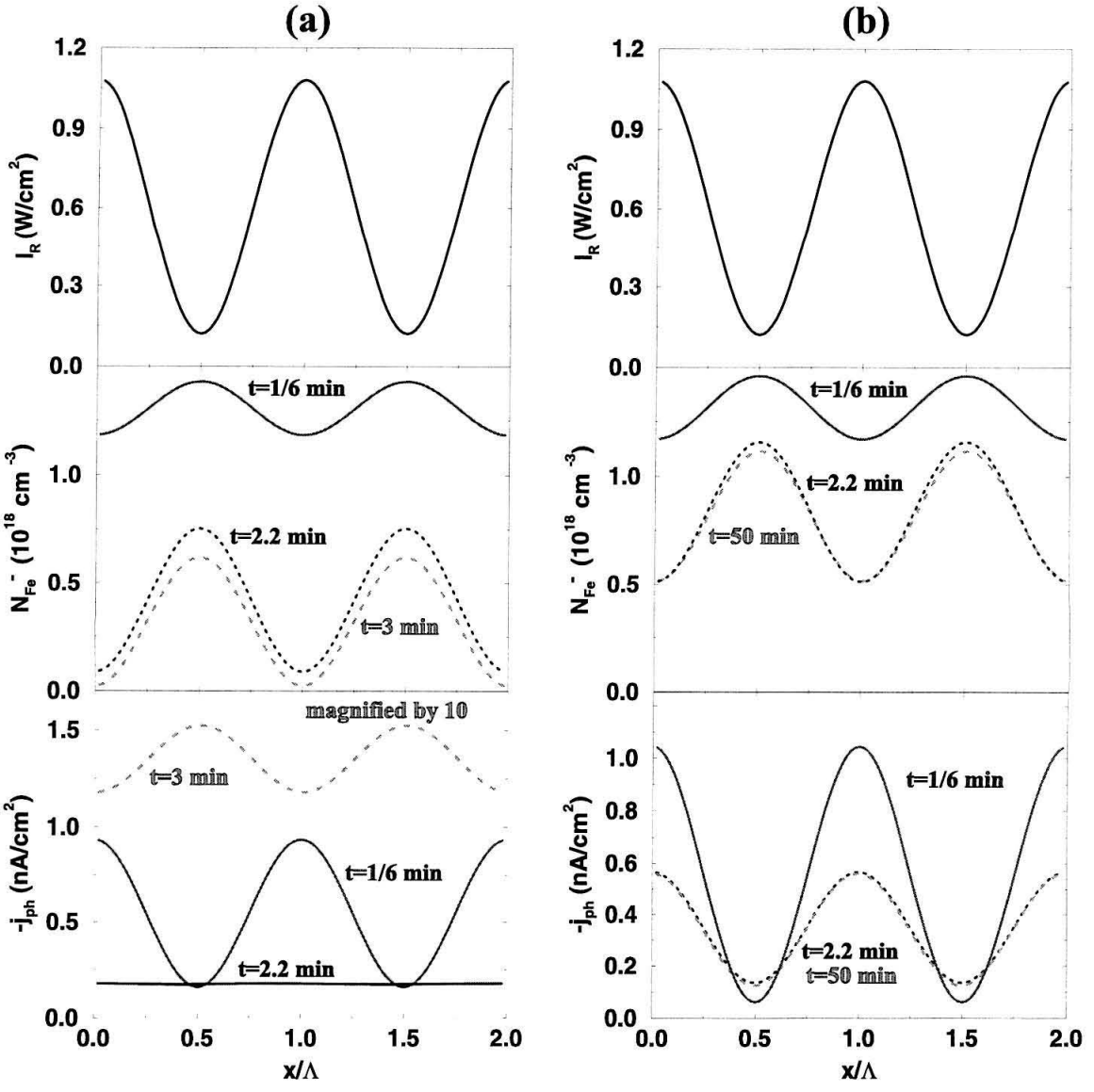

Figure 3.12: Spatial variations of recording intensity (I_{R}), electron concentration in Fe traps (N_{Fe}^{-}), and bulk photovoltaic current (j_{ph}) over two grating periods (Λ) at different times in a thin slice of the crystal during holographic recording. Recording is performed by two red beams (wavelength 633 nm, intensity of each beam 300 mW/cm^2) and (a) without UV illumination during recording, and (b) with simultaneous illumination with a UV beam (wavelength 365 nm, intensity 20 mW/cm^2). In both cases, it is assumed that the crystal was pre–illuminated by the UV beam for two hours before recording.

maximum in the brighter red regions, and minimum in the darker areas. The situation for the Fe^{2+} grating is reverse, introducing a 180° phase difference between the two sinusoidal patterns. The real phase difference is a little bit smaller than 180° due to the movement of electrons in the conduction band before being retrapped. The larger the average distance an electron can move, the larger this phase difference will be. The sum of these gratings produces the space–charge field. With Fe^{2+} and Mn^{2+} concentration gratings like

$$N_{\mathrm{Fe}}^{-} = N_{\mathrm{Fe0}}^{-} - \Delta N \cos(Kx + \phi_{\mathrm{Fe}}) \tag{3.66}$$

$$N_{\mathrm{Mn}}^{-} = N_{\mathrm{Mn0}}^{-} + \Delta N \cos(Kx + \phi_{\mathrm{Mn}}) \,, \tag{3.67}$$

we get the space charge grating

$$\begin{aligned} \rho(z) &= -e\,\Delta N \left[\cos(Kx + \phi_{\mathrm{Mn}}) - \cos(Kx + \phi_{\mathrm{Fe}})\right] \\ &\simeq -e\,\Delta N \left(\phi_{\mathrm{Mn}} - \phi_{\mathrm{Fe}}\right) \sin(Kx) \,, \end{aligned} \tag{3.68}$$

assuming small phase shifts ϕ and overall charge neutrality.

Note that we assumed the peak of the sinusoidal part of the gratings (ΔN) to be approximately the same as the main source for the formation of these patterns is the local transfer of electrons from Fe to Mn centers due to the presence of the recording light. With UV present during recording, the average distance an electron can move is much larger resulting in a larger phase difference between the gratings and therefore much larger diffraction efficiencies. Finally with UV present during recording, we get to a saturation where the space-varying current becomes zero. At saturation, there is no net electron motion in the conduction band resulting in a constant phase difference between the gratings and a constant diffraction efficiency. During read-out with red light only, electrons in the Fe centers move in the reverse direction resulting in the partial erasure of the hologram. The hologram is not completely erased since the electrons can move only a short distance before being trapped in the Mn centers. The final grating is stored in the Mn centers and, therefore, further read-out with red

light is non-destructive.

We can use our theoretical model to verify the above argument. Figure 3.13 shows the concentration of electrons in Fe and Mn traps at different times during recording with simultaneous presence of the UV light. As Figure 3.13 shows, the phase difference between the electron concentration in the two traps is close to 180° at all times. Figure 3.14 shows the deviation of the phase difference between electron concentrations in Mn and Fe traps from 180° (i.e., $\phi_{\mathrm{Mn}} - \phi_{\mathrm{Fe}}$) in Equation (3.68) with time during hologram formation with UV light present. As we explained intuitively, the phase difference between the two gratings in Fe and Mn traps grows with time due to spatial movement of electrons in the traps via the conduction band. Note that Figure 3.14 shows the variation with time only within a thin slice at the light entrance face of the medium. Due to large UV absorption, the speed of hologram formation is smaller in the other slices and, therefore, the speed of formation of the phase difference shown in Figure 3.14 is not the same as the speed of the formation of the hologram which depends on the dynamics of all slices throughout the thickness of the crystal. It is important to note that the two gratings in the two traps are entangled to each other. Any change in one of the gratings results in a corresponding change in the other one. This is due to the fact that any change in the electron concentration of either traps has to be performed via the conduction band, and the probabilities of electron trapping by the Fe and Mn traps are comparable. As Figure 3.13 shows, the final modulation depth of the electron concentration in the Mn traps is much smaller than that before read–out. If we could erase the grating in the Fe traps without affecting that in the Mn traps, we would increase the final diffraction efficiency by a very large factor. Unfortunately, we have not been able to do this due to the entanglement of the two gratings in the two traps.

3.5 Optimization of two–center recording

In this section, we focus on the effects of individual design parameters (i.e., Fe and Mn concentrations, initial electron concentrations in the traps, recording and sensitizing

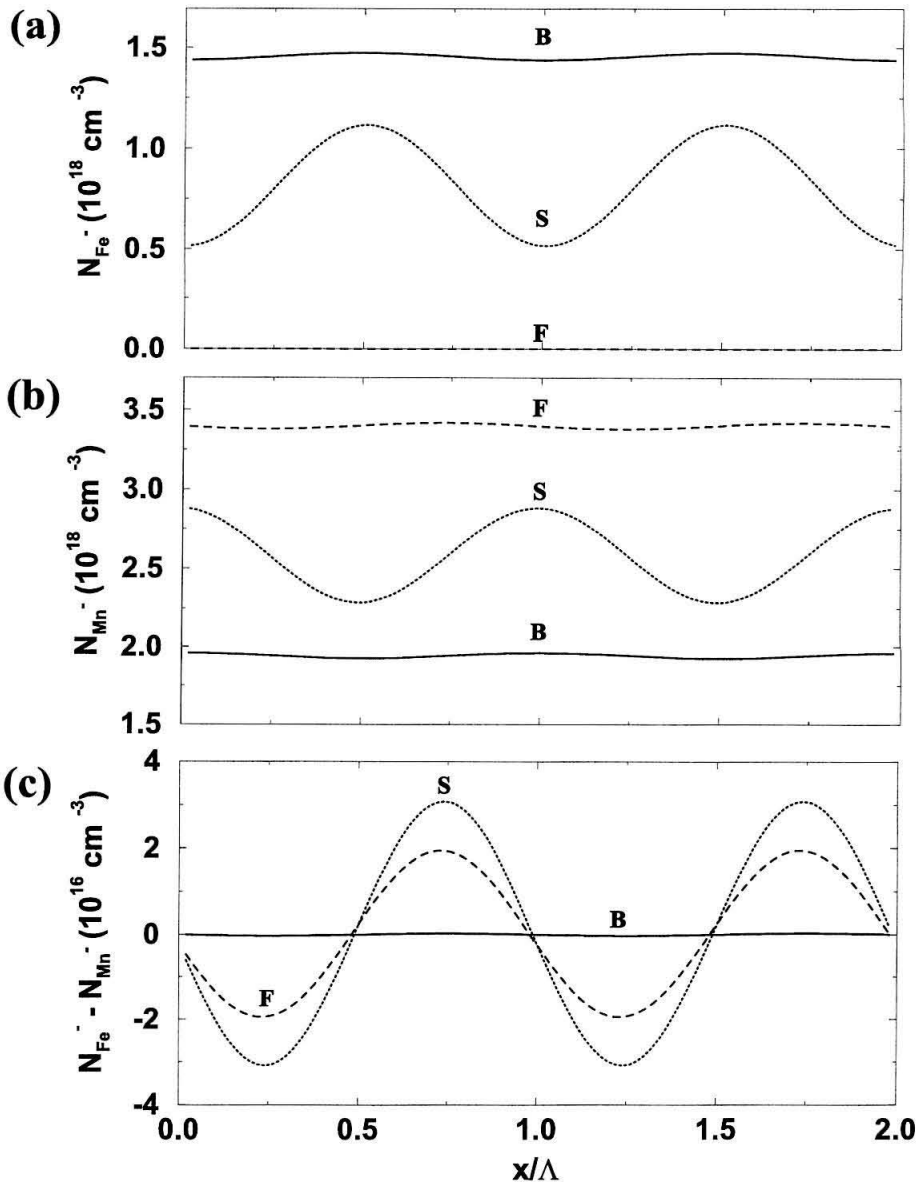

Figure 3.13: Spatial variations of electron concentrations in (a) Fe (N_{Fe}^-) and (b) Mn traps (N_{Mn}^-) and (c) their sum ($N_{\mathrm{Fe}}^- + N_{\mathrm{Mn}}^-$) over two grating periods (Λ) at different times (B: at the beginning of recording, S: at saturation, and F: after sufficient read–out) in a thin slice of the crystal during holographic recording. Recording is performed by two red beams (wavelength 633 nm, intensity of each beam 300 mW/cm^2) with simultaneous illumination with a UV beam (wavelength 365 nm, intensity 20 mW/cm^2). Note that the spatial variation of N_{Fe}^- has 180° phase shift with that of the recording intensity as shown in Figure 3.12 (b).

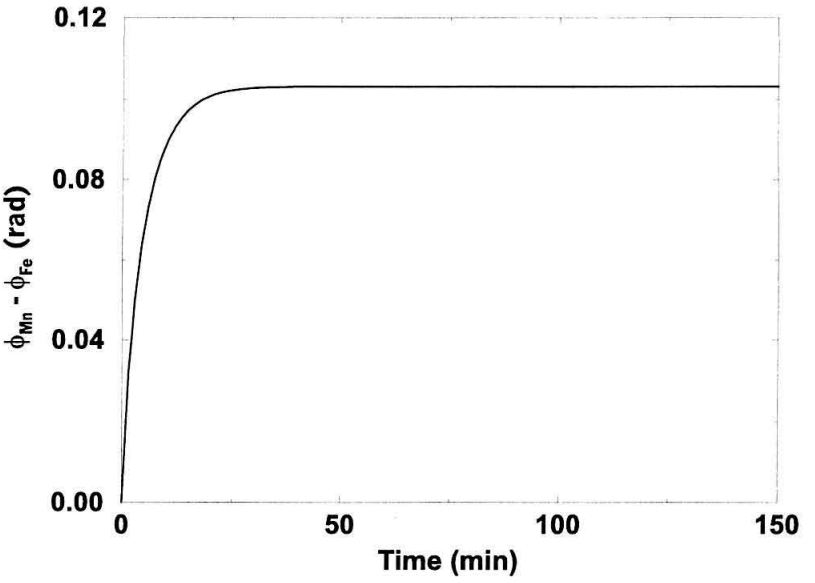

Figure 3.14: Deviation of phase difference between the electron concentrations in Mn and Fe traps from 180° (i.e., $\phi_{\mathrm{Mn}} - \phi_{\mathrm{Fe}}$) during hologram recording by two red beams with simultaneous presence of a UV beam.

intensities and wavelengths, etc.) on the dynamic range of two–center holographic recording systems. A convenient measure for the dynamic range is the $M/\#$ [73]. As we will see later, an approximate measure for the $M/\#$ in two–center holographic recording scheme is the square–root of the final persistent diffraction efficiency. Therefore, we consider this approximate $M/\#$ as the system parameter to optimize. We consider the effect of each of the design parameters on this measure while all other design parameters are fixed. The effects of recording and sensitizing intensities were considered in the last section.

3.5.1 Effect of Fe concentration

Figure 3.15 (a) shows the theoretical variation of the approximate $M/\#$ with Fe concentration while the Mn concentration is fixed at $N_{\mathrm{Mn}} = 3.8\times10^{24}$ m^{-3} (corresponding to 0.01 wt. % MnO doping). In this calculation, we assumed that all Fe traps are initially empty and 90% of the Mn traps are occupied by electrons ($N_{\mathrm{A}} = 3.4\times10^{24}$ m^{-3}).

As Figure 3.15 (a) shows, stronger holograms and larger M/# are obtained at higher Fe concentrations. The variation in Figure 3.15 (a) can be understood by using the energy band diagram in Figure 3.1 (b). Without any Fe traps, we can not record any holograms as red light can not excite electrons from Mn traps to the conduction band. By increasing the concentration of the Fe traps (keeping all of them initially empty), we increase the probability of trapping electrons from the conduction band by Fe traps. This increases the concentration of electrons in the Fe traps that can be used for holographic recording with red light, and therefore stronger holograms can be recorded and a larger $M/\#$ is obtained. In the calculation shown in Figure 3.15 (a), we considered only the practical Fe concentration in $LiNbO_3$ (up to 0.15 wt.% Fe_2O_3). We do not use higher Fe concentration in $LiNbO_3$. However, if we could increase it without limit, we would reach a point where increasing Fe concentration would result in smaller $M/\#$. This is due to the strong erasure during read–out. A strong hologram could be recorded initially, but it would be strongly erased during read–out with red light, resulting in a small persistent diffraction efficiency. This is due to the fact that the probability of trapping electrons from the conduction band by Mn centers would be very small in a crystal with a huge Fe concentration. As a result, the space–charge pattern is mainly in the Fe traps. Such a space–charge pattern is erased strongly during read–out through electron transfer from Fe to Mn traps in a process similar to the erasure process in $LiNbO_3$:Fe crystals. Therefore, the final diffraction efficiency which is due to the hologram recorded in the Mn traps is small. Furthermore, strong absorption of the recording beams may also limit the highest useful Fe concentration.

Figure 3.15 (b) shows the result of holographic recording and read–out experiments performed with two different $LiNbO_3$:Fe:Mn crystals with the same Mn concentration and thickness but different Fe concentrations. The crystals were also annealed together to have similar initial electron concentrations in Mn traps while all Fe traps are initially empty. Recording and read-out is performed with the same system parameters (intensities, grating period, etc.) in both crystals. The experimental parameters are mentioned in the captions. As Figure 3.15 (b) shows, the crystal with 50% more

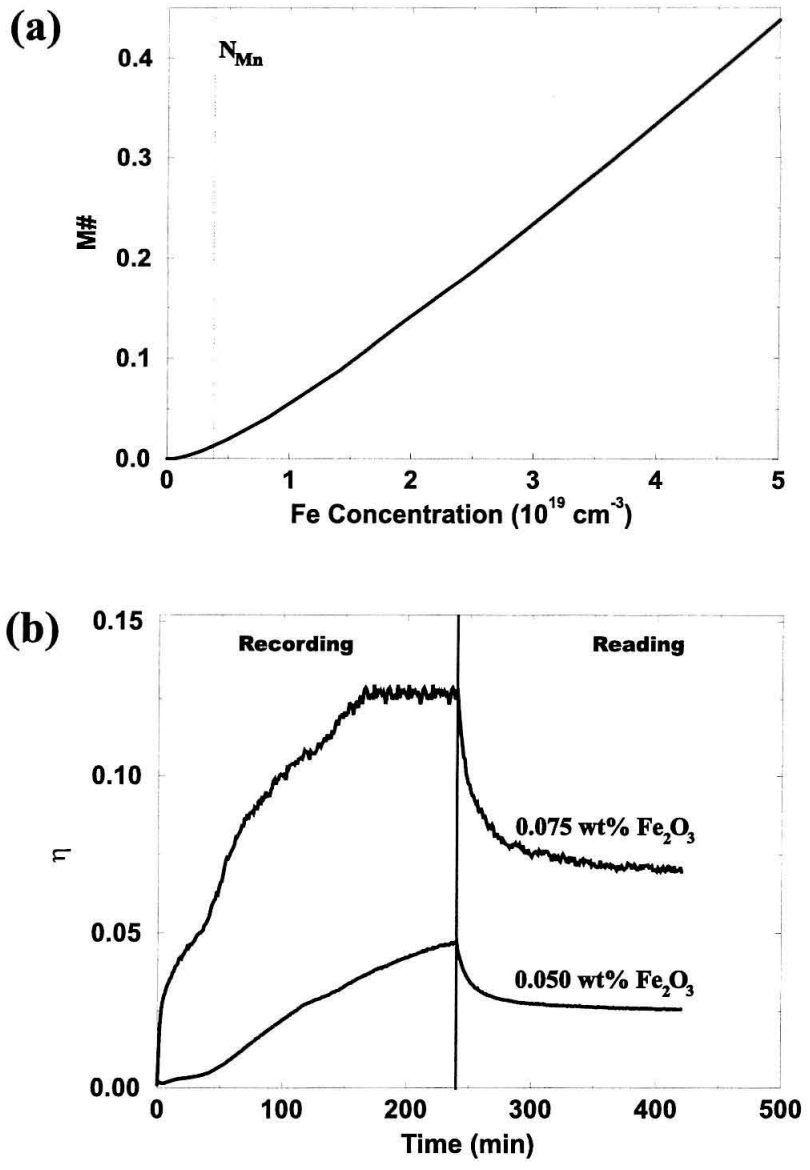

Figure 3.15: Effect of Fe concentration on two–center holographic recording in $LiNbO_3$:Fe:Mn crystals. (a) Theoretical variation of the final hologram strength (approximate M/#) with Fe concentration while Mn concentration is fixed at 3.8×10^{18} cm^{-3} (equivalent to 0.01 wt. % MnO). (b) Recording and read–out curves for two $LiNbO_3$:Fe:Mn crystals each doped with 0.01 wt. % MnO. The Fe doping level for each crystal is shown in the figure. Recording is performed by a UV beam (wavelength 404 nm, intensity 4 mW/cm^2) and two red beams (wavelength 633 nm, intensity of each beam 300 mW/cm^2). Read–out is performed by one of the red recording beams only.

Fe traps has approximately 50% larger $M/\#$ as suggested by Figure 3.15 (a).

The theoretical and experimental results shown in Figure 3.15 suggest that in designing a material for two–center holographic recording, we should choose the highest *practical* doping level for the shallower traps (i.e., Fe in $LiNbO_3$:Fe:Mn).

3.5.2 Effect of Mn concentration

Figure 3.16 (a) shows the theoretical variation of the approximate $M/\#$ with Mn concentration while the Fe concentration is fixed at $N_{\text{Fe}} = 2.5 \times 10^{25}$ m^{-3} (corresponding to 0.075 wt. % Fe_2O_3 doping). In this calculation, we assumed that all Fe traps are initially empty and 90% of the Mn traps are occupied by electrons. All other parameters are also kept constant (as mentioned in the captions). As Figure 3.16 (a) shows, there is an optimum Mn concentration that results in the largest $M/\#$. The variation in Figure 3.16 (a) can be explained by using the energy band diagram in Figure 3.1 (b). Without any Mn traps, we can not record a hologram since all Fe traps are initially empty. In holographic recording with red light using Fe traps, we need to have electrons in these traps. Therefore, we have $M/\# = 0$ at zero Mn concentration. By increasing the Mn concentration from zero (while 90% of them filled with electrons), we increase the number of electrons available for sensitization. Therefore, we get a larger electron excitation rate from Mn traps to the conduction band (rate 1 in Figure 3.1 (b)). On the other hand, since 10% of the Mn traps are empty, we also increase the rate of electron trapping at Mn centers (rate 3 in Figure 3.1 (b)) by increasing the Mn concentration. This acts against sensitization (or electron transfer to Fe traps). Therefore, by increasing the Mn concentration, we have two competing effects in favor of sensitization and against it. If the overall effect is in favor of sensitization, we get more electrons in Fe traps and, therefore, larger $M/\#$ by increasing the Mn concentration. If the overall effect is against sensitization, we obtain a smaller electron concentration in Fe traps and a smaller $M/\#$ by increasing the Mn concentration. In low Mn concentration, the increase in the electron excitation rate predominates the increase in the electron trapping rate by Mn centers, and

we get larger $M/\#$ by increasing the Mn concentration. If we keep increasing the Mn concentration, we get to a point where the increase in the electron trapping rate at Mn centers starts to predominate. Increasing the Mn concentration beyond this point results in smaller $M/\#$. This explains the occurrence of a maximum in the variation of the $M/\#$ with the concentration of the Mn traps. For the intensity ratio chosen in this calculation, the optimum occurs when the Mn concentration is approximately 10% of the Fe concentration.

Figure 3.16 (b) shows the results of holographic recording and read–out experiments performed with three different $LiNbO_3$:Fe:Mn crystals with the same Fe concentration and thickness but different Mn concentrations. The crystals were also annealed together to have similar initial electron concentrations in the Mn traps while all Fe traps are initially empty. Recording and read-out is performed with the same system parameters (intensities, grating period, etc.) in both crystals. The experimental parameters are mentioned in the captions. As Figure 3.16 (b) shows, the crystal whose Mn concentration is approximately equal to 10% of its Fe concentration has the largest persistent diffraction efficiency (and therefore largest M/#). The persistent diffraction efficiency is smaller for crystals with higher Mn concentrations. The experimental results confirm the latter part (after maximum) of Figure 3.16 (a). If we believe that no hologram can be recorded ($M/\# = 0$) without any Mn traps, we can conclude from the experimental results that there is an Mn concentration resulting in the maximum $M/\#$.

The theoretical and experimental results shown in Figure 3.16 suggest that in designing a material for two–center holographic recording, we should choose the optimum doping level for the deeper traps (i.e., Mn in $LiNbO_3$:Fe:Mn). As a rule of thumb, the optimum for any $LiNbO_3$:Fe:Mn crystal occurs when the Mn concentration is approximately 10% of the Fe concentration. Although this result is obtained for a specific crystal and specific intensity ratio, we expect it to be a good starting point in the design of a $LiNbO_3$:Fe:Mn crystal for two–center holographic recording. For any other material and / or dopands, there is always an optimum concentration for the deeper traps that can be found by the method we described.

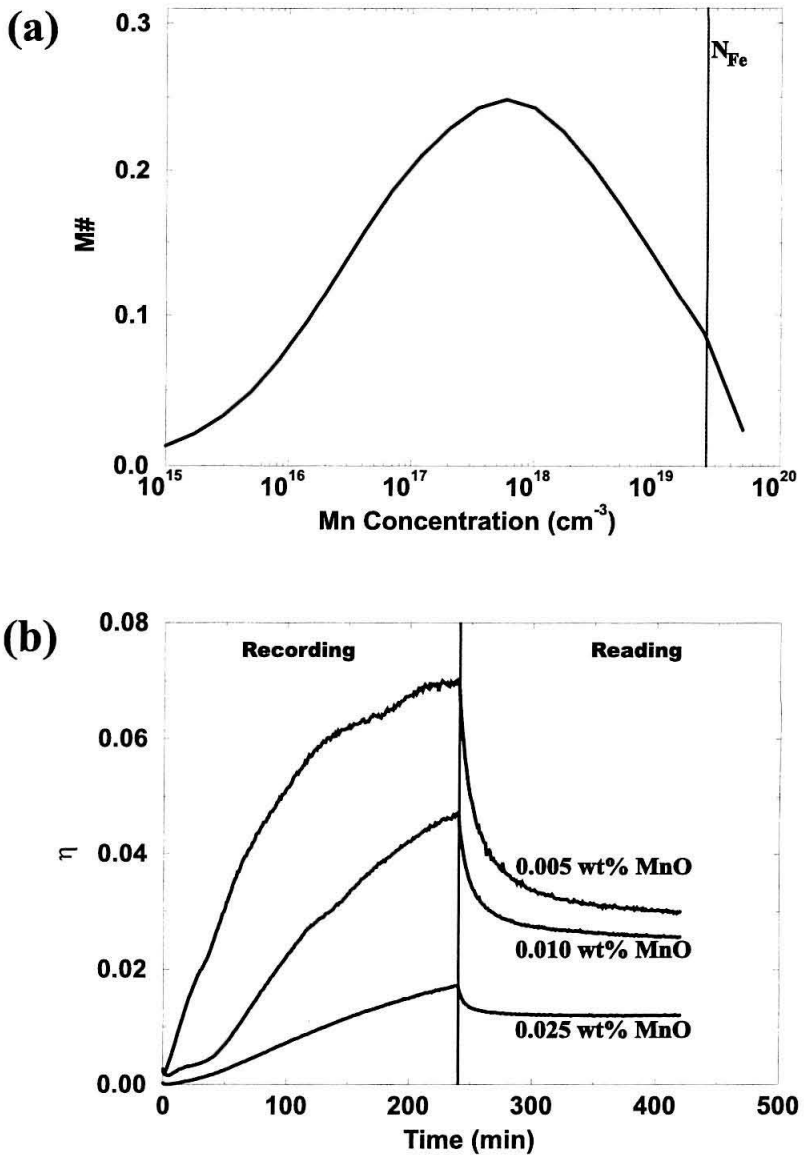

Figure 3.16: Effect of Mn concentration on two–center holographic recording in $LiNbO_3$:Fe:Mn crystals. (a) Theoretical variation of the final hologram strength (approximate M/#) with Mn concentration while Fe concentration is fixed at 2.5×10^{19} cm^{-3} (equivalent to 0.075 wt. % Fe_2O_3). In the simulation, it its assumed that all Fe traps are empty, and 90% of the Mn traps are filled with electrons. (b) Recording and read–out curves for two $LiNbO_3$:Fe:Mn crystals each doped with 0.05 wt. % Fe_2O_3. The Mn doping level for each crystal is shown on the figure. Recording is performed by a UV beam (wavelength 404 nm, intensity 4 mW/cm^2), and two red beams (wavelength 633 nm, intensity of each beam 300 mW/cm^2). Read–out is performed by one of the red recording beams only.

3.5.3 Effect of annealing

Since holographic recording is performed by spatial rearrangement of the electrons in the Fe and Mn traps, the initial electron concentration in the traps has an important effect on the holographic recording performance. The electron concentration in the traps can be varied by annealing [70] the crystal, i.e., heating the crystal at different temperatures in different environments. For $LiNbO_3$, heating the crystal to about 1000 °C in an oxygen (O_2) environment results in the oxidation of the crystal and, therefore, lower electron concentration in the traps. On the other hand, heating a $LiNbO_3$ crystal at about 700–800 °C in an argon (Ar) environment results in the reduction of the crystal, and higher electron concentration in the traps. Since Mn traps are deeper in the band gap than Fe traps, electrons fill the Mn traps before Fe traps when the crystal is reduced. For persistent holographic recording, it is essential that at the end of the annealing process all Fe traps be empty, and only a portion of the Mn traps be filled. Figure 3.17 (a) shows the theoretical variation of the approximate $M/\#$ with the portion of filled Mn traps while the Mn and Fe concentrations are fixed at $N_{\mathrm{Mn}} = 3.785 \times 10^{24}$ m^{-3} (corresponding to 0.01 wt. % MnO doping) and $N_{\mathrm{Fe}} = 2.5 \times 10^{25}$ m^{-3} (corresponding to 0.075 wt. % Fe_2O_3 doping), respectively. In this calculation, we assumed that all Fe traps are initially empty as required to obtain persistence. As Figure 3.17 (a) shows, there is an optimum annealing (or oxidation / reduction) state for the crystal that results in the best $M/\#$. For the crystal with specifications given above, the optimum annealing state is where approximately 95% of the Mn traps are filled, and all Fe traps are empty.

To check the theoretical result and to investigate the effect of the oxidation / reduction state of the crystal, we performed experiments with four x-cut congruent $LiNbO_3$ crystals doped with 0.075 wt. % Fe_2O_3 and with 0.01 wt. % MnO. The crystals were all from the same boule. The samples were strongly oxidized (LN1), oxidized (LN2), weakly oxidized (LN3) and weakly reduced (LN4) by annealing at temperatures between 700 and 1000 °C in oxygen or argon atmosphere for different times. Sample LN1 was 2.9 mm and all others were 0.85 mm thick. The absorption spectra

of the crystals LN1, LN3, and LN4 are shown in Figure 3.18. The absorption spectrum of LN2 is very close to that of LN3, and is not shown to avoid confusion. Almost all traps in the highly oxidized crystal are empty, resulting in small absorption above 420 nm. The absorption below this wavelength comes from band–to–band absorption of $LiNbO_3$, electron transfer from the valance band to Fe traps (hole generation) [74], and possibly some excitation of the few remaining electrons in Mn traps. As we reduce the oxidized sample, more Mn traps become occupied by electrons resulting in stronger absorption above 420 nm (crystals LN2 and LN3). As we continue to reduce the sample, we reach a point where all Mn traps are occupied by electrons, and start to fill Fe traps with electrons. This causes an absorption band to appear at about 477 nm. The absorption in this band becomes stronger as we continue reducing the sample. The behavior observed in Figure 3.18 implies that LN1 has hardly any electrons in either trap, LN2 and LN3 have partially filled Mn traps and empty Fe traps, and LN4 has completely filled Mn traps and partially filled Fe traps. Therefore, we expect to get poor results using either LN1 or LN4. However, LN2 and LN3 are intuitively appropriate for persistent holographic recording.

To check the intuitive arguments mentioned above, we recorded holograms in the four crystals. Recording and read–out curves for the four crystals are shown in Figure 3.17 (b). Strong holograms can not be recorded in LN1 as shown in Figure 3.17 (b). This is because LN1 is a highly oxidized sample. Due to strong oxidation of LN1, only a few electrons are available in Mn traps while all Fe traps are empty in this sample. On the other hand, electrons are essential for holographic recording in $LiNbO_3$ by red light. This explains the very small diffraction efficiency obtained for LN1. Due to strong oxidation, we can not record any hologram in LN1 which does not have electrons in either of the traps. Persistent holograms can be recorded in both LN2 and LN3 with good diffraction efficiencies as shown in Figure 3.17 (b). We think that this is due to the appropriate oxidation / reduction state of these two samples. Compared to LN1, both LN2 and LN3 are reduced with stronger reduction for LN3. Therefore, LN2 and LN3 have more electrons than LN1. These extra electrons are initially in Mn traps as discussed previously. The reduction of LN2 and LN3 are

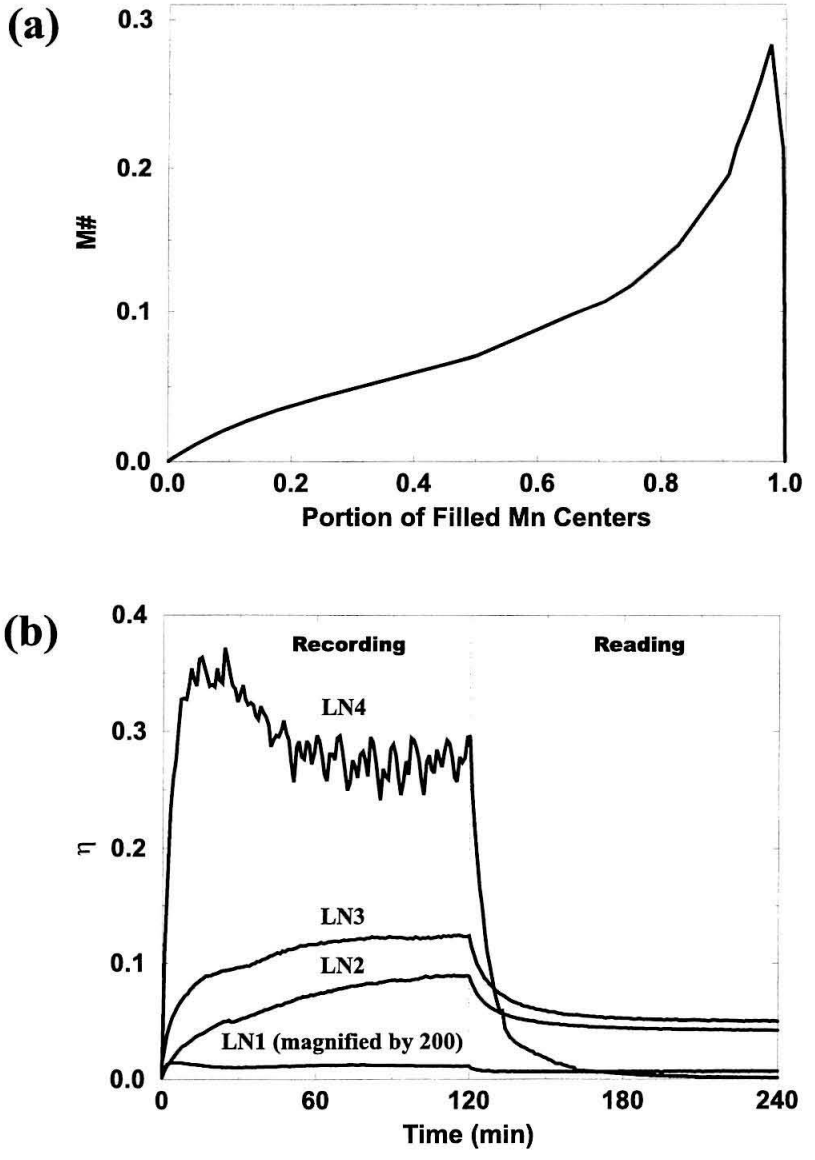

Figure 3.17: Effect of annealing on two–center holographic recording in $LiNbO_3$:Fe:Mn crystals. (a) Theoretical variation of the final hologram strength (approximate M/#) with portion of filled Mn traps while Fe and Mn concentrations are fixed at 2.5×10^{19} cm^{-3} (equivalent to 0.075 wt. % Fe_2O_3) and 3.8×10^{18} cm^{-3} (equivalent to 0.01 wt. % MnO), respectively. (b) Recording and read–out curves for four $LiNbO_3$:Fe:Mn crystals each doped with 0.075 wt. % Fe_2O_3 and 0.01 wt. % MnO. The annealing is performed differently for different crystals (as specified in the text). Recording is performed by a UV beam (wavelength 365 nm, intensity 20 mW/cm^2), and two red beams (wavelength 633 nm, intensity of each beam 300 mW/cm^2). Read–out is performed by one of the red recording beams only.

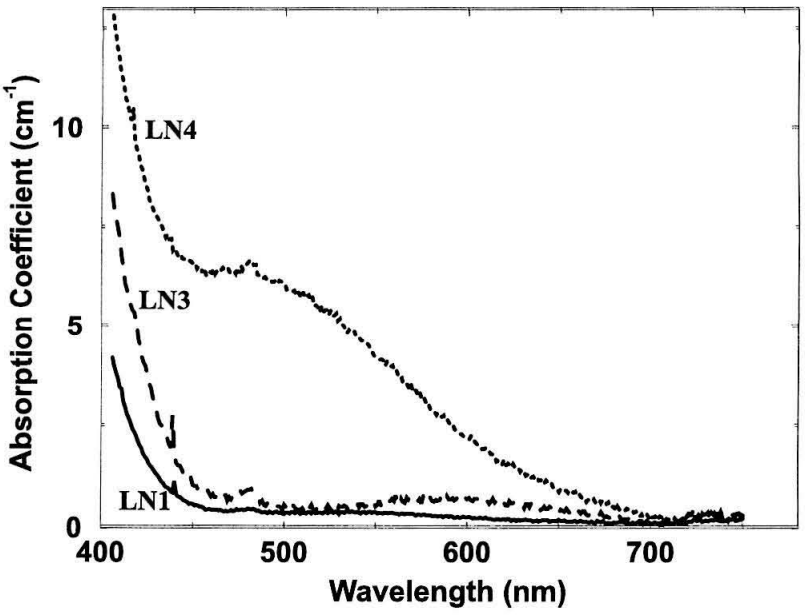

Figure 3.18: Absorption spectra of three $LiNbO_3$:Fe:Mn crystals. The crystals are from the same boule, but they are annealed differently.

not strong enough to fill all Mn traps and start filling Fe traps. Therefore, it is not possible to record any holograms with only red light in LN2 and LN3 initially. As Mn traps are filled with electrons by reduction, more electrons can be transferred to Fe traps by UV light. This is due to both having more electrons in Mn traps and less empty Mn centers to trap electrons from the conduction band. The latter results in a larger probability of electron trapping at Fe centers. Therefore, we can record faster and get larger diffraction efficiencies. During read–out by red light, electrons are transferred from Fe traps to Mn traps resulting in a partial erasure of the hologram. When all electrons are transferred to Mn centers, the remaining hologram persists against further read–out. Therefore, reducing the crystal results in an increase in both sensitivity and the $M/\#$ [75]. This explains the recording and read–out curves for both LN2 and LN3. Since LN3 is more reduced than LN2, it has faster recording and stronger final diffraction efficiency. Finally, Figure 3.17 (b) shows that recording in LN4 is much faster than the other samples, and larger saturation diffraction efficiencies can be obtained in LN4. However, the recorded

hologram is erased during read–out by red light. This is because LN4 is a strongly reduced sample. If we reduce the crystal too much, we reach a point where we do not have enough empty Mn traps to store a strong space–charge pattern, although we have a lot of electrons. Therefore, we can record strong holograms with good speed, but we lose a major part of it during read–out. Therefore, the final persistent diffraction efficiency is limited by the availability of empty Mn traps. The extreme case is when we reduce the crystal so strongly that all Mn traps are filled, and part of Fe traps are filled as well. This is the case for LN4. In this case, we have a very good sensitivity (fast recording) since we do not need electron transfer from Mn traps to already partially–filled Fe traps. We can also record strong holograms due to initial electron population in Fe traps and very effective UV sensitization due to filled Mn traps. However, electrons are transferred during read–out from Fe centers to Mn centers until all Mn centers are occupied. The remaining hologram resides in Fe centers and is totally erased by further read-out. The final diffraction efficiency after considerable read–out would be zero. This explains the recording and read–out curve for LN4.

To summarize, experimental results confirm the theoretical result that there is an optimum oxidation / reduction state for a doubly–doped $LiNbO_3$ crystal that results in the desired performance. This optimum depends on the doping levels of the shallower (Fe) and deeper (Mn) traps and on the intensities of the sensitizing (UV) and recording (red) beams. Figure 3.17 (a) shows that for the crystal used in these experiments, the optimum oxidation / reduction state that results in the best $M/\#$ is when about 95% of the Mn traps are filled with electrons. This is close to the oxidation / reduction state of LN3. Once again, although this result is obtained for a specific crystal and specific intensity ratio, we expect it to be a good starting point in the design of any $LiNbO_3$:Fe:Mn crystal for two–center holographic recording. For any other material and / or dopands, there optimum annealing is when all the shallower traps are empty and a good portion of the deeper traps are filled.

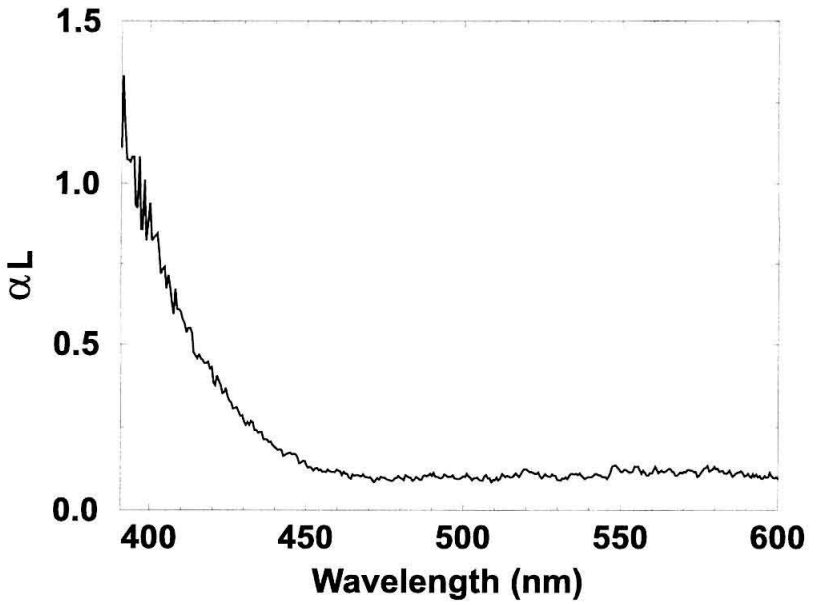

Figure 3.19: Absorption spectrum of a typical $LiNbO_3$:Mn crystal.

3.5.4 Effect of sensitizing wavelength

As mentioned before, one of the main concerns in two–center holographic recording is the large absorption of the sensitizing (UV) beam. The maximum useful crystal thickness depends on how deep the sensitizing beam can penetrate the crystal. Therefore, large UV absorption results in a severe limitation in the maximum useful crystal thickness. Typical absorption coefficient of the $LiNbO_3$:Fe:Mn crystals we used in the previous experiments was 9 mm^{-1}. A large part of this absorption comes from band to band absorption of $LiNbO_3$ that results in the generation of electrons and holes which recombine rapidly. Therefore, this part of the UV absorption is not useful for sensitization. The useful and unavoidable portion of this absorption is due to the electron excitation from Mn and Fe traps to the conduction band. Another portion of this absorption is due to the electron transfer from the valance band to the Fe centers (hole generation). This portion is typically much smaller than the other two portions.

To avoid the unwanted extra absorption of the sensitizing beam, we can increase

sensitizing wavelength. Higher sensitizing wavelengths result in weaker band to band absorption, and therefore larger useful thickness of the material. On the other hand, too high sensitizing wavelength results in an inefficient sensitization due to the smaller sensitivity of the Mn traps to higher wavelengths. Figure 3.19 shows the absorption spectrum of a $LiNbO_3$ crystal doped with Mn only. It is evident from Figure 3.19 that we should not use sensitizing wavelengths above approximately 420 nm. A practical wavelength below this limit is 404 nm that is available from a mercury lamp. Figure 3.20 (a) shows the experimental recording and read–out curves for a $LiNbO_3$:Fe:Mn crystal with different sensitizing wavelengths (365 nm and 404 nm). As Figure 3.20 (a) shows, using 404 nm sensitizing light results in larger persistent diffraction efficiency (and $M/\#$) even with 5 times lower sensitizing intensity. The recording speed for the case of 365 nm sensitizing light is larger only due to 5 times larger sensitizing intensity at this wavelength. Figure 3.20 (b) shows the angular selectivity curves (variation of the persistent diffraction efficiency with angle of the reference beam) of plane–wave holograms recorded in a 0.85 mm thick $LiNbO_3$:Fe:Mn crystal with different sensitizing wavelengths (365 nm and 404 nm). The hologram recorded with 404 nm sensitizing light is more selective suggesting that the effective (or useful) crystal thickness is larger when we use 404 nm light for sensitization.

In general, to obtain the best performance in two–center holographic recording, we must choose the sensitizing wavelength long enough to avoid unwanted absorption (band–to–band, etc.) and short enough to result in efficient sensitization from the deep traps. For $LiNbO_3$:Fe:Mn crystals, the best wavelength is in the 400-410 nm range.

3.6 Discussion

In this section, we discuss the performance of the two–center holographic recording from a system point of view. In any holographic recording system, we would like to have large dynamic range (measured by $M/\#$), fast recording (measured by sensitivity), and long persistence (non–destructive read–out). As explained in Section 3.5, an

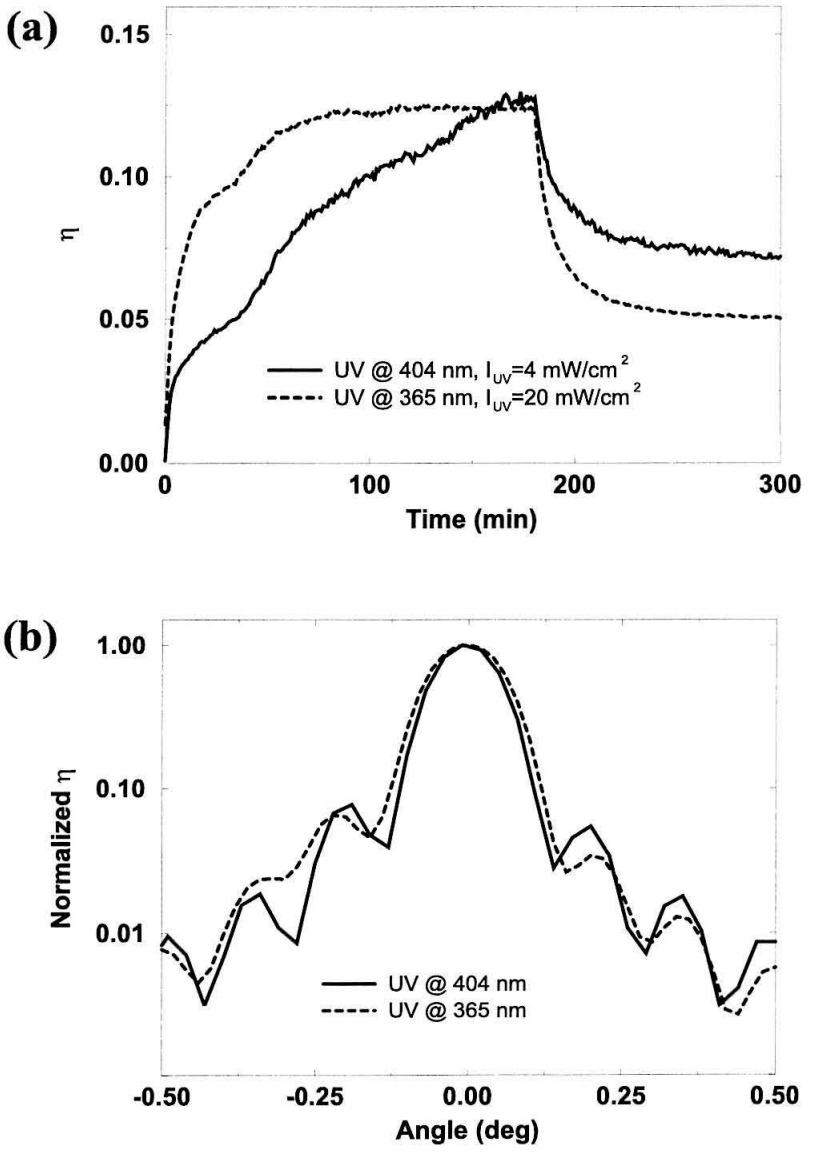

Figure 3.20: Effect of sensitizing wavelength on two–center holographic recording in $LiNbO_3$:Fe:Mn crystals. (a) Recording and read–out curves for a 0.85 mm thick $LiNbO_3$:Fe:Mn crystal doped with 0.075 wt. % Fe_2O_3 and 0.01 wt. % MnO with two different UV wavelengths. Recording is performed by a UV beam (wavelength and intensity in each case specified in the figure), and two red beams (wavelength 633 nm, intensity of each beam 300 mW/cm^2). Read–out is performed by one of the red recording beams only. (b) Selectivity curves of two holograms recorded by the same two red beams and one UV beam with different wavelength.

approximate $M/\#$ can be measured by taking the square root of the final diffraction efficiency (after sufficient read–out) from the recording and read–out curves. In Chapter 4, we will discuss a more exact definition of the $M/\#$ for two–center holographic recording. From Figure 3.20 (a) we can obtain $M/\# \simeq 0.27$. We can improve $M/\#$ by a factor of close to 3 by using extraordinary (in plane) polarization for recording and read–out beams due to the larger electro–optic coefficient of $LiNbO_3$ for extraordinary polarization. Therefore, we expect to have $M/\# \simeq 1$ for a 1 mm thick crystal. In a practical system, we would typically like to have a 1 cm thick crystal. In the absence of absorption, the $M/\#$ scales linearly with the crystal thickness suggesting $M/\# \simeq 10$ for a 1 cm thick sample. In normal holographic recording, the deviation in the linearity of the $M/\#$ with thickness is not large as the absorption of the recording beams can be adjusted properly by annealing treatment. However, the absorption of the sensitizing beam in two–center holographic recording is typically much larger than that of the recording beams. This large absorption reduces the effective thickness of the crystal. Therefore, we can not obtain larger $M/\#$ by simply using thicker crystals. To get an idea about the largest useful thickness of a $LiNbO_3$:Fe:Mn in two–center holographic recording, we used the theoretical model to calculate the variation of the approximate $M/\#$ with crystal thickness for different UV absorption coefficients (α_{UV}). Figure 3.21 shows the results. As Figure 3.21 shows, the largest usable crystal thickness for $\alpha_{UV} = 9$ mm^{-1} is 0.5 mm. This is the case when UV wavelength is 365 nm. However, for $\alpha_{UV} = 1$ mm^{-1} (when UV wavelength is 404 nm) we can use 4–5 mm thick crystals without losing $M/\#$ by much. We can even use 1 cm thick samples if we use two sensitizing beams to sensitize the crystal from the two opposite sides. In this case, each beam sensitizes 5 mm of the crystal effectively, and therefore, the entire crystal thickness is used for holographic recording. As a result, we expect to have $M/\#$ close to 10 for a 1 cm thick crystal in the transmission geometry with extraordinary polarization.

Although the $M/\#$ obtained above is acceptable for many practical applications, the recording speed is too low. A measure for the recording speed is sensitivity (S) defined by the initial slope of the holographic recording curve normalized by recording

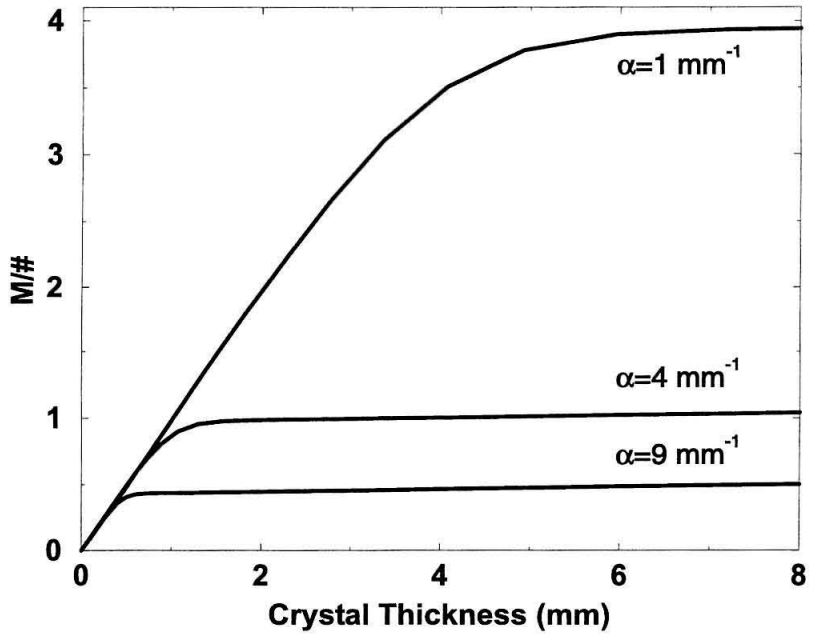

Figure 3.21: Variation of the approximate $M/\#$ with crystal thickness in two–center holographic recording for different absorption coefficients of the sensitizing beam (intensity 20 mW/cm^2). In this calculation, we assumed that recording is performed by the simultaneous presence of the sensitizing beam and two red beams (wavelength 633 nm, intensity of each beam 300 mW/cm^2).

intensity and crystal thickness [76] as

$$S = \frac{(d\sqrt{\eta}/dt) \mid_{t=0}}{I_{\mathrm{Rec}} L} , \tag{3.69}$$

where the unit of S is usually cm/J. Typical sensitivity we obtained for recording with red light with ordinary polarization is $S = 0.0035$ cm/J. We can increase this value to $S \simeq 0.01$ cm/J by using extraordinary polarization for recording and read–out beams. However, this value of S is still one order of magnitude lower than what is needed (about $S = 0.1$ cm/J) for practical applications. Therefore, finding ways to improve the sensitivity of two–center holographic recording is essential for the success of this method for practical holographic recording systems. We will discuss the sensitivity issues in two–center holographic recording in detail in Chapter 4.

The third important property for any holographic recording system is persistence (non–destructive read–out). Two–center holographic recording with red light has excellent persistence as shown in Figure 3.5. One measure for persistence is the erasure time constant during read–out with some pre–specified reading intensity. Figure 3.22 shows the variation of the erasure speed (the inverse of erasure time constant) of the final hologram with the intensity of the reading red beam. To obtain the experimental data depicted in Figure 3.22, we first recorded a hologram with simultaneous presence of two red beams (wavelength 633 nm, intensity of each beam 300 mW/cm^2) and one sensitizing beam (wavelength 404 nm, intensity 4 mW/cm^2). Then, we read–out the hologram for 24 hours with one of the red beams to make sure that almost all of the electrons in Fe traps are transferred to Mn traps. Then, we read–out the hologram with one red beam with different intensities for at least 10 hours in each case. The erasure time constant (τ_e) was then calculated by fitting the erasure curve to a monoexponential function like

$$\sqrt{\eta} \;=\; A \exp(-t/\tau_e) \, . \tag{3.70}$$

The deviation of the data from a linear curve is partly due to the error in measuring

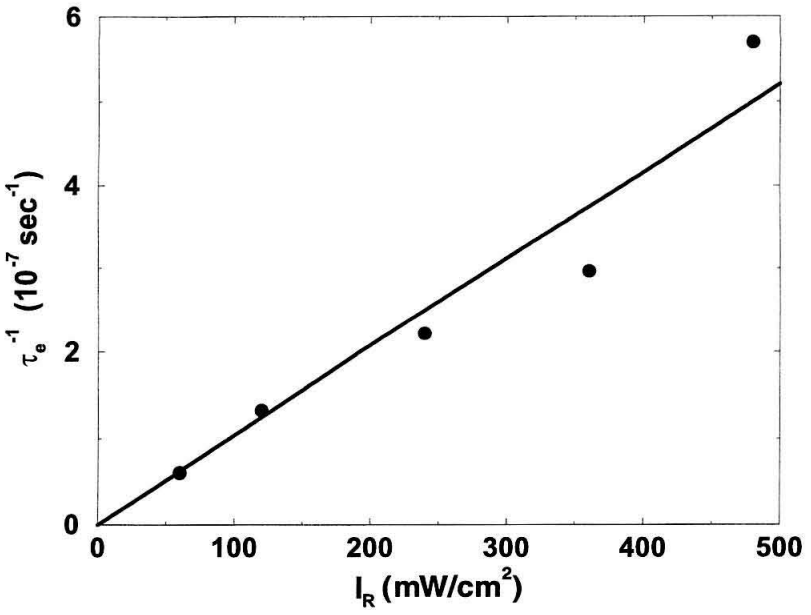

Figure 3.22: Variation of the erasure speed ($1/\tau_e$) with the intensity of the red reading beam (I_{R}) in two–center holographic recording.

the erasure time constant (due to the very long nature of the erasure process), and partly due to the fact that we have two traps instead of one. In other words, the erasure from the Mn traps is performed by redistributing electrons among the Mn traps via the conduction band either without intermediate trapping at the Fe centers or with the intermediate trapping at the Fe centers, and the corresponding erasure dynamics of these two erasure pathways are different.

We now give an example to show the excellent persistence of the two–center holographic recording. Let's assume that we use a reading intensity of 100 mW/cm^2 in a practical holographic memory module consisting of 1000 holograms each with a diffraction efficiency of 10^{-4}. We also assume that we need to read each hologram for approximately 5 μs (with 100 mW/cm^2 reading intensity) to accumulate enough electrons in the detector. From Figure 3.22, the erasure time constant at 100 mW/cm^2 is approximately 10^7 seconds. Therefore, we can read one hologram for approximately 3.5×10^6 seconds or $3.5 \times 10^6/5 \times 10^{-6} = 7 \times 10^{11}$ times (calculated using Equation (3.70)) before the diffraction efficiency drops to 50% of its original value. As a

result, we can read the entire memory module (entire 1000 holograms) 700 million times before we need to refresh the information in the memory. This is practically equivalent to saying that we do not need to refresh the information in the memory at all. In the next two chapters, we will elaborate more on this measure of persistence and the details of the above calculations.

A very interesting property of two–center recording is the possibility of recording strong localized holograms [77, 78]. Using two–center recording, we can record holograms in slices or even small spots of the crystal. This property is the result of the sensitization process, i.e., we can not record holograms without the presence of the sensitizing beam. Therefore, we can define the extent of a hologram by shaping the sensitizing beam appropriately. This is not hard to accomplish since the sensitizing beam is homogeneous. Figure 3.23 shows the idea of recording multiple holograms in slices of a $LiNbO_3$:Fe:Mn crystal. The sensitizing beam (UV) and the reference beam (red) are focused by a cylindrical lens to illuminate only a slice of the material in which a hologram is recorded. The signal beam (red) illuminates the entire crystal, but it records a hologram only at the sensitized slice. The signal beam does not significantly affect the holograms recorded in other slices due to the insensitivity of the deeper traps (Mn centers) to recording light (red). Therefore, we can record multiple strong holograms using this method. Note than similar idea does not work well in normal recording in singly doped crystals, since the signal beam corresponding to each hologram erases the holograms recorded in previous slices. Using two–center recording, we can also record holograms in small spots of the crystal by focusing the sensitizing beam to a small spot.

3.7 Conclusions

Two–center holographic recording is a promising method for persistent holographic recording in $LiNbO_3$ crystals. It is based on using a sensitizing beam and two recording beams to record a hologram in a doubly–doped crystal. Both traps are so deep that thermal depopulation of either trap can be neglected. The crystal needs to be

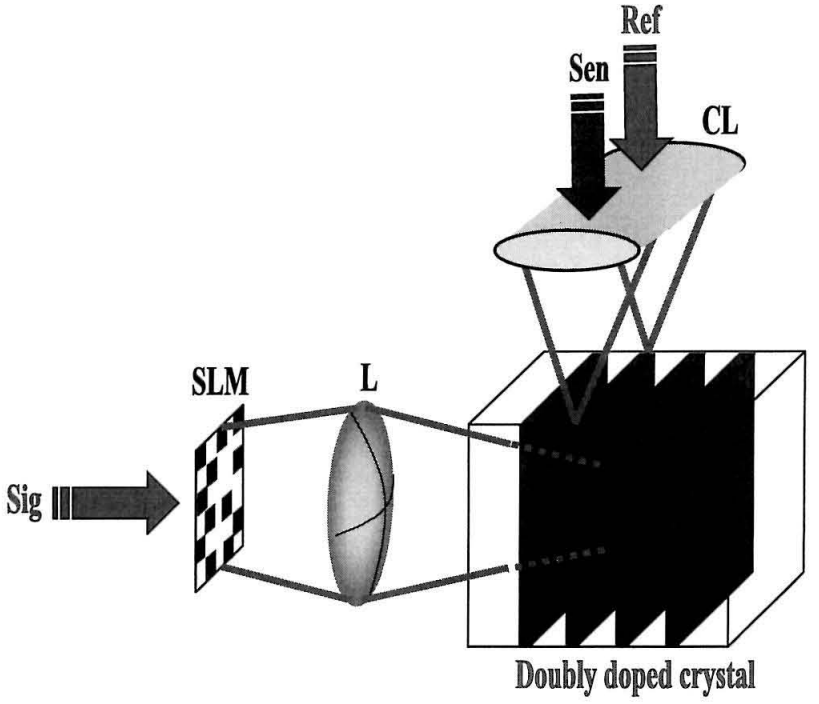

Figure 3.23: Recording multiple holograms in slices of a doubly–doped $LiNbO_3$ crystal. Here, Sen, Ref, and Sig represent sensitizing, reference, and signal beams, respectively, while SLM, L, and CL are spatial light modulator, normal (spherical) lens, and cylindrical lens, respectively.

annealed properly to make sure that initially all shallower traps as well as a portion of the deeper traps are empty. The success of the method is due to a big asymmetry in the physical mechanisms responsible for recording and read–out. During recording, an electron on the average undergoes many cycles of excitation from traps to the conduction band, moving in the conduction band, and getting trapped. During read–out, an electron on the average is limited to only a few of these cycles. Therefore, read–out only causes a partial erasure of the stored information, and after that the remaining hologram can be read–out for a very long time without considerable erasure. Although the hologram is initially recorded in both traps, it is finally recorded in the deeper traps after sufficient read–out. The presence of UV light during recording is crucial for the asymmetry between recording and read–out. Without UV light during recording, a strong hologram can not be recorded.

Initial experimental results suggest that it is possible to obtain $M/\# \simeq 10$ for a 1 cm thick $LiNbO_3$:Fe:Mn crystal. The $M/\#$ depends mainly on the ratio of the recording and sensitizing intensities. Sensitization and bleaching experiments are very helpful in choosing these intensities. It can be optimized by choosing the correct ratio among the excitation and recombination rates of the two traps. This entangles the concentrations of the traps, the oxidation / reduction state of the crystal, and sensitizing and recording intensities. The best M/# can be obtained by choosing the concentration of the shallower traps as high as practically possible, then optimize the concentration of the deeper traps and the oxidation / reduction state. As a rule of thumb for a $LiNbO_3$:Fe:Mn, the best Mn concentration would be 10% of that of Fe concentration, and the best annealing state is when about 95% of the Mn traps are filled while all Fe traps are empty. The choice of the sensitizing wavelength is also a crucial step in improving the $M/\#$. This wavelength should be long enough to avoid extra absorption due to band–to–band absorption of $LiNbO_3$. On the other hand, it needs to be short enough to provide effective sensitization from the deeper traps.

Although two–center holographic recording has impressing persistence and very good $M/\#$ for most practical applications, its sensitivity is at least one order of magnitude smaller than what is needed. Therefore, sensitivity improvement is very

important for the practicality of two–center holographic recording. This issue will be discussed in detail in Chapter 4.

Chapter 4 System issues in two–center holographic recording

4.1 Introduction

In Chapter 3, we explained the basic idea of two–center holographic recording in doubly–doped $LiNbO_3$ crystals. We showed that persistent holographic recording can be achieved by proper annealing of the crystal and by using appropriate wavelengths and intensities for sensitizing and recording beams. The major problem in the initial experimental results of the two–center recording described in Chapter 3 was the low sensitivity ($S \simeq 0.003$ cm/J). To design a practical holographic read / write memory system, sensitivity needs to be at least in the order of $S \simeq 0.1$ cm/J. Therefore, finding possible ways for improving sensitivity in two–center recording is very crucial. In this chapter, we discuss the possibility of improving the sensitivity of two–center recording by reducing the recording wavelength and by increasing the electron mobility in the recording material.

Another system issue that we discuss in this chapter is the effect of fanning in two–center recording. Fanning is a major noise source in holographic recording. It is caused by the recording of unwanted holograms during both recording and read–out of the stored information. In this chapter, we compare the strength of fanning in two–center recording with that in normal recording.

All holographic recording experiments described in Chapter 3 consisted of the recording of a single hologram. In a practical holographic storage system, we need to record many holograms in the same location of the recording medium to obtain large storage capacities. In multiplexing many holograms, we need to record different holograms for different amounts of time based on a recording schedule to ensure that all recorded holograms are equally strong. In this chapter, we propose and

demonstrate such a recording schedule for two–center recording.

4.2 Improving sensitivity in two–center recording by using a shorter recording wavelength

One reason for the very low sensitivity of two–center recording with UV and red (wavelength 633 nm) in $LiNbO_3$:Fe:Mn crystals is the small absorption cross section of the Fe traps at 633 nm. Figure 4.1 shows the absorption spectrum of a typical $LiNbO_3$:Fe crystal. The crystal is highly reduced to clearly show the broad absorption band of Fe traps centered at about 477 nm. As Figure 4.1 shows, the absorption coefficient of the crystal (that is linearly proportional to the absorption cross section of the Fe traps) at red is much less than that at blue (wavelength 488 nm). Therefore, a more effective wavelength for recording from Fe traps is 488 nm. However, non-destructive read–out can not be obtained at 488 nm due to considerable absorption of Mn traps at 488 nm. We can use recording wavelengths between 488 nm and 633 nm to make a compromise between persistence and sensitivity. Shorter wavelengths result in better sensitivity and worse persistence while longer wavelengths result in worse sensitivity and better persistence. One of the wavelengths in this range that can be easily obtained from an Ar ion laser is 514 nm. In the rest of this section, we consider different aspects of two–center recording in a $LiNbO_3$:Fe:Mn crystal using 404 nm for the sensitization beam and 514 nm for the recording beams [79].

4.2.1 Two–center recording experiments using 514 nm light for recording

We performed experiments with a congruently melting x–cut 0.85 mm thick $LiNbO_3$ crystal doped with 0.075 wt. % Fe_2O_3 and 0.01 wt. % MnO. The crystal was first oxidized for 4 hours at 1000 °C in O_2 atmosphere and then reduced for 1 hour at 700 °C in Ar atmosphere to obtain the best dynamic range parameter ($M/\#$) [75] while keeping non–destructive read–out [80]. This annealing treatment results in fully empty

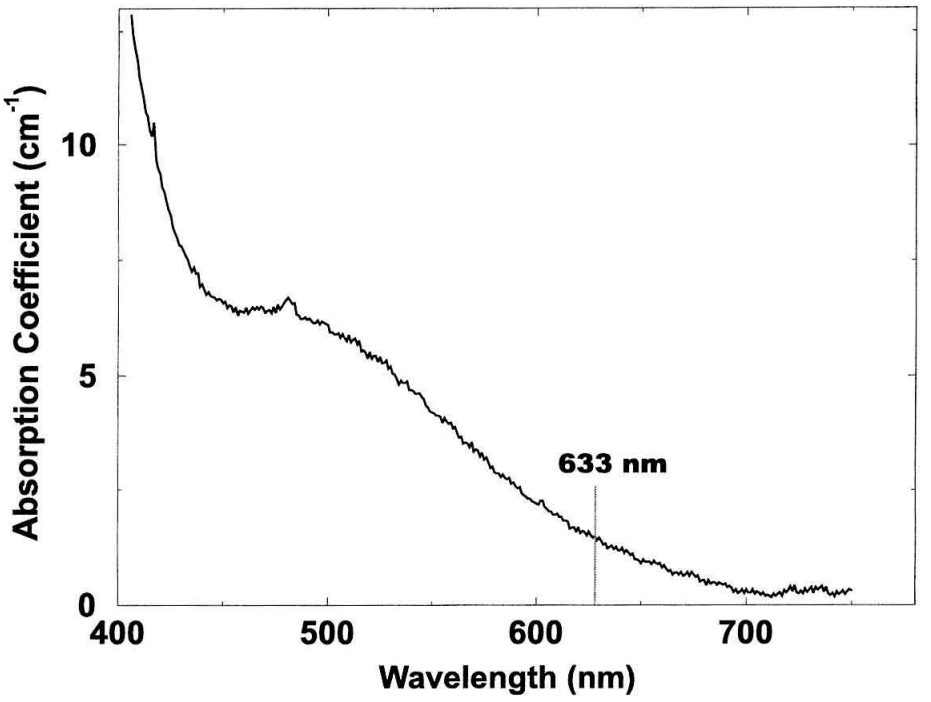

Figure 4.1: Absorption spectrum of a highly reduced $LiNbO_3$:Fe crystal. The broad absorption band at about 477 nm is due to the Fe traps.

Fe traps and partially (more than 90%) filled Mn traps before sensitization. UV light was from a 100 W mercury lamp (wavelength 404 nm, unpolarized, intensity 4 mW/cm^2, homogeneous). Recording is performed with two plane waves of coherent light (wavelength 514 nm, intensity of each beam 17 mW/cm^2, ordinary polarization) interfering inside the crystal with the UV light simultaneously illuminating the crystal. The angle between each beam and the normal to crystal surface outside the crystal was 21°. The grating vector was aligned parallel to the c axis of the sample. The crystal was homogeneously pre–exposed to ultraviolet light for at least one hour before recording. Then a plane–wave grating was recorded and reconstructed in each experiment. Read–out of each hologram was performed by one of the recording beams only with the UV beam blocked.

Figure 4.2 shows the recording and read–out curve. As Figure 4.2 shows, the recording dynamics in recording with UV and green are similar to those in two–center recording with UV and red discussed in Chapter 3. However, the recording intensity is much smaller in recording with UV and green (34 mW/cm^2 compared to 600 mW/cm^2). Therefore, sensitivity (S) is improved by recording with UV and green instead of UV and red. We can measure S from Figure 4.2 using

$$S = \beta \frac{(d\sqrt{\eta}/dt)\mid_{t=0}}{I_{\mathrm{R}} L}\ , \tag{4.1}$$

to be $S \simeq 0.07$ cm/J, that is almost 20 times bigger than the sensitivity obtained in recording with UV and red ($S \simeq 0.003$ cm/J). In Equation (4.1), β is the ratio of $\sqrt{\eta}$ after sufficient read–out to $\sqrt{\eta}$ at the end of recording (before any read–out). Furthermore, η, I_{R}, and L are diffraction efficiency, total recording intensity, and crystal thickness, respectively.

The sensitivity in holographic recording using red light is smaller than that using blue or green light for both normal and two–center recording. This is due to the position of Fe traps in the band gap of $LiNbO_3$. The absorption spectrum of a typical $LiNbO_3$:Fe crystal shows a broad maximum centered at 477 nm. The absorption cross section of Fe traps at 633 nm is smaller than that at 514 nm. The bulk photovoltaic

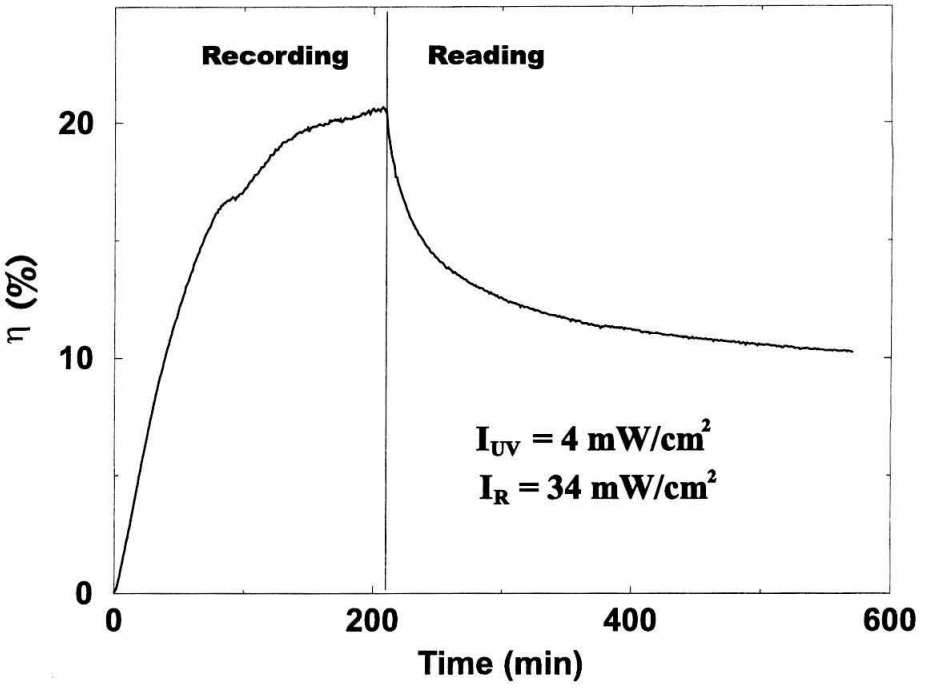

Figure 4.2: Recording and read-out curve for a plane–wave hologram in a 0.85 mm thick $LiNbO_3$:Fe:Mn crystal. Recording is performed by simultaneous presence of a homogeneous UV beam and two green beams (wavelength 514 nm). Read–out is performed by one of the recording beams with no UV light present.

coefficient of Fe traps has similar variation with the wavelength. Therefore, we need to use higher red light intensities to obtain comparable excitation rate from Fe traps to the conduction band, comparable photovoltaic current, and comparable recording dynamics to those in recording with green light. This results in lower sensitivity as S varies as $1/I_{\mathrm{R}}$ for a fixed $d\sqrt{\eta}/dt$.

The effect of different absorption cross sections of Fe traps at different wavelengths can be better understood by the bleaching experiments shown in Figure 4.3 (a). The crystal is first sensitized by UV light for at least one hour, then the sensitized crystal is illuminated with a green or red beam and the transmitted beam is monitored. As electrons are transferred from Fe to Mn traps during bleaching, the absorption of the monitoring beam is reduced. As Figure 4.3 (a) shows, to obtain comparable bleaching speed with red and green light we need to have a much stronger red beam ($\mathrm{I_{Red}} = 300$ mW/cm^2 compared to $\mathrm{I_{Green}} = 17$ mW/cm^2). Therefore, we expect the sensitivity using green and UV to be about $300/17 \simeq 18$ times better than the sensitivity using UV and red. The small difference between this value and the actual measured value of 20 for sensitivity improvement is due to the role of better photovoltaic constant of the Fe traps at 514 nm, and the small difference between the bleaching time constants for red and green in Figure 4.3 (a). The results of the bleaching experiment can be used along with those of the sensitization experiment shown in Figure 4.3 (b) to show that the recording and sensitizing intensities used for the two–center holographic recording experiments are appropriate. In the sensitization experiment, the crystal was illuminated with the UV beam while the transmitted power of a very weak green beam was monitored to obtain the dynamics of electron transfer from Mn to Fe centers. As Figure 4.3 shows, the intensities used for UV and green (or red) beams result in comparable sensitization and bleaching speed. This is desirable for obtaining strong diffraction efficiencies in two–center holographic recording. Much faster sensitization (stronger UV) results in the strong erasure of the hologram by UV light, while much faster bleaching (stronger green or red intensity) results in the strong bleaching of the Fe traps. Both cases result in small diffraction efficiencies.

It is helpful to note that the typical sensitivities obtained in normal holographic

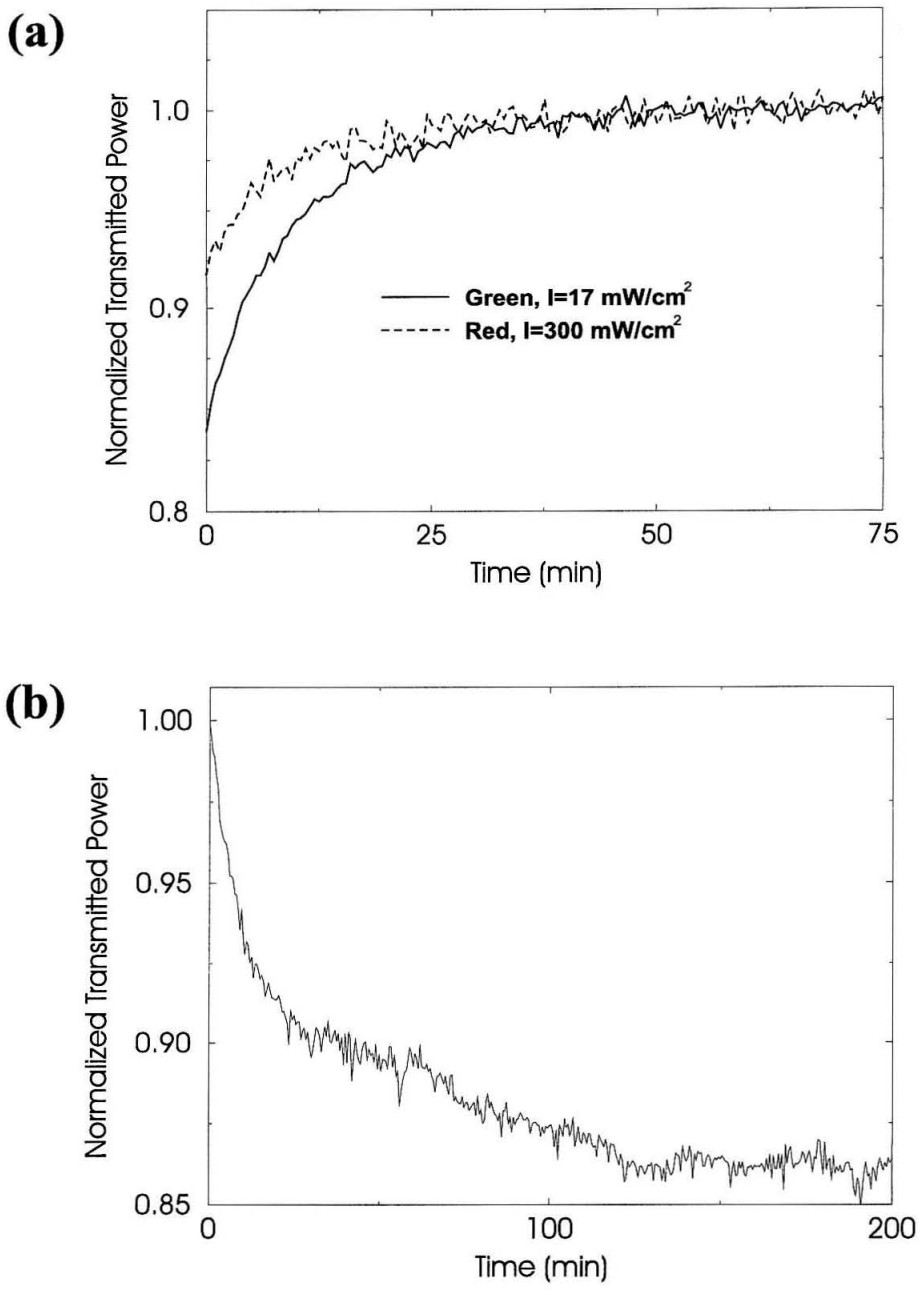

Figure 4.3: Normalized transmitted light intensity in a 0.85 mm $LiNbO_3$:Fe:Mn crystal. (a) Bleaching experiment: The sensitized crystal is bleached with a strong green (wavelength 514 nm) or red (wavelength 633 nm) beam with ordinary polarization, (b) Sensitization experiment: The crystal is sensitized with a homogeneous UV beam (wavelength 404 nm, intensity 4 mW/cm^2) while monitored by a weak green beam (wavelength 514 nm, intensity 0.2 mW/cm^2, ordinary polarization).

recording in $LiNbO_3$:Fe crystals in transmission geometry with ordinary polarization are $S \simeq 0.05 - 0.3$ cm/J for recording with blue light (488 nm), and $S \simeq 0.01 - 0.1$ cm/J with red light (633 nm). Typical sensitivities obtained in two–center holographic recording in $LiNbO_3$:Fe :Mn crystals are $S' = 0.0033$ cm/J and $S' = 0.07$ cm/J with red (633 nm) and green (514 nm) light, respectively (Figure 4.2). The main reason for the smaller sensitivity obtained in two–center holographic recording compared to that in normal recording is the recording mechanism. When recording in a $LiNbO_3$:Fe crystal, electrons are excited from Fe traps to the conduction band by the recording light, move a short distance in the conduction band, and get trapped at Fe traps. This cycle of excitation, movement, and trapping is repeated while the hologram becomes stronger. Due to the small mobility of electrons in the conduction band of $LiNbO_3$, electrons need to go through this cycle many times for recording strong holograms. In two–center recording, electrons are excited by ultraviolet light either from Mn or from Fe traps into the conduction band while red light excites electrons only from the shallower Fe traps, and green light excites electrons mostly from Fe traps. The conduction band electrons can recombine with both centers. Due to the extra sensitization (electron transfer from Mn to Fe traps) process, two–center holographic recording is less sensitive than normal recording: During two–center holographic recording, the recording light excites electrons mainly from Fe centers to the conduction band. These electrons are trapped at either Fe or Mn centers after moving a short distance in the conduction band. The electrons trapped in Fe centers can be used in the next cycle of excitation, movement, and trapping, while those trapped in Mn centers need to be transferred back to Fe centers (via the conduction band) by UV light before participating in another cycle. This increases the average time of each cycle resulting in a lower sensitivity. This sensitivity loss can be reduced by using higher UV intensities. Another reason for the smaller sensitivity in two–center recording is the partial erasure during read–out represented by β in Equation (4.1). In the recording experiments shown in Figure 4.2, β is about 0.7.

4.2.2 Partial loss of persistence in recording with 514 nm light

Although we can improve the sensitivity of two–center holographic recording by a factor of 20 through the use of green instead of red recording light, using green light results in a partial loss of the persistence due to the faster erasure of the hologram in Mn traps. As Figure 4.2 shows, the read–out curve has a small downward slope even after sufficient read–out. One measure for the severity of this erasure is the number of times we can read the entire stored information in a practical memory system before the diffraction efficiency of each hologram is dropped to 50% of the original value. To calculate this, we first determine the erasure time constant by fitting the end part of the read–out curve in Figure 4.2 to an exponential function

$$\sqrt{\eta} = C \exp(-t/\tau) \ . \tag{4.2}$$

The curve fitting results in $\tau = 2 \times 10^5$ s for an erasing intensity of $I = 17$ mW/cm^2. We then assume that the memory module has a 1×1×1 cm^3 crystal with M/#=10, and 1000 holograms each with diffraction efficiency of $\eta = 10^{-4}$ are recorded. We also assume that each hologram contains a 1000×1000 two-dimensional data page (corresponding to 10μm×10μm pixels) resulting in a total capacity of 1 Gbit for the memory module and that successful read–out of each hologram requires the accumulation of 1000 photons per pixel. We also assume that both recording and read–out intensities are 100 mW/cm^2. Therefore, the read–out time for each hologram is

$$t_{\text{read}} = \frac{1000}{A\eta I/(h\nu)} \simeq 39\mu\text{s} \ , \tag{4.3}$$

where $A = 10^{-6}$ cm^2, η, I, h, and ν are pixel area, diffraction efficiency of each hologram, read–out intensity, Plank's constant, and optical frequency of the read–out beam, respectively. Therefore, the read–out time for the entire 1 Gbits memory is 1000×39 μs $= 39$ ms. Since the erasure time constant is inversely proportional to the

reading intensity, we can calculate the erasure time constant at 100 mW/cm^2 from the value we measured at 17 mW/cm^2 to be $\tau = (17/100) \times 2 \times 10^5$ s$= 3.4 \times 10^4$ s. The total time we can read the hologram before the diffraction efficiency (η) drops to half of its original value (or $\sqrt{\eta}$ drops to 70% of its original value) is $t = \tau \ln(\sqrt{2}) = 1.2 \times 10^4$ seconds. Therefore, we can read the entire information in the memory module approximately 300,000 times before the diffraction efficiency drops to 50% of its original value.

When the diffraction efficiency of each hologram falls below some minimum value, we need to refresh the entire memory module by reading out and re-recording all holograms. To calculate the refreshing time of the memory we described above, we assume that we use in–plane (or extraordinary) polarization for the recording beams to obtain $S' = 3 \times 0.07 = 0.21$ cm/J due to the larger electro–optic coefficient of $LiNbO_3$ for extraordinary polarization ($r_{33} \simeq 3r_{13}$). Using Equation (4.1) and assuming that the recording dynamics are linear for small diffraction efficiencies, we can calculate the recording time of a hologram with diffraction efficiency of 10^{-4} to be 0.5 s for a 1 cm thick crystal with a recording intensity of 100 mW/cm^2. To record 1000 holograms with equal diffraction efficiencies (each equal to 10^{-4}), we need to use the recently–proposed recording schedule for two–center holographic recording [81]. Taking into account different recording times for the different holograms and assuming the recording time of the last hologram to be 0.5 sec, we obtain a total recording time of $t \simeq 1000 \ln(1000) \times 0.5$ s$\simeq 3500$ s.

Although the focus of this chapter is sensitivity improvement by using green light, we also improve the dynamic range parameter, $M/\#$, by using green light. This can be inferred from Figure 4.2. The final diffraction efficiency obtained in recording with green light is about 40% better than that obtained in recording with red light. This results in an improvement in the $M/\#$ by at least 20%. The approximate $M/\#$ (square root of the final diffraction efficiency) for recording with green and UV can be measured from Figure 4.2 to be $M/\# \simeq 0.33$. If we use extraordinary polarization, we can obtain $M/\# \simeq 1$ for our 0.85 mm thick sample. Using a 1 cm thick sample can result in M/# more than 10. This is in agreement of the $M/\# = 10$ we assumed

in the persistence calculation of this section.

4.3 Effect of carrier mobility in holographic recording

Recording and erasure time constants in holographic recording are approximately inversely proportional to the mobility of carriers responsible for recording (i.e., electrons in the conduction band or holes in the valence band). Holograms can be recorded faster if we can increase the mobility of carriers responsible for recording. Therefore, one idea for increasing sensitivity could be increasing the carrier mobility. In almost all holographic recording experiments in $LiNbO_3$, these carriers are electrons in the conduction band. The mobility of these electrons can be varied by changing the stoichiometry of $LiNbO_3$. Congruently melting $LiNbO_3$ crystals (typical ratio of Li to Nb about 94%) have the lowest electron mobility while perfectly stoichiometric crystals (ratio of Li to Nb ions equal to 1) have the highest electron mobility. The mobility of electrons in the conduction band of $LiNbO_3$ can also be varied by highly doping the crystal with magnesium (Mg). Typical doping levels required are in the order of 4 wt. % of MgO [45].

In this section, we investigate the possibility to increase the holographic recording sensitivity (S) in $LiNbO_3$ through increasing electron mobility (μ). Our assumption is that other material properties (i.e., absorption cross section and recombination coefficient for the different traps, etc.) are fixed, and we only change the mobility of electrons in the conduction band. To clarify the effect of electron mobility on sensitivity and $M/\#$, we first consider normal recording with single wavelength in a typical $LiNbO_3$:Fe crystal. Then, we will discuss the role of electron mobility in two–center holographic recording and compare it with that in normal recording.

4.3.1 Effect of carrier mobility in normal holographic recording

To study the effect of electron mobility (μ) on $M/\#$ and S, we only need to consider the dependence of saturation hologram strength (A_0) and recording time constant (τ_r) on μ. We assume that recording and erasure time constants are approximately the same resulting in

$$\begin{aligned} M/\# &= \frac{A_0 \tau_e}{\tau_r} \\ &\simeq A_0 \,, \end{aligned} \tag{4.4}$$

where τ_e is the erasure time constant. Note that even if τ_r and τ_e are not the same, they have similar variations with electron mobility. Therefore, the main parameter that represents the effect of μ on $M/\#$ is the saturation hologram strength A_0. Note also that A_0 is linearly proportional to saturation space–charge field $E_{1,sat}$. Therefore, we can use

$$M/\# \;\propto\; A_0 \propto E_{1,sat} \tag{4.5}$$

to study the effect of μ on $M/\#$. The effect of μ can be studied by using the formula for S in terms of $E_{1,sat}$ and τ_r as

$$S = \frac{A_0/\tau_r}{I_R L} \propto \frac{E_{1,sat}}{\tau_r} \,, \tag{4.6}$$

where I_R and L represent recording intensity and crystal thickness, respectively. Both I_R and L are independent of μ.

The approximate formulas for $E_{1,sat}$ and τ_r are

$$E_{1,sat} = -\frac{j_{phv1} + j_{diff1}}{e\mu n_0} \tag{4.7}$$

$$\tau_r = \frac{\epsilon\epsilon_0}{e\mu n_0} \,, \tag{4.8}$$

where e and n_0 are the electronic charge and the average (DC) electron concentration in the conduction band, respectively. Furthermore, j_{phv1} and j_{diff1} are the first Fourier components of bulk photovoltaic and diffusion current densities, respectively. Furthermore, n_0 can be approximately represented by

$$n_0 \simeq \frac{q_{\text{Fe}} s_{\text{Fe}} N_{\text{Fe0}}^{-} I_{\text{R0}}}{\gamma_{\text{Fe}} (N_{\text{Fe}} - N_{\text{Fe0}}^{-})} , \tag{4.9}$$

where $q_{\text{Fe}} s_{\text{Fe}}$ and γ_{Fe} represent the absorption cross section from Fe traps to the conduction band and recombination coefficient of the Fe traps, respectively. Furthermore, N_{Fe}, N_{Fe0}^{-}, and I_{R0} represent total Fe concentration, electron concentration in the Fe traps, and average (DC) recording intensity, respectively. The formulas for j_{phv1} and j_{diff1} in a $LiNbO_3$:Fe crystal are

$$j_{\text{phv1}} \simeq \kappa_{\text{Fe}} N_{\text{Fe0}}^{-} I_{\text{R1}} \tag{4.10}$$

$$j_{\text{diff1}} = k_{\text{B}} T \mu \nabla n_1 = i K k_{\text{B}} T \mu n_1 . \tag{4.11}$$

Here, κ_{Fe} and I_{R1} in Equation (4.10) are bulk photovoltaic constant of the Fe traps at recording wavelength and the amplitude of sinusoidal recording intensity, respectively. In Equation (4.11), k_{B}, T, K, and n_1 represent Boltzmann constant, absolute temperature, amplitude of grating vector of the hologram, and the first Fourier component of the electron concentration in the conduction band. For holographic recording in congruently melting $LiNbO_3$:Fe crystals using transmission geometry, the bulk photovoltaic current is dominant and the diffusion current density (j_{diff1}) in Equation (4.7) can be neglected resulting in

$$E_{1,\text{sat}} \simeq -\frac{j_{\text{phv1}}}{e\mu n_0} \simeq -\frac{\kappa_{\text{Fe}} N_{\text{Fe0}}^{-} I_{\text{R1}}}{e\mu n_0} . \tag{4.12}$$

Replacing n_0 in Equation (4.12) by its equivalent from Equation (4.9), we obtain

$$|E_{1,\text{sat}}| \simeq \frac{\kappa_{\text{Fe}} \gamma_{\text{Fe}} (N_{\text{Fe}} - N_{\text{Fe0}}^{-}) I_{\text{R1}}}{e q_{\text{Fe}} s_{\text{Fe}} I_{\text{R0}}} \frac{1}{\mu} \propto \frac{1}{\mu} . \tag{4.13}$$

Putting Equations (4.13) and (4.8) into Equations (4.5) and (4.6), we obtain the dependence of $M/\#$ and S on μ as

$$M/\# \sim \frac{1}{\mu} \tag{4.14}$$

$$S \simeq C\,, \tag{4.15}$$

where C represents some constant independent of μ. Note that Equations (4.14) and (4.15) are valid only in the regime of the domination of bulk photovoltaic current. Therefore, these equations can be applied to congruently melting crystals. Equations (4.14) and (4.15) suggest that we can not increase sensitivity by increasing mobility, while we lose M/# by increasing mobility. This result might seem strange at the beginning since we know that the holograms are recorded faster at higher electron mobility (recording time constant becomes smaller at higher mobility). However, sensitivity depends on the ratio of saturation hologram strength (A_0) and recording time constant (τ_r). When the bulk photovoltaic current is dominant, both A_0 and τ_r decrease with increasing μ in a similar way resulting in approximate independence of sensitivity from μ.

The situation is completely different in the regime of the domination of diffusion current. This is the case for stoichiometric $LiNbO_3$:Fe crystals, or in some cases, for congruently melting crystals in the 90° geometry. The saturation space–charge field in this regime can be represented by

$$E_{1,\mathrm{sat}} = -\frac{j_{\mathrm{diff1}}}{e\mu n_0} \simeq -iK\frac{k_B T}{e}\frac{n_1}{n_0}\,. \tag{4.16}$$

Assuming unity modulation depth of recording intensity, we can use $n_1 \simeq n_0$ to simplify Equation (4.16) as

$$|E_{1,\mathrm{sat}}| \simeq \frac{k_B T}{e} K\,. \tag{4.17}$$

Equation (4.17) suggests that in the regime of the domination of diffusion current, saturation space–charge field is approximately independent of μ. Using this result,

we can summarize the dependence of $M/\#$ and S on μ in this regime as

$$M/\# \sim C' \tag{4.18}$$

$$S \simeq \mu\,, \tag{4.19}$$

where C' is a constant independent of μ. Equations (4.18) and (4.19) suggest that increasing mobility in the regime of the domination of diffusion current is a good idea for increasing sensitivity without affecting $M/\#$. In this regime, the saturation hologram strength is independent of μ. Therefore, increasing μ results in increasing sensitivity by reducing the recording time constant. The domination of diffusion current in $LiNbO_3$ occurs in near stoichiometric crystals or the crystals that are highly doped with MgO, or in some cases in the 90° geometry with small grating period (or high spatial frequency).

As discussed above, we need to get to the regime of domination of diffusion current in $LiNbO_3$: Fe to start improving sensitivity by increasing μ. To do this, we need to increase μ by using stoichiometric crystals, for example. However, we lose $M/\#$ by a large factor in going from the regime of domination of photovoltaic current to that of the domination of diffusion current. This is clearly depicted in Figure 4.4 that shows the theoretical variation of the saturation hologram strength ($A_0 \simeq M/\#$) and sensitivity (S) with electron mobility (μ) in a 0.85 mm thick $LiNbO_3$ crystal doped with 0.075 wt.% Fe_2O_3. The calculation is performed by solving Kukhtarev's equations [59] numerically using Fourier development explained before. We assumed that recording was performed by two red beams (wavelength 633 nm, intensity of each beam 250 mW/cm^2). Although 633 nm is not the best wavelength for recording from Fe traps, we chose it to be the same as the recording wavelength in two–center recording discussed later. The two curves in each part of Figure 4.4 are calculated with and without considering diffusion current to show the regimes of the domination of the different components of current. As Figure 4.4 shows, we need to increase μ by more than one order of magnitude from that of a typical congruently melting $LiNbO_3$ crystal to enter into the regime of the domination of the diffusion current

where sensitivity can be improved by increasing μ further. During this process, M/# is reduced by more than one order of magnitude before getting to the diffusion domination regime where it becomes almost independent of μ. It is important to note that the range of μ shown in Figure 4.4 is not the practical range that can be obtained by changing the stoichiometry of $LiNbO_3$ crystals. It is not practically possible to increase electron mobility in $LiNbO_3$ by three orders of magnitude by simply changing the stoichiometry of the crystal or by doping it with MgO. Therefore, the usage of stoichiometric crystals or crystals doped highly with MgO in the transmission geometry is not a good idea to improve S. While sensitivity of these materials is similar to that of congruently melting crystals, their dynamic range ($M/\#$) is much smaller than that of the congruently melting crystals.

Figure 4.5 shows the recording and read–out curve for a plane wave hologram recorded in a 0.85 mm thick $LiNbO_3$ crystal doped with 0.25 wt.% Fe_2O_3 and 4.3 wt.% MgO. Recording is performed in transmission geometry by two plane waves (wavelength 488 nm, intensity of each beam 15.5 mW/cm^2, ordinary polarization) while reading is performed by one of the recording beams. The values of $M/\#$ and S calculated from Figure 4.5 are $M/\# = 0.15$ and $S = 0.15$ cm/J. Although $S = 0.15$ cm/J is in the same order of sensitivities that can be obtained in congruently melting $LiNbO_3$:Fe crystals, the value of the $M/\#$ is much lower than those obtained in congruent $LiNbO_3$:Fe crystals with similar properties.

4.3.2 Effect of carrier mobility in two–center holographic recording

One might expect that similar behavior of $M/\#$ and S with carrier mobility is obtained in two–center recording since changing mobility affects electron transport in the conduction band that is similar for both normal and two–center recording. However, the effect of mobility on $M/\#$ and S in two–center recording is very different from that in normal recording. Figure 4.6 shows the theoretical variation of sensitivity (S) and final saturation hologram strength (approximate $M/\#$) with electron mobil-

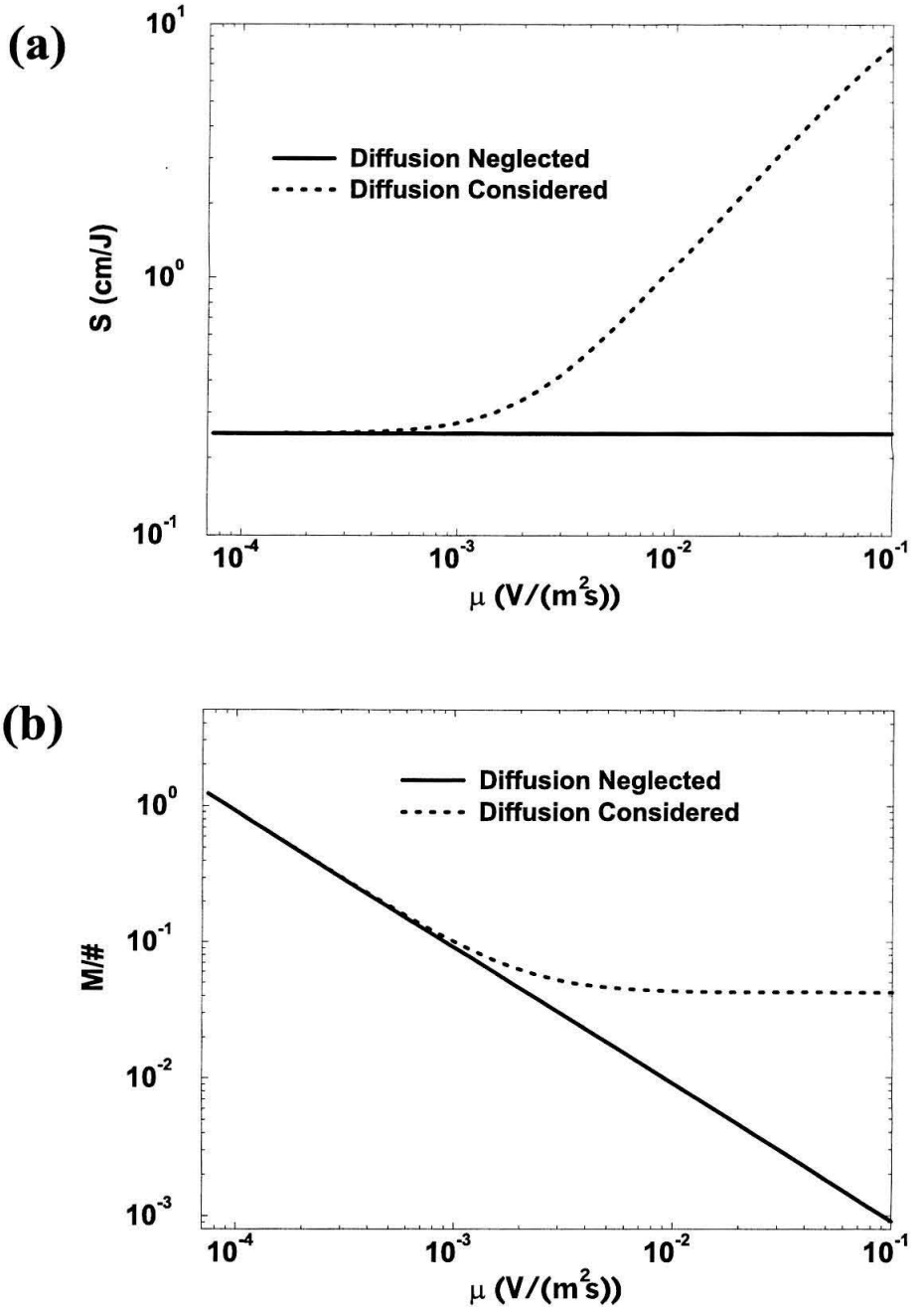

Figure 4.4: Theoretical variations of (a) sensitivity (S), and (b) approximate $M/\#$ with electron mobility (μ) for a 0.85 mm thick $LiNbO_3$:Fe crystal in normal recording. It is assumed that recording is performed by two red beams (wavelength 633 nm, intensity of each beam 250 mW/cm^2, ordinary polarization).

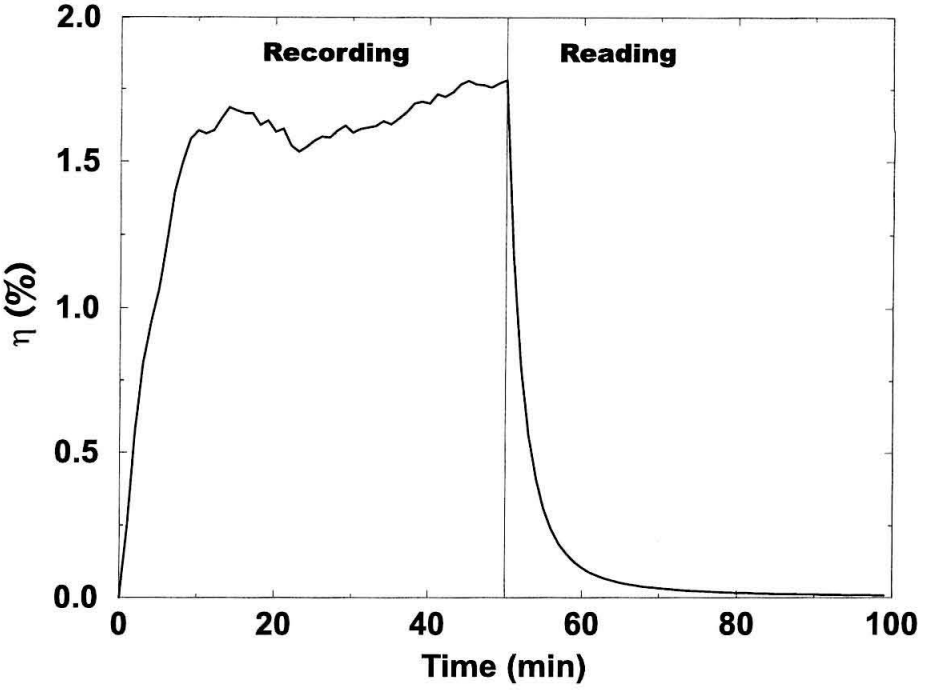

Figure 4.5: Recording and read–out curve for a plane wave hologram in a 0.85 mm thick $LiNbO_3$:Fe:Mg crystal. Recording is performed by two coherent beams (wavelength 488 nm, intensity of each beam 15.5 mW/cm^2, ordinary polarization). Read–out is performed by one of the recording beams.

ity (μ) in two–center holographic recording in a $LiNbO_3$ crystal doped with 0.075 wt. % Fe_2O_3 and 0.01 wt. % MnO. In this calculation we assumed that all Fe traps as well as 10% of the Mn traps are initially empty. We also assumed that recording was performed by one UV beam (wavelength 365 nm, intensity 20 mW/cm^2) and two red beams (wavelength 633 nm, intensity of each beam 250 mW/cm^2). The two curves in each part of Figure 4.6 are calculated with and without considering diffusion current to show the regimes of the domination of diffusion and bulk photovoltaic currents. As Figure 4.6 (a) shows, the variation of sensitivity (initial recording slope normalized by recording intensity and crystal thickness) in two–center recording is similar to that in normal recording (Figure 4.4 (a)). However, the variation of the persistent $M/\#$ with μ in two–center recording is totally different from that in normal recording as Figure 4.6 (b) shows. The $M/\#$ in two–center recording decreases initially with increasing μ going to zero at one value of μ. It then increases with further increasing μ, and finally becomes constant in the diffusion dominated regime.

To understand the unexpected variation of persistent $M/\#$ with μ, it is helpful to think about the reason for obtaining persistence in two–center recording in a $LiNbO_3$:Fe:Mn crystal, i.e., the asymmetry between the average number of excitation to the conduction band, movement in the conduction band, and trapping cycles for an electron during recording and read–out. An electron on the average goes through many of these cycles to record a strong hologram at very low values of mobility, while it goes through only a few cycles during read–out due to trapping at Mn centers. Therefore, we only see a small partial erasure of the hologram during read–out at low values of μ, and we observe relatively high persistent $M/\#$ at low μ. The asymmetry between the number of cycles during recording and read–out is reduced as μ increases since the average distance an electron moves in the conduction band in each cycle is linearly proportional to μ. Therefore, the average number of cycles an electron undergoes during recording decreases with increasing μ. On the other hand, the average number of cycles an electron undergoes during read–out does not strongly depend on μ as it is mainly determined by the relative probabilities for electron trapping at Fe and Mn centers. Therefore, the average distance an electron moves backward during

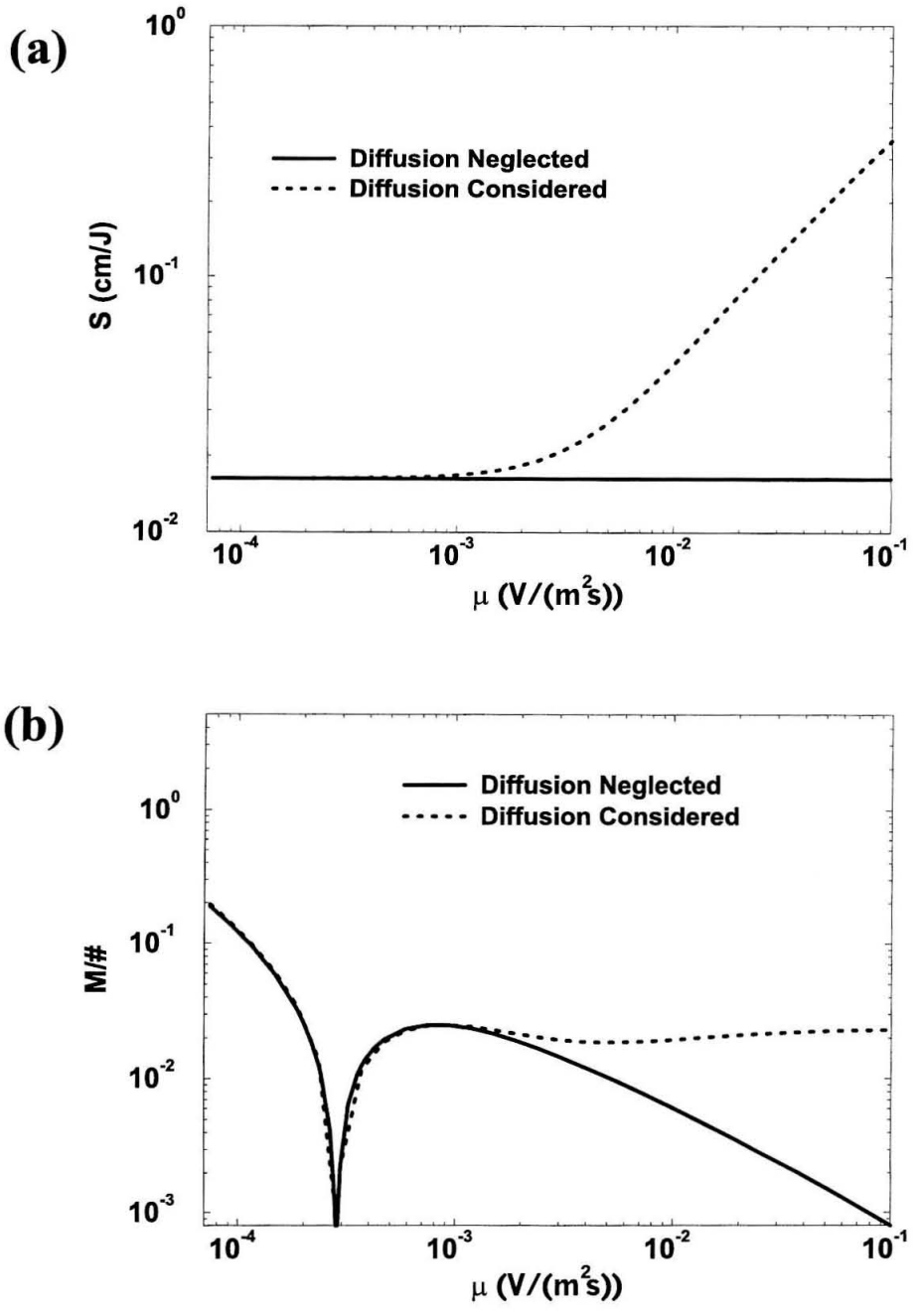

Figure 4.6: Theoretical variations of (a) sensitivity (S), and (b) approximate $M/\#$ with electron mobility (μ) for a 0.85 mm thick $LiNbO_3$:Fe:Mn crystal in two–center recording. It is assumed that recording is performed by one UV beam (wavelength 365 nm, intensity 20 mW/cm^2) and two red beams (wavelength 514 nm, intensity of each beam 250 mW/cm^2, ordinary polarization).

read–out becomes closer to the average distance an electron moves forward during recording as μ increases. This results in a stronger partial erasure and smaller persistent $M/\#$ at higher values of μ. The lowest persistent $M/\#$ is obtained at the specific value of μ that results in the total disappearance of the asymmetry during recording and read–out. For this specific value of μ, the hologram is completely erased during read–out resulting in zero persistent $M/\#$. If we increase μ further, the hologram will undergo a 180° phase shift during read–out. In other words, the electron transfer from Fe traps to Mn traps during read–out causes the diffraction efficiency to go first to zero at some time. At this time, the two holograms in Fe traps and Mn traps are equally strong, but they are exactly 180° out of phase. Therefore, the total hologram strength (sum of the two holograms) is zero. The remaining space–charge pattern (or electron concentration) in the Fe traps will be transferred to the Mn traps via the conduction band during further read–out. However, these electrons move in the conduction band, and this movement results in a nonzero hologram strength. The phase difference between this newly revealed hologram and the original one is 180°. As μ increases from its specific value (resulting in zero persistent $M/\#$), the revealed hologram during read–out becomes stronger. Therefore, $M/\#$ increases with increasing μ after that specific value of μ that results in zero persistent $M/\#$ as shown in Figure 4.6 (b). Figure 4.7 shows the theoretical recording and read–out curves for plane wave holograms recorded in the $LiNbO_3$:Fe:Mn crystal discussed before at different values of μ. The 180° phase shift obtained during read–out at very high μ as well as the total erasure of the hologram during read–out at a specific value of μ are evident from Figure 4.7.

It is important to note that the sensitivity values shown in Figure 4.4 (a) were calculated without considering persistence. If we are interested in the persistent sensitivity, we need to modify this value by the partial erasure of the hologram during read–out as explained in Chapter 3. This results in even lower values of sensitivity, especially around the specific value of μ that results in zero $M/\#$.

To investigate the possibility of sensitivity improvement in two–center recording by increasing electron mobility, we performed experiments with a 5 mm thick $LiNbO_3$

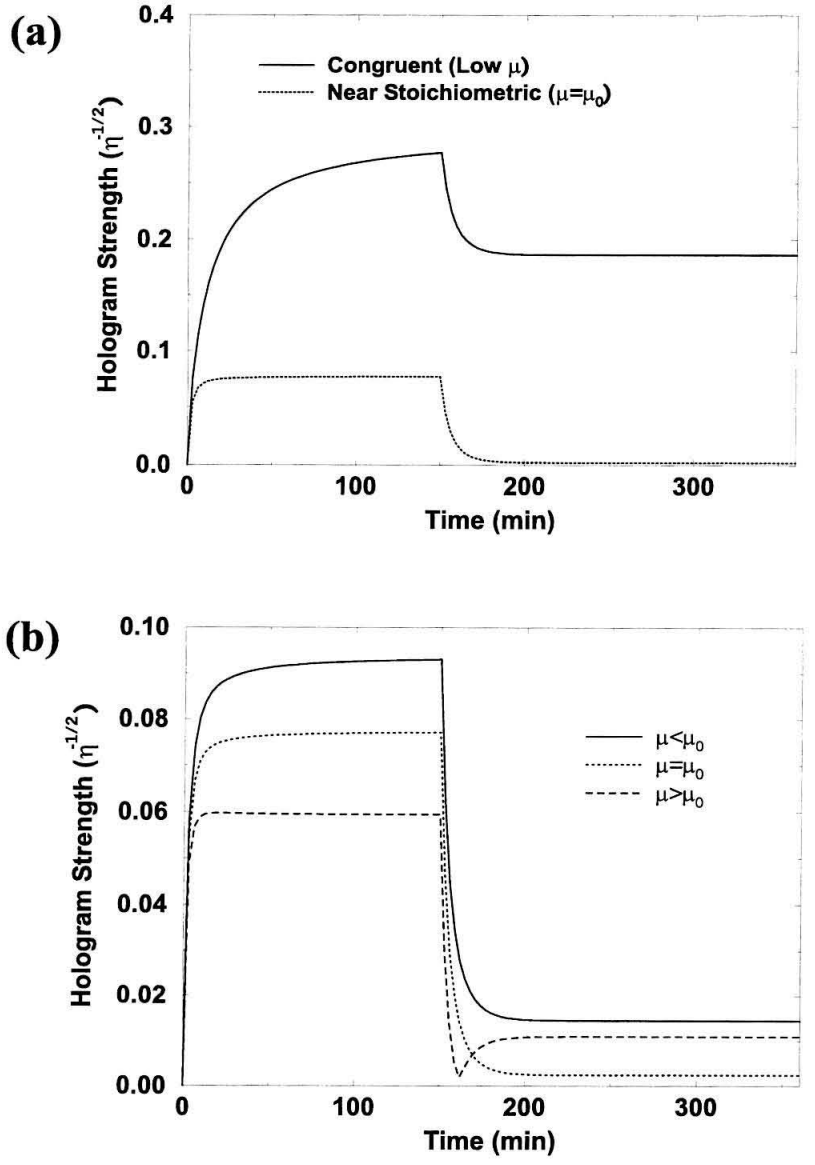

Figure 4.7: Theoretical recording and readout curves for a 0.85 mm thick $LiNbO_3$:Fe:Mn crystal in two–center recording. The curves were calculated using different values of electron mobility (μ). It is assumed that recording is performed by one UV beam (wavelength 365 nm, intensity 20 mW/cm^2) and two red beams (wavelength 633 nm, intensity of each beam 250 mW/cm^2, ordinary polarization). (a) Comparison of recording and read–out curves of a congruent (low mobility) crystal with that of a crystal with a special mobility value (μ_0 resulting in zero final $M/\#$. (b) Comparison of the recording and read–out curves for different values of mobility in the vicinity of $\mu = \mu_0$.

crystal doped with 0.075 wt. % Fe_2O_3, 0.01 wt. % MnO, and 4.3 wt. % MgO. The oxidation of the crystal to the level that all Fe traps as well as a portion of Mn traps are empty was very difficult. This difficulty is a typical property of the Mg doped or stoichiometric $LiNbO_3$ crystals making the optimization of annealing in two–center recording sophisticated or even impossible. The physical reason is that more stoichiometric or Mg doped crystals have less defects that allow charge compensation upon thermal annealing. Although we oxidized the crystal for three consecutive days at 1000–1100 °C in O_2 atmosphere, there was still a small electron concentration in Fe traps, and all Mn traps were occupied by electrons. We recorded a plane wave hologram using one homogeneous sensitizing beam (wavelength 404 nm, intensity 3.6 mW/cm^2) and two recording beams (wavelength 514 nm, intensity of each beam 17 mW/cm^2, ordinary polarization) in transmission geometry. To have a recording curve that is appropriate for measuring sensitivity, we first recorded a hologram after pre–exposing the crystal to the sensitizing beam for 2 hours. Then, we rotated the crystal until the read–out of the hologram was negligible. This preparation assures that a steady–state balance between sensitization and bleaching is already achieved, and the electron concentrations in the Mn and Fe traps are now very close to the steady state values that is obtained during recording. After this careful adjustment of the starting condition, we recorded a hologram in the new location while monitoring its diffraction efficiency with time. Read–out of the hologram was then performed by one of the recording beams. The experimental recording and read–out curve is shown in Figure 4.8. The value of sensitivity from Figure 4.8 is $S = 0.05$ cm/J that is not better than that obtained with a congruently melting $LiNbO_3$ crystal with similar Fe and Mn concentrations. Note that the crystal used in this experiment was too reduced for persistent two–center holographic recording. The excessive reduction results in the higher value of sensitivity than that obtained in a crystal with correct oxidation /reduction state. Therefore, we would expect that persistent sensitivity in the $LiNbO_3$:Fe:Mn:Mg crystal is not better than that in the congruently melting $LiNbO_3$:Fe:Mn crystal.

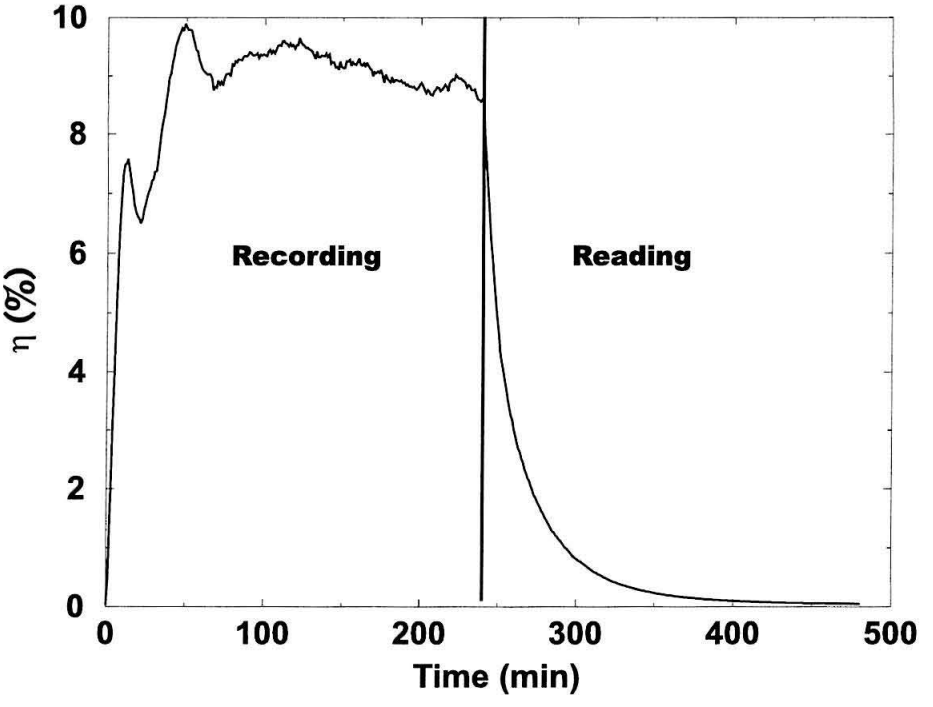

Figure 4.8: Recording and read–out curve for a plane wave hologram in a 5 mm thick $LiNbO_3$:Fe:Mn:Mg crystal. Recording is performed by one sensitizing beam (wavelength 404 nm, intensity 3.6 mW/cm^2) and two coherent beams (wavelength 514 nm, intensity of each beam 17 mW/cm^2, ordinary polarization). Read–out is performed by one of the recording beams.

4.3.3 Summary

We can not increase sensitivity in either normal or two–center holographic recording in $LiNbO_3$ crystals by increasing electron mobility. The practical electron mobility that can be obtained by using stoichiometric crystals or by doping the crystal highly with MgO is not high enough to increase sensitivity considerably beyond that obtained in congruently melting crystals. On the other hand, we lose $M/\#$ by a large factor by using stoichiometric or Mg doped $LiNbO_3$ crystals in both normal and two–center recording.

The understanding of the effect of electron mobility on the performance of two–center holographic recording systems discussed in this section is very important in the investigation of other materials for persistent two–center holographic recording. It is logical to use materials with lower values of carrier mobility to obtain good persistent $M/\#$ in two–center recording. Therefore, in designing a holographic recording system using $LiNbO_3$, we need to use a congruently melting doubly–doped crystal. Note that crystals with smaller Li concentrations than that in a congruently melting crystal can be grown, too. Such crystals have smaller μ values than that of a congruently melting crystal. However, the crystal quality is not as good as the congruently melting crystals.

4.4 Reduction of fanning in two–center recording

Fanning and holographic scattering are among the important noise sources that degrade the quality of reconstructed holograms [82, 83]. They reduce signal to noise ratio and increase the probability of error. Fanning and holographic scattering occur due to light scattering inside the recording medium. When a coherent light beam passes through the medium, it gets scattered by the scattering centers in the medium. The simultaneous presence of the original (or reference) beam and each scattered beam records a hologram that enhances itself in time as long as the reference beam is illuminating the medium. Since scattering occurs in many directions, a lot of these

scattering holograms are recorded. During the recording of a hologram by a reference beam and a signal beam, both beams get scattered inside the medium resulting in fanning. During read–out, the presence of the reading (or reference) beam causes fanning. The quality of the reconstructed beam during read–out of a hologram degrades in time as fanning builds up.

The buildup of the scattering holograms depends on the recording sensitivity and the dynamic range of the medium, especially during read–out. This is due to the fact that the average reading time in practical storage systems is much longer than the average recording time. The effect of fanning during read–out can be observed by recording a single hologram of a two–dimensional bit pattern (or a mask) and read the hologram while monitoring the reconstructed image over time.

Suppression or reduction of fanning without sacrificing sensitivity is a challenging task in normal recording. More sensitive materials fan more due to the fast recording of the scattering holograms. The sensitivity of the materials used in normal recording during read–out is the same as that during recording. However, fanning is highly reduced in two–center recording due to the inherent mechanisms involved in this type of recording. The presence of the incoherent homogeneous sensitizing (UV) beam during recording does not let scattering holograms buildup by erasing them. This can also be understood by recalling that the strength of a hologram in two–center recording depends on the ratio of the recording and sensitizing intensities. This intensity ratio is optimally chosen for the desired hologram, but it is far from the optimum for the scattering holograms since the recording intensity of the scattering hologram is much less than that of the desired hologram. Fanning occurs only in a short initial period during read–out of a hologram in two–center recording. This period consists of the time interval in which electrons are transferred from shallower to deeper traps. All shallower traps become empty after this initial period resulting in the insensitivity of the material to the reading beam. Therefore, fanning can not buildup after the initial period. Reducing the recording wavelength in two–center recording for improving the sensitivity can cause a very mild buildup of fanning due to the small sensitivity for recording scattering holograms from the deeper traps.

To compare fanning in normal and two–center recording, we performed holographic recording experiments with two $LiNbO_3$:Fe:Mn crystals. The doping levels were 0.075 wt. % Fe_2O_3 and 0.01 wt. % MnO in both crystals. One crystal (XTAL1) was annealed properly to have all Fe traps as well as a portion of the Mn traps initially empty. The other crystal (XTAL2) was highly reduced to have all Mn traps as well as a portion of the Fe traps occupied by electrons. Therefore, XTAL1 is appropriate for persistent two–center recording while XTAL2 is appropriate for normal single wavelength recording as it acts like a reduced $LiNbO_3$:Fe crystal.

We recorded a transmission geometry Fourier plane hologram of a two–dimensional data mask with 120 μm $\times$ 120 μm pixels in each case. Two–center recording in XTAL1 was performed by one sensitizing beam (wavelength 404 nm, intensity 3 mW/cm^2, homogeneous) and two recording beams (wavelength 514 nm, intensity of each beam at the crystal about 10 mW/cm^2, ordinary polarization). Recording in XTAL2 was performed by the same two recording beams without any sensitizing beam. The diffraction efficiency of the recorded holograms in both cases was about 1%. Each hologram was then read by the corresponding reference beam, and the reconstructed image was monitored during read–out by a CCD camera. The signal-to-noise ratio (SNR) of the reconstructed hologram was then computed by measuring the intensities of the on and off pixels in the digitized image. Each bit on the data mask, a square measuring 120 microns on a side, imaged to occupy a square of roughly 14 $\times$ 14 CCD pixels. A 20 $\times$ 20 grid of these bits, from the center of the reconstructed image, was used for computing the SNR. The average of the pixel values were calculated for each bit, and the mean and standard deviation of these average pixel values were computed separately for the data bits which were supposed to be"on" and"off." The SNR was then calculated as:

$$SNR = (m_1 - m_0)/\sqrt{\sigma_1^2 + \sigma_0^2}\,, \tag{4.20}$$

where m_1 and m_0 are the mean values of the "on" and "off" pixels, respectively, while σ_1 and σ_0 are the standard deviations of the "on" and "off" pixels, respectively.

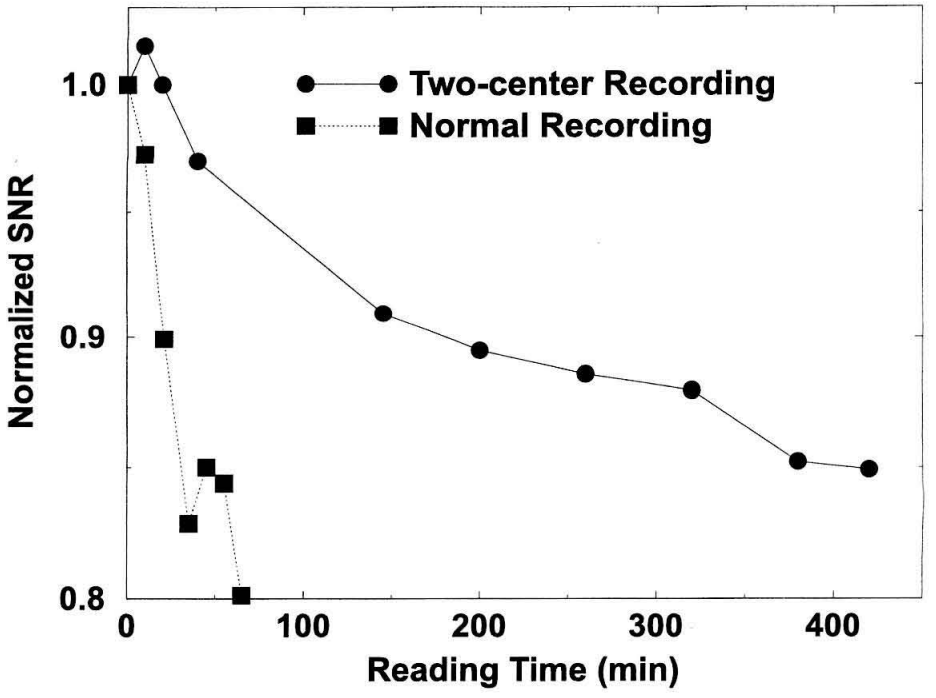

Figure 4.9: Comparison of the variations of the signal to noise ratio (SNR) with time in normal and two–center recording. The details of the experiments are described in the text.

Figure 4.9 shows the loss in normalized signal to noise ratio (SNR) during read–out for the two cases. As Figure 4.9 shows, two–center recording suffers from fanning during read–out only in an initial period. The loss in SNR after that initial period is very slow as explained before. On the other hand, SNR in normal recording drops much faster and finally falls below the minimum acceptable value. Note that due to the loss in diffraction efficiency during read–out, we need to change the gain of the camera at different times. This results in the increase of the calculated SNR with time at a few data points that is not a physical effect.

Figure 4.10 shows a small portion of the reconstructed images at different times during continuous read–out in the two cases. It can be seen from Figure 4.10 that the quality of the reconstructed image in two–center recording after 7 hours of read–out is still comparable to the initial quality. However, the quality of the reconstructed image in normal recording is highly degraded after 80 minutes.

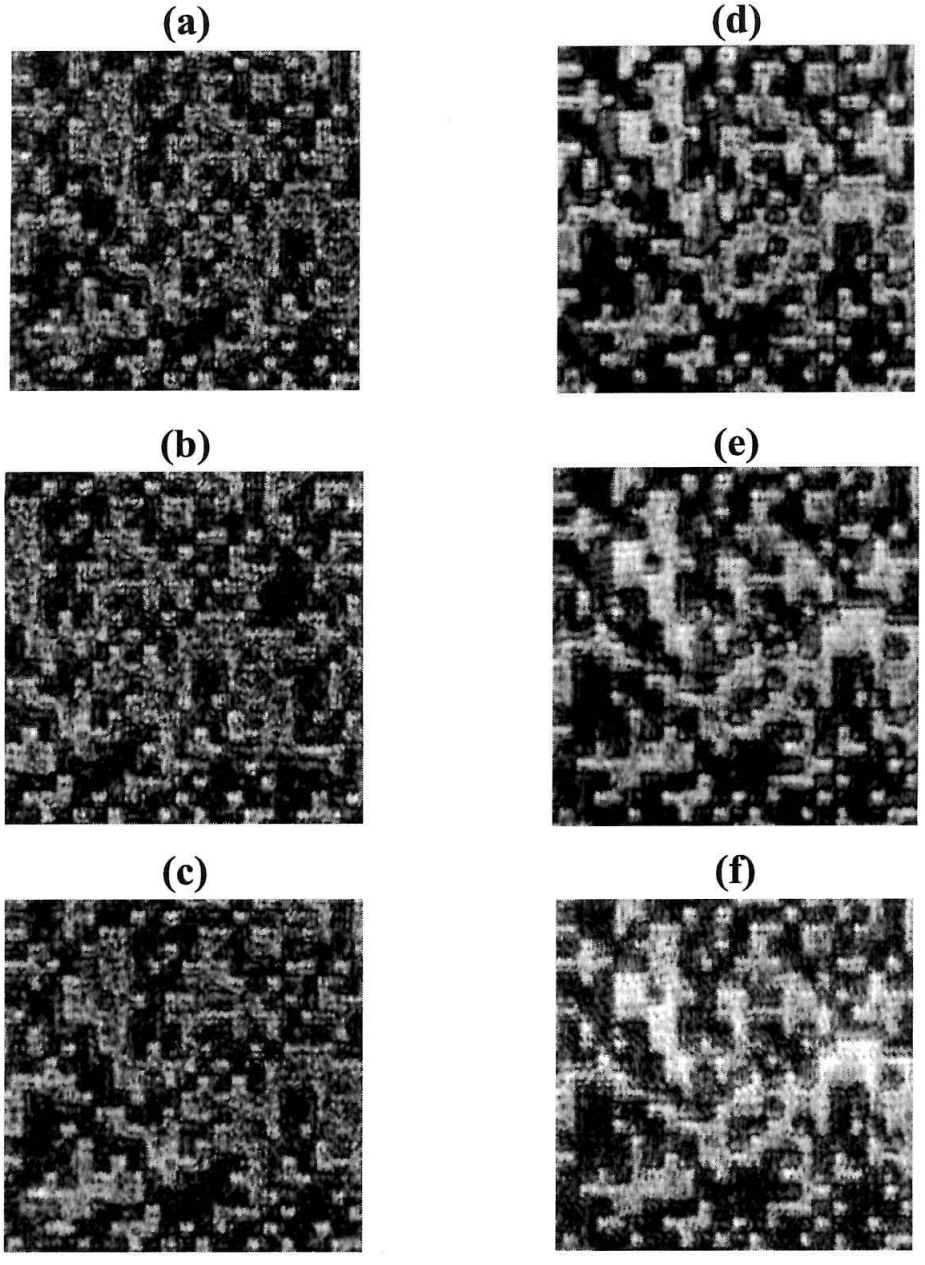

Figure 4.10: Comparison of the evolution of the qualities of reconstructed images with time in normal and two–center recording. The Figures (a), (b), and (c) show a portion of the reconstructed image in two–center recording at the end of recording (beginning of the read–out), after 40 minutes of continuous read–out, and after 420 minutes of continuous read–out, respectively. The Figures (d), (e), and (f) show a portion of the reconstructed image in normal recording at the end of recording (beginning of the read–out), after 45 minutes of continuous read–out, and after 80 minutes of continuous read–out, respectively. The details of the experiments are described in the text.

It can be concluded from Figures 4.9 and 4.10 that two–center holographic recording has an advantage over normal recording by suffering much less from fanning. It is important to note that the effect of fanning in two–center recording with red light would be even less due to the smaller sensitivity of holographic recording from Fe traps at red light.

4.5 Multiplexing holograms in two–center recording

In multiplexing many holograms, we need a recording schedule to equalize the diffraction efficiencies of all holograms. This is due to the fact that each hologram is partially erased during recording of the subsequent holograms. Therefore, we need to record the earlier holograms longer than the later ones. There is a well–known recording schedule for the case where recording and erasure dynamics of a single hologram can be represented by mono–exponential formulas [73]. In this type of dynamics, the hologram strength (A) can be represented by

$$\sqrt{\eta} = A_0[1 - \exp(-t/\tau_r)] \,, \tag{4.21}$$

during recording and by

$$\sqrt{\eta} = A_1 \exp(-t/\tau_e)] \,, \tag{4.22}$$

during erasure. Here, A_0, A_1, τ_r, and τ_e are saturation hologram strength, hologram strength at the beginning of the erasure, recording time constant, and erasure time constant, respectively. Multiplexing holograms using incremental recording has also been investigated for mono–exponential recording and erasure dynamics [84, 85]. In this multiplexing scheme, holograms are recorded subsequently for the same short time. After recording the last hologram for this short time, we go back to the first hologram to start the next cycle of recording all holograms for a short time. Strong

holograms with equal diffraction efficiencies can be recorded using this recording scheme after many such cycles.

In two–center recording, however, the erasure curves are not mono–exponential and therefore a modified recording schedule must be employed. In this section, we propose and experimentally demonstrate such a recording schedule for multiplexing many persistent holograms in doubly–doped $LiNbO_3$ with equal diffraction efficiencies. All experiments reported in this section were performed with a 0.85 mm thick congruently melting x–cut $LiNbO_3$ crystal doped with 0.075 wt. % Fe_2O_3 and 0.01 wt. % MnO. The crystal was oxidized so that, initially, all Fe traps are empty, and a portion of the Mn traps are filled. Recording was performed using one sensitizing beam (wavelength 404 nm, intensity 4 mW/cm^2) and two recording beams (wavelength 633 nm, intensity of each beam 300 mW/cm^2, ordinary polarization). All holograms were recorded using transmission geometry. Read–out of the hologram was performed using one of the recording beams. The angle between each recording beam and the normal to crystal surface outside the crystal was 21°, and the grating vector was aligned parallel to the c axis of the sample. Figure 4.11 shows the recording and read–out curve for this crystal.

4.5.1 Dynamics of recording and erasure in two–center recording

When multiple holograms are recorded using two–center recording, each hologram is erased by both sensitizing and recording beams during the recording of subsequent holograms. We performed a series of recording and erasure experiments to assess the dynamics of the processes and to measure the time constants involved. Erasure is performed by the UV light and one of the red beams to get information about the erasure of a hologram while subsequent holograms are recorded. Experimental results for 4 cycles of recording and erasure are depicted in Figure 4.12. The experimental conditions are as described above. The first recording curve looks different than the rest. This is due to the UV pre–exposure of the sample before the experiment. It

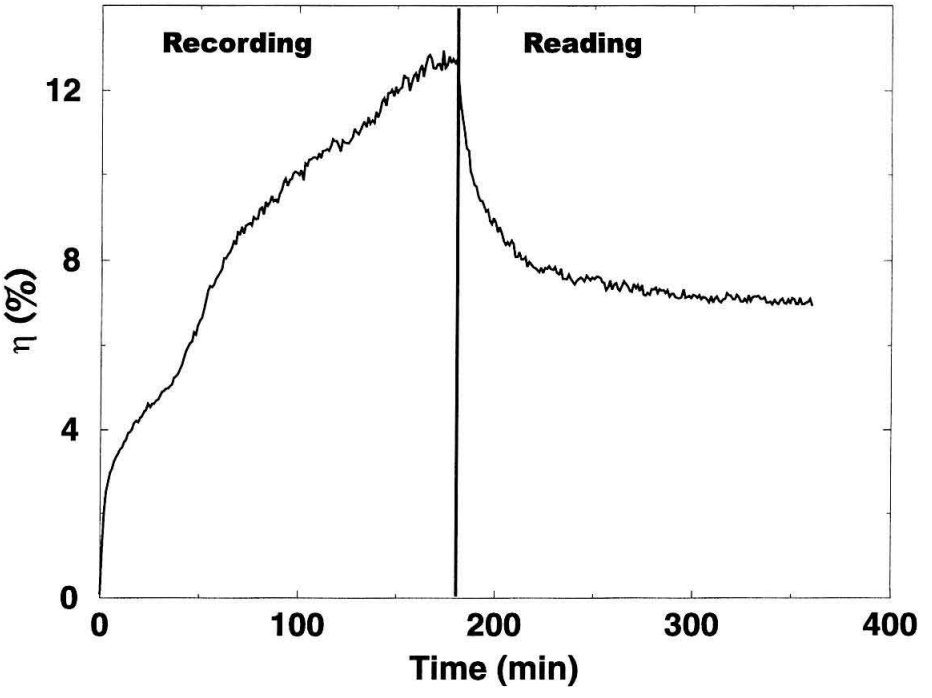

Figure 4.11: Recording and read-out curve for a plane–wave hologram in a 0.85 mm thick $LiNbO_3$:Fe:Mn crystal. The crystal was homogeneously pre–exposed to UV light for at least one hour before the experiment. Then a plane–wave hologram was recorded using two red beams (wavelength 633 nm, intensity of each beam 300 mW/cm^2) with simultaneous presence of the UV beam (wavelength 404 nm, intensity 4 mW/cm^2). The hologram was then read–out by one of the recording beams.

results in a larger electron concentration in the Fe traps than the steady–state value (which is due to the simultaneous presence of UV and red, not UV only). This yields a faster initial recording. The recording curves can be approximated by mono–exponential formulas as

$$\sqrt{\eta} = A_0[1 - \exp(-t/\tau_r)]. \tag{4.23}$$

The erasure curves can be approximated by bi–exponential formulas as

$$\sqrt{\eta} = A\exp(-t/\tau_{e1}) + B\exp(-t/\tau_{e2}). \tag{4.24}$$

In these equations, η is the intensity diffraction efficiency of the hologram, τ_r is the recording time constant, and τ_{e1} and τ_{e2} are the two erasure time constants. Typical mean–square errors for the recording and erasure fits are 2×10^{-8} and 4×10^{-9}, respectively. The bi–exponential behavior of the erasure is due to the fact that the overall space–charge pattern is the sum of the two space–charge patterns in Fe and Mn centers. The space–charge pattern in Fe centers gets erased (and transferred to Mn centers) faster than the portion in Mn centers due to the presence of the strong red light. When the whole space charge pattern settles down in Mn centers, the erasure is performed more slowly as only UV light can excite electrons from these centers to the conduction band for erasure. Figure 4.13 shows the effect of different erasure mechanisms. Three different erasure curves after recording a plane–wave hologram to saturation are depicted in Figure 4.13. These three mechanisms are erasure with UV and one red beam, erasure with UV only, and partial erasure by red light to a steady state and then final erasure by UV only. The curves are normalized to result in the same starting point for all three curves. As Figure 4.13 shows, for erasure with red light, only part of the hologram is erased due to the transfer of electrons from Fe to Mn centers. This partial erasure can not be represented very well by a mono–exponential formula due to the bleaching of Fe centers by red light. The average electron concentration in Fe centers becomes smaller and smaller with time during red illumination resulting in slower erasure with time. After all electrons are transferred to Mn centers, the remaining hologram can be erased with UV light only, and the

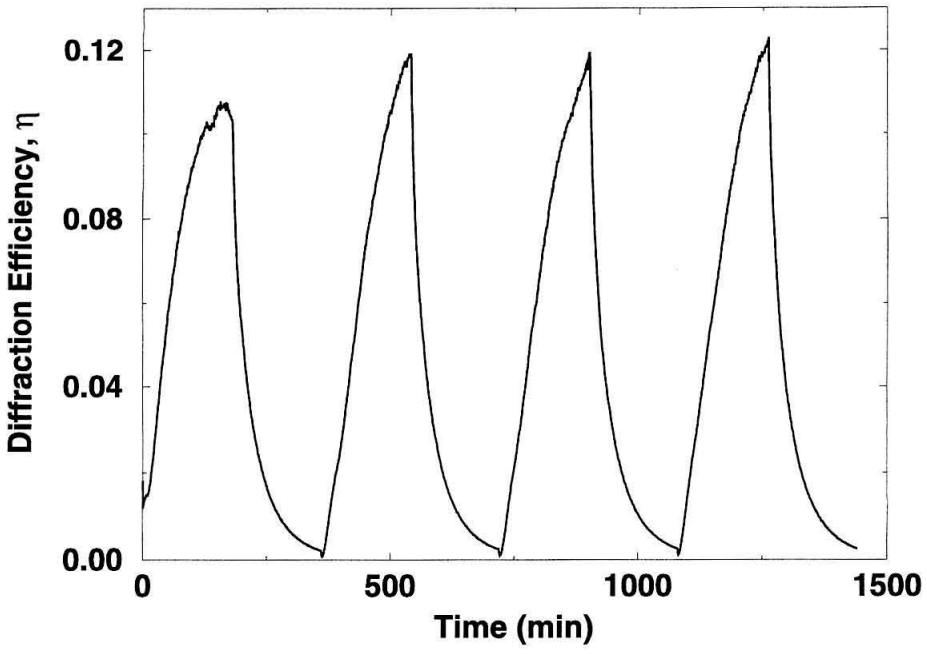

Figure 4.12: Diffraction efficiency η versus time for four cycles of recording and erasure with UV and red light in a $LiNbO_3$:Fe:Mn crystal.

erasure can be represented very well by a mono-exponential formula (typical mean square error of 2×10^{-9}). The hologram can also be erased from the beginning with UV light only resulting in a bi–exponential erasure. However, the erasure behavior is closer to mono–exponential compared to erasure with UV and red. This is because the excitation rate of the electrons from Fe and Mn centers are closer to each other when there is no red light during the erasure.

During hologram multiplexing, each hologram is erased by the UV and red beams that record the subsequent holograms. Therefore, the erasure is bi–exponential, and the conventional recording schedule [73] can not be used. However, the following observation can lead us to a similar recording schedule. When the holograms are read–out at the end of the recording sequence, the electronic charge remaining in Fe centers is transferred to Mn centers resulting in some partial erasure. The erasure during the read–out is different for different holograms in the sequence. The holograms that are recorded earlier have less charge in Fe centers than those recorded later in

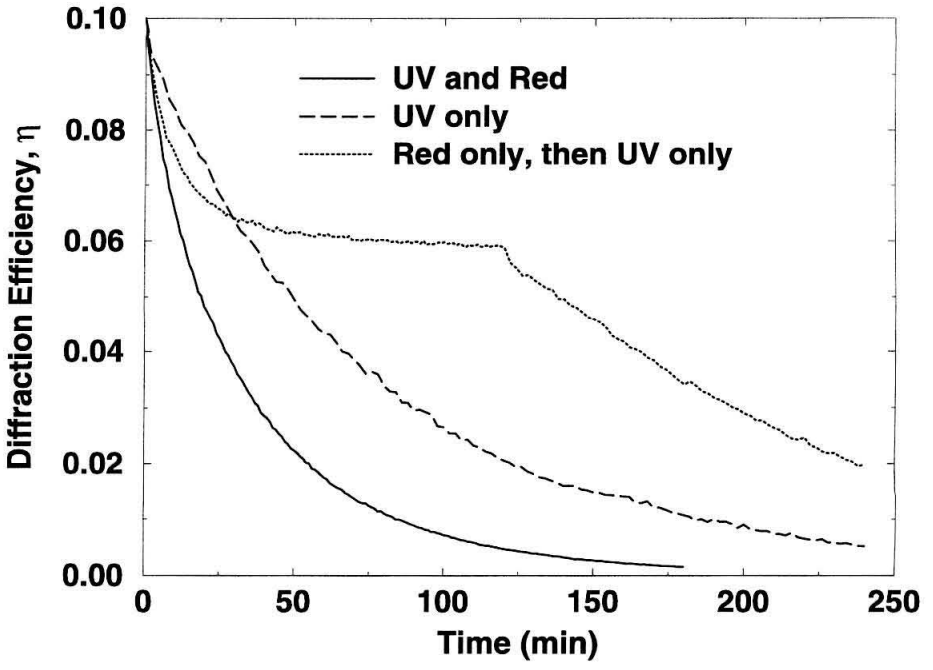

Figure 4.13: Normalized diffraction efficiency η versus time for different erasure mechanisms in two-center holographic recording.

the recording sequence, since the earlier holograms are erased longer than the later ones. Therefore, the later holograms suffer more from partial erasure during read–out. After sufficient read–out, this partial erasure is complete for all holograms and further read–out is non–destructive. If each hologram is the sum of a red–erasable part and a non–red-erasable part, we will have only the non–red–erasable part remaining after sufficient read–out. During the exposure schedule, this part is erased mainly by UV light (with some help from red light) and its erasure is represented by one of the exponentials (the one with larger time constant) in Equation (4.24). Therefore, we can ignore the red–erasable part, represent the effective erasure by a mono–exponential formula, and use the conventional recording schedule [73] to record many holograms. The $M/\#$ is given by

$$M/\# = \beta A_0 \frac{\tau_{e2}}{\tau_r} \tag{4.25}$$

where β represents the partial loss of the hologram due to electron transfer from Fe

to Mn centers. The value of βA_0 can be measured experimentally by recording a grating to saturation and reading it out for a long time with only red light as shown in Figure 4.11. The remaining persistent diffraction efficiency is $(\beta A_0)^2$.

4.5.2 Hologram multiplexing experiments

We used angle multiplexing to record many plane wave holograms in the same volume of the crystal. To do this, we rotated the crystal after recording each hologram and before recording the next one. The angular separation of the holograms in angle multiplexing depends on the selectivity of each hologram. Figure 4.14 shows the angular selectivity curve for one grating. Note that due to non-uniform intensity of the recording and read-out beams and the large absorption of the UV light inside the crystal, the selectivity curve is not a simple $\mathrm{sinc}^2(\theta/\theta_0)$ function. The average angle between the main lobe and the first nulls outside the crystal is 0.15°, resulting in an effective thickness of 0.80 mm for the hologram. This effective thickness is a bit smaller than the real thickness of the crystal (0.85 mm) due to the absorption of the UV beam. Based on Figure 4.14, we chose $\theta = 0.4°$ as the angular separation between consecutive holograms.

The recording and erasure time constants for our crystal can be calculated from Figure 4.12 as $\tau_r = (4520 \pm 270)$ s, $\tau_{e1} = (675 \pm 67)$ s, and $\tau_{e2} = (5780 \pm 115)$ s. The corresponding recording and read–out intensities are given in the caption of Figure 4.11. Note that during multiplexing, τ_{e1} and τ_{e2} are smaller than the values given above since the erasure is performed by the UV light and both recording red beams. The recording schedule is derived by assuming an effective mono–exponential erasure with time constant τ_{e2}. When we multiplex M holograms, the recording time of the n-th hologram, t_n, is given by

$$t_n = \frac{\tau_{e2}}{n + R - 1} \tag{4.26}$$

where $R = \tau_{e2}/t_1$. In designing the experiment, we start with τ_{e2} given above, and try to get the best multiplexing performance by fine–tuning it. The effect of the partial erasure (given by τ_{e1}) is shown in Figure 4.15. Figure 4.15 (a) shows the

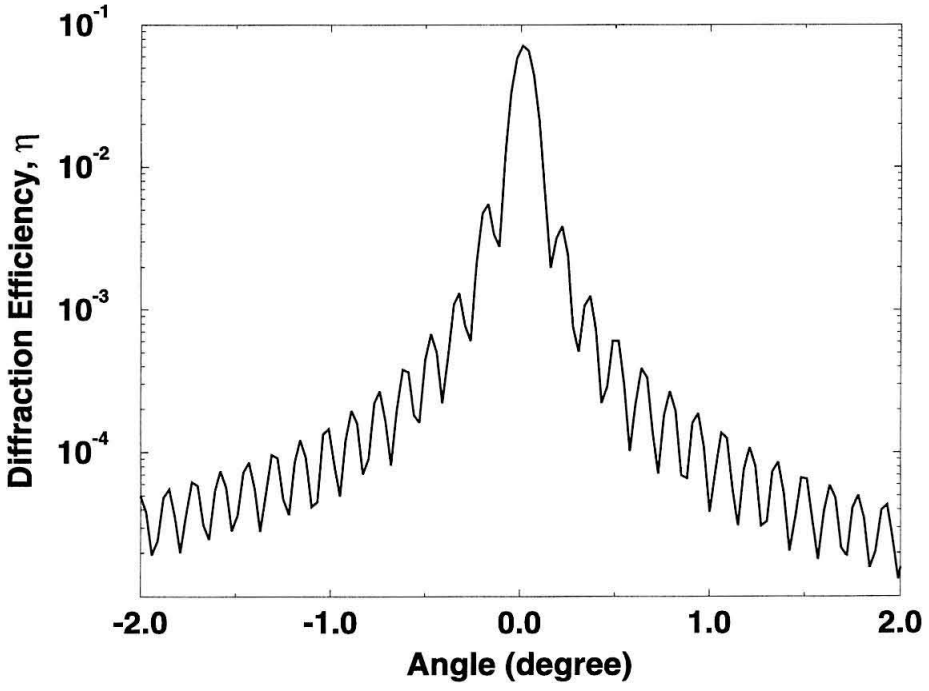

Figure 4.14: Selectivity curve (variation of the diffraction efficiency with the rotation angle of the crystal after recording) for a plane–wave hologram recorded in a $LiNbO_3$:Fe:Mn crystal.

diffraction efficiency vs. angle for 50 plane–wave holograms right after recording all holograms, while Figure 4.15 (b) depicts the same curve after 1 hour of read-out with red light. Note that the partial erasure due to read–out occurs mainly for the last few holograms. We used $\tau_{e2} = 5000$ s and $t_1 = 2500$ s for this experiment. We also measured $\beta A_0 = \sqrt{0.07} = 0.26$ from Figure 4.11. Putting these values in Equation (4.25), we get $M/\# = 0.29$. Based on this $M/\#$, we expect the diffraction efficiency of each hologram to be $\eta = (\frac{M/\#}{M})^2 = 3.2 \times 10^{-5}$, which is in good agreement with the experimental results.

To confirm the improvement of the $M/\#$ by recording with green light as suggested in Section 4.2, we multiplexed 50 plane–wave holograms using the proposed recording schedule. The results are shown in Figure 4.16. The intensity of each recording beam (wavelength 514 nm) was 17 mW/cm^2, and that of the sensitizing beam (wavelength 404 nm) was 3.8 mW/cm^2. After recording all holograms, the crystal was illuminated with one of the recording beams for 2 hours before measuring the diffraction efficiency of each hologram (shown in Figure 4.16). From Figure 4.16, we can calculate $M/\# = 0.4$. From Figure 4.2, the diffraction efficiency of a single hologram recorded with UV and green after sufficient read–out is about $0.1 \simeq (0.33)^2$. Therefore, we would expect an $M/\#$ of at least 0.33. The difference between this value and the measured value of 0.4 from Figure 4.16 is due to the asymmetry between recording and erasure time constants. Using extraordinary polarization for the recording beams, we obtain $M/\# \simeq 1.1$ for a 0.85 mm thick crystal.

4.5.3 Hologram multiplexing using incremental recording

The incremental recording method can also be used for the doubly–doped material by the same observation as before, i.e., each hologram at a specific time is the sum of a red–erasable part (A_e) and a non–red–erasable part (A_{ne}). For multiplexing M holograms, we can represent these portions of each hologram after the $(n+1)$-th recording cycle as

$$A_e(n+1) = \beta A_0[1 - \exp(-t_0/\tau_r)] + A_e(n)\exp(-Mt_0/\tau_{e1}) \qquad (4.27)$$

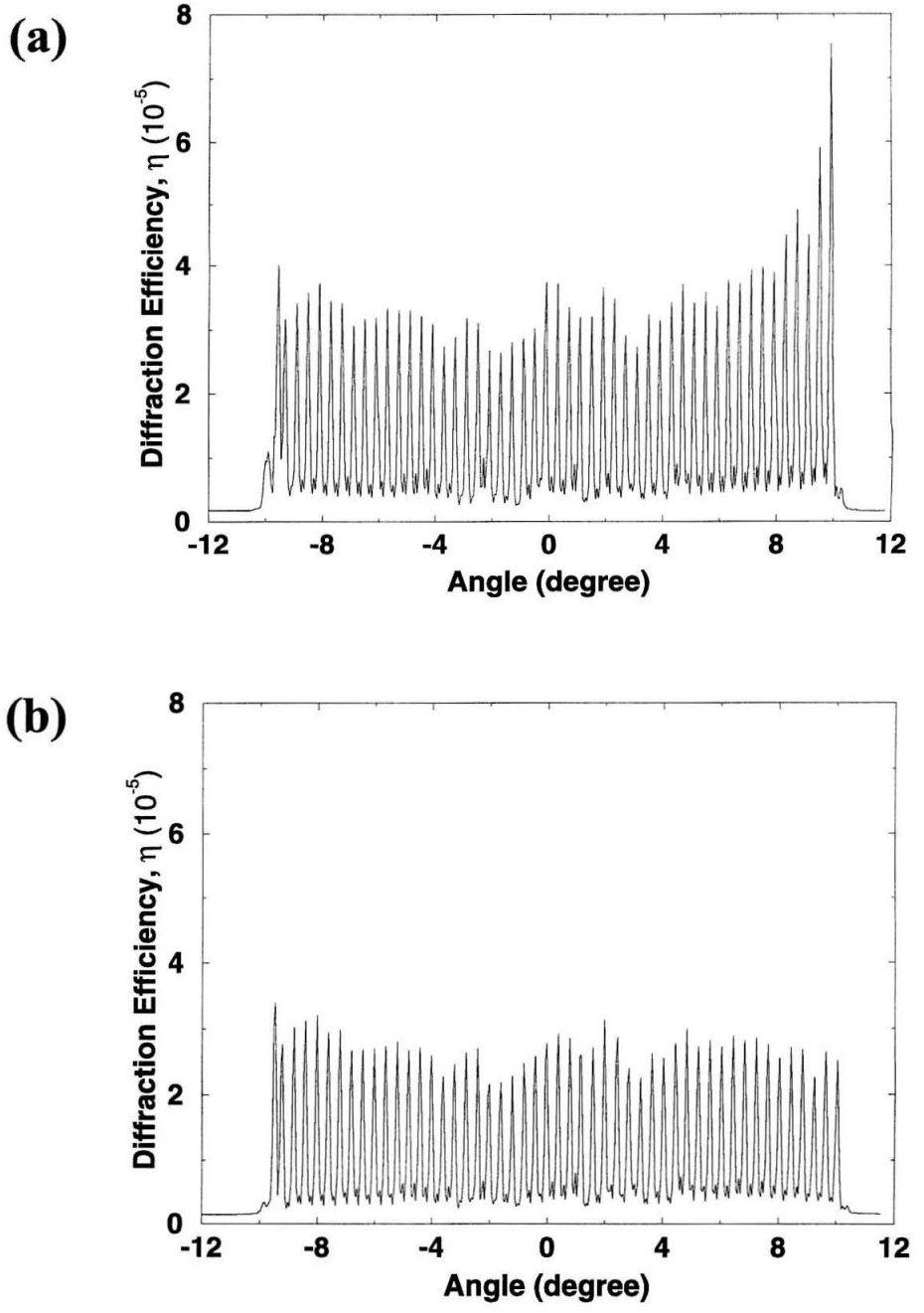

Figure 4.15: Diffraction efficiency η versus angle for 50 angle–multiplexed holograms (a) at the end of recording (no read-out), and (b) after 1 hour read-out (exposure by one red beam). Recording was performed by one UV and two red beams. The details of the experiment are described in the text.

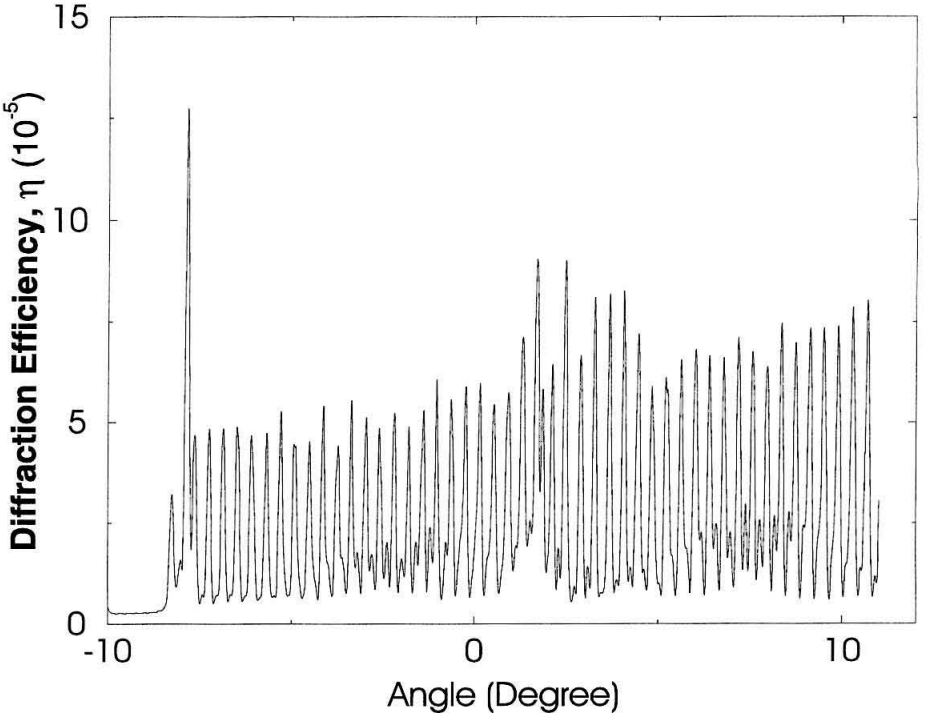

Figure 4.16: Diffraction efficiency η versus angle for 50 angle–multiplexed holograms after 2 hours of continuous read-out (exposure by one green beam). Recording was performed by one UV and two green beams. The details of the experiment are described in the text.

$$A_{ne}(n+1) = \gamma A_0[1 - \exp(-t_0/\tau_r)] + A_{ne}(n)\exp(-Mt_0/\tau_{e2}) \qquad (4.28)$$

where t_0 and A_0 are recording time for each hologram in one cycle and saturation value of $\sqrt{\eta}$, respectively. The erasable and non–erasable portions of a hologram are represented by β and γ, respectively. Since the erasable portion is erased after sufficient read–out, we design the incremental recording based on Equation (4.28) which is identical to the equation representing incremental recording in a conventional (single dopand) photorefractive crystal. Therefore, the conventional incremental recording [84] can be employed.

4.6 Conclusions

We showed that the sensitivity of two–center holographic recording in $LiNbO_3$:Fe:Mn crystals can be improved by at least one order of magnitude through using shorter wavelength (514 nm) for recording beams. Using 514 nm for recording causes a partial loss in persistence due to the small sensitivity of Mn traps at this wavelength. However, the remaining persistence is still acceptable for all practical purposes.

We showed that increasing electron mobility by using either stoichiometric or Mg doped crystals is not a good idea for improving sensitivity. Using these crystals in either normal or two–center recording in transmission geometry results in a big loss in $M/\#$ without improving sensitivity. In addition, using stoichiometric or Mg doped $LiNbO_3$ crystals in two–center recording can result in a big loss in persistence due to the reduction in the asymmetry between recording and erasure mechanisms. Therefore, it is recommended to use only congruently melting crystals in both normal and two–center recording.

We showed that the effect of fanning in two–center recording is much lass than that in normal recording. This is due to the presence of incoherent sensitizing beam during recording and lack of sensitivity to reading beam during read–out (except for the initial reading interval).

Finally, we demonstrated that the conventional recording schedule can be used for

multiplexing holograms using two–center holographic recording method if the correct erasure time constant is used. Such a recording schedule results in holograms with equal diffraction efficiencies after sufficient read-out. Using the appropriate erasure time constant, we can also use the conventional incremental recording strategy to record multiple holograms with equal diffraction efficiencies in two–center recording.

Chapter 5 Comparison of two–step and two–center holographic recording methods

5.1 Introduction

In previous chapters we discussed two important strategies (two–step and two–center recording) for persistent holographic recording in $LiNbO_3$ crystals. The basic ideas of both strategies are the same: recording is performed by the presence of a sensitizing (or gating) beam and two recording beams. A strong hologram can not be recorded without the presence of the sensitizing beam. Therefore, we could consider both methods as two versions of the two–color gated recording method. To obtain persistence in gated recording, it is necessary to have two sets of traps. The deeper traps are the final storage sites for the space–charge field. The electrons that are initially in the deeper traps are transferred to the shallower traps by the sensitizing beam. The hologram is recorded by the recording light which excites the electrons in shallower traps to the conduction band.

Although both the two–step and the two–center recording methods use the same principles for persistent holographic recording, they have different characteristics as they use different types of traps. Both traps in two–center recording are due to impurities (for example Fe and Mn traps in $LiNbO_3$), while either the shallower traps or both traps in two–step recording are due to intrinsic polarons or bipolarons. In this chapter, we discuss the major differences between the performance characteristics of the two methods. We first consider the qualitative theoretical differences between the two methods by using a general two–center model that can be applied to both methods with different parameters. We then compare the performance of different versions of the two methods published in the literature [61, 62, 64, 65, 80, 81], and comment on the reasons for those differences.

5.2 General two–center model

In this section, we compare the performance characteristics of two–center recording in a $LiNbO_3$:Fe:Mn crystal with those of two–step recording in a $LiNbO_3$:Fe crystal (with shallower traps being due to Nb_{Li} polarons). Our goal is to find the conceptual differences between the methods rather than comparing the exact numbers. To evaluate the parameters of the two methods, we use a model similar to the ones discussed in Chapters 2 and 3.

The energy band diagram along with possible electron transitions in two-color gated recording is depicted in Figure 5.1. The main mechanisms that we should explain are sensitization, recording, and the dark depopulation of the shallow traps (electron transfer from the shallow traps to the deep ones without light intervention).

The main goal in sensitization is electron transfer from the deep traps to the shallow ones. This can be done either directly (transition 1) or via the conduction band (transitions 2 and 7) as shown in Figure 5.1. The relative strengths of these sensitization paths depend on the concentrations of the deep and shallow traps, their relative absorption cross sections and electron recombination coefficients, and sensitization light intensity. For two–step recording in a congruent $LiNbO_3$ crystal doped with a fair amount of iron the direct pathway is more important, while for nominally undoped stoichiometric $LiNbO_3$ the indirect pathway might become dominant due to smaller polaron concentrations. On the other hand, the direct electron transition between the traps is negligible in two–center recording in a $LiNbO_3$:Fe:Mn crystal due to the very small doping levels that can be practically used.

Recording is performed from the shallow traps through electron transfer to the conduction band induced by the recording light. These electrons then move in the conduction band and they are trapped by deeper and shallower traps (transitions 8, and to some degree 7 in Figure 5.1). The relative strengths of the holograms recorded in the deeper and the shallower traps depend on the properties of the traps as mentioned for the sensitization processes. In two–center recording, the strength of the hologram recorded in the shallower traps is comparable to that recorded in the

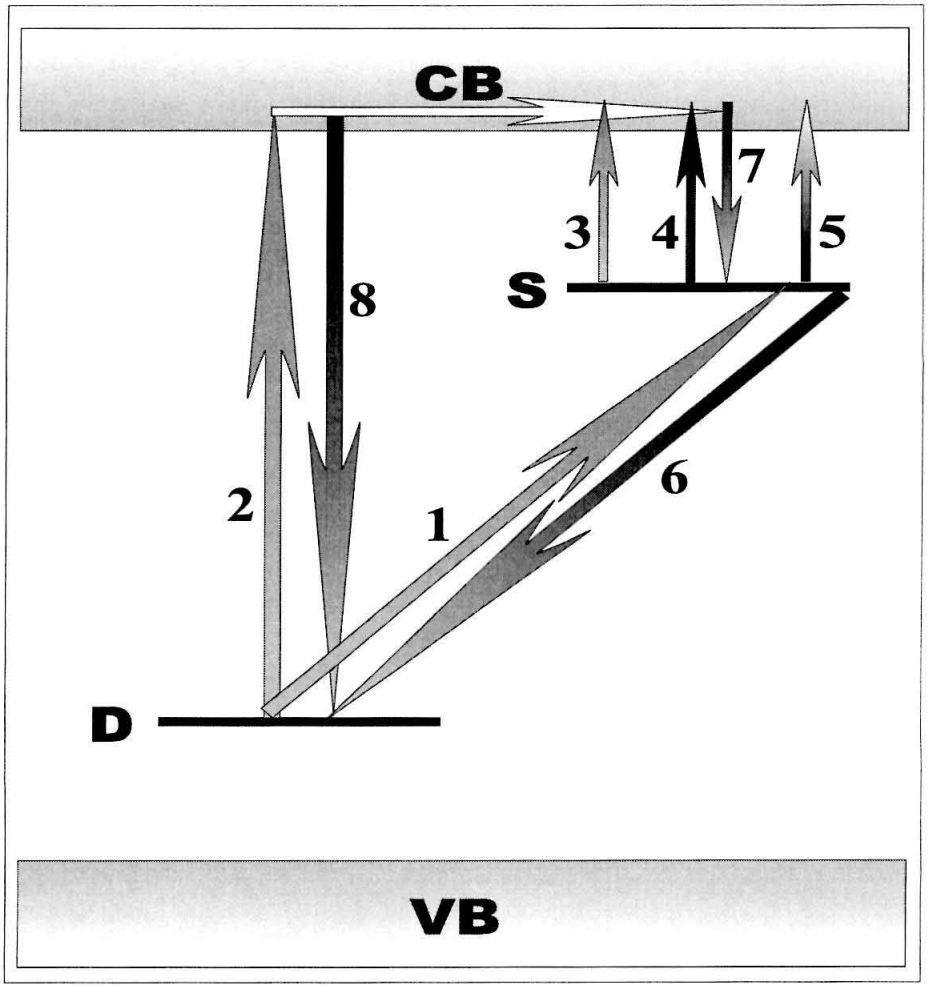

Figure 5.1: Energy band diagram and possible electron transitions for two-color gated holographic recording. Transitions 1, 2, and 3 are caused by the sensitizing beam, and transition 4 by the recording beams. Transition 5 is caused by thermal excitation, and all other transitions occur in dark without light assistance. VB, CB, D, and S stand for valance band, conduction band, deep trap, and shallow trap, respectively.

deep traps. On the other hand, the hologram is mainly recorded in the deeper traps in two–step holographic recording in a congruently melting $LiNbO_3$ crystal. Using a near stoichiometric, reduced and undoped $LiNbO_3$ crystal in two–step recording might result in comparable strengths of the holograms recorded in the shallower and deeper traps, especially when bipolarons with small concentration are used as deeper traps. The portion of the hologram recorded in the shallow traps is finally transferred to the deep traps and combined with the hologram already recorded there. This transfer is performed by the read–out beam during reading of the hologram in two–center recording, while it is performed by dark depopulation of the shallow traps (for example, by thermal excitation) in two–step recording.

Finally, we should consider the dark mechanisms (those that are present regardless of the presence of light). These mechanisms are negligible in two–center recording at room temperature since both traps are considerably deep in the band gap of $LiNbO_3$. On the other hand, the polaron levels in two–step recording are depopulated in dark (either by direct electron transfer between shallower and deeper traps or via the conduction band by thermal excitation) resulting in a short lifetime for the electrons in these shallow polaron traps. The lifetime of the polaron states could be from microseconds to milliseconds and even seconds depending on the material growth and temperature. The dark mechanisms could also be divided into direct (transition 6 in Figure 5.1) and indirect via the conduction band due to thermal excitations (transitions 5 and 8 in Figure 5.1). The light-assisted depopulation of the shallow traps caused by the sensitizing light and the dc part of the recording light is also present (combination of transitions 3 or 4 with transition 8 in Figure 5.1) in both methods. Again, the relative strength of the different mechanisms depends on the concentrations and the properties of the shallow and deep traps and the light intensities involved. Temperature is also important for the thermal excitation mechanism (transition 5 in Figure 5.1) in two–step recording. For example, the direct mechanism (transition 6 in Figure 5.1) is the major cause for the dark depopulation of the shallow traps in two–step recording in a congruently melting $LiNbO_3$:Fe crystal, while the dark depopulation mechanism via the conduction band by thermal excitation is the dominant

one for nominally undoped stoichiometric $LiNbO_3$ at room temperature. As we will see in the rest of this chapter, these differences between the positions of the traps in the band gap and the dominant mechanism for charge transfer between the traps (either direct or via the conduction band) result in the different characteristics of the two methods.

The basic set of equations for two–color gated holographic recording can be written using the different transitions in Figure 5.1 as

$$\begin{aligned}
\frac{\partial N_{\mathrm{D}}^{-}}{\partial t} &= -[q_{\mathrm{D}} s_{\mathrm{D}} + q_{\mathrm{DS}} s_{\mathrm{DS}} (N_{\mathrm{S}} - N_{\mathrm{S}}^{-})] I_{\mathrm{S}} N_{\mathrm{D}}^{-} \\
&\quad + (\gamma_{\mathrm{S}} n + \gamma_{\mathrm{SD}} N_{\mathrm{S}}^{-})(N_{\mathrm{D}} - N_{\mathrm{D}}^{-}) \,, \qquad (5.1) \\
\frac{\partial N_{\mathrm{S}}^{-}}{\partial t} &= -[\beta_{\mathrm{S}} + q_{\mathrm{S,S}} s_{\mathrm{S,S}} I_{\mathrm{S}} + q_{\mathrm{S,R}} s_{\mathrm{S,R}} I_{\mathrm{R}} + \gamma_{\mathrm{SD}} (N_{\mathrm{D}} - N_{\mathrm{D}}^{-})] N_{\mathrm{S}}^{-} \\
&\quad + (\gamma_{\mathrm{S}} n + q_{\mathrm{DS}} s_{\mathrm{DS}} I_{\mathrm{S}} N_{\mathrm{D}}^{-})(N_{\mathrm{S}} - N_{\mathrm{S}}^{-}) \,, \qquad (5.2) \\
j &= e\mu n E + \kappa_{\mathrm{D}} N_{\mathrm{D}}^{-} I_{\mathrm{S}} + \kappa_{\mathrm{S,S}} N_{\mathrm{S}}^{-} I_{\mathrm{S}} + \kappa_{\mathrm{S,R}} N_{\mathrm{S}}^{-} I_{\mathrm{R}} + k_{\mathrm{B}} T \frac{\partial n}{\partial x} \,, \qquad (5.3) \\
\frac{\partial j}{\partial x} &= -e \left(\frac{\partial N_{\mathrm{D}}^{-}}{\partial t} + \frac{\partial N_{\mathrm{S}}^{-}}{\partial t} + \frac{\partial n}{\partial t} \right) \,, \qquad (5.4) \\
\frac{\partial E}{\partial x} &= \frac{-e}{\epsilon \epsilon_0} (N_{\mathrm{D}}^{-} + N_{\mathrm{S}}^{-} + n - N_{\mathrm{A}}) \,, \qquad (5.5)
\end{aligned}$$

where sensitizing and recording intensities are represented by I_{S} and I_{R}, respectively. The parameters in these equations are similar to those defined in the similar set of equations in Chapter 2. The definitions of the parameters can be obtained by replacing Fe by D, X by S, G by S, and IR by R in Table 2.1 in Chapter 2. The values of the parameters depend on the method. For example, direct electron transfer between the deeper and the shallower traps as well as thermal excitation of electrons from either traps can be neglected in two–center recording. This results in $\gamma_{\mathrm{SD}} = 0$, $q_{\mathrm{DS}} s_{\mathrm{DS}} = 0$, and $\beta_{\mathrm{S}} = 0$ for two–center recording. Other parameters for two–center recording are the same as those in Table 3.1 of Chapter 3 (by replacing Fe with S, Mn with D, and UV with D).

The recording medium in two–step recording is assumed to be a congruently melting $LiNbO_3$:Fe crystal (doped with 0.035 wt.% Fe_2O_3) with shallow traps due to intrinsic Nb_{Li} polarons. The concentration of these shallow polaron levels is assumed

to be 10^{26} m^{-3} unless otherwise stated. We also assume that about 50 % of Fe traps as well as all shallower traps are initially empty. These material properties are very similar to those of the crystal we used in both theoretical simulations and experiments in Chapter 2. The recording medium in the simulations of two–center recording is assumed to be a $LiNbO_3$:Fe:Mn crystal (doped with 0.075 wt. % Fe_2O_3 and 0.01 wt. % MnO). We also assume that all Fe traps as well as 10% of Mn traps are initially empty unless otherwise stated. This is the crystal used in the initial experiments of two–center recording discussed in Chapter 3. In both cases, we assume that a plane–wave hologram is recorded with cw light with ordinary polarization for recording beams. Furthermore, we assume that the intensities of the two recording beams are equal resulting in a modulation depth of 1 for recording intensity I_R. Sensitization and recording wavelengths in two–step recording are assumed to be 532 nm and 1064 nm, respectively, while those in two–center recording are assumed to be 365 nm and 633 nm, respectively. In the simulations, we assume no absorption for either the recording or sensitizing beam in both methods. Although this assumption might be very difficult to fulfill in practice, it gives us an idea about the best performance we could obtain in each case.

To solve Equations (5.1)–(5.5), we assume that the intensity of the sensitizing beam (I_S) is constant, and that of the recording beam (I_R) is a sinusoidal function of space. Therefore, we can use Fourier development to find and solve two sets of equations for the zeroth and first order Fourier components of each variable as we discussed in previous chapters. The details of the solution are exactly the same as those discussed before, and thus, are not presented here.

5.3 Theoretical comparison of two–step and two–center recording methods

In this section, we use the general two–center model to compare the performance characteristics of two–step recording in a congruently melting $LiNbO_3$:Fe crystal with

those of two–center recording in a congruently melting $LiNbO_3$:Fe:Mn crystal. In this comparison, we use the saturation value of the space–charge field as the measure for hologram strength. The saturation value of space–charge field in two–center recording is calculated after sufficient read–out to account for the partial erasure of the hologram during read–out. Note that the saturation space–charge field is linearly proportional to both the saturation change in the index of refraction and the dynamic range parameter ($M/\#$). Therefore, the conclusions about the variation of the saturation space–charge field can be applied to the other two parameters, too.

Figure 5.2 shows typical recording and read-out curves for the two cases. Recording is performed for 100 seconds with the sensitizing and recording beams on. Then the grating is read-out for 200 seconds with one of the recording beams while all other beams are blocked. The intensity of the sensitizing beam is $I_S = 1$ W/cm^2 and the intensity of each recording beam is 2 W/cm^2. Excellent persistence (non–destructive read–out) in both cases along with partial erasure during read–out in two-center recording is evident from Figure 5.2. It can also be seen that two-center recording can result into much higher space–charge field, resulting in better $M/\#$. This is mainly due to the lack of dark depopulation of the shallow traps in two-center recording.

5.3.1 Effect of the concentrations of deeper and shallower traps

To see the effect of the deeper trap concentration (which can be easily varied in both cases), we assume that it is varied in a long but practical range while all other parameters are kept constant, and calculate the final saturation space–charge field for both cases. We also assume that a fixed portion of the deeper traps is occupied by electrons initially, while all shallow traps are initially empty. The results are depicted in Figure 5.3. Due to large concentration of polarons assumed (10^{26} m^{-3}), and the strong dark depopulation effects, the saturation field in the two–step method slightly increases by increasing the concentration of the deeper traps, getting close to

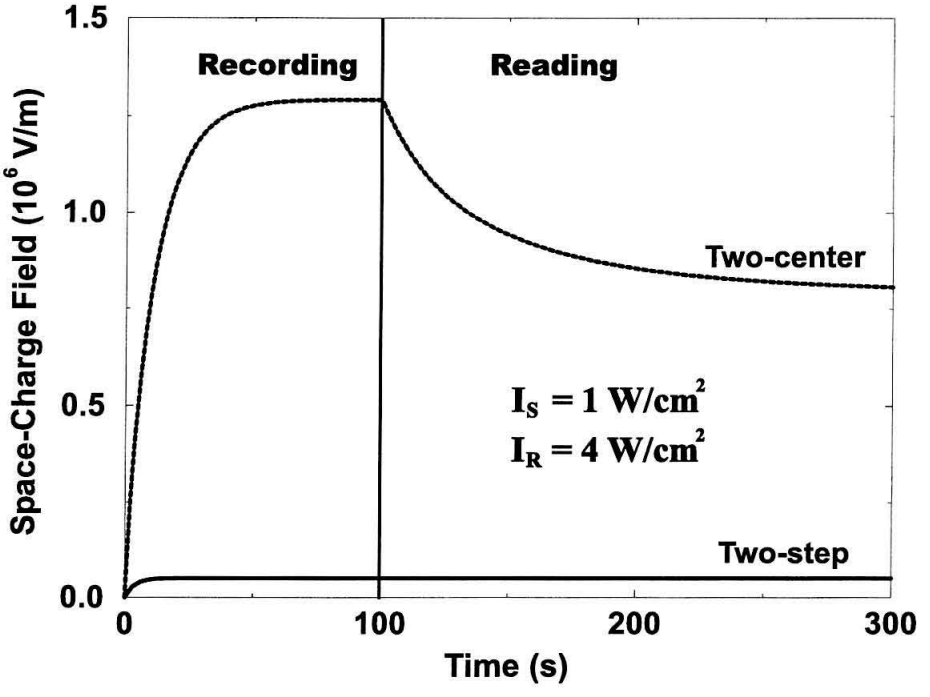

Figure 5.2: Theoretical recording and read-out curves for two-step and two-center methods. Recording is performed for the first 100 seconds where sensitizing and recording beams are all present. For the next 200 seconds, the sensitizing beam and one of the recording beams are blocked and read-out is performed with the other recording beam. The intensity of the sensitizing beam is $I_S = 1$ W/cm^2, and the intensity of each recording beam is 2 W/cm^2 ($I_R = 4$ W/cm^2).

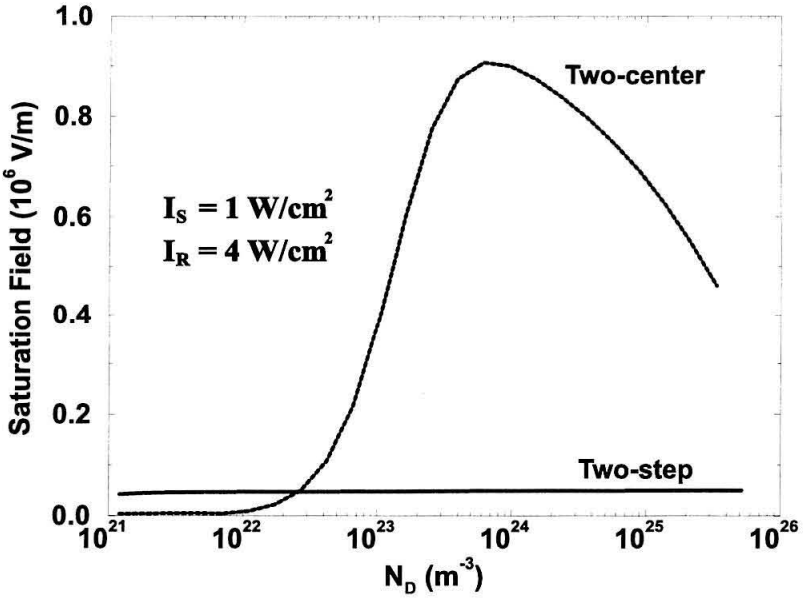

Figure 5.3: Variation of final (persistent) saturation space–charge field with deeper trap concentration (N_D) for two-step and two–center recording methods. The concentrations of shallower traps are fixed at $N_S = 10^{26}$ m^{-3} and $N_S = 2.5 \times 10^{25}$ m^{-3} for two–step and two–center recording, respectively.

a saturation at very high doping concentrations. Therefore, adding more deep traps means adding more electrons for recording resulting in a stronger hologram until we get to saturation (although it might occur at non-practical doping levels). The reason for this saturation is that increasing the concentration of the deeper traps increases also the dark depopulation rate due to the presence of more empty deep traps (a fixed portion of deep traps are initially empty).

The situation in the two-center method is different. The main competition there is between the two traps to capture the electrons from the conduction band. Each capture rate depends on the recombination coefficient of the traps involved (usually larger for the deeper traps), the concentration of empty traps, and the concentration of electrons in the conduction band. Although increasing the concentration of the deeper traps results in increase of the sensitization rate by sending more electrons to the conduction band, it also increases the probability of electron capture by the deep traps (since a fixed portion of the deeper traps are empty), and therefore, decreases

the sensitization efficiency. Due to this trade off, an optimum is expected, which occurs within practical doping levels.

Figure 5.4 shows the dependence of saturation space–charge field on the concentration of the shallower traps. Note that the curve for two–center recording is stopped at $N_S = 5 \times 10^{25}$ m^{-3} (corresponding to 0.15 wt. % Fe_2O_3 doping) that is the practical limit of useful Fe concentration in $LiNbO_3$. However, the concentration of polarons (shallower traps in two–step recording) can be easily in the order of $N_S \sim 10^{26}$ m^{-3} in congruently melting $LiNbO_3$. The concentration of polarons in $LiNbO_3$ can be varied by changing the degree of stoichiometry of the crystal. It is evident from Figure 5.4 that higher concentration of shallower traps in both two–center and two–step recording results in the recording of a stronger hologram. This is due to the fact that the electron concentration in the shallower traps increases with increasing the concentration of these traps. Since recording is performed by using electrons from shallower traps, higher concentration of the shallower traps results in the recording of a stronger hologram.

5.3.2 Effect of sensitizing and recording intensities

Figure 5.5 shows the variation of the saturation space–charge field with recording and sensitizing light intensities. From Figure 5.5(c) it becomes obvious that in two-center recording, the saturation field depends only on the intensity ratio and not on the absolute intensities. This is due to the fact that too high recording intensities result in the bleaching of the shallow traps by the dc light while too high sensitizing beam intensities result in the strong erasure of any possible hologram. In other words, the electrons in the shallow traps should be used by the nonuniform part of the recording intensity to result in a hologram. There are three other mechanisms competing with this desirable mechanism, namely bleaching of the shallow traps by the dc part of the recording intensity pattern, depopulation of the shallow traps by the sensitizing beam, and erasure of the holograms in both traps by the sensitizing beam. The optimum intensity ratio results in the best balance between the desirable

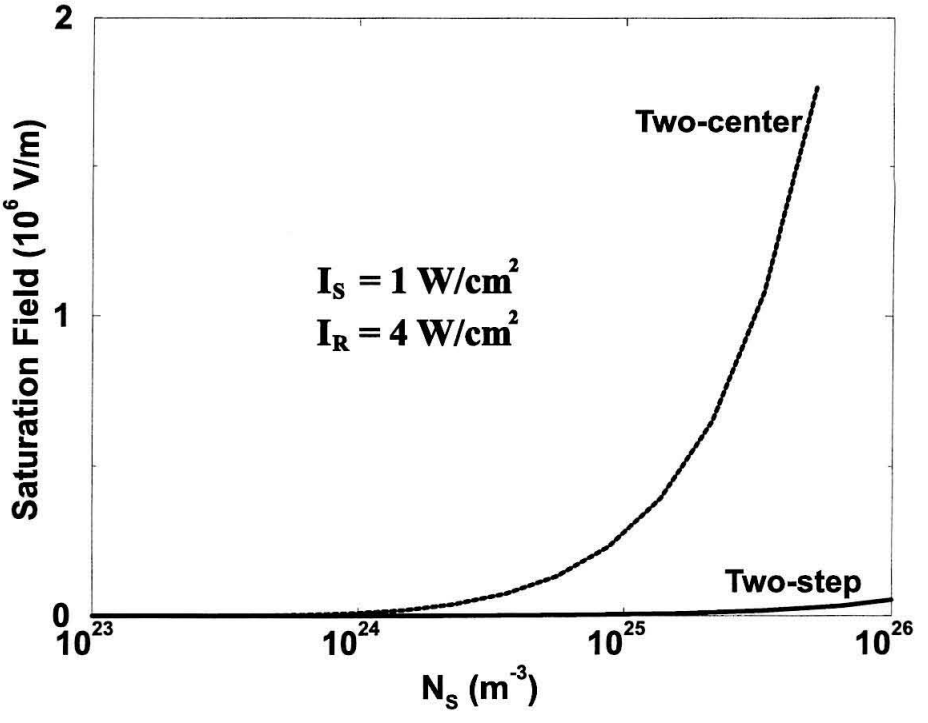

Figure 5.4: Variation of final (persistent) saturation space–charge field with shallower trap concentration (N_S) for two-step and two–center recording methods. The concentrations of deeper traps are fixed at $N_D = 1.2 \times 10^{25}$ m^{-3} and $N_D = 3.8 \times 10^{24}$ m^{-3} for two–step and two–center recording, respectively.

and undesirable mechanisms.

The dominant processes are totally different for two–step recording. Due to the strong dark depopulation mechanisms, increasing recording and sensitizing beam intensities will both increase the saturation field as they both help getting more electrons for the desirable mechanism in competition with all undesirable mechanisms dominated by the dark depopulation processes.

Besides having much higher diffraction efficiencies and therefore higher $M/\#$, two-center recording has another major advantage over two–step recording as suggested by Figure 5.5(c): there is no intensity threshold for two-center recording, but there is always one for two–step recording. In other words, we can record strong hologram with very low sensitizing and recording intensities using two–center recording if we use the correct sensitizing to recording intensity ratio. However, it is not possible to record a strong hologram in two–step recording with sensitizing and recording intensities below some threshold. This major problem in two–step recording is due to the presence of the dark depopulation mechanisms in this method. It is now clear that the main problem of two–step recording is dark depopulation of the shallower traps that can be rephrased as short lifetime of the shallower traps.

It is important to note that two–step recording can have higher saturation space–charge field (or $M/\#$) at very high recording intensities as shown in Figure 5.5 (b). The strength of the dark depopulation of the shallower traps is independent of the recording intensity, while the strength of the electron excitation from the shallower traps to the conduction band (that is essential for holographic recording) is linearly proportional to recording intensity. Therefore, a larger portion of electrons in the shallower traps is used for recording at higher recording intensities resulting in higher saturation space–charge field. Since the concentration of the shallower traps in two–step recording can be huge compared to that in two–center recording, we can record stronger holograms in two–step recording if we use very high recording intensities. To fulfill this possible advantage of two–step recording it is necessary to use a congruently melting $LiNbO_3$:Fe crystal to have both the huge concentration of the shallower traps (polarons) and the dominance of direct electron transfer between deeper and

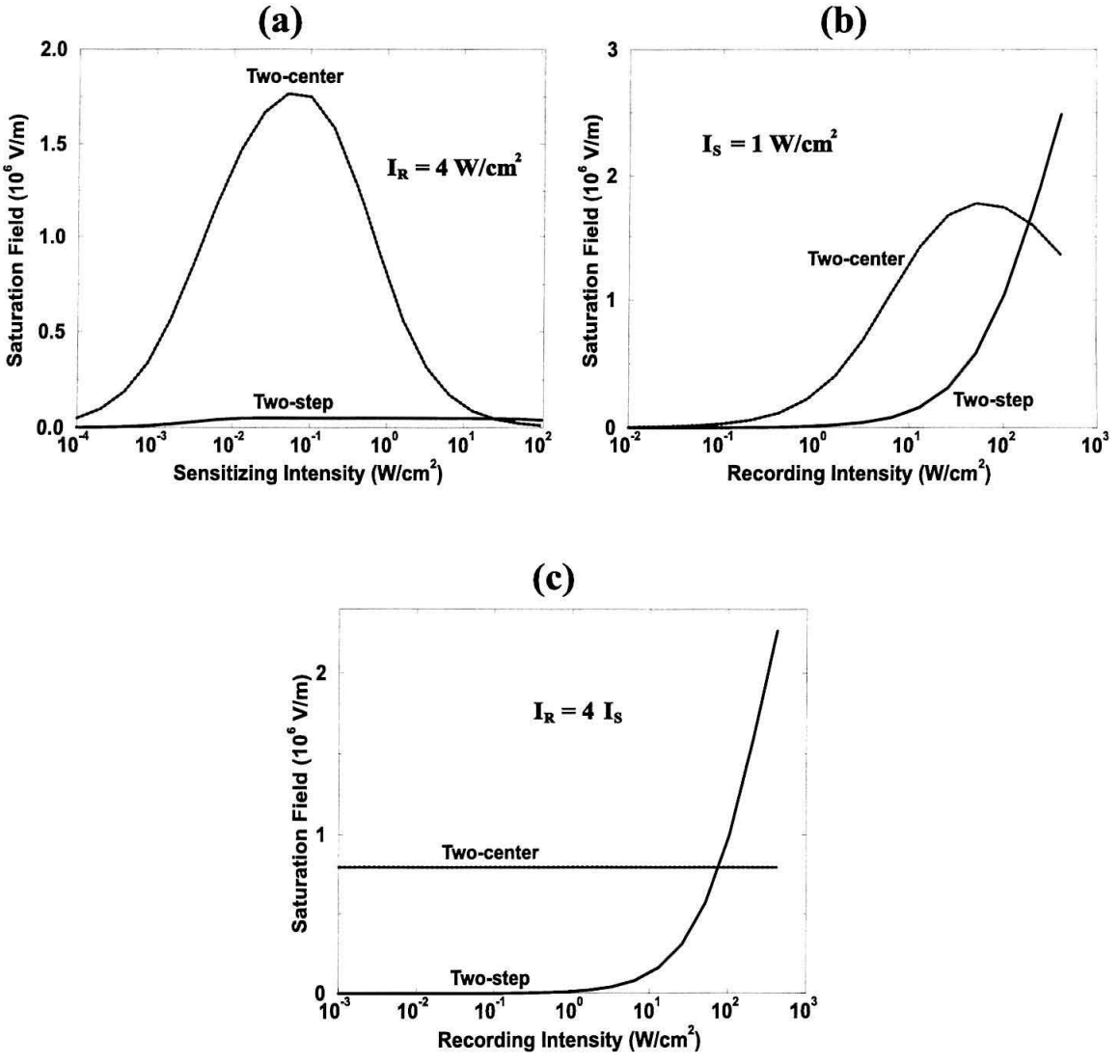

Figure 5.5: Effect of sensitizing and recording beam intensities: (a) variation of final (persistent) saturation space–charge field with sensitizing intensity when each recording beam has a fixed intensity of 2 W/cm^2 ($I_R = 4$ W/cm^2), (b) variation of final saturation space–charge field with total recording intensity when sensitizing beam has a fixed intensity of $I_S = 1$ W/cm^2, and (c) variation of final saturation space–charge field with total recording intensity when the ratio of the total recording intensity to sensitizing intensity is fixed at 4.

shallower traps. Note that without the dominance of direct electron transfer between the traps, electron transfer mechanisms in two–step recording become similar to those in two–center recording, eliminating the increase in saturation space–charge field with increasing recording intensity shown in Figure 5.5 (b) for two–step recording.

5.4 Comparison of experimental results

In this section we compare the experimental results for the performance characteristics of two–color gated recording methods published to date. Since the main focus in all proposed methods is to develop holographic memory systems with as low intensity requirements as possible, we only consider the holographic recording experiments performed with cw light. The experiments for two–center recording are performed by us at Caltech. We also report experimental results for two–step recording published by research groups at IBM [61], Stanford University [62], and Stanford Research Institute (SRI) [63, 64]. The main properties considered in the comparison of different cases are dynamic range parameter ($M/\#$) normalized to the thickness of the recording medium, sensitivity (S), and persistence. All results are normalized for extraordinary polarization of recording and reading beams in transmission geometry. Although widely accepted numerical measures exist for dynamic range and sensitivity, there is no well–defined numerical measure for persistence. Therefore, we report this property by either *excellent* or *acceptable* where *excellent* is used for the cases with very long erasure time constants that allows continuous read–out of the hologram for weeks without considerable erasure, and *acceptable* is used for the cases where one hologram can be read at least a billion times with normal intensities in the range of 100 mW/cm^2 before its diffraction efficiency drops to 50% of its original value. In the next chapter, we define a numerical measure for persistence.

The performance characteristics of different methods at low recording intensities are summarized in Table 5.1. The details about the recording medium, especially the sources of traps suggested by the authors, are also shown in Table 5.1. Numerical results for the values of $M/\#$ and sensitivity were not reported by the research group

at SRI. However, it can be inferred from the other reported results in Refs. [63, 64] that the performance characteristics are not better than those reported by research groups at IBM [61] and Stanford University [62]. The results summarized in Table 5.1 suggest that two–center holographic recording has at least one order of magnitude better sensitivity and two orders of magnitude better $M/\#$ at low recording intensities with much lower sensitizing intensity. This is due to the lack of any intensity threshold (due to the dark depopulation of the shallower traps) in two–center recording as explained before.

Research group	IBM	Stanford	Caltech	Caltech
Recording scheme	Two-Step	Two-Step	Two-Center	Two-Center
Recording material	$LiNbO_3$	$LiNbO_3$	$LiNbO_3$:Fe:Mn	$LiNbO_3$:Fe:Mn
Stoichiometry	stoichiometric	stoichiometric	congruent	congruent
Annealing	highly reduced	highly reduced	oxidized	oxidized
Shallower traps	Polarons	Polarons	Fe	Fe
Deeper traps	Fe/Bipolarons	Bipolarons	Mn	Mn
λ_S (nm)	488	475	404	404
λ_R (nm)	852	800	633	514
I_S (W/cm^2)	1	0.1	0.004	0.004
I_R (W/cm^2)	0.6	10	0.6	0.034
$M/\#/L$ (cm^{-1})	0.03	N/A	2.7	4
S (cm/J)	0.0025	0.002	0.0033	0.07
Persistence	excellent	acceptable	excellent	acceptable
Dark erasure	slow	slow	very slow	very slow
Reference	[61]	[62]	[65]	[79]

Table 5.1: Comparison of the experimental results reported by different research groups for two–step and two–center holographic recording methods at low intensities. Here, λ_S, λ_R, I_S, I_R, and L are sensitizing wavelength, recording wavelength, sensitizing intensity, recording intensity, and the crystal thickness, respectively.

One advantage of two–step recording discussed theoretically in the last section is the possibility of recording strong holograms at high recording intensities. In fact, all good performance results reported in the literature for two–step recording were obtained by using high recording intensities (a few W/cm^2). Therefore, we have summarized the best performance characteristics reported in each case in Table 5.2. As Table 5.2 shows, even with a great deal of optimization of recording material and

Research group	IBM	Stanford	Caltech	Caltech
Recording scheme	Two-Step	Two-Step	Two-Center	Two-Center
I_S (W/cm^2)	1	0.4	0.004	0.004
I_R (W/cm^2)	4	10	0.6	0.034
$M/\#/L$ (cm^{-1})	0.8	0.8	7.5	10
S (cm/J)	0.01	0.015	0.01	0.2

Table 5.2: Comparison of the best experimental results reported by different research groups for two–step and two–center holographic recording methods. Here, I_S, I_R, and L are sensitizing intensity, recording intensity, and the crystal thickness, respectively. Other experimental conditions are the same as those shown in Table 5.1.

recording and sensitizing intensities in different two–step recording strategies, two–center recording still has better performance characteristics with much lower intensity requirements. It is also important to note that there is a lot of room for improvement in two–center recording by using other materials and dopands as we have only tested one material with two dopands ($LiNbO_3$:Fe:Mn).

5.5 Discussion

The impressive reduction in the intensity requirement for two–step recording in recent years [61, 62, 63, 64, 86] is due to the use of reduced nominally undoped near–stoichiometric $LiNbO_3$ crystals. Using near–stoichiometric undoped crystal results in much lower concentrations of both the deeper traps (either Fe or bipolarons) and the shallower traps (polarons). Reducing the crystal decreases the concentration of empty deeper traps by providing more electrons in these traps. The combination of these effects results in a higher average distance between the shallower traps and empty deeper traps, and this results in longer effective lifetime of the electrons in the shallower traps by making depopulation of the shallower traps more difficult. Therefore, better $M/\#$ and sensitivity can be obtained at low intensities. However, this new strategy for two–step recording has some major disadvantages. First of all, the linearity of saturation space–charge field (or $M/\#$) with recording intensity shown in Figure 5.5 (b) goes away at recording intensity of a few W/cm^2 because

this linearity of $M/\#$ with recording intensity is mainly a result of direct electron transfer from the deeper traps to the shallower ones. Reducing the concentration of both traps increases the average distance between the deeper and the shallower traps, thus reducing the strength of this direct electron transfer. As a result, $M/\#$ saturates at lower recording intensities. Therefore, the usage of undoped near–stoichiometric crystals washes out the main and possibly the only advantage of two–step recording.

The second disadvantage of using undoped near–stoichiometric crystals is the very low concentration of both deeper and shallower traps that limits the $M/\#$ and sensitivity that can be obtained as shown in Figures 5.3 and 5.4. In fact, the concentrations of both traps are so low in these materials that we can not expect to obtain better values of $M/\#$ and sensitivity than those reported after a lot of optimization efforts.

Another substantial disadvantage of using stoichiometric materials is the higher dark conductivity of these materials due to larger electron mobility in the conduction band. This reduces the dark storage time of stored holograms. Furthermore, using intrinsic traps like polarons and bipolarons reduces the degrees of freedom in optimizing the performance of the material. The concentration of these traps can not be varied arbitrarily and independently of each other. The energy levels of these traps can not be varied arbitrarily, either. Furthermore, these traps are intrinsic in $LiNbO_3$. If we want to use another crystal, we need to first look for the possibility of having similar intrinsic traps. This reduces the generality of the method.

It is important to note that if we try to further increase the effective lifetime of electrons in the shallower traps (polarons) in two–center recording by reducing the concentrations of the deeper and shallower traps, we will reduce the role of direct electron transfer between the traps to a level where it is no longer the dominant mechanism for sensitization. In this case, the dominant mechanism for electron transfer between the traps is via the conduction band. This makes the dominant mechanisms in two–step recording exactly the same as those in two–center recording. In this case, there is a partial erasure of the hologram during read–out (and even in the dark due to thermal excitation) in two–step recording similar to what exists in two–center recording. Such a partial erasure has been reported in highly reduced undoped near–

stoichiometric $LiNbO_3$ crystals [61]. The main difference remaining between the two methods in this case is that we have a lot of parameters to optimize in the two–center recording, but we do not have that many in two–step recording. Furthermore, there is a dark depopulation mechanism for the shallower traps (through thermal excitation of the electrons to the conduction band) in two–step recording that is not present in two–center recording.

To summarize, it seems that despite impressing recent progress and great optimization efforts in two–step recording using cw light in undoped near–stoichiometric $LiNbO_3$ crystals, the best obtained performance characteristics in two–step recording are at least one order of magnitude below those in the initial results in two–center recording. Furthermore, there is still a lot of room for improving the performance of two–center recording by using other dopands and other materials while further optimization of two–step recording might not be possible.

5.6 Conclusions

We compared the performance characteristics of two–step and two–center holographic recording methods in $LiNbO_3$ crystals both theoretically and experimentally. The best performance characteristics obtained in two–step recording after a lot of efforts for optimization are at least one order of magnitude below those in two–center recording. The performance of two–step recording is limited by dark depopulation of the shallower traps that results in a short effective lifetime for electrons in these traps. Increasing this effective lifetime reduces the intensity threshold required for recording strong holograms in two–step recording at the expense of reducing the highest possible values of $M/\#$ and sensitivity that can be obtained at very high intensities. Moving in the direction of increasing this effective lifetime by using highly reduced undoped near–stoichiometric crystals will finally make two–step recording very similar to two–center recording. This eliminates the only possible advantage of two–step recording, i.e., having better $M/\#$ at very high intensities.

To conclude, it can be said from these comparisons that two–center holographic

recording is the best available method for persistent holographic recording in $LiNbO_3$ crystals, especially at low intensities. Two–center recording is a promising method with still a lot of room for improvement and optimization.

Chapter 6 Potentials of doubly–doped $LiNbO_3$ crystals for holographic recording

6.1 Introduction

In previous chapters we showed that persistent holograms can be recorded in doubly–doped $LiNbO_3$ crystals. We also discussed the performance improvement and optimization of two–center holographic recording in such crystals. For example, we showed that sensitivity can be greatly improved by sacrificing some persistence. The focus in all previous discussions was to keep persistence while optimizing and improving other holographic recording properties. Therefore, all holographic recording experiments were performed with one sensitizing beam and two recording beams. In this chapter we consider the possibility of recording with only two recording beams of the same wavelength (without any sensitizing beam) in doubly–doped $LiNbO_3$ crystals. The goal is to understand and appraise the range of performance characteristics that can be obtained by using doubly–doped $LiNbO_3$ crystals and compare it with that obtained in singly–doped crystals. We also define a quantitative measure for persistence to make the comparison of different cases easier. Finally, we will consider the trade–offs involved in holographic recording in doubly–doped $LiNbO_3$ crystals and show that by using these materials we can span a much larger range of performance characteristics than that in singly–doped $LiNbO_3$ crystals.

6.2 Experiments

We performed experiments with two $LiNbO_3$:Fe:Mn crystals from the same boule each doped with 0.075 wt. % Fe_2O_3 and 0.01 wt. % MnO. Both crystals were first oxidized for 1 hour at 1000 °C in O_2 atmosphere. The crystals were then reduced at 800 °C in

Ar atmosphere for either one hour (XTAL1) or four hours (XTAL2). All Fe traps in XTAL1 are empty while more than 90% of the Mn traps in this crystal are occupied by electrons. On the other hand, all Mn traps as well as a portion of Fe traps are initially occupied by electrons in XTAL2. With this annealing treatment XTAL1 is appropriate for persistent holographic recording (two–center recording) while XTAL2 is good for normal single wavelength recording with destructive read–out.

We performed holographic recording experiments with two plane waves (wavelength 488 nm, intensity of each beam 17 mW/cm^2, ordinary polarization) in XTAL2. Read–out of the hologram was performed with one of the recording beams. The result of this experiment is shown in Figure 6.1 (a). We performed three different recording experiments with XTAL1. First, we recorded a plane wave hologram with two plane waves (wavelength 514 nm, intensity of each beam 17 mW/cm^2, ordinary polarization). Read–out of the hologram is performed with one of the recording beams. The result of this experiment is shown in Figure 6.1 (b). We also performed two different recording and read–out experiments using two–center recording. The sensitizing beam in both experiments was a homogeneous beam from a 100 W UV lamp (wavelength 404 nm, intensity 4 mW/cm^2). Recording was performed with the sensitizing beam and two red beams (wavelength 633 nm, intensity of each beam 300 mW/cm^2, ordinary polarization) in one case and two green beams (wavelength 514 nm, intensity of each beam 17 mW/cm^2, ordinary polarization) in the other case. The results of these two experiments are shown in Figures 6.1 (c) and (d), respectively.

The wide range of performance characteristics shown in Figure 6.1 is very interesting. It is important to note that the crystals used in all four cases depicted in Figure 6.1 are essentially the same as the only difference between XTAL1 and XTAL2 is their oxidation / reduction state. Figure 6.1 (a) shows that recording in a reduced crystal is fast and strong, but read–out erases the hologram very fast. Strong holograms can be recorded with one wavelength (normal recording) in the more oxidized crystal (XTAL1), but recording is very slow. The holograms recorded in such a crystal have good persistence as they can be read–out for a long time before their diffraction efficiency drops too much (Figure 6.1 (b)). Figures 6.1 (c) and

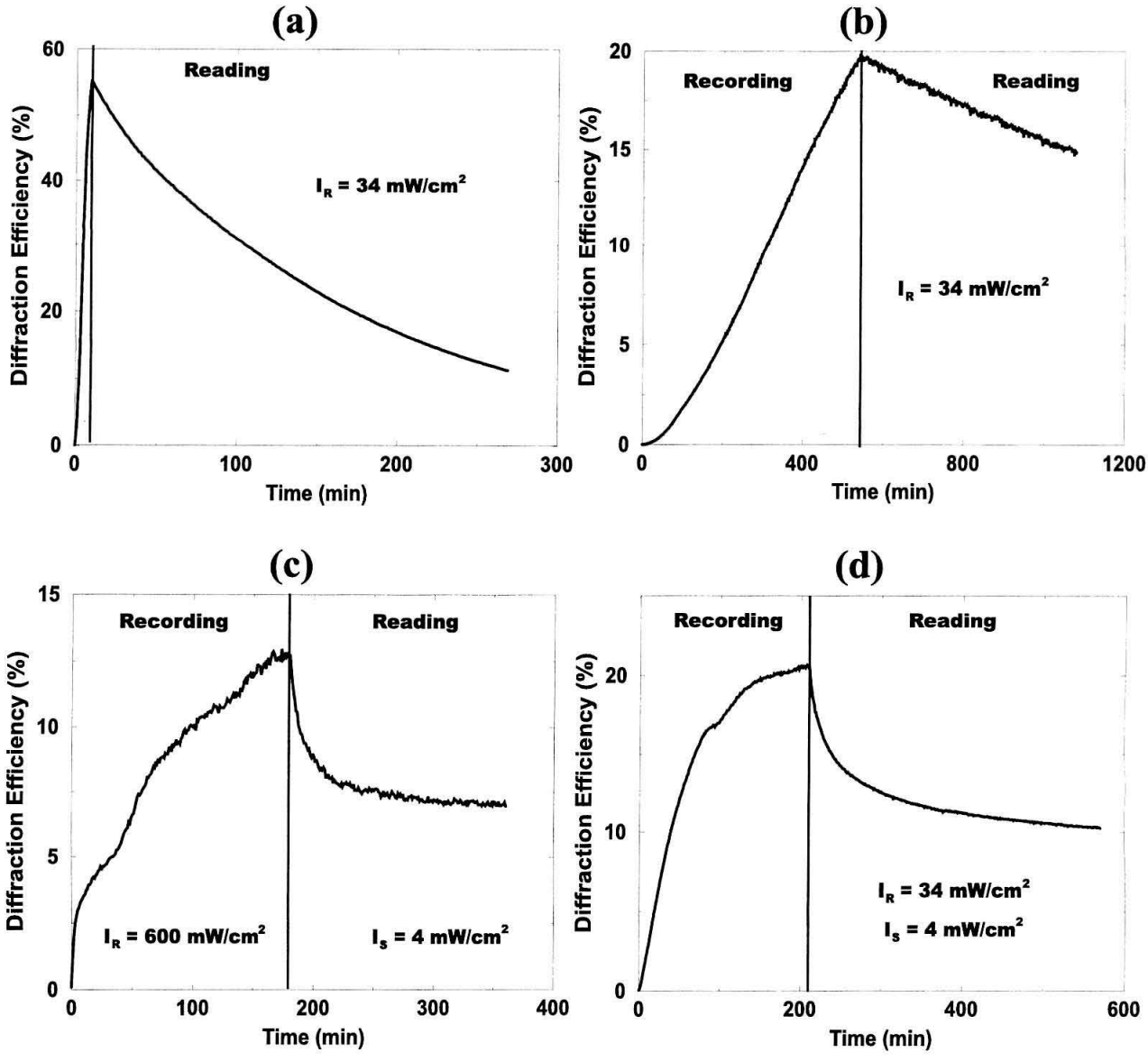

Figure 6.1: Recording and read–out curves for a plane–wave hologram in a $LiNbO_3$:Fe:Mn crystal: (a) recording with two plane waves (wavelength 488 nm) in the highly reduced sample XTAL2, (b) recording with two plane waves (wavelength 514 nm) in the lightly oxidized sample XTAL1, (c) recording with two plane waves (wavelength 633 nm) and one sensitizing beam (wavelength 404 nm) in XTAL1, and (d) recording with two plane waves (wavelength 514 nm) and one sensitizing beam (wavelength 404 nm) in XTAL1. Recording and sensitizing intensities (I_R and I_S, respectively) are shown in the figures. Further details are mentioned in the text.

(d) show that by adding one homogeneous sensitizing beam to the recording system and using the more oxidized crystal (XTAL1) we can add another dimension to the performance characteristics. This added dimension is persistence. Recording with red light has better persistence than recording with green light, sensitivity is much better in recording with green light. This means that we can improve sensitivity by sacrificing some persistence. This range of performance characteristics obtained by using a doubly–doped $LiNbO_3$ crystal can not be obtained by using a singly–doped crystal by any means. For example, the range of performance in normal recording in a $LiNbO_3$:Fe:Mn crystal covers from that of a highly oxidized $LiNbO_3$:Mn crystal to that of a highly reduced $LiNbO_3$:Fe crystal. Furthermore, we can add persistence by bringing in a sensitizing beam. The range of performance that can be obtained in a $LiNbO_3$:Fe crystal covers only from that of a highly oxidized $LiNbO_3$:Fe crystal to that of a highly reduced $LiNbO_3$:Fe crystal without the possibility of persistence.

6.3 Quantitative performance measures

In Section 6.2 we discussed qualitatively the differences among the four recording experiments shown in Figure 6.1 based on dynamic range (or recording strength), sensitivity (or recording speed) and persistence (or non–destructive read–out). It is important to note that hologram strength, recording sensitivity, and persistence are not fully independent. For example, we can read a very strong hologram with much lower intensity than a weak hologram to obtain the same output intensity. However, the erasure of the hologram depends on reading intensity. Therefore, we should not consider the erasure time constants obtained at the same reading intensity as a measure for persistence. This means that we can not compare the persistence of the four cases depicted in Figure 6.1 by just looking at how fast the holograms are erased during read-out. It is important to have good quantitative measures for different performance characteristics to compare the different cases and to study the trade–offs involved in holographic recording in a doubly–doped $LiNbO_3$ crystal. In this section, we discuss such quantitative measures for dynamic range, recording speed,

and persistence.

6.3.1 Measure for dynamic range, $M/\#$

We have previously defined $M/\#$ [75] as the measure for dynamic range in holographic recording. In normal recording, $M/\#$ is typically defined as the product of initial recording slope and erasure time constant as

$$M/\# = \frac{A_0 \tau_e}{\tau_r}, \tag{6.1}$$

where A_0 is the saturation hologram strength, and τ_r and τ_e are recording and erasure time constants, respectively. The same formula can be used in two–center holographic recording if A_0 and τ_e are defined appropriately as discussed in Chapter 4. The importance of $M/\#$ becomes clear in multiplexing many holograms. If we multiplex M holograms using an appropriate recording schedule [73, 81], all holograms will have the same diffraction efficiency (η) equal to

$$\eta = \left(\frac{M/\#}{M}\right)^2. \tag{6.2}$$

The minimum acceptable diffraction efficiency of each hologram in a holographic storage system is typically dictated by the noise and crosstalk level of the system and the minimum acceptable signal to noise ratio (or probability of error). Therefore, we would like $M/\#$ to be as large as possible to be able to record more holograms with the pre–specified diffraction efficiency. In other words, larger $M/\#$ results in higher storage capacity.

6.3.2 Measure for recording speed, sensitivity (S)

We have previously defined sensitivity (S) as the measure for recording speed in holographic recording [76]. In normal recording, S in units of cm/J is defined as the initial recording slope (A_0/τ_e) normalized to total recording intensity (I_R) and the

thickness of the recording medium (L) as

$$S = \frac{\frac{d\sqrt{\eta}}{dt}|_{t=0}}{I_{\mathrm{R}}L} = \frac{A_0/\tau_{\mathrm{r}}}{I_{\mathrm{R}}L} . \tag{6.3}$$

Equation (6.3) can be easily modified for the calculation of sensitivity in two–center recording as explained in Chapter 4.

Sensitivity is a very important measure as it defines the recording rate (i.e., number of bits recorded in a unit of time).

6.3.3 Measure for persistence, $R/\#$

Unlike sensitivity and $M/\#$ there has been no quantitative measure for persistence in holographic recording. To define such a measure, we first need to define a reference storage system. We assume that such a system is composed of $M = 1000$ holograms multiplexed in the same volume of 1 cm $\times$ 1 cm $\times$ 1 cm with the minimum acceptable intensity of each reconstructed plane–wave hologram being 5×10^{-3} mW/cm^2. This assumption for minimum reconstructed intensity is equivalent to assuming a minimum acceptable diffraction efficiency of $\eta_{\mathrm{min}} = 5 \times 10^{-5}$ with standard reading intensity of $I_{\mathrm{STD}} = 100$ mW/cm^2. We also assume that in such a system with the specified minimum intensity of the reconstructed beam, we need to have $N_{\mathrm{ph}} = 1000$ photons for each 10 μm $\times$ 10 μm pixel at the detector to obtain an acceptable signal to noise ratio. The measure for persistence, $R/\#$, is defined as the number of times we can read the information in the entire module (all 1000 holograms) before the intensity of the reconstructed beam falls below the minimum acceptable value. To derive a formula for $R/\#$, we assume that the erasure of the hologram during read–out has monoexponential dynamics, i.e.,

$$\sqrt{\eta} = \sqrt{\eta_0}\exp(-t/\tau_{\mathrm{e}}) , \tag{6.4}$$

where η_0 and τ_e are initial diffraction efficiency and erasure time constant, respectively. To apply Equation (6.4) to two–center recording, we assume that we read the hologram for sufficient time after recording to transfer all electrons in shallower traps to deeper traps. The initial diffraction efficiency η_0 can also be represented as

$$\eta_0 = \left(\frac{M/\#}{M}\right)^2 , \tag{6.5}$$

with M being the number of holograms multiplexed in the same location. We can now calculate the maximum reading time (t_{max}) of a hologram before its diffraction efficiency falls below a pre–specified minimum value η_{min} as

$$\begin{aligned} t_{max} &= \tau_e \ln\left(\frac{\sqrt{\eta_0}}{\sqrt{\eta_{min}}}\right) \\ &= \tau_e \ln\left(\frac{M/\#}{M\sqrt{\eta_{min}}}\right) . \end{aligned} \tag{6.6}$$

The erasure time constant τ_e in these equations is inversely proportional to the reading intensity I_{RD}. To calculate $R/\#$, we need to use the erasure time constant of the standard system, $\tau_{e,STD}$. To calculate $\tau_{e,STD}$ from an experimental measurement of $\tau_{e,RD}$ at reading intensity I_{RD}, we use

$$\tau_{e,STD} = \tau_{e,RD}\frac{I_{RD}}{I_{STD}} , \tag{6.7}$$

where I_{STD} is the average reading intensity of the standard system. Typically, I_{STD} is chosen high enough to ensure at least the minimum acceptable intensity for the reconstructed beam. On the other hand, we choose I_{STD} and as low as possible to minimize the erasure during read–out (maximize $R/\#$).

The reading time of each hologram (t_h) depends on the intensity of the reconstructed beam and the number of photons per pixel (N_{ph}) required to obtain acceptable signal to noise ratio. The formula for t_h can be written as

$$t_h = \frac{N_{ph}h\nu}{I_{out}A_{pixel}} , \tag{6.8}$$

where $h\nu$ is the energy of a single photon at the reading light frequency, and I_{out} and A_{pixel} are output (or reconstructed) intensity and the area of each pixel, respectively. Knowing the maximum possible reading time and the reading time for each hologram, we can calculate $R/\#$ as the number of times we can read the entire information in the memory module (M holograms) as

$$\begin{aligned} R/\# &= \frac{t_{\max}}{M t_{\text{h}}} \\ &= \frac{\tau_{\text{e,SD}}}{M t_{\text{h}}} \ln\left(\frac{M/\#}{M\sqrt{\eta_{\min}}}\right) . \end{aligned} \tag{6.9}$$

Note that if η_0 and $\eta_{\min}$ are very different, we need to put an effective (or averaged) value for $\tau_{\text{e,SD}}$ since the reading intensity of the standard system might vary in a large range to guarantee the minimum acceptable output intensity.

Equation (6.9) suggests that $R/\#$ is dependent on both $M/\#$ and the erasure time constant of the recorded holograms. The dependence on the erasure time constant is clear as the stored information can be read for a longer time (or more times) at longer erasure time constants. The dependence on the $M/\#$ comes from the fact that the diffraction efficiency of each hologram at the end of recording is larger for larger $M/\#$. Therefore, we can read the holograms with lower intensities to obtain the same minimum acceptable intensity of the reconstructed beams. Using lower intensities results in lower erasure time constants and larger $R/\#$. In a practical storage system, we need to have $R/\#$ in the order of a million. This allows us to read the entire information in a storage module (with capacity in the order of 1 Gbit) at least one million times before we need to refresh the stored information.

6.3.4 Relations among the quantitative performance measures

It is important to note that $M/\#$, S, and $R/\#$ are not totally independent from each other. For example, the relation between $M/\#$ and S can be seen from Equations (6.1) and (6.3). If we increase the saturation strength of the hologram (A_0) while

keeping the time constants fixed, we can increase both $M/\#$ and S. Increasing A_0 will also increase $R/\#$ as $R/\#$ increases with increasing $M/\#$. On the other hand, if we try to increase S by decreasing the recording time constant (τ_r) as Equation (6.3) suggests, we typically decrease the erasure time constant (τ_e) and in many cases the saturation hologram strength (A_0), too. As a result both $M/\#$ and $R/\#$ become smaller in this case.

6.4 Comparison of different recording strategies in doubly–doped $LiNbO_3$

In this section, we compare the quantitative characteristics measures for the four different cases shown in Figure 6.1. The values for $M/\#$, S, and $R/\#$ for these four cases are summarized in Table 6.1. The last column in Table 6.1 comments about the strength of holographic scattering and fanning as the sources for deterioration of the holograms especially during read–out. As Table 6.1 suggests, the numbers are all good for single wavelength (488 nm) recording in the reduced sample XTAL2. However, there exist two difficulties in using this crystal. First, the absorption of the recording and reading light inside the crystal goes up with crystal thickness. Although the absorption of the 0.85 mm thick sample of XTAL2 was not very high, it becomes high if we use a 1 cm thick crystal that is more practical. Secondly, fanning is very strong in the reduced sample XTAL2 resulting in the fast deterioration of the stored information. Normal recording with only one wavelength in the more oxidized sample XTAL1 has good $M/\#$ and $R/\#$ while the absorption of the recording and read–out beams is low enough for all practical applications. However, the sensitivity is too low in this case. Recording with red (633 nm) in the presence of a sensitizing UV beam (wavelength 404 nm) results in an excellent $R/\#$ and a barely acceptable $M/\#$, but the sensitivity is very low. Furthermore, absorption of the recording light and fanning are not critical issues here. The best combination of both quantitative measures ($M/\#$, S, and $R/\#$) and qualitative measures (absorption and fanning) for

a practical read / write memory system is obtained by using two–center holographic recording in XTAL1 with green light (wavelength 514 nm) for recording and UV (wavelength 404 nm) for sensitization.

Recording scheme	Normal	Normal	Two–Center	Two–Center
Crystal	XTAL2	XTAL1	XTAL1	XTAL1
Annealing	reduced	oxidized	oxidized	oxidized
Sensitizing wavelength (nm)	–	–	404	404
Sensitizing intensity (mW/cm^2)	–	–	3.8	3.8
Recording wavelength (nm)	488	514	633	514
Recording intensity (mW/cm^2)	31	34	600	34
$(M/\#)/L$ (cm^{-1})	75	55	7.5	10
S (cm/J)	1.2	0.018	0.01	0.2
$R/\#$ (10^6)	0.6	4.8	100	0.3
Fanning	severe	small	very small	small
Absorption of recording beam	high	low	low	low

Table 6.1: Comparison of the performance measures of different recording schemes in a $LiNbO_3$:Fe:Mn crystal.

6.5 Trade–offs in holographic recording in doubly–doped $LiNbO_3$

The major challenge in designing a holographic storage system is the trade–offs among $M/\#$, S, and $R/\#$ along with the qualitative measures for absorption and fanning. Depending on the application, the main concern might be a subset of these measures. For example, if we do not want to write new information frequently but we need to read the information a lot, we need to use a recording scheme with large $R/\#$ and we can even sacrifice S to obtain better $R/\#$. In such a case, we might use two–center holographic recording with red and UV in a properly oxidized $LiNbO_3$:Fe:Mn crystal (Figure 6.1 (c)). If we need larger $M/\#$ than that obtained in two–center recording with red and UV, we can sacrifice some persistence ($R/\#$) for $M/\#$ by using two–center holographic recording with green and UV (Figure 6.1 (d)).

It is evident from Table 6.1 that by adding long–term persistence through using two–center recording, we sacrifice both $M/\#$ and S. One obvious reason for this loss in $M/\#$ and S is that two–center recording has an extra step of bringing electrons from the deeper traps (Mn) to the shallower ones (Fe). This extra step reduces the recording speed compared to normal recording in singly–doped crystals where we directly record from the shallower traps. The presence of the sensitizing UV beam also decreases the modulation depth for the electron concentration in the conduction band resulting in a smaller $M/\#$. There is another important reason for losing $M/\#$ and S in two–center holographic recording in $LiNbO_3$:Fe:Mn crystals: to obtain the best persistence we need to choose recording wavelength high enough to suppress the erasure of the hologram recorded in the deeper traps during read–out. Therefore, we need to use red light for recording in $LiNbO_3$:Fe:Mn crystals. However, red light is not the best wavelength for recording from Fe traps in $LiNbO_3$. The smaller absorption cross section of the Fe traps at 633 nm compared to that at 488 nm (that is a more appropriate wavelength for recording holograms from Fe traps in $LiNbO_3$) results in a big loss in S. The photovoltaic coefficient of Fe traps at 633 nm is also much smaller than that at 488 nm resulting in losing $M/\#$, too. This extra loss due to the inefficiency of recording wavelength is the major source of loss in $M/\#$ and S in two–center holographic recording with red and UV in $LiNbO_3$:Fe:Mn crystals. These extra losses can be avoided by finding better dopands or even better materials. For example, if we replace Fe by another trap in $LiNbO_3$ that is the most sensitive to red light, we can obtain excellent persistence without losing a lot in $M/\#$ and S. The position of such an ideal shallower trap in the band gap of $LiNbO_3$ is shown by Z in Figure 6.2. Finding such a trap and using it instead of Fe also allows us to replace Mn by copper (Cu) that lies closer than Mn to the conduction band in the band gap of $LiNbO_3$ as shown in Figure 6.2. This allows us to use blue light (wavelength 430 nm) for sensitization in order to avoid extra absorption of the sensitizing beam due to band–to–band absorption of $LiNbO_3$. Therefore, one important challenge in optimizing the recording material is to find a better shallower trap than Fe. Possible choices for this shallower trap along with other ways for improving material properties

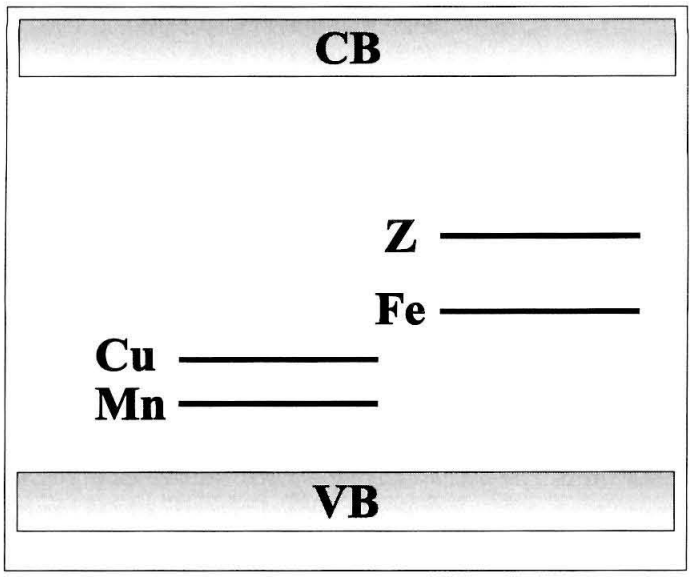

Figure 6.2: (a) Relative positions of the different traps in the band gap of $LiNbO_3$. Z represents an ideal shallower trap for two–center recording. CB and VB stand for conduction band and valance band, respectively.

in two–center holographic recording will be discussed in Chapter 7.

6.6 Designing trap properties by using doubly–doped crystals

The number of known dopands that act as photorefractive centers in $LiNbO_3$ is very small. Only iron (Fe), copper (Cu), manganese (Mn), and chromium (Cr) are known to show photorefractive behavior with acceptable strength for holographic recording in $LiNbO_3$. This limits the choice of trap properties even for normal recording with a single wavelength to just four different sets of parameters. The performance characteristics highly depend on the trap's properties like absorption cross section and photovoltaic constant at the recording wavelength, recombination coefficient for trapping electrons from the conduction band, etc. As a result, we can not always have the material properties appropriate for a specific application. However, we can use two

different dopands and choose their concentrations and oxidation / reduction states to design an effective trap that fits better for our specific application than a single trap. This allows us to obtain a large range of performance characteristics even if we want to use normal holographic recording with a single wavelength. For example, we can obtain a performance range from that of a highly oxidized $LiNbO_3$:Mn crystal to that of a highly reduced $LiNbO_3$:Fe crystal by using a $LiNbO_3$:Fe:Mn crystal at different oxidation / reduction states. These two extreme cases are shown in Figures 6.1 (a) and (b). We can obtain any performance between these two extremes by simply changing the oxidation / reduction state of the same crystal. We can also alter these two extremes by changing the concentrations of Fe and Mn traps. Therefore, we can design an effective trap (Eff) that would lie between Fe and Mn traps in the band gap of $LiNbO_3$ as shown in Figure 6.3. Note that such an effective center can be used for example as the effective deeper trap in two–center holographic recording utilizing another effective center for the shallower trap. Also note that this idea of designing an effective trap is not limited to $LiNbO_3$ crystal. This opens up the general idea of using multiply doped crystals for holographic recording to obtain the specific characteristics for a specified application.

6.7 Conclusions

We defined for the first time a quantitative measure for persistence ($R/\#$) in holographic recording. We also compared different strategies for holographic recording in a $LiNbO_3$:Fe:Mn crystal based on the dynamic range parameter ($M/\#$), sensitivity (S) and persistence ($R/\#$) as well as qualitative measures of the absorption of the recording and reading beams, and fanning. The performance range that can be obtained by using a doubly–doped $LiNbO_3$ crystal is much broader than that obtained in a singly–doped crystal even if recording is performed by only two recording beams without sensitizing light (normal recording). By adding a sensitizing beam to the holographic recording system (two–center recording), we can add one dimension for performance characteristics (persistence) that further broadens the range of

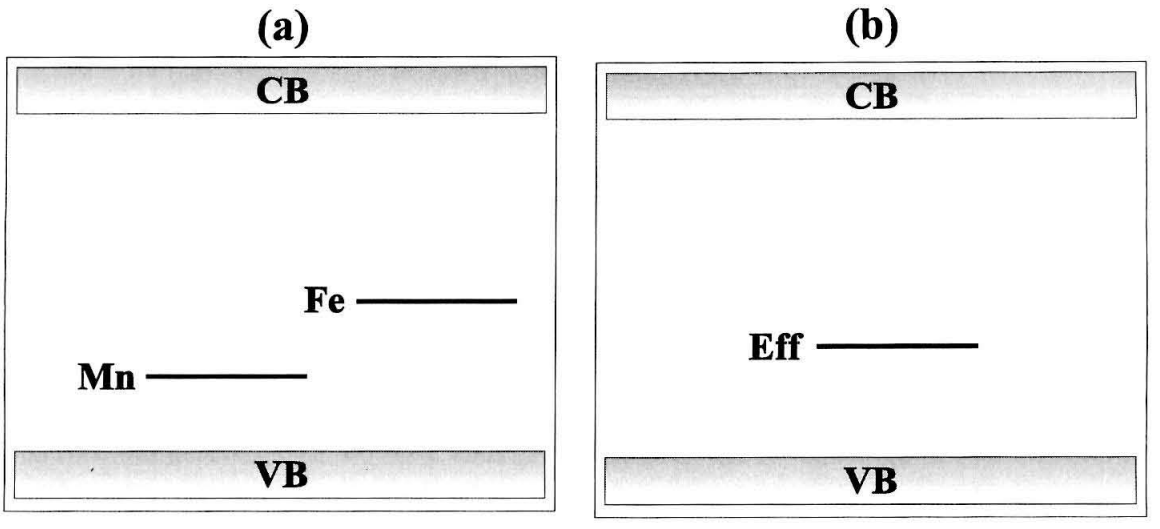

Figure 6.3: (a) Energy band diagram of a $LiNbO_3$:Fe:Mn crystal. (b) Energy band diagram of a $LiNbO_3$ crystal having an effective trap (Eff) that acts the same as the $LiNbO_3$:Fe:Mn crystal whose diagram shown in part (a). The position and properties of the effective traps (Eff) depend on the relative concentrations of the Fe and Mn traps, and the oxidation / reduction state of the crystal.

performance characteristics that can be obtained. We can dope the crystal with two sets of dopands to design an effective trap with appropriate properties for a desired performance.

The main challenges in holographic recording are the trade–offs among $M/\#$, S, $R/\#$ and qualitative measures like fanning and absorption. The material properties (dopands, oxidation / reduction state, etc.) as well as the system properties (recording and sensitizing wavelengths and intensities, etc.) should be chosen to obtain the desired characteristics by possibly sacrificing some parameters that are not the main concern in order to improve those that are crucial.

We showed that two–center holographic recording with green (wavelength 514 nm) and UV (wavelength 404 nm) in an appropriately annealed $LiNbO_3$:Fe:Mn crystal is the best strategy for designing a practical read / write storage module with acceptable persistence. Furthermore, by choosing the deeper and shallower traps appropriately (if practically possible) in two–center recording, we can add persistence without sac-

rificing a lot in $M/\#$ and S. Finding the ideal traps, especially the shallower ones, in $LiNbO_3$, is an important challenge in improving the performance of two–center holographic recording. In Chapter 7 we consider the system design and possible ways for further performance improvement in two–center holographic recording.

Chapter 7 System design

7.1 Introduction

In previous chapters, we discussed several issues regarding the recording material and some system issues in two–center holographic recording. When talking about materials, we can summarize the necessary information by three important parameters. These material parameters are dynamic range parameter ($M/\#$), sensitivity (S), and persistence measure ($R/\#$). On the other hand, the design criteria of a storage system are usually expressed in terms of storage capacity (C), recording rate (R_{Rec}), access time (t_{access}), and read–out rate (R_{Read}). Therefore, it is necessary to understand the relation among the material parameters and the system parameters.

In this chapter, we first derive formulas that relate the system parameters and the material parameters. We then use the derived formulas to see what system characteristics are obtained with the existing materials. This is very important in judging about the practicality of holographic memory systems with current materials and techniques. We also discuss an outline for the design of a system using the existing materials and techniques. The main issues we discuss are the choice of recording geometry, the choice of multiplexing scheme, and the choice of recording material. We will conclude this chapter with summarizing the general guidelines for designing the appropriate recording materials that can be used as a basis for the future research.

7.2 System parameters

In this section, we find the relation among the system parameters (C, R_{rec}), t_{access}, and (R_{read}) and the material parameters ($M/\#$, S). The system measure we choose for persistence is the same as the material parameter $R/\#$. In the derivations described in this section, we assume that our storage module consists of a crystal with thickness

L whose area perpendicular to the thickness dimension is A. We also assume that we multiplex M holograms in the same volume with each hologram consisting of a $N \times N$ two–dimensional array of pixels. The area of each pixel is assumed to be $A_{\text{pixel}} \simeq A/N^2$. Therefore, each hologram (or data page) has N^2 bits. We also assume that the signal beam in holographic recording is modulated by a spatial light modulator (SLM) with an efficiency of 100%, for simplicity. Finally, the recording and read–out intensities are represented by I_{Rec} and I_{Read}, respectively.

7.2.1 Recording rate

From the formula for sensitivity

$$S = \frac{\frac{d\sqrt{\eta}}{dt}|_{t=0}}{I_{\text{Rec}} L}, \tag{7.1}$$

we can find the recording time for a weak hologram with diffraction efficiency $\eta = [(M/\#)/M]^2$ (or $\sqrt{\eta} = (M/\#)/M$) to be

$$t_{\text{R}} = \frac{\frac{M/\#}{M}}{I_{\text{Rec}} LS}, \tag{7.2}$$

where we assumed that the recording dynamics of the weak hologram can be approximated by a linear function. The number of holograms recorded per unit time is simply $1/t_{\text{R}}$. Since each hologram consists of N^2 bits, the recording rate (R_{Rec}) in units of bits/s is

$$R_{\text{Rec}} = \frac{N^2 I_{\text{Rec}} LS}{\frac{M/\#}{M}}. \tag{7.3}$$

7.2.2 Access time and read–out rate

To calculate the read–out rate, we assume that by using the fast ways of addressing the different pages during read–out (for example, using micro–electro–mechanical systems

(MEMS) or vertical cavity surface emitting lasers (VCSEL's)), the access time of each hologram is limited by the integration time of the detector. We assume that we need to integrate N_e electrons per each pixel at the detector to obtain acceptable signal to noise ratio (SNR). If the read–out of a hologram with diffraction efficiency $\eta = [(M/\#)/M]^2$ is performed by the light of optical frequency ν_R and intensity I_{Read}, the number of photons per pixel (NPP) per unit time will be

$$\begin{aligned} NPP &= \frac{\left(\frac{M/\#}{M}\right)^2 I_{Read} A_{pixel}}{h\nu_R} \\ &= \frac{\left(\frac{M/\#}{M}\right)^2 I_{Read} A}{h\nu_R N^2}, \end{aligned} \tag{7.4}$$

where h is Plank's constant. Assuming 100% quantum efficiency for the detector (i.e., each photon at the detector results in one electron), the access time required for the integration of N_e electrons (or photons) per pixel at the detector will be

$$t_{access} = \frac{N_e}{NPP} = \frac{N_e h\nu_R N^2}{\left(\frac{M/\#}{M}\right)^2 I_{Read} A}. \tag{7.5}$$

Since each hologram consists of N^2 bits, the read–out rate (R_{Read}) in units of bits per second is

$$R_{Read} = \frac{N^2}{t_{access}} = \frac{\left(\frac{M/\#}{M}\right)^2 I_{Read} A}{N_e h\nu_R}. \tag{7.6}$$

7.2.3 Storage capacity

Since we multiplex M holograms each consisting in N^2 bits of data in the same volume of the crystal, the storage capacity (C) in units of bits is easily calculated to be

$$C = MN^2, \tag{7.7}$$

and the volume information density in units of bits/m^3 is

$$D = \frac{MN^2}{AL} . \tag{7.8}$$

7.2.4 System parameters for the existing materials

Since we are interested in having persistence along with fast recording, fast read–out, and large storage capacity in our memory system, we use two–center recording in a $LiNbO_3$:Fe:Mn crystal with UV light (wavelength 404 nm) for sensitization and green light (wavelength 514 nm) for recording. The best material parameters for a 1 cm thick crystal are obtained by recording in transmission geometry with extraordinary polarization for recording light. These parameters are $(M/\#)/L \simeq 10$ cm^{-1}, $S \simeq 0.2$ cm/J, and $R/\# \simeq 3 \times 10^6$.

We assume that our memory module consists of $M = 1000$ holograms in a 1 cm $\times$ 1 cm $\times$ 1 cm crystal. Since the recording material has $M/\# = 10$, the diffraction efficiency of each hologram is $\eta = 10^{-4}$. We also assume that the dimensions of each pixel are 10 μm $\times$ 10 μm which is 10 times bigger in each dimension than the practical limit of the pixel size in holographic recording in $LiNbO_3$ [87]. Therefore, the number of pixels (or bits) in each hologram (page size) is

$$N = \frac{A}{A_{\text{pixel}}} = \frac{1\text{cm}^2}{100\mu\text{m}^2} = 10^6 . \tag{7.9}$$

We assume that we need to integrate $N_e = 1000$ electrons per each pixel at the detector to obtain acceptable signal to noise ratio. Finally, we assume that recording and reading intensities are $I_{\text{Rec}} = I_{\text{Read}} = 100$ mW/cm^2. Putting the values of the different parameters in Equations (7.3) and (7.5)–(7.8) results in the following system

parameters:

$$R_{\text{Rec}} = 2 \text{ Mb/s}, \tag{7.10}$$

$$t_{\text{access}} = 3.9 \ \mu\text{s}, \tag{7.11}$$

$$R_{\text{Read}} = 250 \text{ Gb/s}, \tag{7.12}$$

$$C = 1 \text{ Gb}, \tag{7.13}$$

$$D = 1 \text{ Gb/cm}^3, \tag{7.14}$$

that are good compared to similar system parameters for a commercial hard drive. The impressing recording and read–out rates are the direct result of the huge parallelism in holographic recording, i.e., by reading each hologram (or data page) we read 100 Mb in parallel. We can therefore conclude that two–center holographic recording with UV and green with the existing materials is very promising for the realization of a practical holographic storage systems. Note that two–center recording is still at its early stages of progress with a lot of room for improvement.

7.3 Recording geometry

Holograms can be recorded using transmission geometry, 90° geometry, and reflection geometry, although the first two geometries are more appropriate for the design of read / write memory systems in $LiNbO_3$ crystals.

The advantages of the 90° geometry are the good overlap of the reference and signal beams over a large range, very good angle (or wavelength) selectivity due to small grating period, good tolerance to scattering (as scattering light during read–out is mainly centered around the strong reference beam and does not have a large extent around the reconstructed beam), and the possibility of usage in the compact lensless architecture [88]. However, recording with extraordinary polarization is not possible in 90° geometry since the polarizations of the reference and signal beams have to be the same. Due to the 90° angle between the directions of propagation of the two beams, they must have out of plane (or ordinary) polarization (or at least an ordinary

component). This results in a loss by a factor of 3 in both $M/\#$ and S due to smaller electro–optic coefficient of $LiNbO_3$ for ordinary polarization. On the other hand, we can use extraordinary polarization for the recording beams in transmission geometry to obtain a factor of 3 improvement in both $M/\#$ and S. It is important to note that the use of extraordinary polarization for recording beams results in stronger inter–pixel crosstalk. There are some proposed methods for reducing inter–pixel crosstalk, and the issue is still under research.

It seems that at least with the existing materials, we need to use transmission geometry with extraordinary polarization. This is due to the fact that the existing system parameters calculated in Section 7.2 are barely comparable with those of the other memory systems (like hard drives). Therefore, we can not afford to loose both $M/\#$ and S by a factor of 3. However, if future research results in much bigger values of $M/\#$ and S, we may want to use 90° geometry to take advantage of its nice features.

7.4 Choice of multiplexing method

The best method for hologram multiplexing in a practical storage system is wavelength multiplexing as it does not need any moving parts. The use of tunable laser diodes as the source of the recording beams is probably the best choice. However, a practical holographic storage system using wavelength multiplexing requires fast switching from one wavelength to another wavelength. The wavelength tuning range needs to be large enough to accommodate the multiplexing of many holograms in the same volume. With the current advances in the design of tunable laser diodes, it is hopeful that the requirements of wavelength multiplexing for practical holographic storage systems can be satisfied in the near future.

We can also use angle multiplexing in our memory module. To have fast access time (limited only by the detector integration time), the use of MEMS for changing the angle of the reference beam is recommended.

7.5 Choice of recording material

The best present method that has all the required system parameters for a practical read / write storage system is two–center holographic recording with UV (wavelength 404 nm) and green (wavelength 514 nm) in doubly–doped $LiNbO_3$ crystals. The best existing material for this recording scheme is congruently melting $LiNbO_3$:Fe:Mn. The material has to be congruent, and not stoichiometric as explained in Chapter 4. Later in this chapter, we will discuss the possible ways of improving the material properties.

7.6 A system prototype

Figure 7.1 shows our proposed memory module using the compact lensless architecture [88] with phase conjugate read–out. The system incorporates two–center recording in a doubly–doped crystal. Two sensitizing beams sensitize the crystal from the top and the bottom while the recording beams record a hologram in a 90° geometry. Read–out of each hologram is performed by the phase conjugate of its corresponding reference beam. The ideal case in this system is to have a material that is best sensitized by blue light (wavelength 430 nm) with the most sensitive wavelength for recording in the red (around 670 nm). This allows us to use high power blue LED's for the sensitizing beam and laser diodes as the source of the recording beams. To realize such an ideal system, it is crucial to improve the material to have the required properties.

7.7 Improving the recording material

To choose the correct directions for future research in recording materials, we need to have a good understanding of the general criteria for designing the recording material and choosing the parameters (wavelength, intensity, etc.) of sensitizing and recording beams. Although we have mentioned most of these criteria in different places previously, it is helpful to summarize them here. These criteria can be used as the

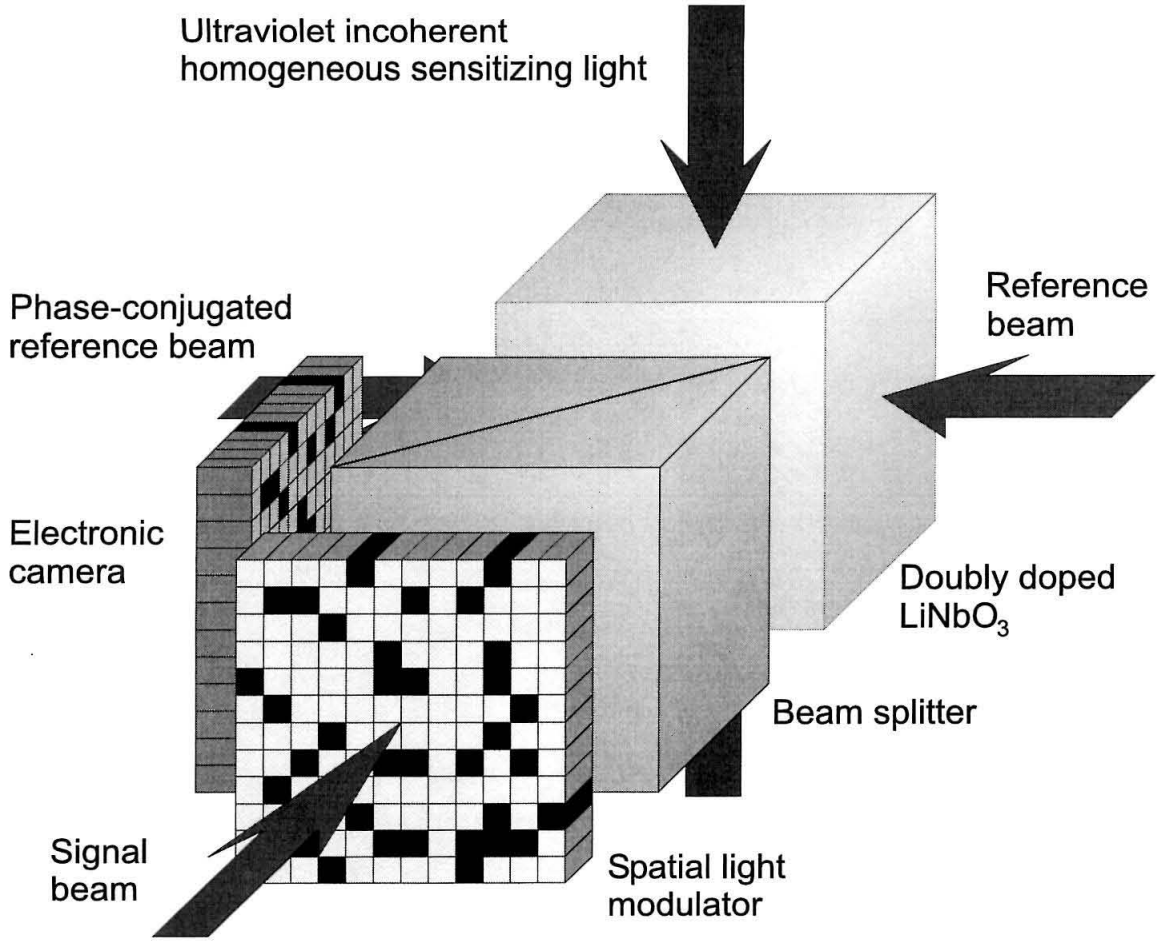

Figure 7.1: A proposed memory module using two–center recording in compact lensless architecture with phase conjugate read–out.

cookbook for designing other materials with other dopands.

7.7.1 Material design criteria

Choice of the photorefractive material

1. The band gap of the recording material must be large enough to place two different sets of traps (shallower and deeper traps) far enough from each other for obtaining good persistence.

2. The material needs to have good optical quality to ensure weak light scattering. The minimum acceptable diffraction efficiency ($\eta_{\min}$) of each hologram becomes higher at stronger scattering, and the number of holograms that can be multiplexed in the same volume is smaller at larger diffraction efficiencies ($M = (M/\#)/\sqrt{\eta_{\min}}$). Therefore, strong scattering results in the loss of storage capacity.

3. The material must have small dark conductivity to ensure long dark storage time (at least 6 months).

4. The material must be sensitive enough for holographic recording either in the undoped form or when doped with appropriate impurities. Furthermore, the wavelength that the material is most sensitive to must be practical.

5. The material must have large electro–optic coefficients that can be used for holographic recording.

6. The material must be easy to grow with good repeatability.

The best materials that satisfy these requirements are lithium niobate ($LiNbO_3$) and lithium tantalate ($LiTaO_3$). Although $LiNbO_3$ has been extensively used in different applications, and therefore it is very easy to obtain and to work with, $LiTaO_3$ might be advantageous in some applications due to its larger band gap.

Choice of the dopands (or traps)

1. Both dopands (for shallower and deeper traps) should act as photorefractive centers in the crystal, i.e., they must occur with two different valance states inside the recording material. In other words, it must be possible to excite an electron to the conduction band (or a hole to the valance band) from the trap levels corresponding to both dopands. The traps corresponding to both dopands must be able to capture (or trap) electrons from the conduction band. It is also necessary to have control on the initial electron concentration in the traps corresponding to the dopands. An example of a photorefractive center is Fe in $LiNbO_3$ that occurs as either Fe^{2+} or Fe^{3+}. The initial electron concentration in the Fe traps in $LiNbO_3$ can be changed by annealing.

2. The position of each trap (or dopand) in the band gap of the recording material must correspond to some practical optical wavelength range for excitation.

3. The absorption cross section and the bulk photovoltaic constant (if applicable) of each trap at its excitation wavelength must be large enough to result in large $M/\#$ and S.

4. The deeper traps must be far enough from the top of the valance band to reduce the extra absorption of the sensitizing beam due to band to band electron excitation.

5. The shallower traps must be far enough from the bottom of the conduction band to reduce the possibility of the depopulation of the these traps by thermal excitation.

6. The deeper traps and the shallower traps must be far enough from each other to ensure good persistence.

It is important to note that the simultaneous satisfaction of these conditions to the level of perfection might not be possible in many cases. In such cases, we need to trade–off $M/\#$, S, and $R/\#$ to obtain the best condition for the desired application.

The usage of large band gap materials provides us with more room to put the traps far enough from each other and from the corresponding band. Therefore, the usage of high band gap recording material is preferable.

Choice of the sensitizing and recording wavelengths

1. Sensitization must be performed with the wavelength that the deeper traps are most sensitive to. However, if the deeper traps are close to the valance band of the recording material, we may need to choose the sensitizing wavelength longer than the best wavelength to avoid the strong band to band absorption. In such cases sensitizing wavelength must still be low enough to result in good sensitization from the deeper traps.

2. Recording must be performed with the wavelength that the shallower traps are most sensitive to. However, if the shallower traps and the deeper traps are close to each other, we must use higher wavelengths to ensure acceptable persistence. Choosing the recording wavelength higher than the best wavelength results in some loss in S and $M/\#$.

3. Both optimum sensitizing and recording wavelength must be easy to provide by using practical light sources.

In many cases, we might also not be able to simultaneously satisfy all these criteria to the level of perfection. In such cases, we need again to trade off $M/\#$, S, and $R/\#$ to obtain the best condition for the desired application. This might involve sacrificing one or two of the material parameters for the sake of the desired parameter. Here, the usage of high band gap material is also preferable as it is possible to have larger distance between the traps and also between each trap and its corresponding band (valance band or conduction band).

Choice of doping levels, annealing, and sensitizing and recording intensities

After choosing the recording material and the corresponding appropriate traps, we can use the optimization strategy described in Chapter 3 to choose the concentrations of the deeper and the shallower traps, the initial electron concentration in each trap, and the recording and sensitizing intensities. Some rules of thumb are as follows:

1. The concentration of the shallower traps is typically chosen as high as practically possible.

2. The optimum ratio of the recording and sensitizing intensities is chosen by keeping in mind the practicality of such intensities.

3. The optimum concentration of the deeper traps is chosen.

4. The crystal must be annealed properly (or put into other appropriate processes for changing electron concentrations in the traps) so that all the shallower traps as well as a portion of the deeper traps are initially empty. The optimum portion of the filled deeper traps must be chosen as discussed in Chapter 3.

Note that these optimization rules (intensity ratio, concentration, annealing, etc.) are not totally independent. This is due to the fact that holographic recording performance is the result of the act of different excitation and recombination (or trapping) mechanisms. To optimize the recording performance, we need to optimize the rates for these mechanisms. Each excitation rate depends on the product of an electron concentration and an intensity causing the dependence of the optimum concentrations and the annealing state on the intensities and vice versa.

Summary

We already know how to optimize the concentrations of the different traps, the annealing state, and the intensities of the sensitizing and recording beams. The optimum values of these parameters depend on the recording material and the dopands chosen

for the shallower and the deeper traps. Knowing the material and the traps, it is easy to find appropriate wavelengths for sensitization and recording. Therefore, future research for improving the properties of two–center recording must be focused on finding appropriate recording material and appropriate dopands. Due to its crucial importance, we consider this issue in more details next.

7.7.2 Improving $LiNbO_3$ crystals for two–center recording

Congruently melting $LiNbO_3$ is an excellent candidate for the recording material in two–center recording due to its ease of growth, excellent optical quality, very small dark conductivity, and strong bulk photovoltaic effect. The dopands known to act as photorefractive centers in $LiNbO_3$ are iron (Fe), copper (Cu), manganese (Mn), and chromium (Cr). Unfortunately, the traps corresponding to these dopands are all fairly deep in the band gap of $LiNbO_3$ with Fe being the shallowest one. Therefore, we have multiple choices for the deeper traps in $LiNbO_3$, and we need to focus our future research on finding other traps that are closer to the conduction band (shallower) than Fe traps. Possible choices for the traps are transition metals and lanthanides. However, heavy elements are not appropriate to use as they can not be put with high concentration into $LiNbO_3$. Therefore, we should limit our search to the first two rows of the transition metals, and possibly lanthanides. On the other hand, all lanthanides tested in $LiNbO_3$ have failed to act as photorefractive centers. We did some characterization experiments with a $LiNbO_3$ crystal doped with Ce. The results of these experiments show that Ce is not a good candidate for a photorefractive trap in $LiNbO_3$.

Figure 7.2 shows the periodic table of elements with crosses on the elements that are proven not to act as effective photorefractive centers in $LiNbO_3$. It is known, e.g., from Ti–indiffused optical waveguides, that Ti (even in very high concentrations) is not a photorefractive center in $LiNbO_3$ [89]. Furthermore, Au and Ag are used in integrated optics for indiffusion and making contacts without enhancing photorefractive effect [89]. Some impurities like Zn, In, and Mg, which are called damage–resistant,

can be added to $LiNbO_3$ to change the degree of stoichiometry of the crystal without acting as efficient photorefractive centers [90, 91, 92, 93, 94, 95]. Some impurities (like Pt) do not melt at $LiNbO_3$ growth temperature and can not be put into $LiNbO_3$ (the crucibles for the growth of $LiNbO_3$ are usually made from Pt), while some other impurities (like Hg) are impossible to bring into $LiNbO_3$ due to too much difference of the vapor pressure. Finally, holographic recording experiments with $LiNbO_3$ crystals doped with Pr, Sc, Co, Ni, Rh, and Tb show that these impurities are not efficient photorefractive centers in $LiNbO_3$ [61, 96, 97]. We performed some experiments to investigate the role of Ce in $LiNbO_3$ for holographic recording [98]. The results, that are presented in the Section 7.7.3, show that Ce is not a very good candidate for a shallower trap in $LiNbO_3$. The remaining choices to test are vanadium (V) in the first row of and a few elements in the second row of the transition metals. A good candidate to test in the future is ruthinium (Ru) since it is below Fe in the periodic table. The electronic configuration in the last shell of Ru is similar to that of Fe. However, since the last shell of Ru is farther from the nucleus, it must be easier to excite one electron from Ru than from Fe in similar ionic states. Therefore, we might expect Ru to result in the traps in $LiNbO_3$ that are shallower than Fe. However, this is just a possibility. The traps corresponding to Ru might be too shallow, or they might not have the required absorption cross section or photovoltaic constant. If none of the remaining choices for the shallower traps in $LiNbO_3$ works, we need to use $LiNbO_3$:Fe:Mn for two–center recording, or switch to another host material.

7.7.3 Role of cerium in $LiNbO_3$ for holographic recording

In Section 7.7.2 we discussed the importance of finding a better red–sensitive photorefractive center than Fe in $LiNbO_3$. Previous experimental results suggest cerium (Ce) might be a good candidate. Cerium is known to be an effective trap center, which can provide and capture charge carriers, in different kinds of photorefractive crystals including strontium-barium niobate (SBN) [99] and barium titanate ($BaTiO_3$) [100, 101]. Ce-doped SBN has a very high sensitivity [99], and Ce-doped $BaTiO_3$ is

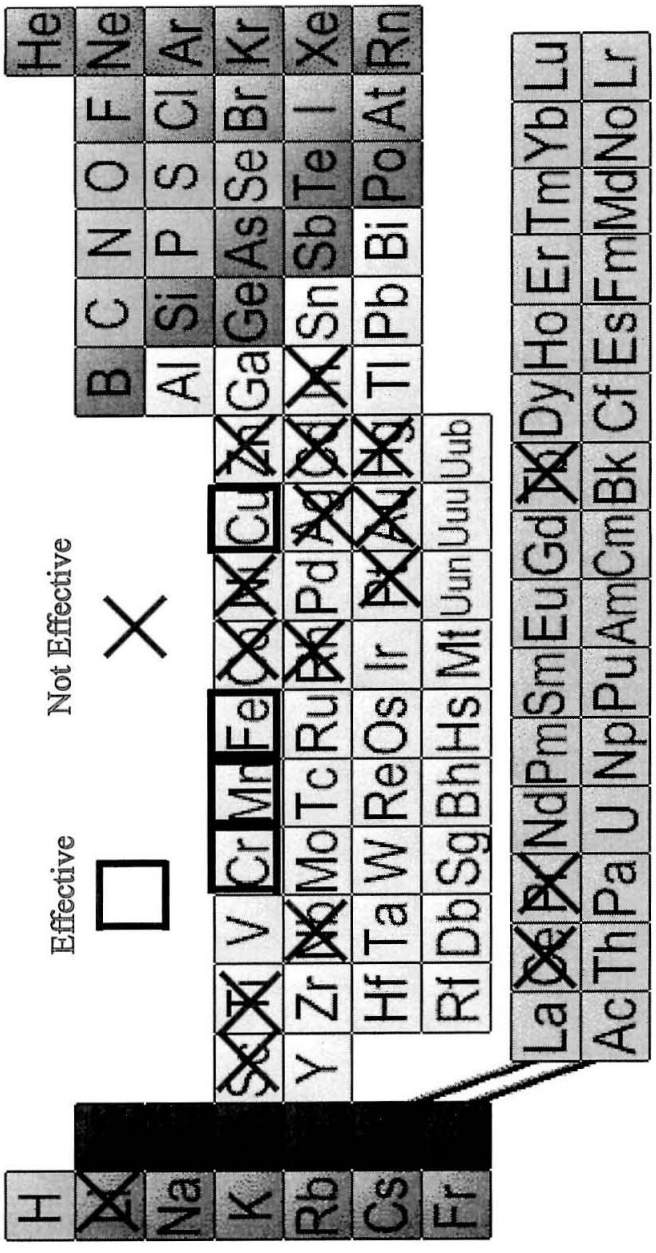

Figure 7.2: The periodic table of elements. The elements that can act as photorefractive centers in $LiNbO_3$ as well as those that can not act effectively are marked on the table.

sensitive to both visible and near infrared light [100, 101]. Some reports on Ce and Fe doubly–doped $LiNbO_3$ appeared showing that this material has a wide spectral response and shows higher sensitivity [102, 103]. Although charge transport from and to Fe centers in $LiNbO_3$ is already well–known, the impact of Ce doping on the build–up of space-charge fields in $LiNbO_3$ is still unclear. McMillen et al. have reported holographic recording in specially–doped $LiNbO_3$ crystals including a Ce singly–doped one [97], but no systematic consideration for the role of cerium has been carried out. In this section, we investigate the photorefractive performance of Ce–doped $LiNbO_3$ crystals. Comparisons will be made among the nominally pure, Ce–, Fe–, and Mn–doped samples.

Since there has been no systematic research on the role of Ce in $LiNbO_3$, we performed several experiments with singly–doped (Ce, Fe, and Mn) and doubly–doped (Ce:Mn, Fe:Mn) $LiNbO_3$ samples as well as with a nominally pure one. All samples are y-cut and polished to optical quality. Notations, doping levels, and dimensions of the samples are listed in Table 7.1. All doping levels refer to the values introduced into the melt. It is known that even in nominally pure crystals there are usually some background impurities incorporated [38]. However, the concentrations of such background impurities are generally much smaller than the intentionally doped impurity levels. To change the electron concentrations in different traps, we conducted thermal annealing (oxidation and reduction). During oxidation, the samples are kept in an oven with oxygen atmosphere at 1000 °C for at least 12 h, while they are heated to 1000 °C in argon atmosphere for 12 h during reduction.

Sensitization experiments

We performed sensitization experiments with three different crystals (LN:Mn:Fe, LN:Mn:Ce, and LN:Mn). The crystals were first oxidized to ensure that the shallower traps (Ce or Fe) are initially empty. During sensitization experiments, the crystals were illuminated by a homogeneous UV beam (wavelength 404 nm, intensity 4 mW/cm^2) while monitoring the transmission of a very weak red beam (wavelength 633 nm, ordinary polarization). Figure 7.3 shows the variation of the normalized

Notation	Dopand	Doping Level (wt.%)	Dimensions (mm^3)
LN	nominally pure	–	$5 \times 5 \times 7$
LN:Ce	Ce	0.01-0.02	$5 \times 5 \times 7$
LN:Fe	Fe	0.01-0.02	$5 \times 5 \times 7$
LN:Mn	Mn	0.05	$4 \times 1 \times 6$
LN:Mn:Ce	Mn Ce	0.01 0.085	$10 \times 2 \times 10$
LN:Mn:Fe	Mn Fe	0.01 0.085	$10 \times 2 \times 10$

Table 7.1: Description of the samples used in the experiments. The doping concentrations are wt.% of the oxide (Fe_2O_3, Ce_2O_3, and MnO) in the melt, and dimensions are $a \times b$(thickness) $\times c$ in mm^3

transmission with time for different samples. The relative change of transmission in LN:Mn:Ce is much larger than that of LN:Mn:Fe. We performed the sensitization experiment with the Mn singly–doped sample (LN:Mn), too. As it is seen from Figure 7.3, no change in absorption can be observed in this case. This means that the absorption variation in LN:Mn:Ce can be attributed to the filling of Ce traps with the help of UV light, and not to some kinds of emptied background impurities (that would be present in LN:Mn, too).

Figure 7.4 shows the transmission spectra of LN:Mn:Ce before and after UV illumination for 2 hours. It is seen from Figure 7.4 shows that after 2 h UV illumination, there is a broad induced absorption in the range from 450 nm to 650 nm. The large absorption caused by UV makes the material promising for two-center holographic recording at red.

Holographic Recording experiments

We first performed normal holographic recording experiments (with only two recording beams) with crystals LN, LN:Fe, LN:Ce, and LN:Mn:Ce. We recorded and read–out a plane wave hologram in transmission geometry by two red beams (wavelength 633 nm, total intensity 26 mW/cm^2, ordinary polarization) illuminating the crystal symmetrically at an incident angle (between the propagation direction of each red

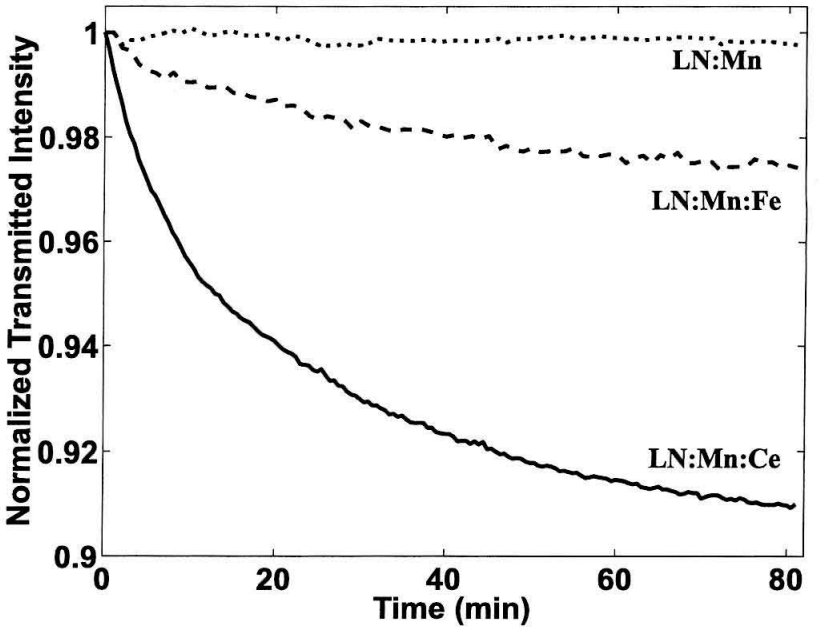

Figure 7.3: Variation of normalized transmitted intensity of a very weak red beam (wavelength 633 nm) during illumination with UV light (wavelength 404 nm and intensity 4 mW/cm^2) for variously–doped $LiNbO_3$ crystals. The samples were first strongly oxidized to ensure that most of the shallower centers are initially empty.

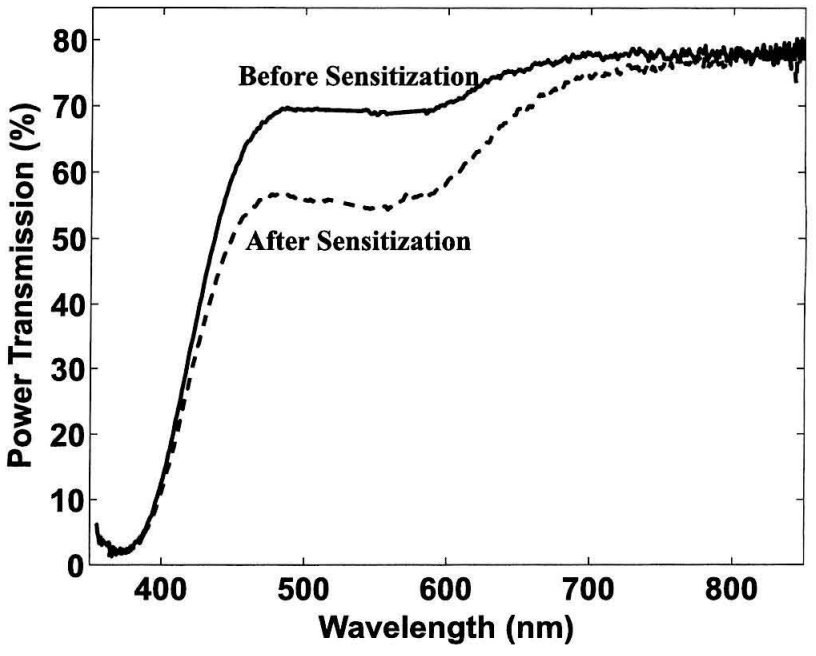

Figure 7.4: Transmission spectra of a $LiNbO_3$:Mn:Ce crystal (LN:Mn:Ce) before and after 2 hours sensitization with UV light (wavelength 404 nm and intensity 4 mW/cm^2).

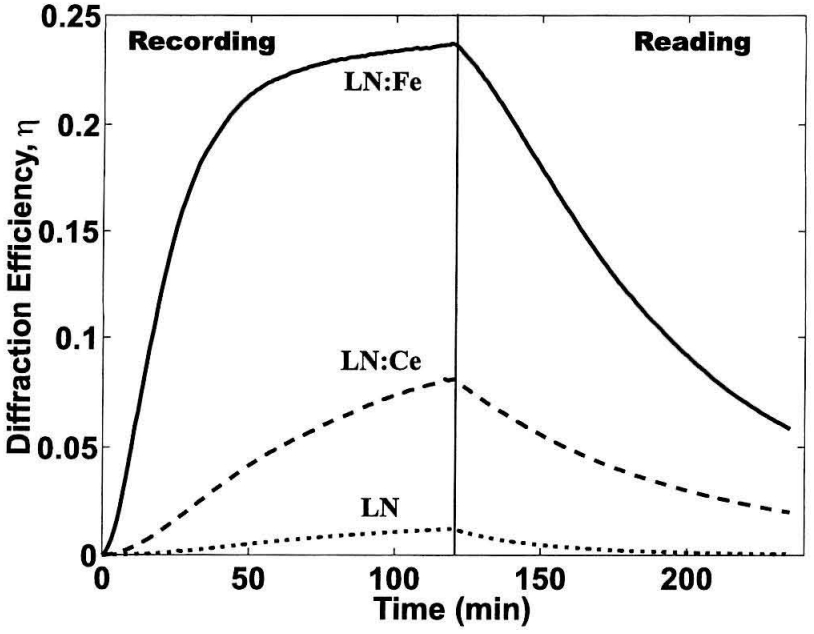

Figure 7.5: Recording and read–out curves for nominally pure, Ce–doped and Fe–doped $LiNbO_3$. The three samples have the same dimensions with the thickness $d = 5$ mm. Recording is performed with two red beams (Wavelength 633 nm, total intensity 26 mW/cm^2, ordinary polarization, grating vector along c-axis, and grating period 0.8 μm), and read–out is performed with one of the recording beams.

beam and the surface normal of the entrance face of the crystal) of 23° in air. The grating vector of the interference pattern was parallel to the $c-$axis of the crystal.

Figure 7.5 shows the recording and read–out curves for the four crystals. All crystals were strongly reduced before the experiments to ensure that the shallower traps (that are used in holographic recording with red light) are partially populated. The holographic recording sensitivity for each crystal can be measures from Figure 7.5. The measured sensitivity values are S(LN)=0.002 cm/J, S(LN:Ce)=0.007 cm/J, S(LN:Mn:Ce)=0.020 cm/J, S(LN:Fe)=0.033 cm/J. Clearly, the increase of Ce concentration leads to an increase of recording sensitivity. Note that Mn centers are too deep to participate in holographic recording with red light. Therefore, the $LiNbO_3$:Mn:Ce crystal (LN:Mn:Ce) acts like a singly–doped one with a Ce level of 0.085 wt%, which corresponds to a Ce concentration of $C_{Ce} = 14 \times 10^{24}$ m^{-3}. This is twice as large as the Fe concentration in LN:Fe ($C_{Fe} \leq 7 \times 10^{24}$ m^{-3}). Despite the

larger doping concentration, the sensitivity in LN:Mn:Ce is still smaller than that in LN:Fe. Therefore, Fe is a more effective impurity than Ce for holographic recording in $LiNbO_3$ in transmission geometry.

We also performed two–center holographic recording experiments with doubly–doped crystals LN:Mn:Ce and LN:Mn:Fe. The crystals were oxidized to ensure that the shallower traps as well as a portion of the deeper traps are initially empty. The crystals were first illuminated with UV light for 2 hours. Then, a plane wave hologram in transmission geometry was recorded for 3 hours with UV (wavelength 404 nm, intensity 4 mW/cm^2) and two recording red beams (wavelength 633 nm, total intensity 26 mW/cm^2). After recording, UV and one of the red beams were blocked, and the hologram was read–out by the other recording beam. Figure 7.6 shows the recording and read–out curves for LN:Mn:Ce. As Figure 7.6 shows, the maximum diffraction efficiency obtained in two–center recording in LN:Mn:Ce is 2.5%. We also performed a similar experiment with LN:Mn:Fe using the same setup and the same experimental conditions. We obtained a maximum diffraction efficiency of 25% for LN:Mn:Fe, which is approximately ten times as large as that obtained in LN:Mn:Ce.

Explanation of the experimental results

Although sensitization experiments suggest that Ce is more sensitive to red light than Fe, holographic recording experiments show the reverse. To investigate the reason for these two different results, we performed bulk photovoltaic current measurements on LN:Fe and LN:Ce. As explained in previous chapters, one advantage of $LiNbO_3$:Fe crystals is the large bulk photovoltaic constant (at the right wavelength). Recording sensitivity and saturation diffraction efficiency in holographic recording depend on the photovoltaic constant [13, 72], especially in transmission geometry. A small bulk photovoltaic constant of a trap (at recording wavelength) in $LiNbO_3$ results in small recording sensitivity and saturation diffraction efficiency even if the crystal has good absorption at the recording wavelength.

The conventional method for measuring the bulk photovoltaic constant of a crystal at a specific wavelength is to illuminate the crystal with the light of that wavelength

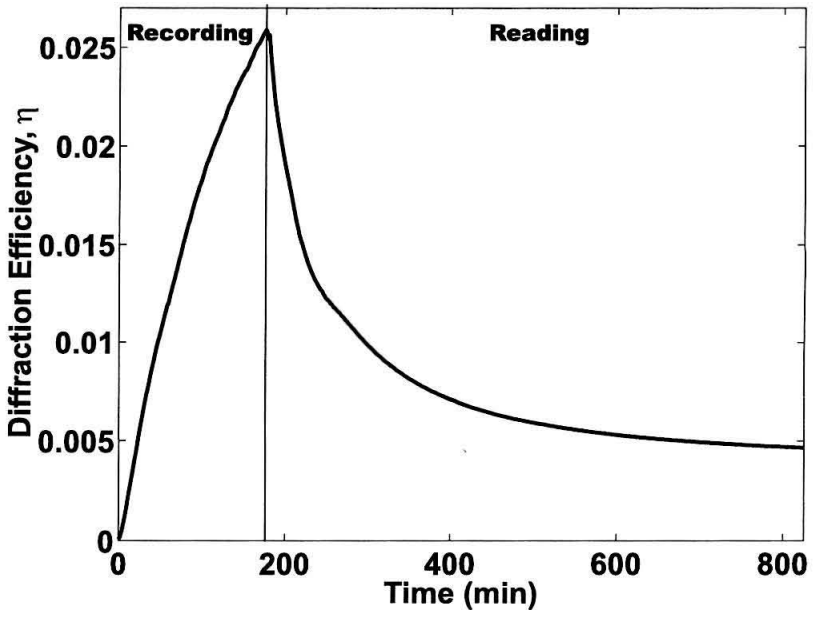

Figure 7.6: Recording and read–out curves for two–center holographic recording with UV and red in LN:Mn:Ce. During recording, a UV beam (wavelength 404 nm and intensity 4 mW/cm^2) as well as two recording beams illuminate the crystal. The properties of the recording (red) beams are the same as those described in the caption of Figure 7.5.

and measure the current in the short–circuited situation. By homogeneous illumination, the bulk photovoltaic current density is proportional to the absorbed power density, i.e.,

$$J = \kappa' \alpha I, \tag{7.15}$$

where I is the incident intensity, α is the absorption coefficient, and κ' is the bulk photovoltaic constant depending mainly on absorption center and wavelength. For thick samples, light depletion due to absorption must be considered and an averaged light intensity $\bar{I} = I[1-\exp(-\alpha d)](\alpha d)^{-1}$ must be used. Note that Equation (7.15) for the bulk photovoltaic current is different from the ones we used in previous chapters, i.e.

$$J = \kappa_{\mathrm{Fe}} N_{\mathrm{Fe}}^{-} I \tag{7.16}$$

for $LiNbO_3$:Fe crystals. Therefore, we used κ' instead of κ for the bulk photovoltaic constant in Equation (7.15). The reason for using a different formula is that κ' is easier to measure from Equation (7.15), since α, I, and J are easily measured. Since κ' and κ are proportional, we can easily calculate κ from κ'.

Measurements of the photocurrents were made with an electrometer having an input impedance much less than the crystal impedance. For illumination, we used a diode-pumped frequency-doubled Nd:YAG laser (wavelength 532 nm and power 400 mW). We expanded the ordinarily polarized beam to illuminate the whole sample homogeneously. All measurements were made at room temperature (25°C). After illuminating the sample for at least 10 minutes, the steady-state photocurrent was detected. The delay is required to eliminate the influence of pyroelectric currents. The determined photovoltaic constant for reduced LN:Fe is $\kappa' = 1.3 \times 10^{-9}$ cm/V at 532 nm, which is in good agreement with the results reported by Krätzig and Kurz [72]. For reduced LN:Ce, we measured $\kappa' = 0.4 \times 10^{-9}$ cm/V at 532 nm. We also illuminated the samples with ordinarily polarized red light (633 nm) to measure κ'

at red wavelength. We obtained $\kappa' = 0.8 \times 10^{-9}$ cm/V for LN:Fe, while the value of the κ' in LN:Ce could not be determined under our experimental accuracy.

Our results suggest that Ce acts as a photorefractive center in $LiNbO_3$. However, it does not have a large photovoltaic constant, especially at red. Therefore, the role of diffusion in holographic recording in $LiNbO_3$:Ce crystals becomes important. The diffusion field (E_D) is equal to

$$E_D = \frac{k_B T}{q} K = \frac{k_B T}{q} \frac{2\pi}{\Lambda} , \tag{7.17}$$

where K and Λ are the magnitude of the grating vector and grating period, respectively. Furthermore, k_B, T, and q are the Boltzmann constant, absolute temperature, and electronic charge, respectively. As Equation (7.17) shows, we can increase the diffusion field by reducing the grating period (Λ). This can be accomplished by increasing the angle between the recording beams. Therefore, the largest value of E_D is obtained in reflection geometry.

To compare the role of diffusion in $LiNbO_3$:Ce and $LiNbO_3$:Fe crystals, we performed holographic recording experiments with LN:Fe and Ln:Ce in reflection geometry. Both crystals were highly reduced before the experiment to ensure adequate electron concentration in the effective traps (Fe or Ce). In our experiment, two ordinarily polarized beams impinge on the two opposite c-faces of the LN:Ce crystal, with an angle of incidence of about 5° in air. The length of the sample along the c-axis is 7 mm. The diffraction efficiency as a function of recording time is monitored. For the sake of comparison with the performance of transmission gratings, we convert the efficiency into modulation of refractive index by taking into account of reflection by using the following relations [52]

$$\eta = R \sin^2 \left(\frac{\pi \Delta n d}{\lambda \cos \theta_i} \right) , \tag{7.18}$$

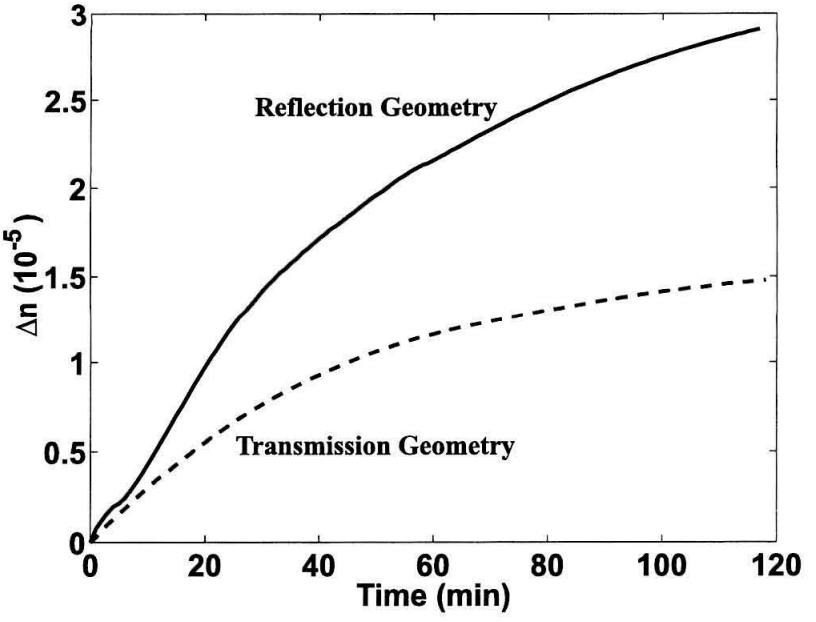

Figure 7.7: Modulation of the refractive-index as a function of recording time for a reflection geometry and a transmission geometry hologram in LN:Ce. Wavelength and total intensity of the recording beams are 633 nm and 26 mW/cm^2, respectively. In transmission geometry both beams impinge on the $b-$face with an angle of 23° while in reflection geometry both beams impinge on the two opposite $c--$faces with an angle of 5° in air. The grating vector of the interference pattern in both cases was parallel to the $c--$axis of the crystal.

for transmission grating and

$$\eta = R\tanh^2\left(\frac{\pi\Delta nd}{\lambda\cos\theta_{\rm i}}\right) \tag{7.19}$$

for reflection grating. In the above equations, R is the factor caused by reflection loss, $\theta_{\rm i}$ is the angle of incidence inside the crystal, d is the crystal thickness, and the absorption is not considered due to the small value at red.

Figure 7.7 shows the recording curve for a transmission geometry and a reflection geometry plane–wave hologram recorded in LN:Ce. As shown in Figure 7.7, recording sensitivity in the reflection geometry is higher than that in the transmission geometry. The corresponding sensitivity in case of reflection geometry is $S = 0.009$ cm/J. The modulation of refractive-index (Δn) in the reflection geometry is twice that in the

transmission geometry for LN:Ce. In LN:Fe, however, the reflection grating is only 1.4 times stronger than the transmission grating. This shows that the role of diffusion in $LiNbO_3$:Ce crystals is more important than that in $LiNbO_3$:Fe crystals. This can also be seen from the following formula for the saturation space–charge field (E_{sc}) [59]

$$E_{sc} = -\left[\frac{E_P^2 + E_D^2}{(1 + E_D/E_q)^2 + (E_P/E_q')^2}\right]^{1/2} , \tag{7.20}$$

where E_P is the photovoltaic field that is proportional to the bulk photovoltaic constant (κ or κ'), and E_q and E_q' are limiting space-charge fields determined by effective trap density and filled trap density, respectively. Since we used strongly reduced crystals in our experiments, no limitation of space-charge fields is present. Therefore we can simplify Equation (7.20) to obtain

$$|E_{sc}| = (E_P^2 + E_D^2)^{1/2} . \tag{7.21}$$

Generally, the photovoltaic field is independent of grating period, but the diffusion field is larger at smaller grating periods. Therefore, the total space-charge field in the reflection geometry is larger than that in the transmission geometry due to the increase of the diffusion field. The enhancement of performance for the Fe-doped sample in the reflection geometry is not so large. This can be attributed to a much higher photovoltaic field in $LiNbO_3$:Fe crystals. However, the enhancement of performance in reflection geometry is significant in $LiNbO_3$:Ce crystals due to the small photovoltaic field.

In conclusion, our results show that Ce is an active red-sensitive photorefractive center in $LiNbO_3$ and can play an important role in the charge transport during holographic recording. However, the photovoltaic constant in $LiNbO_3$:Ce crystals is smaller than that in $LiNbO_3$:Fe crystals. As a result, sensitivity and $M/\#$ in holographic recording in $LiNbO_3$:Ce crystals are smaller than those in $LiNbO_3$:Fe crystals. Therefore, Ce is not a good choice to replace Fe in $LiNbO_3$ in both normal

and two–center recording.

7.7.4 Using $LiTaO_3$ crystals for two–center recording

If we can not find appropriate shallower traps in $LiNbO_3$, it is highly recommended to test $LiTaO_3$. The properties of $LiTaO_3$ are similar to those of $LiNbO_3$. The advantage of $LiTaO_3$ is its wide energy gap ($\simeq$ 4 eV) that opens up the possibility of finding more photorefractive centers that might be too shallow or too deep in $LiNbO_3$, but not in $LiTaO_3$. Even if we can find appropriate shallower traps in $LiNbO_3$, we still recommend testing $LiTaO_3$ for two–center recording.

7.8 Conclusions

We showed that two–center recording has promising system parameters. This increases the hope for the realization of practical holographic read / write memory systems. We also outlined the design of such a practical memory system. The main challenge in such a design is to use the best trade off among the dynamic range ($M/\#$), sensitivity (S), and persistence ($R/\#$). To improve the performance of two–center recording, it is required to find shallower traps in $LiNbO_3$ that are most sensitive to red. The use of $LiTaO_3$ is also a possibility due to its wide band gap.

Chapter 8 Conclusions and future work

8.1 Conclusions

Our main accomplishment in this thesis is solving satisfactorily the most important and long lasting problem of erasure during read–out of holograms recorded in photorefractive crystals. This accomplishment is the result of the careful investigation and good understanding of the physical mechanisms responsible for the drawbacks of the pre–existing methods for solving the same problem. The initial performance measures of our proposed method (two–center recording) even at low intensities are in all aspects at least one order of magnitude better than those of the highly optimized competing methods with much higher intensity requirements. We believe that there is still a lot of room for improving our proposed method. The invention of two–center recording revitalized the hope for the realization of holographic read / write memory systems. The important results obtained in the individual chapters of this thesis are as follows:

In Chapter 2, we proposed for the first time the most complete explanation of persistent two–step holographic recording in $LiNbO_3$:Fe crystals using green or blue light for sensitization and infrared light for recording. These explanations were based on the development of an analytic solution for the governing equations of two–step recording. The analytic solution agrees very well with both the numerical solution and the experimental results. It turns out that the most important drawback of two–step recording methods using polarons as shallow traps is the short effective lifetime of the electrons in these traps. This drawback results in very high intensity requirements for recording in congruently melting $LiNbO_3$:Fe crystals. Although the usage of undoped stoichiometric $LiNbO_3$ alleviates the intensity requirements to some extent, it limits the maximum obtainable dynamic range and sensitivity to a large extent. Therefore, it is preferable to replace polarons with some long lifetime traps. This can be done

by using doubly–doped crystals. This important conclusion was the initial gateway toward the invention of two–center holographic recording.

In Chapter 3, we showed that the basic idea of using a doubly–doped $LiNbO_3$ crystal with one sensitizing beam and two recording beams for persistent holographic recording works very well if the crystal is properly annealed. To understand the main physical mechanisms responsible for two–center holographic recording, we developed a theoretical model for holographic recording in $LiNbO_3$:Fe:Mn crystals. We performed several experiments to obtain the necessary unknown parameters of the model that were not available in the literature. The model agrees very well with the experimental results. With the help of this model, we developed a good understanding of the physical processes involved in two–center recording. As an example, the presence of two gratings in the deeper and shallower traps and the role of sensitizing and recording beams were fully understood. The obvious result of this understanding was the successful explanation of all observed experimental results and the finding of possible ways to solve the remaining problems of the method. Furthermore, we proposed and demonstrated an optimization scheme with the help of the model for optimizing the performance of two–center recording.

In Chapter 4, we covered some of the remaining system issues in two–center recording. We showed that the sensitivity of the method can be highly improved by using green light instead of red light for recording. Using green light for recording results in a partial loss in persistence, but the remaining persistence is acceptable for most practical purposes. We also showed that we can not improve the sensitivity of either normal recording or two–center recording by increasing electron mobility through using stoichiometric or Mg doped crystals. Furthermore, we showed that the conventional recording schedule for hologram multiplexing can be used in two–center recording if we use appropriate values for saturation hologram strength and erasure time constant. Finally, we showed that the effect of fanning in two–center recording is much less than that in normal recording.

In Chapter 5, we compared two–center and two–step recording methods. We showed that two–step recording using polarons always suffers from the existence of

an intensity threshold for recording and sensitizing beams, although there is no intensity threshold in two–center recording. The only possible advantage of two–step recording is the possibility of obtaining higher dynamic range at huge intensities. The performance of two–center recording depends mainly on the ratio of the intensities of recording and sensitizing beams and not on the absolute intensities. This results in the lack of both an intensity threshold and high dynamic range at huge intensities. By comparing the existing experimental results, we showed that the initial performance measures of two–center recording at low intensities are already better than the best values obtained in highly optimized two–step recording at high intensity by at least one order of magnitude. The difference between the performance measures of the two systems is very large at low intensities due to the existence of the intensity threshold in two–step recording. All these advantages of two–center recording over two–step recording are due to the very long lifetime of the shallower traps (as well as the deeper traps) in this recording scheme.

In Chapter 6 we showed that the range of performance characteristics obtained by using doubly–doped $LiNbO_3$ crystals is much larger than that obtained by using single doped crystals even in normal recording (recording with only two recording beams). We can even design some effective traps by using doubly–doped crystals. Using two–center recording in doubly–doped crystals results in having persistence as another degree of freedom in the design of holographic storage systems. We defined for the first time a measure for persistence ($R/\#$) as the number of times the entire information in a standard memory module can be read before the diffraction efficiency drops below some standard value. The main challenge in designing holographic storage system is the wise trade off among dynamic range ($M/\#$), sensitivity (S), and persistence ($R/\#$) to obtain the appropriate performance for the desired application.

In Chapter 7, we derived the relationship among the material parameters ($M/\#$, S, and $R/\#$) and the system parameters like recording and read–out rates, access time, and storage capacity. We also presented an outline for the design of a practical compact memory module along with possible ways for improving the performance of two–center recording.

8.2 Future work

The aim of this thesis is to cover all the details that need to be understood in two–center recording. Although most of the basic features of the method have been addressed in this work, the novel nature of the method opens up many doors for future research in theory, material improvement, and system design and demonstration.

8.2.1 Theory

Although the model we developed explains all the experimental results, it is useful to find approximate analytic solutions for the governing equations of two–center recording. Such an analytic solution might have an impact on the directions for future research. Note that the analytic solution we developed for two–step recording lead us to a very good understanding of the method and the problems involved, and finally resulted in the invention of two–center method. Therefore, finding analytic formulas for the important performance parameters of two–center recording is important. For example, we mentioned in the optimization of two–center recording that the optimization procedures for the different design parameters (concentrations, intensities, etc.) are not independent from each other. The analytic formulas for the important parameters of two–center recording uncover these dependences and make a more complete and global optimization possible.

8.2.2 Improving material properties

This part of the research has the highest priority as the design of successful practical storage systems depends on the material properties we can obtain. As explained in Chapter 7, two parallel directions must be taken for improving material properties. The first one is the trial of the possible candidates for the shallower traps that are most sensitive to red light. These candidates include vanadium (V) from the first row and a few other elements from the second row of transition metals, especially ruthinium (Ru).

The second research direction involves the detailed investigation of $LiTaO_3$ as a possible substitute for $LiNbO_3$. The photorefractive centers that work in $LiNbO_3$ must be put into $LiTaO_3$ as dopands and their relative positions in the band gap of $LiTaO_3$ must be understood. Other dopands that do not work in $LiNbO_3$ but are known to have different valance states must be tested in $LiTaO_3$ as they might be too shallow or too deep for $LiNbO_3$ and not for $LiTaO_3$. Furthermore, the important properties (absorption cross section, photovoltaic coefficient, etc.) of the different working traps in $LiTaO_3$ must be measured by performing appropriate experiments. Normal recording as well as two–center recording experiments must be performed using $LiTaO_3$ crystals doped with different dopands, and the obtained performance parameters ($M/\#$, S, and $R/\#$) must be compared with those obtained by using $LiNbO_3$.

Another direction for future research in recording materials is to develop a model that can at least approximately predict the properties of the different traps in $LiNbO_3$. Even first order approximations might be helpful in assigning the priorities for testing different candidates for the shallower traps.

8.2.3 System design

Several projects can be defined for the future work in two–center recording systems. One interesting possibility is the demonstration of a simple prototype of a memory module consisting of 1000 multiplexed holograms in a $LiNbO_3$:Fe:Mn crystal using two–center recording. Sensitization and recording in such a memory module must be performed with UV (wavelength 404 nm) and green (wavelength 514 nm) light, respectively. If better materials are developed, they must be used in such modules. Careful experiments for multiplexing many data holograms using both angle multiplexing and wavelength multiplexing and comparing the performance of the two multiplexing schemes is another interesting task to do. Careful evaluation of signal to noise ratio in all cases and understanding the dominant noise sources are necessary in designing practical memory modules. Finally, a careful experimental comparison of

transmission and 90° recording geometries and finding the ways to solve the problem of each geometry is also important in the design of the memory module.

8.2.4 Localized holographic recording

Two–center holographic recording enables us to record holograms in slices or even small spots of the material. Multiplexing holograms by recording them in different slices of the recording material can be performed by sensitizing only one slice at a time. These slices can be non–overlapping. Therefore, a recorded hologram is not erased during the recording of the subsequent holograms, and we can record multiple strong holograms. The investigation of the different properties of these multiplexed holograms is a very interesting project. A complete work in this direction must include the variation of the diffraction efficiency of each hologram with the total number of holograms, possible redefinition of the $M/\#$ for this case, finding the limitations on the maximum number of holograms we can record, investigating the effect of noise and crosstalk in localized recording, and comparison of the performances of normal and localized two–center recording. We can also try to record holograms in small spots of the material by focusing the sensitizing beam to a small spot.

Another interesting project in this direction is to record a specified pattern of permittivity ($\epsilon(x, y, z)$) by recording several holograms in the slices of the material. Calculation of the minimum feature size we can record, and comparing it to that obtained by normal two–center recording is very interesting. Experimental demonstration of the theoretical findings would also be challenging and interesting.

Bibliography

[1] J. Baquedano, M. Carrascosa, L. Arizmendi, and J. M. Cabrera, "Erasure Kinetics and Spectral Dependence of the Photorefractive Effect in Fe:$LiNbO_3$," J. Opt. Soc. Am. B **4**, 309 (1987).

[2] D. Gabor, "A New Microscopic Principle," Nature **161**, 777 (1948).

[3] H. J. Caulfield, *Handbook of Optical Holography.* Academic Press, San Diego, 1979.

[4] R. J. Collier, C. B. Burckhardt, and L. H. Lin, *Optical Holography.* Academic Press, New York, 1980.

[5] G. O. Reynolds, J. B. DeVelis, G. B. Parrent, Jr., and B. J. Thompson, *Physical Optics Notebook: Tutorials in Fourier Optics.* SPIE Optical Engineering Press (Bellingham, Washington), 1989.

[6] F. T. S. Yu and S. Jutamulia, *Optical Signal Processing, Computing and Neural Networks.* John Wiley & Sons Inc., 1992.

[7] S. Breer and K. Buse, "Wavelength Demultiplexing with Volume Phase Holograms in Photorefractive Lithium Niobate," Appl. Phys. B **66**, 339 (1998).

[8] D. Psaltis and F. Mok, "Holographic Memories," Scientific American, **273**, 70 (1995).

[9] I. McMichael, W. Christian, D. Pletcher, T. Y. Chang, and J. H. Hong, "Compact Holographic Storage Demonstrator with Rapid Access," Appl. Opt. **35**, 2375 (1996).

[10] J. Ashley, M.-P. Bernal, M. Blaum, G. W. Burr, H. Coufal, R. K. Grygier, H. Günter, J. A. Hoffnagle, C. M. Jefferson, R. M. MacFarlane, B. Mar-

cus, R. M. Shelby, G. T. Sincerbox, and G. Wittmann, "Holographic Storage Promises High Data Density," Laser Focus World, pp. 81–93 (November 1996).

[11] H. M. Smith (Editor), *Holographic Recording Materials, Topics in Applied Physics (Vol. 20)*. Springer (Berlin, Heidelberg), 1977.

[12] P. Günter and J. P. Huignard (Editors), *Photorefractive Materials and Their Applications I, Topics in Applied Physics (Vol. 61)*. Springer (Berlin, Heidelberg), 1988.

[13] A. M. Glass, D. von der Linde, and T. J. Negran, "High–Voltage Bulk Photovoltaic Effect and the Photorefractive Process in $LiNbO_3$," Appl. Phys. Lett. **25**, 233 (1974).

[14] A. Ashkin, G. D. Boyd, J. M. Dziedzic, R. G. Smith, A. A. Ballman, J. J. Levinstein, and K. Nassau, "Optically–Induced Refractive Index Inhomogeneities in $LiNbO_3$ and $LiTaO_3$," Appl. Phys. Lett. **9**, 72 (1966).

[15] H. Kurz, E. Krätzig, W. Keune, H. Engelmann, U. Gonser, B. Dischler, and A. Räuber, "Photorefractive Centers in $LiNbO_3$, studied by Optical–, Mössbauer– and EPR–Methods," Appl. Phys. **12**, 355 (1977).

[16] H. Franke, H. G. Festl, and E. Krätzig, "Light–Induced Refractive Index Changes in PMMA Films doped with Styrene," Colloid and Polymer Science **262**, 213 (1984).

[17] K. Curtis and D. Psaltis, "Recording of Multiple Holograms in Photopolymer Films," Appl. Opt. **31**, 7425 (1992).

[18] L. Dhar, A. Hale, H. E. Katz, M. L. Schilling, M. G. Schnoes, and F. C. Schilling, "Recording Media that Exhibit High Dynamic Range for Digital Holographic Data Storage," Opt. Lett. **24**, 487 (1999).

[19] S. J. Zilker, T. Bieringer, D. Haarer, R. S. Stein, J. W. van Egmond, and S. G. Kostromine, "Holographic Data Storage in Amorphous Polymers," Adv. Mater. **10**, 855 (1998).

[20] S. Follonier, C. Bosshard, F. Pan, and P. Günter, "Photorefractive Effects Observed in 4–N, N–dimethylamino–4'–N'–methyl–stilbazolium toluene–p–sulfonate," Opt. Lett. **21**, 1655 (1996).

[21] K. Meerholz, B. L. Volodin, Sandalphon, B. Kippelen, and N. Peyghambarian, "A Photorefractive Polymer with High Optical Gain and Diffraction Efficiency near 100%," Nature **371**, 497 (1994).

[22] J. J. Amodei and D. L. Staebler, "Holographic Pattern Fixing in Electro–Optic Crystals," Appl. Phys. Lett. **18**, 540 (1971).

[23] F. Micheron and G. Bismuth, "Electrical Control of Fixation and Erasure of Holographic Patterns in Ferroelectric Materials," Appl. Phys. Lett. **20**, 79 (1972).

[24] D. von der Linde, A. M. Glass, and K. F. Rodgers, "Multiphoton Photorefractive Processes for Optical Storage in $LiNbO_3$," Appl. Phys. Lett. **25**, 155 (1974).

[25] H. Vormann and E. Krätzig, "Two Step Excitation in $LiTaO_3$:Fe for Optical Data Storage," Solid State Commun. **49**, 843 (1984).

[26] H. C. Külich, "A New Approach to Read Volume Holograms at Different Wavelengths," Opt. Commun. **64**, 407 (1987).

[27] E. Chuang and D. Psaltis, "Storage of 1000 Holograms with use of a Dual–Wavelength Method," Appl. Opt. **36**, 8445 (1997).

[28] R. A. Rupp, "Investigation of the Dynamic Recording Process of Thick Refractive Index Gratings in Photorefractive Crystals by the Microphotometric Method," Appl. Phys. B **42**, 21 (1987).

[29] K. Buse, L. Holtmann, and E. Krätzig, "Activation of $BaTiO_3$ for Infrared Holographic Recording," Opt. Commun. **85**, 183 (1991).

[30] K. Buse, S. Breer, K. Peithmann, S. Kapphan, M. Gao, and E. Krätzig, "Origin of Thermal Fixing in Photorefractive Lithium Niobate Crystals," Phys. Rev. B **56**, 1225 (1997).

[31] L. Arizmendi, E. M. de Miguel–Sanz, and M. Carrascosa, "Lifetimes of Thermally Fixed Holograms in $LiNbO_3$:Fe Crystals," Opt. Lett. **23**, 960 (1998).

[32] R. S. Cudney, J. Fousek, M. Zgonik, P. Günter, M. H. Garrett, and D. Rytz, "Enhancement of the Amplitude and Lifetime of Photoinduced Space–Charge Fields in Multidomain Ferroelectric Crystals," Phys. Rev. Lett. **72**, 3883 (1994).

[33] J. Ma, T. Y. Chang, J. H. Hong, and R. R. Neurgaonkar, "Enhancement of Multiplexed Holograms in Cerium–Doped $Sr0.75Ba_{0.25}Nb_2O_6$," Phys. Rev. Lett. **78**, 2960 (1997).

[34] J. Ma, T. Chang, J. Hong, and R. Neurgaonkar, "Electrical Fixing of 1000 Angle–Multiplexed Holograms in SBN:75," Opt. Lett. **22**, 1116 (1997).

[35] S. Fries, S. Bauschulte, E. Krätzig, K. Ringhofer, and Y. Yacoby, "Spatial Frequency Mixing in Lithium Niobate," Opt. Commun. **84**, 251 (1991).

[36] S. Fries, "Spatial–Frequency Mixing in Electro–optic Crystals – Application to Nondestructive Read–Out of Optically Erasable Volume Holograms," Appl. Phys. A **55**, 104 (1992).

[37] F. H. Mok, "Angle–Multiplexed Storage of 5000 Holograms in Lithium Niobate," Opt. Lett. **18**, 915 (1993).

[38] K. Buse, "Light–Induced Charge Transport Processes in Photorefractive Crystals I: Models and Experimental Methods," Appl. Phys. B **64**, 273 (1997).

[39] K. Buse, "Light–Induced Charge Transport Processes in Photorefractive Crystals II: Materials," Appl. Phys. B **64**, 391 (1997).

[40] R. A. Rupp, H. C. Külich, U. Schürk, and E. Krätzig, "Diffraction by Difference Holograms in Electro–optic Crystals," Ferroelectrics **8**, 25 (1987).

[41] K. Buse, F. Jermann, and E. Krätzig, "Two–Step Photorefractive Hologram Recording in $LiNbO_3$:Fe," Ferroelectrics **141**, 197 (1993).

[42] K. Buse, F. Jermann, and E. Krätzig, "Infrared Holographic Recording in $LiNbO_3$:Cu," Appl. Phys. A **58**, 191 (1994).

[43] K. Buse, F. Jermann, and E. Krätzig, "Infrared Holographic Recording in $LiNbO_3$:Fe and $LiNbO_3$:Cu," Optical Materials **4**, 237 (1995).

[44] M. Horowitz, B. Fischer, Y. Barad, and Y. Silberberg, "Photorefractive Effect in a $BaTiO_3$ Crystal at the 1.5 μm Wavelength Regime by Two–Photon Absorption," Opt. Lett. **21**, 1120 (1996).

[45] B. C. Grabmaier, W. Wersing, and W. Koestler, "Properties of Undoped and MgO–Doped $LiNbO_3$; Correlation to the Defect Structure," J. Cryst. Growth **110**, 339 (1991).

[46] N. Iyi, K. Kitamura, F. Izumi, J. K. Yamamoto, T. Hayashi, H. Asano, and S. Kimura, "Comparative Study of Defect Structures in Lithium Niobate with Different Compositions," J. Solid State Chem. **101**, 340 (1992).

[47] N. Zotov, H. Boysen, J. Schneider, and F. Frey, "Application of Combined Neutron and X–Ray Powder Diffraction Refinements to the Structure of Congruent Lithium Niobate," Materials Science Forums **166–169**, 631 (1994).

[48] F. Jermann and J. Otten, "The Light–Induced Charge Transport in $LiNbO_3$:Fe at High Light Intensities," J. Opt. Soc. Am. B **10**, 2085 (1993).

[49] F. Jermann and E. Krätzig, "Charge Transport Processes in $LiNbO_3$ at High Intensity Laser Pulses," Appl. Phys. A **55**, 114 (1992).

[50] L. Paraschis, M. C. Bashaw, A. Liu, and L. Hesselink, "Resonant Two–Photon Processes for Nonvolatile Holography in Photorefractive Crystals under Continuous–Wave Illumination," J. Opt. Soc. Am. B **14**, 2670 (1997).

[51] G. E. Peterson, A. M. Glass, and T. J. Negran, "Control of the Susceptibility of Lithium Niobate to Laser–Induced Refractive Index Change," Appl. Phys. Lett. **19**, 130 (1971).

[52] H. Kogelnik, "Coupled Wave Theory for Thick Hologram Gratings," Bell Syst. Tech. J. **48**, 2909 (1969).

[53] R. T. Smith and F. S. Welsh, "Temperature Dependence of the Elastic, Piezoelectric, and Dielectric Constants of Lithium Tantalate and Lithium Niobate," J. Appl. Phys. **42**, 2219 (1971).

[54] A. Mansingh and A. Dhar, "The AC Conductivity and Dielectric Constant of Lithium Niobate Single Crystals," J. Phys. D: Appl. Phys. **18**, 2059 (1985).

[55] K. Onuki, N. Uchida, and T. Saku, "Interferometric Method for Measuring Electro–Optic Coefficients in Crystals," J. Opt. Soc. Am. **62**, 1030 (1972).

[56] G. J. Edwards and M. Lawrence, "A Temperature–Dependent Dispersion–Equation For Congruently Grown Lithium–Niobate," Opt. Quant. Electron. **16**, 373 (1984).

[57] Y. Ohmori, M. Yamaguchi, K. Yoshino, and Y. Inuishi, "Electron Hall Mobility in Reduced $LiNbO_3$," Jpn. J. Appl. Phys. **15**, 2263 (1976).

[58] N. V. Kukhtarev, "Kinetics of Hologram Recording and Erasure in Electro–optic Crystals," Sov. Tech. Phys. Lett. **2**, 438 (1976).

[59] N. V. Kukhtarev, V. B. Markov, S. G. Odoulov, M. S. Soskin, and V. L. Vinetskii, "Holographic Storage in Electro–optic Crystals," Ferroelectrics **22**, 949 (1979).

[60] C.-T. Chen, D. M. Kim, and D. von der Linde, "Efficient Hologram Recording in $LiNbO_3$:Fe Using Optical Pulses," Appl. Phys. Lett. **34**, 321 (1979).

[61] H. Guenther, R. Macfarlane, Y. Furukawa, K. Kitamura, and R. Neurgaonkar, "Two–Color Holography in Reduced Near–Stoichiometric Lithium Niobate," Appl. Opt. **37**, 7611 (1998).

[62] L. Hesselink, S. S. Orlov, A. Liu, A. Akella, D. Lande, and R. R. Neugaonkar, "Photorefractive Materials for Nonvolatile Volume Holographic Data Storage," Science **282**, 1089 (1998).

[63] Y. S. Bai, R. R. Neurgaonkar, and R. Kachru, "Resonant Two–Photon Photorefractive Grating in Praeseodymium–Doped Strontium Barium Niobate with cw Lasers," Opt. Lett. **21**, 567 (1996).

[64] Y. S. Bai and R. Kachru, "Nonvolatile Holographic Storage with Two–Step Recording in Lithium Niobate using cw Lasers," Phys. Rev. Lett. **78**, 2944 (1997).

[65] K. Buse, A. Adibi, and D. Psaltis, "Non–Volatile Holographic Storage in Doubly Doped Lithium Niobate Crystals," Nature **393**, 665 (1998).

[66] K. Buse, A. Adibi, and D. Psaltis, "Efficient Non–Volatile Holographic recording in Doubly Doped Lithium Niobate," J. Opt. A **1**, 237–238 (1999).

[67] A. Adibi, K. Buse, and D. Psaltis, "Two–Center Holographic recording," Submitted to J. Opt. Soc. Am. B (2000).

[68] D. L. Staebler and W. Phillips, "Hologram Storage in Photochromic $LiNbO_3$," Appl. Phys. Lett. **24**, 268 (1974).

[69] O. Thiemann and O. F. Sxhirmer, "Energy levels of several 3d impurities and EPR of Ti^{3+} in $LiNbO_3$," Proceedings of SPIE **1018**, 18 (1988).

[70] W. Phillips, J. J. Amodei, and D. L. Staebler, "Optical and Holographic Storage Properties of Transition Metal Doped Lithium Niobate," RCA Rev. **33**, 94 (1972).

[71] E. Krätzig and H. Kurz, "Photo–Induced Currents and Voltages in $LiNbO_3$," Ferroelectrics **13**, 295 (1976).

[72] E. Krätzig and H. Kurz, "Photorefractive and Photovoltaic Effects in Doped $LiNbO_3$," Optica Acta **24**, 475 (1977).

[73] D. Psaltis, D. Brady, and K. Wagner, "Adaptive Optical Networks using Photorefractive Crystals," Appl. Opt. **27**, 1752 (1988).

[74] R. Orlowski and E. Krätzig, "Holographic Method for the Determination of Photo–Induced Electron and Hole Transport in Electro–Optic Crystals," Solid State Commun. **27**, 1351 (1978).

[75] F. H. Mok, G. W. Burr, and D. Psaltis, "System Metric for Holographic Memory Systems," Opt. Lett. **21**, 896 (1996).

[76] P. Günter and J.-P. H. (eds.), *Topics in Applied Physics: Photorefractive Materials and their Applications I*, **61**. Springer Verlag, 1987.

[77] C. Moser, B. Schupp, and D. Psaltis, "Localized Holographic Recording in Doubly Doped Lithium Niobate," Opt. Lett. **25**, 162–164 (2000).

[78] C. Moser, I. Maravic, B. Schupp, A. Adibi, and D. Psaltis, "Diffrection Efficiency of Localized Holograms," Submitted to Opt. Lett. (2000).

[79] A. Adibi, K. Buse, and D. Psaltis, "Sensitivity improvement in two–center holographic recording," Opt. Lett. **25**, 539 (2000).

[80] A. Adibi, K. Buse, and D. Psaltis, "Effect of annealing in two–center holographic recording," Appl. Phys. Lett. **74**, 3767 (1999).

[81] A. Adibi, K. Buse, and D. Psaltis, "Multiplexing holograms in $LiNbO_3$: Fe: Mn crystals," Opt. Lett. **24**, 652 (1999).

[82] J. Feinberg, "Asymmetric Self–Defocusing of an Optical Beam from the Photorefractive Effect," J. Opt. Soc. Am. **72**, 46 (1982).

[83] R. Magnusson and T. K. Gaylord, "Laser Scattering Induced Holograms in Lithium Niobate," Appl. Opt. **13**, 1545 (1974).

[84] Y. Taketomi, J. E. Ford, H. Sasaki, J. Ma, Y. Fainman, and S. H. Lee, "Incremental Recording for Photorefractive Hologram Multiplexing," Opt. Lett. **16**, 1774 (1991).

[85] K. Peithmann, K. Buse, A. Wiebrock, and E. Krätzig, "Incremental Holographic Recording in Lithium Niobate with Active Phase Locking," Opt. Lett. **23**, 1927 (1998).

[86] H. Guenther, G. Wittmann, R. M. Macfarlane, and R. R. Neurgaonkar, "Intensity Dependence and White–Light Gating of Two–Color Photorefractive Gratings in $LiNbO_3$," Opt. Lett. **22**, 1305–1307 (1997).

[87] W. Liu and D. Psaltis, "Pixel size limit in holographic memories," Opt. Lett. **24**, 1340 (1999).

[88] J.-J. P. Drolet, E. Chuang, G. Barbastathis, and D. Psaltis, "Compact, Integrated Dynamic Holographic Memory with Refreshed Holograms," Opt. Lett. **22**, 552 (1997).

[89] T. Tamir, *Guided-Wave Optoelectronics.* Springer (Berlin, Heidelberg, New York), 1990.

[90] R. J. Holmes, Y. S. Kim, C. D. Brandle, and D. M. Smyth, "Evaluation of Crystals of $LiNbO_3$ Doped with MgO or TiO_2 for Electro–optic Devices," Ferroelectrics **51**, 41 (1983).

[91] J. Wen, L. Wang, Y. Tang, and H. Wang, "Enhanced Resistance to Photorefraction and Photovoltaic Effect in Li–Rich $LiNbO_3$:Mg Crystals," Appl. Phys. Lett. **53**, 260 (1988).

[92] F. Nitanda, Y. Furukawa, S. Makio, M. Sato, and K. Ito, "Increased Optical Damage Resistance and Transparency in MgO–Doped $LiTaO_3$ Crystals," Jpn. J. Appl. Phys. **34**, 1546 (1995).

[93] T. R. Volk and N. M. Rubinina, "Nonphotorefractive Impurities in Lithium Niobate: Magnesium and Zinc," Sov. Phys. Solid State **33**, 674 (1991).

[94] T. Volk, M. Wöhlecke, N. Rubinina, N. V. Razumovski, F. Jermann, C. Fischer, and R. Böwer, "$LiNbO_3$ with the damage Resistant Impurity Indium," Appl. Phys. A **60**, 217 (1995).

[95] T. R. Volk, N. V. Razumovski, A. V. Mamaev, and N. M. Rubinina, "Hologram Recording in Zn–doped $LiNbO_3$ Crystals," J. Opt. Soc. Am. B **13**, 1457 (1996).

[96] J. K. Yamamoto, T. Yamazaki, and Y. Yamamishi, "Noncritical phase matching and photorefractive damage in SC_2O_3:$LiNbO_3$," Appl. Phys. Lett. **64**, 3228 (1994).

[97] D. K. McMillen, T. D. Hudson, J. Wagner, and J. Singleton, "Holographic Recording in Specially Doped Lithium Niobate Crystals," Opt. Express **2**, 491 (1998).

[98] X. Yue, A. Adibi, T. Hudson, K. Buse, and D. Psaltis, "Role of Cerium in Lithium Niobate for Holographic Recording," J. Appl. Phys. **87**, 4051 (2000).

[99] K. Megumi, H. Kozuka, M. Kobayashi, and Y. Furuhata, "High–Sensitive Holographic Storage in Ce–Doped SBN," Appl. Phys. Lett. **30**, 631 (1977).

[100] C. Yang, Y. Zhang, P. Yeh, Y. Zhu, and X. Wu, "Photorefractive Properties of Ce–$BaTiO_3$ Crystals," Opt. Commun. **113**, 416 (1995).

[101] S. X. Dou, Y. W. Lian, H. Gao, Y. Zhu, X. Wu, C. X. Yang, and P. X. Ye, "Self–Pumped Phase–Conjugation Properties of Cerium–Doped $BaTiO_3$ Crystals in the Near–Infrared," Appl. Opt. **34**, 2024 (1995).

[102] K. Xu, H. Xu, Y. Yuan, J. Hong, and Y. Xu, "Real–Time Holographic Optical Storage," Proceedings of SPIE **1078**, 331 (1989).

[103] S. Yin and F. T. S. Yu, "Specially Doped $LiNbO_3$ Crystal Holography Using a Visible–Light Low–Power Laser Diode," IEEE Photonics Technol. Lett. **5**, 581 (1993).